

# Modulation of Catalyst@MOF Host-Guest Composites in Pursuit of Synthetic Artificial Enzymes:

Author: Thomas M. Rayder

Persistent link: <http://hdl.handle.net/2345/bc-ir:108930>

This work is posted on [eScholarship@BC](#),  
Boston College University Libraries.

---

Boston College Electronic Thesis or Dissertation, 2020

Copyright is held by the author, with all rights reserved, unless otherwise noted.

# Modulation of Catalyst@MOF Host-Guest Composites in Pursuit of Synthetic Artificial Enzymes

Thomas M. Rayder

A dissertation  
submitted to the Faculty of  
the department of Chemistry  
in partial fulfillment  
of the requirements for the degree of  
Doctor of Philosophy

Boston College  
Morrissey College of Arts and Sciences  
Graduate School

April, 2020



**Modulation of Catalyst@MOF Host-Guest Composites in Pursuit of  
Synthetic Artificial Enzymes**

Thomas M. Rayder

Advisor: Chia-Kuang (Frank) Tsung, PhD and Jeffery A. Byers, PhD

Biological systems have evolved over time to favor structures beneficial for the efficient transformation of simple feedstocks to sophisticated products. In particular, enzymes have evolved such that cooperative and geometrically controlled interactions between active sites and substrates enhance catalytic activity and selectivity. Separation of these active sites from other incompatible catalytic components allows for chemical transformation in a stepwise fashion, circumventing the inherent limitations to performing reactions in a single step. This dissertation describes the use of porous crystalline materials called metal-organic frameworks (MOFs) as hosts to mimic the component separation and precise active site control observed in nature. The first phase of these efforts explores the use of dissociative “aperture-opening” linker exchange pathways in a MOF to encapsulate transition metal complexes for carbon dioxide hydrogenation to formate. This strategy is then used to separate two incompatible complexes and perform the cascade conversion of carbon dioxide to methanol, resulting in unique and previously unobserved network autocatalytic behavior. Finally, the modularity of the MOF host is leveraged to install beneficial functionality in close proximity to the encapsulated transition metal complex, leading to activity exceeding that of any reported homogeneous system for carbon dioxide reduction. The insights gained through these studies can inform the development of composites for other reactions, allowing for access to new and unique reaction manifolds.



## ACKNOWLEDGMENTS

I was once told by one of my PIs, “If getting a PhD was easy, everyone would have one.” I went into this journey knowing full well that it would be difficult, but went through with it regardless, and I’m extremely glad I did. If not for this experience I wouldn’t know even a fraction of what I know now, about chemistry or life. I was told by the same PI that going through graduate school as a joint student between two groups required something special. That something special for me is the people that have been there for me throughout this process and supported me the entire time. Without their support, I wouldn’t have lasted a year in graduate school, let alone five.

First, foremost, and above all else, I want to thank my fiancée Kristina, who has been supportive, loving, and understanding through all of the ups and downs of this process. Even when I was distant, stressed, or upset, you were always there to give me the stability and support that I needed. You mean more to me than I could ever put into words. I would never have reached this point without you, and I’m excited to spend the rest of our lives seeing what comes next.

I want to thank my friends, especially Zach. You’ve been a consistent steadying presence in the face of my anxiety and inconsistency for the past eight-plus years, and I even couldn’t begin to thank you properly for all that you’ve helped me get through. There was never any doubt in my mind who I would choose as my Best Man.

Thanks to my family, and especially my sister Kacey, who despite living on the other side of the country for the duration of my time at Boston College has always been there for me when I needed her. Here’s to the future adventures of the Rayder sibs.

Obviously, Frank and Jeff deserve thanks, for having faith in me through my slow start and for unique perspectives that resulted in the unique science that drove this thesis. I would not be the scientist or the man that I am today without guidance from both of you. It has been an absolute privilege working for both of you and learning from the well of knowledge you both provided. Especially in the last year, I feel that I have grown immensely as a chemist and a person and I owe you both a debt of gratitude for that.

Thanks to my friends in the Tsung and Byers labs, having people to vent to about science or life without judgment on whether I deserve to be where I am has been invaluable.

I want to thank the New England music scene for shaping my personality and giving me an escape when I needed to clear science from my mind, even if only for a few hours.

Finally, I want to extend thanks to my committee members, Prof. Matthias Waagele and Prof. Peter Zhang for valuable suggestions, especially early on in the multicomponent catalysis project.

## TABLE OF CONTENTS

<b>Table of Contents .....</b>	<b>i</b>
<b>List of Tables.....</b>	<b>iii</b>
<b>List of Figures .....</b>	<b>v</b>
<b>List of Schemes.....</b>	<b>ix</b>
<b>List of Abbreviations.....</b>	<b>x</b>
<b>1.0 Application of Host-Guest Chemistry in Metal-Organic Frameworks for New Catalytic Behavior .....</b>	<b>1</b>
<b>1.1 Introduction to Host-Guest Catalytic Systems.....</b>	<b>2</b>
1.1.1 Enzymes.....	3
1.1.1 Supramolecular Cages .....	4
1.1.1 Zeolites .....	5
1.1.1 Metal-Organic Frameworks.....	7
<b>1.2 Separating Catalytic Active Sites within a MOF.....</b>	<b>10</b>
1.2.1 Tethering of Active Species to Metal-Organic Frameworks.....	11
1.2.2 Enzyme encapsulation in MOFs.....	14
1.2.3 MOF-Encapsulated Nanoparticles .....	15
1.2.4 Noncovalent Encapsulation of Molecular Catalytic Guests.....	16
<b>1.3 Applying Host-Guest Constructs in Multicomponent Catalysis .....</b>	<b>18</b>
1.3.1 MOFs as Multicomponent Catalysts.....	19
1.3.2 Enzyme@MOF Composites in Tandem Catalysis.....	20
1.3.3 Multicomponent Catalysis in MOFs using NP@MOF Hybrids .....	22
1.3.4 Molecular Catalysts in MOF-Based Tandem Catalysis .....	24
<b>1.4 Employing Host Functionality Toward Noncovalent Influence in Catalysis ...</b>	<b>25</b>
1.4.1 Introduction of functionality in MOFs to control pore environment.....	26
1.4.2 Effects of MOF pore environment on dye behavior .....	27
1.4.3 Controlling catalytic behavior through MOF pore functionality .....	29
<b>1.5 The Scope of this Dissertation .....</b>	<b>30</b>
<b>2.0 Aperture-Opening Encapsulation of a Transition Metal Catalyst in a Metal-Organic Framework for CO<sub>2</sub> Hydrogenation to Formic Acid .....</b>	<b>40</b>
<b>2.1 Determining the Effectiveness of Aperture-Opening Encapsulation in UiO-66..</b>	<b>41</b>
2.1.1 Encapsulating Dye via Aperture-Opening Pathways in UiO-66.....	42
<b>2.2 Application of a Catalyst@UiO-66 Hybrid Formed by Aperture-Opening Encapsulation of a Transition Metal Complex .....</b>	<b>49</b>
2.2.1 Encapsulating a Ruthenium-PNP Complex in UiO-66.....	49
2.2.2 Assessing the Catalytic Behavior of 2-1@UiO-66 .....	51

2.2 Conclusion.....	57
<b>3.0 A Bioinspired Multicomponent Catalytic System for Converting Carbon Dioxide into Methanol.....</b>	<b>76</b>
3.1 Developing and Optimizing a Multicomponent System for CO <sub>2</sub> Hydrogenation to Methanol .....	78
3.1.1 Separating Active Components to Achieve Cascade Catalysis.....	81
3.1.2 Improving Activity by Manipulating Alcohol Additive Identity.....	90
3.2 Improving Catalyst Lifetime Through Heterogenization .....	94
3.2.1 Imparting Recyclability Through Full Heterogenization.....	94
3.2.2 Observing Network Autocatalytic Behavior at Low Additive Loadings.....	100
3.3 Conclusion .....	108
<b>4.0 Enzyme-Mimetic Modulation of Host Functionality Leading to Unprecedented Activity in CO<sub>2</sub> Hydrogenation to Methanol .....</b>	<b>136</b>
4.1 Improving Catalytic Activity by Introducing Outer-Sphere Functionality ....	139
4.1.1 Investigating the effect of linker functionality on catalytic activity .....	140
4.1.2 Characterizing the Ammonium Functionality .....	141
4.1.3 Exploring the role of the ammonium functionality in catalysis.....	143
4.1.4 Investigating the mechanistic role of the ammonium functionality .....	149
4.2 Increasing Methanol Production Through Full Catalyst Heterogenization ..	154
4.2.1 Improving catalyst lifetime through heterogenization .....	155
4.2.2 Tuning Network Autocatalytic Behavior in a Fully Heterogeneous System ....	157
4.3 Conclusion .....	163

## LIST OF TABLES

### CHAPTER 2

**Table 2-1.** Fluorescence intensity for dye-incorporated samples normalized by the total amount of dye incorporated as measured by UV/Vis absorbance for R6G-on-UiO-66 (left) compared to that of R6G@UiO-66 formed by encapsulation in n-butanol at 85 °C (middle) or deionized water at 55 °C (right).

**Table 2-2.** Determination of conditions under which the conversion of carbon dioxide to formate is not base-limited for **2-1**

### CHAPTER 3

**Table 3-1.** Esterification of formic acid to formate ester using UiO-66 as Lewis acid catalyst

**Table 3-2.** Table detailing optimization of carbon dioxide conversion to methanol using the described multicomponent system. <sup>a</sup>TON calculated based on highest loading between **3-1** and **3-2**

**Table 3-3.** Activity of carbon dioxide hydrogenation reactions under using various catalytic components: **3-1** ( $2.23 \times 10^{-7}$  mmol) or **3-1**@UiO-66 (10 mg, [Ru] =  $2.23 \times 10^{-7}$  mmol), UiO-66 (10 mg), and **3-2** ( $2.23 \times 10^{-7}$  mmol). Check marks indicate which species are present in each reaction. Reaction mixtures analyzed by <sup>1</sup>H NMR spectroscopy, Error in entry 1 (TON  $\pm$  150) is the average error of 3 runs (Figure 3-3).

**Table 3-4.** Assessment of cascade reaction through alterations intended to affect a single step. (<sup>a</sup>Formate product observed, TON(DBU):  $1.5 \times 10^6$ , TON(NEt<sub>3</sub>):  $8.3 \times 10^5$ ; <sup>b</sup>no EtOH; <sup>c</sup>**3-1**@“30-benz”-UiO-66; <sup>d</sup>**3-1**@“40-benz”-UiO-66; <sup>e</sup>**3-1**@Hf-UiO-66)

**Table 3-5.** Summary of catalysis results with alterations to standard conditions listed in reaction scheme

**Table 3-6.** Comparative test by ICP-OES for the loading of **3-4** complex in place of **3-1** to determine relative loading of **3-1** and **3-2** within [**3-1**,**3-2**]@UiO-66.

**Table 3-7.** Comparison between turnover number for **3-5** (TON<sub>(3-5)</sub>) and the multicomponent system of **3-1**@UiO-66 and **3-2** developed in this chapter (TON<sub>(MC)</sub>) at various pressures, temperatures, and reaction times in conditions otherwise optimized for that catalyst. Optimal conditions for **3-5**: **3-5** ( $5 \times 10^{-5}$  mmol), <sup>i</sup>Pr<sub>2</sub>NH (3.5 mmol), NaOEt (0.15 mmol), toluene (3 mL). Optimal conditions for **3-1**@UiO-66 + **3-2**: **3-1**@UiO-66 ( $2.2 \times 10^{-7}$  mmol Ru), **3-2** ( $2.2 \times 10^{-7}$  mmol), TFE (10 mmol), DMF (3 mL). \* = TON at optimized conditions, <sup>a</sup> = TON at reduced additive loading (0.35 mmol <sup>i</sup>Pr<sub>2</sub>NH for **3-5**,  $2.2 \times 10^{-7}$  mmol TFE for **3-1**@UiO-66 + **3-2**)

### CHAPTER 4

**Table 4-1.** Effect of host functionality on cascade production of methanol from carbon dioxide

**Table 4-2.** NMR titration of UiO-66-NH<sub>3</sub><sup>+</sup> against triethylamine.

**Table 4-3.** Effect of confinement and direct interaction between encapsulated catalyst and functionality on TON. Entries in which no additive is specified do not include an additive. (<sup>a</sup>10 mmol, <sup>b</sup>50 mmol)

**Table 4-4.** Effect of host functional group on the hydrogenation of carbon dioxide to formate

**Table 4-5.** Comparison of desiccant capabilities and selectivity for water over methanol for different porous solids used in the described cascade transformation. Quantification was performed by <sup>1</sup>H-NMR in CDCl<sub>3</sub> using tetrachloroethane as an external standard.

## LIST OF FIGURES

### CHAPTER 1

**Figure 1-1.** Structural representations of enzymes, supramolecular cages, zeolites and metal-organic frameworks

**Figure 1-2.** Summary of the directed evolution method for controlled enzyme function

**Figure 1-3.** Rate enhancement of Nazarov cyclization by  $[\text{Ga}_4\text{L}_6]^{12-}$

**Figure 1-4.** The ADOR method for zeolite modification, allowing access to IPC-2 and IPC-4 frameworks that are inaccessible by *de novo* assembly

**Figure 1-5.** Representation of reactions catalyzed by MOFs, including the esterification of levulinic acid by UiO-66 and conversion of propylene oxide to propylene carbonate by PCN-700.

**Figure 1-6.** Modification of metal-organic frameworks by node or linker elimination, or linker exchange

**Figure 1-7.** Accessible nodes allow for efficient catalysis in the use of MOF-808-pydc in the Meerwein-Ponndorf-Verley reduction of cyclohexanone and Ru-HKUST-1 in the dimerization of ethylene to 1-butene

**Figure 1-8.** Method used to tether a palladium complex to a MOF

**Figure 1-9.** UiO-67-bipy derivatives as hosts for transition metal catalysts in Suzuki-Miyaura cross-coupling and low-pressure carbon dioxide reduction

**Figure 1-10.** Post-synthetic metal exchange in “pincerMOFs”

**Figure 1-11.** Prevention of enzyme denaturation by unfolding through encapsulation in ZIF-90

**Figure 1-12.** Activity of nanoparticle@MOF composites for hydrogen evolution from hydrazine borane and carbon monoxide oxidation

**Figure 1-13.** Representation of two different strategies for electrostatically driven catalyst encapsulation as employed for the carboxylation of phenylacetylene and the hydrogenation of olefins

**Figure 1-14.** Use of linker/node tandem catalysis for the one-pot semisynthesis of artemisinin from dihydroartemisinic acid

**Figure 1-15.** Representation of multicomponent electro- or photocatalytic conversion of carbon dioxide to formate using encapsulated FDH@NU-1006-Rh

**Figure 1-16.** Representation of the tandem Au@MOF-Mo system enabling conversion of cyclooctene to cyclooctene oxide selectively over alkene hydrogenation using oxygen as the source oxidant

**Figure 1-17.** Representation of the FLP@MIL-101 cooperative system for imine reduction

**Figure 1-18.** The effect of functional groups on MOF-based catalysis exemplified by the influence of UiO-66 substituent on carbon dioxide cycloaddition

**Figure 1-19.** Representation of bathochromic shift in emission  $\lambda_{\text{max}}$  for CL-BI dye as a result of increasing MOF pore size

**Figure 1-20.** Influence of functional group on reactivity in the Knoevenagel condensation

## CHAPTER 2

**Figure 2-1.** Solvent and temperature dependency of encapsulation of R6G in UiO-66

**Figure 2-2.** Effect increasing exogenous linker concentration on R6G encapsulation in methanol and DMF

**Figure 2-3.** Nitrogen adsorption and desorption of UiO-66 before and after exposure to methanol at 55 °C for five days in the absence of guest

**Figure 2-4.** Dye encapsulation and leaching in various solvents. A) Amount of dye encapsulated in MOF in neat solvent at 55 °C for 5 days, B) percent of original encapsulated dye remaining in R6G@UiO-66 after exposure to solvents at 55 °C for 2 days represented in histogram and table form.

**Figure 2-5.** A) top: encapsulation of R6G in UiO-66; bottom: attempted encapsulation of Brilliant Blue G (BBG) in UiO-66. Both experiments conducted in methanol at 55 °C for five days. B) Dialysis experiment conducted by Zhehui Li with UiO-66 in water at 55 °C for 18 days; empirical formula for UiO-66 as determined from TGA analysis of MOF shown below corresponding dialysis bags.

**Figure 2-6.** Dialysis experiment carried out by Zhehui Li to probe dissociative linker exchange mechanism. A) TGA trace of UiO-66 before (black) and after after dialysis (red) after thermal activation; B) Diagram of species represented in each mass loss regime in the displayed TGA curve.

**Figure 2-7.** Comparison of molecular size between A) MOF host and B) Rhodamine 6G, C) Brilliant Blue G, or D) (<sup>t</sup>BuPNP)Ru(CO)HCl (**2-1**); E) Comparison between R6G and BBG encapsulated in UiO-66 or on its surface.

**Figure 2-8.** Effect of pre-treatment on Ruthenium loading in **2-1**@UiO-66 and **2-1**-on-UiO-66. A) Ruthenium concentration remaining in **2-1**@UiO-66 before pretreatment, after pre-treatment, and after multiple exposures to reaction conditions. B) Ruthenium loading in **2-1**-on-UiO-66 before and after exposure to reaction conditions.

**Figure 2-9.** PXRD of UiO-66, **2-1**@UiO-66 and **2-1**@UiO-66 after 5 cycles of CO<sub>2</sub> hydrogenation.

**Figure 2-10.** A) Activity of **2-1**@UiO-66 (TON = mmol HCOO<sup>-</sup>/mmol Ru) upon catalyst recycling. B) comparison of catalyst activity in first cycle (dark) to that upon addition of a second aliquot of DBU (light). C) Activity for **2-1** (blue) and **2-1**@UiO-66 (red) at different catalyst concentrations (mM).

**Figure 2-11.** Comparison of the activity of homogeneous (left) and encapsulated (right) catalysts in the presence of differently sized thiol poisons.

## CHAPTER 3

**Figure 3-1.** A) Biological inspiration for the reported cascade hydrogenation of carbon dioxide to methanol; B) The multicomponent system detailed in this chapter

**Figure 3-2.** Graphical representation of the dependence of TON for the hydrogenation of carbon dioxide to methanol on reaction temperature

**Fig. 3-3.** Representative <sup>1</sup>H-NMR spectrum for cascade production of methanol from CO<sub>2</sub>, with methanol CH<sub>3</sub> peak (δ = 2.827 ppm) integrated against tetrachloroethane standard peak (δ = 5.852 ppm), displaying the absence of any peaks for formate ester or formic acid



**Figure 3-4.**  $^1\text{H}$ -NMR Spectra from before (top) and after (bottom) control reactions showing no conversion of formic acid ( $\delta = 5.86$  ppm) to methanol ( $\delta = 2.83$  ppm) in the absence of alcohol additive.

**Figure 3-5.** TON in multicomponent system as a function of A) The length of linear alcohols or the degree of branching and B) the  $\text{pK}_a$  of the alcohol (red) affected activity. Light red circle denotes TON to or through formate ester.

**Figure 3-6.** A Hammett plot for carbon dioxide hydrogenation reactions carried out with various *para*-substituted aromatic alcohols suggests negative charge buildup ( $\rho = 0.166$ ) during the rate-determining step (Conditions for all reactions:  $2.23 \times 10^{-7}$  mmol Ru per catalyst, 10 mmol alcohol additive, 37 bar  $\text{H}_2$ , 3 bar  $\text{CO}_2$ , 70  $^\circ\text{C}$ , 16 h).

**Figure 3-7.** A) Turnover number (TON) observed for reactions using either or both of **3-1** and **3-2** encapsulated in UiO-66. TON is expressed as mmol methanol per mmol **3-1** and represents an average of three reactions (error expressed as average error). B) Recyclability studies for five cycles in the two fully heterogenized systems, **3-1**@UiO-66 + **3-2**@UiO-66 and [**3-1,3-2**]@UiO-66. Each cycle denoted by a black outlined box and numbered in white. Turnover number for each reaction is represented to the right of each column.

**Fig. 3-8.** SEM images of the samples before and after subjection to reaction conditions

**Fig. 3-9.** Crystallinity of the catalysts before and after the reactions as shown by powder X-ray diffraction patterns

**Figure 3-10.** Comparison of observed examples of A) direct autocatalysis in the Soai reaction resulting in amplified enantioenrichment, B) network autocatalysis observed by Whitesides and co-workers in azide-alkyne cyclization with accelerated rate over time through catalysis promoted more effectively by product-ligated copper species, and C) network autocatalysis in production of ethylene during fruit ripening

**Figure 3-11.** Effect of varying the concentration of TFE additive on catalyst productivity with respect to ruthenium and TFE. Data points collected when the reaction is catalytic in TFE are denoted with an open marker. Data is represented as an average of three runs and error bars represent average error.

**Figure 3-12.** Reaction coordinate diagram for converting carbon dioxide to methanol proceeding through a N,N'-diisopropylformamide, 2,2,2-trifluoroethyl formate ester, or methyl formate ester intermediate. Energies shown are enthalpic heats of reaction ( $\Delta H_{\text{rxn}}$ , kcal/mol), which were obtained directly from thermochemical data or calculated using Benson group increments.

## CHAPTER 4

**Figure 4-1.** Potentiometric titration of UiO-66- $\text{NH}_3^+$  with NaOH

**Figure 4-2.** Hydrogenation of carbon dioxide to methanol in the presence of ethanol as an additive with different amine-based substitutions on the host framework

**Figure 4-3.** Effect of acid treatment conditions on the hydrogenation of carbon dioxide to methanol: A) acid identity and B) amount of HCl added

**Figure 4-4.** Catalytic activity in the cascade reduction of  $\text{CO}_2$  to methanol with **4-1** (red) or **4-2** (blue) as the heterogeneous species in a partially homogeneous reaction

**Figure 4-5.** Esterification of formic acid to 2,2,2-trifluoroethyl formate using differently functionalized UiO-66 derivatives

**Figure 4-6.** Comparison of partially homogeneous (solid lines) and fully heterogeneous (dotted lines) systems for the conversion of CO<sub>2</sub> to methanol A) as a function of time and B) after resubjecting the same catalysts to reaction conditions as listed for 16 hours

**Figure 4-7.** Recycling of the fully heterogeneous cascade system over ten cycles

**Figure 4-8.** Effect of additive amount on turnover number at 4 hours and 16 hours for 4-1@UiO-66 (blue) and 4-1@UiO-66-NH<sub>3</sub><sup>+</sup> (grey and orange)

**Figure 4-9.** Turnover number as a function of time in the cascade hydrogenation of carbon dioxide to methanol with a fully heterogeneous multicomponent system

**Figure 4-10.** Determination of activity for the conversion of formic acid to trifluoroethyl formate by UiO-66 (blue) or 3 Å molecular sieves (grey)

**Figure 4-11.** Network autocatalytic behavior as a function of time in the cascade hydrogenation of carbon dioxide to methanol using a fully heterogeneous multicomponent system with (solid lines) or without (dotted lines) the addition of 3 Å molecular sieves

## LIST OF SCHEMES

### CHAPTER 2

**Scheme 2-1.** Representation of aperture-opening encapsulation of a transition metal complex and its application in catalysis

### CHAPTER 3

**Scheme 3-1.** Strategies employed by Sanford, Olah and Prakash, and Wass in the hydrogenation of carbon dioxide to methanol with amine additives

**Scheme 3-2.** Previous examples of cascade hydrogenation of carbon dioxide to methanol through formic acid and ester intermediates reported by Sanford and Goldberg

**Scheme 3-3.** Procedures for the synthesis of Ru-<sup>t</sup>BuPNN-Br

### CHAPTER 4

**Scheme 4-1.** Comparison of natural system for CO<sub>2</sub> reduction to fuel (top) to the developed system (bottom)

**Scheme 4-2.** Diagram of components used in catalysis in this work

**Scheme 4-3.** Catalytic cycle for CO<sub>2</sub> reduction to formic acid

**Scheme 4-4.** Catalytic cycle for formic acid esterification

**Scheme 4-5.** Catalytic cycle for ester reduction to methanol

## LIST OF ABBREVIATIONS

MOF: Metal-Organic Framework  
UiO: University of Oslo  
ZIF: Zeolitic Imidazolate Framework  
R6G: Rhodamine 6G  
DMSO: Dimethyl Sulfoxide  
DMF: N,N'-dimethylformamide  
mg: milligrams  
d: days  
MeOH: Methanol  
nBuOH: n-butanol  
BET: Brunauer-Emmett-Teller  
DBU: 1,8-diaza[5.4.0]bicycloundec-7-ene  
TGA: Thermogravimetric Analysis  
BBG: Brilliant Blue G  
ICP-OES: Inductively Coupled Plasma-Optical Emission Spectroscopy  
PXRD: Powder X-Ray Diffraction  
<sup>1</sup>H-NMR: Proton Nuclear Magnetic Resonance Spectrometry  
TON: Turnover Number  
G3P: Glyceraldehyde-3-phosphate  
TFE: 2,2,2-trifluoroethanol  
EtOH: Ethanol  
GC: Gas Chromatography  
SEM: Scanning Electron Microscopy  
DMSO: Dimethyl Sulfoxide  
TOF: Turnover Frequency  
BuOH: Butanol  
MeCN: Acetonitrile

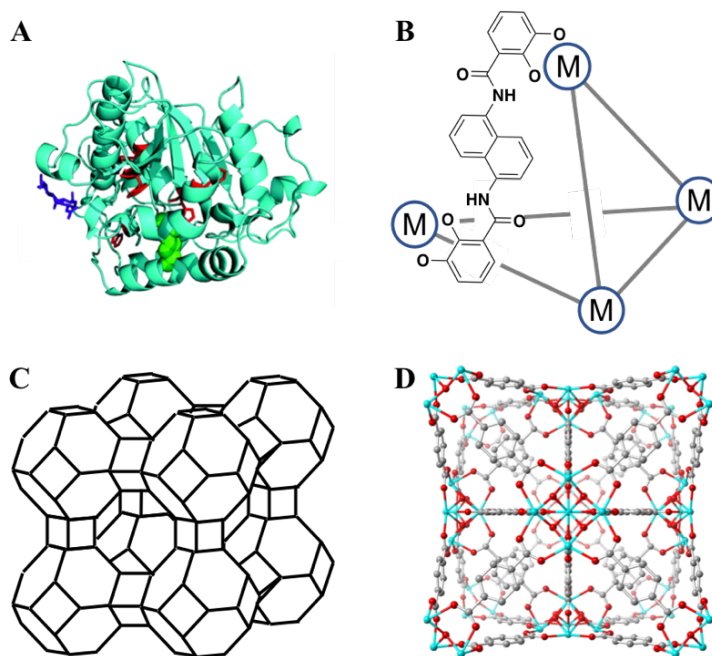
## 1.0 CHAPTER 1

### Application of Host-Guest Chemistry in Metal-Organic Frameworks for New Catalytic Behavior

Nature has evolved systems over millennia that are capable of rapid and selective chemical transformations.<sup>1</sup> This efficiency is a result of several defining properties, including isolation of active components, employment of multiple catalytically active sites for complex transformations, and the influence of secondary interactions in the active site.<sup>2</sup> These natural systems have inspired the design of a diverse array of synthetic catalysts, ranging from direct analogues for the same transformations<sup>3</sup> to indirect mimicry.<sup>4</sup> While this analogy is most commonly applied in the design of ligands for homogeneous catalysts,<sup>5</sup> much of the benefit gained in Nature results from the supramolecular assemblies that host the active components.<sup>6</sup> A number of developments have been made in synthetic host-guest systems based on these superstructures, resulting in catalytic constructs with lifetimes and activity not otherwise observed and, in some cases, reactivity not observed in typical homogeneous systems. Described herein is a summary of recent developments in metal-organic framework-based host-guest chemistry toward improving catalytic reactions.

## 1.1 INTRODUCTION TO HOST-GUEST CATALYTIC SYSTEMS

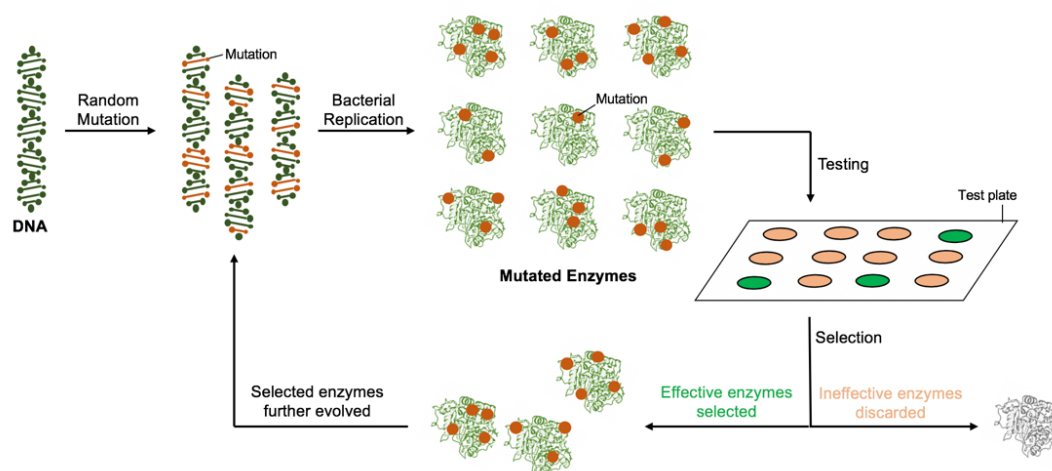
The most commonly reported developments in controlling catalytic activity are a result of synthetically modifying the ligand framework in molecular transition metal complexes.<sup>5</sup> However, this approach is limited by the complexity of existing ligands and the intensive synthetic methods necessary to make impactful structural changes. The use of supramolecular coordinating assemblies or hosts to influence function without directly altering the molecular structure of a complex has emerged as a promising alternative method. This method has been applied using a range of different hosts (Figure 1-1) such as precisely engineered supramolecular cages<sup>7</sup> and extended porous crystals like zeolites<sup>8</sup> and metal-organic frameworks.<sup>9</sup> Depending on the desired effect, these strategies can be employed to significantly improve the catalytic performance of a guest.<sup>10,11</sup>



**Figure 1-1.** Structural representations of A) enzymes,<sup>6</sup> B) supramolecular cages,<sup>7</sup> C) zeolites,<sup>8</sup> and D) metal-organic frameworks.<sup>9</sup>

### 1.1.1 Enzymes

Enzymes serve as the inspiration for many host-guest systems, as their extremely high activity and selectivity result from the precise geometric and electrostatic environment in their active sites, controlled by characteristic supramolecular protein assemblies.<sup>12</sup> These biological catalysts have been employed for a number of challenging chemical transformations, including kinetic resolution of esters,<sup>13</sup> polymerization,<sup>14</sup> and intermolecular nitrogen-atom transfer.<sup>15</sup> However, most enzymes are only stable in a relatively narrow range of conditions,<sup>16</sup> restricting the accessible reaction space to reactions that can be performed with substrates and products compatible with the enzyme itself and often mild, aqueous conditions. Recent developments in improved enzyme function have come as a result of directed evolution (Figure 1-2), allowing for controlled enzyme function by high-throughput iterative testing and mutation.<sup>17</sup> Improvements to enzyme stability have also been made through encapsulation in host materials.<sup>18</sup> The most common route by which chemists have attempted to mimic enzymatic supramolecular assemblies is through the design of these host materials, more specifically supramolecular cages, zeolites, and metal-organic frameworks.



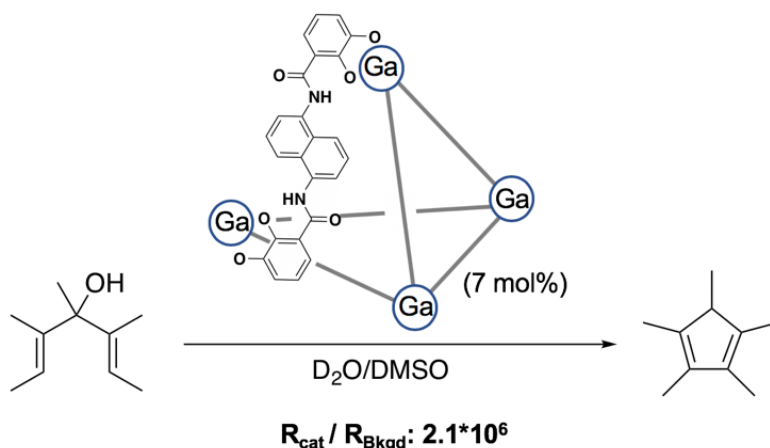
**Figure 1-2.** Summary of the directed evolution method for controlled enzyme function<sup>17</sup>

### 1.1.2 Supramolecular cages

Although many host-guest systems involve extended crystalline structures, some supramolecular cages have been developed that are closer to the size of molecular catalysts to serve as hosts.<sup>7</sup> These cages are composed of metal vertices and organic multidentate ligands, forming polyhedra into which a guest can be introduced. These cages can be catalytically active (Figure 1-3),<sup>19</sup> and the properties of both the cage and the guest can be manipulated to engineer a catalytic host-guest construct for a specific purpose<sup>20</sup> such as aza-cope electrocyclization.<sup>21</sup> Furthermore, these cages can be designed to stabilize molecular species that would otherwise be unstable in solution.<sup>22</sup> This stabilization has been leveraged in several cases to improve the rate of catalytic processes such as hydroformylation.<sup>23</sup> These cages represent promising hosts for molecular guests in their precisely controlled structures and functionality. However, the synthesis of ligands for new supramolecular cages is often a long, multistep synthetic process, inhibiting the ability to conduct a rapid systematic study on structure-



function relationships between hosts and guests.<sup>24</sup> Additionally, these cages are difficult to reuse or recycle in catalysis, and thus are not as advantageous for applications necessitating recyclable catalysts.<sup>24</sup>

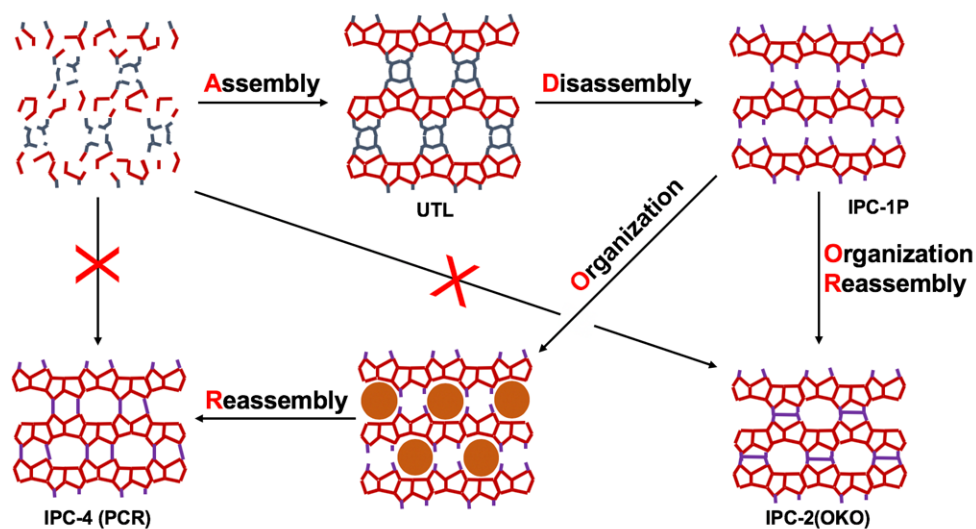


**Figure 1-3.** Rate enhancement of Nazarov cyclization by  $[\text{Ga}_4\text{L}_6]^{12-}$  reported by Raymond, Bergman, and co-workers<sup>22</sup>

### 1.1.3 Zeolites

The most common examples of stable hosts are zeolites. Zeolites are porous three-dimensional inorganic materials synthesized at high temperatures and pressures.<sup>25</sup> As of 2018, 245 different zeolite structures had been developed, with different properties based on chemical makeup.<sup>8</sup> Their remarkable stability largely results from the strong bonds in their aluminosilicate structure, which lends to their utilization in water purification,<sup>26</sup> gas and liquid sorption,<sup>27</sup> gas separation,<sup>28</sup> and catalysis.<sup>29</sup> While these zeolites were originally believed to be synthetically rigid, recent developments in assembly, disassembly, organization, reassembly (ADOR) processes (Figure 1-4),<sup>30</sup> during which the zeolite structure partially disassembles and can then be reassembled into a different structure using a directing guest, have allowed

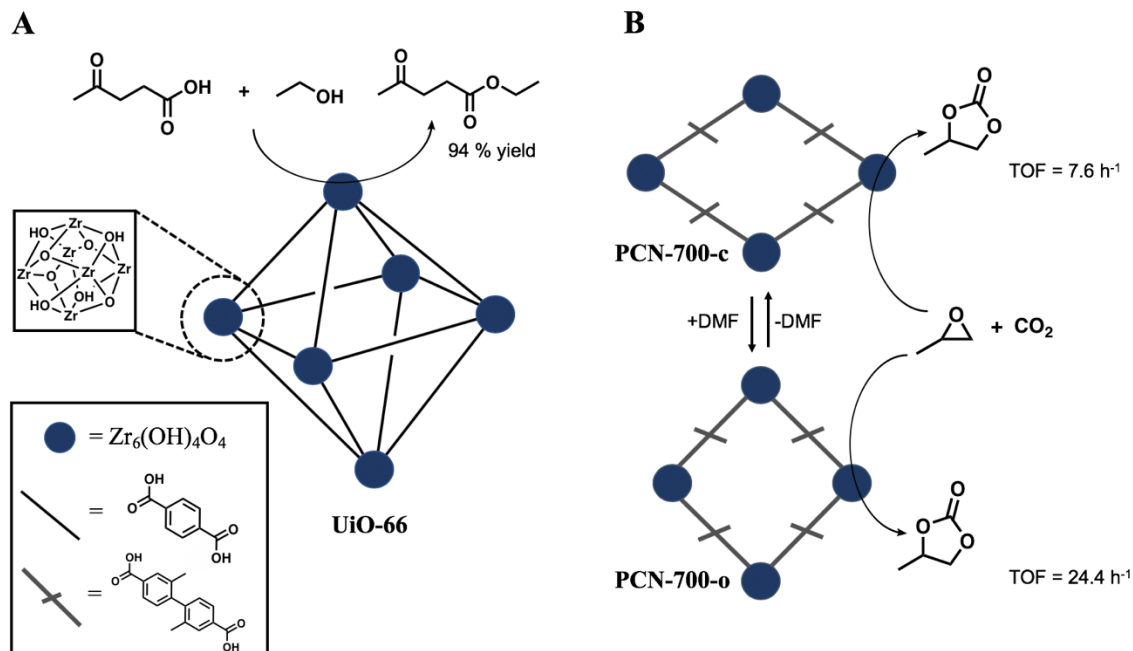
access to an even larger library of previously inaccessible structures with unique properties. In addition to their applicability as Lewis acid catalysts, zeolites have been employed in various industrial processes.<sup>31</sup> Despite this inherent catalytic activity and the ability to uncover new structures through ADOR, structural disassembly and reassembly is not conducive to the controlled encapsulation of catalytic guests: the controlled organization step requires a guest molecule to direct the pore arrangement and occupies the pore space intended for the catalytic guest. Furthermore, reassembly without guest-directed organization leads to less reproducible zeolite structures and thus less control over guest encapsulation. This inhibits the development of systems that require a logical design process for catalyst construction based on experimentation and interpretation. Thus, a host with inherent modularity and distinct components that can be modified in a precise and targeted manner is ideal.



**Figure 1-4.** The ADOR method for zeolite modification, allowing access to IPC-2 and IPC-4 frameworks that are inaccessible by *de novo* assembly<sup>29</sup>

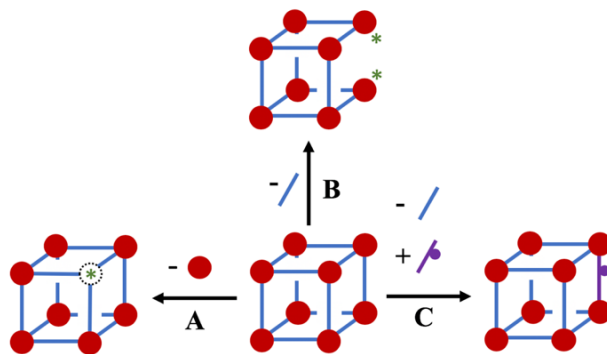
#### 1.1.4 Metal-Organic Frameworks

Metal-Organic Frameworks (MOFs) serve as hosts that incorporate the molecular definition of supramolecular cages and the extended crystallinity and stability of zeolites. MOFs are crystalline coordination polymers formed from inorganic nodes and organic bridging ligands, or linkers.<sup>9</sup> The variety in these components has resulted in over 70,000 unique framework structures<sup>32</sup> with a wide range in stability, catalytic activity, and structure. This structural diversity and ability to precisely modulate these frameworks has resulted in a diverse catalog of applications, including gas sorption,<sup>33,34</sup> drug delivery,<sup>35-37</sup> and substrate sensing.<sup>38</sup> Additionally, some MOFs exhibit catalytic properties depending on their composition and pore structure.<sup>39</sup> For example, Llabres i Xamena and co-workers leveraged the Lewis acidity of high-oxidation state metal nodes to promote esterification of carboxylic acids<sup>40</sup> and Zhou and co-workers showed that framework flexibility and node accessibility can allow for switching between slow conversion and rapid conversion for carbon dioxide cycloaddition (Figure 1-5).<sup>41</sup>



**Figure 1-5.** Representation of reactions catalyzed by MOFs, including A) the esterification of levulinic acid by UiO-66<sup>40</sup> and B) conversion of propylene oxide to propylene carbonate by PCN-700.<sup>41</sup>

Engineering of MOF structures through linker modification has also allowed for diverse reactivity. Manipulation of this linker functionality has proven to be a promising method for directly controlling the catalytic properties of MOFs. Cohen and co-workers employed a UiO-66 derivative with multiple variants of terephthalic acid linkers for the degradation of chemical warfare agent simulants,<sup>42</sup> and Farha and co-workers demonstrated the importance of linker selection in the synthesis of NU-903, NU-904, and NU-1008 and their resulting activity in the fixation of carbon dioxide.<sup>43</sup> Even in MOFs that are not catalytically active in their native form, catalytic characteristics can be installed post-synthetically (Figure 1-6).<sup>44</sup>

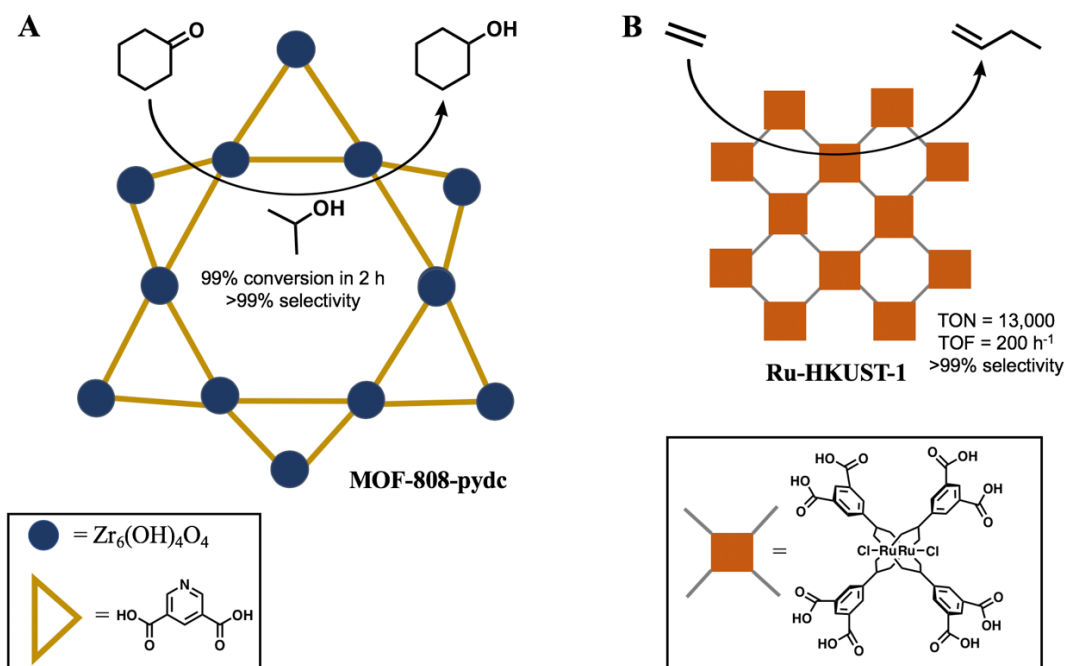


**Figure 1-6.** Modification of metal-organic frameworks by A) node or B) linker elimination,<sup>45</sup> or C) linker exchange<sup>46</sup>

Methods have been developed for the post-synthetic elimination of linkers or nodes (Figure 1-6A and 1-6B),<sup>45</sup> resulting in reduced coordinative saturation and a decrease in steric bulk within a framework. Increased accessibility to MOF nodes was beneficial in the Meerwein-Ponndorf-Verley reduction of cyclohexanone by Llabrés I Xamena and co-workers (Figure 1-7A)<sup>47</sup> as well as ethylene dimerization to 1-butene reported by Soukri and co-workers (Figure 1-7B).<sup>48</sup> Conversely, functionality can be added to a structure through synthetic modification of functional groups already present.<sup>49</sup> In some instances, linker exchange has been utilized to expand MOF pores,<sup>50</sup> allowing access to previously obscured active sites.

Exchange of the MOF's constituent linkers is a recently popularized method for the introduction of catalytic functionality in MOFs (Figure 1-6C), often referred to as “solvent-assisted linker exchange (SALE) or “post-synthetic linker exchange” (PSLE), in which two linkers are interchanged,<sup>46</sup> sometimes occurring despite the stability of a framework.<sup>51</sup> Though the precise mechanism of this linker exchange is unclear in many cases,<sup>52</sup> it could be considered analogous to ligand exchange in coordination complexes.<sup>53</sup> The associative and dissociative pathways for ligand exchange, when applied to an extended inorganic solid, lead to intriguing behavior: the introduction of

a new ligand can result in the permanent expansion of a pore<sup>50</sup> or the dissociation of a linker can lead to a pore aperture larger than its original size, allowing for large guests to diffuse into the MOF pores.<sup>54</sup> Even more interesting behavior can be observed in these frameworks upon the incorporation of a catalytic guest species.



**Figure 1-7.** Accessible nodes allow for efficient catalysis in the use of A) MOF-808-pydc in the Meerwein-Ponndorf-Verley reduction of cyclohexanone<sup>47</sup> and B) Ru-HKUST-1 in the dimerization of ethylene to 1-butene.<sup>48</sup>

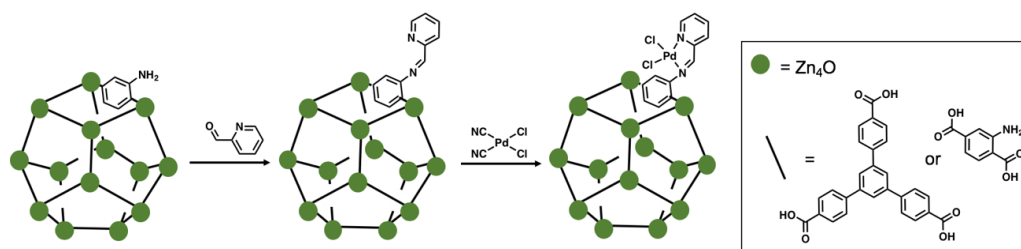
## 1.2 SEPARATING CATALYTIC ACTIVE SITES WITHIN A MOF

One of the most commonly utilized aspects of catalytic host-guest systems is the isolation of active sites to prevent decomposition. This separation mimics that achieved in enzymes through the coordination of active metal sites within a supramolecular protein assembly.<sup>12</sup> MOFs are promising hosts for the isolation of individual catalytic components.<sup>55,56</sup> A variety of MOF-based host guest systems have

been developed as a result of the variety in viable methods for MOF encapsulation of a guest, including attachment to the pore structure,<sup>57,58</sup> synthesis of the framework around a guest,<sup>59</sup> synthesis of the guest from a seed within the MOF,<sup>60</sup> and diffusion of catalytic species into the structure.<sup>61</sup>

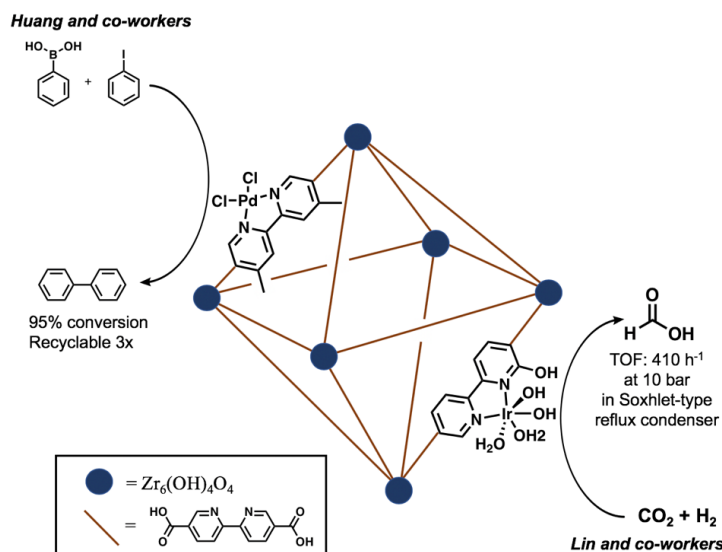
### 1.2.1 Tethering of Active Species to Metal-Organic Frameworks

Host-guest composites can be constructed in a straightforward manner by attachment of catalytically active species to the MOF structure. While examples of catalyst tethering to MOF nodes exist,<sup>57</sup> tethering in MOFs is most commonly performed either by reaction of a catalyst precursor with a ligand functional group<sup>58</sup> or chelation of a metal center by the framework through preinstalled ligand functionality.<sup>62,63</sup> These methods both lead to covalent attachment of the active species directly to the framework and can impart the benefits and drawbacks of such binding. Yaghi and co-workers have previously demonstrated the construction of a ligand from MOF linker functionality and the subsequent coordination of palladium to that ligand (Figure 1-8).<sup>58</sup> Through this method, the amine functional groups of the MOF were quantitatively converted to iminopyridine functional groups, which were then metallated.



**Figure 1-8.** Method used by Yaghi and co-workers to tether a palladium complex to a MOF.<sup>58</sup>

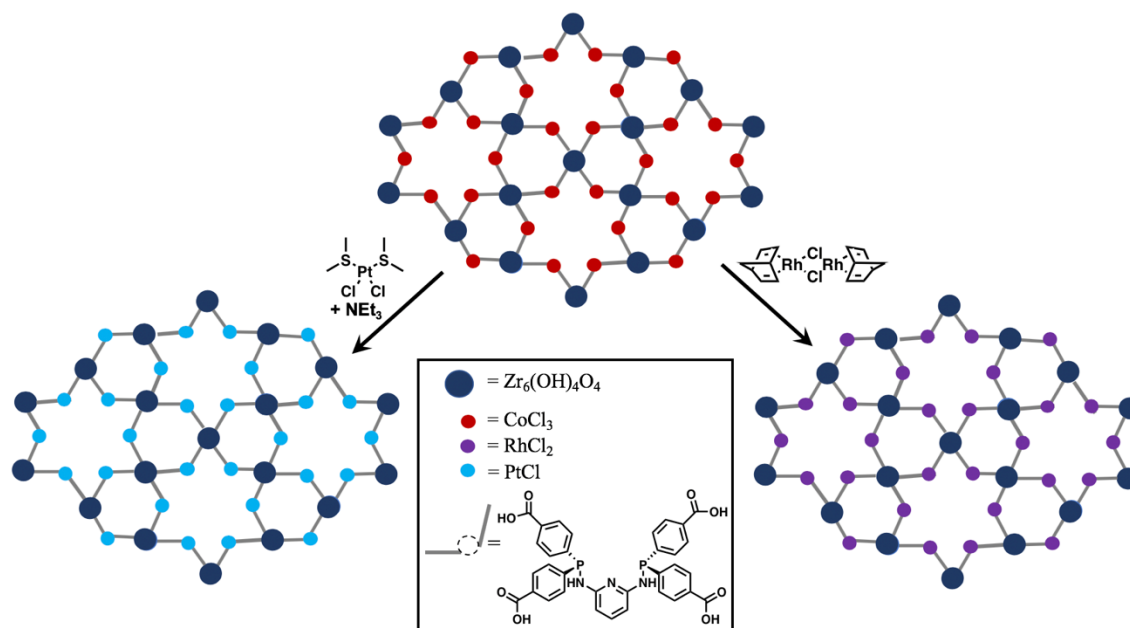
Another method for catalyst attachment to a MOF is the binding of a metal center by functionality already present in the linkers. A particularly popular example of this is 2,2'-bipyridyl (bipy)-based linkers, which have been employed to great effect by Huang and co-workers toward Suzuki-Miyaura cross-coupling using palladium dichloride (Figure 1-9, left)<sup>62</sup> as well as by Lin and co-workers low-pressure carbon dioxide hydrogenation using an iridium catalyst (Figure 1-9, right),<sup>63</sup> both of which were bound to the zirconium-based MOF UiO-67-bipy or its further functionalized derivatives. The ability of the same framework to act as a host for catalytic guests in two distinct catalytic processes is a testament to the tunability and adaptability of MOFs as hosts. Furthermore, Yaghi, Toste, and co-workers also observed the improved stability of a gold catalyst ligated by the biphenyl dicarboxylate linkers of bio-MOF-100,<sup>64</sup> improving turnover frequency in the cycloisomerization of enynes and mitigating catalyst decomposition to impart recyclability not observed in homogeneous analogues.



**Figure 1-9.** UiO-67-bipy derivatives as hosts for transition metal catalysts in Suzuki-Miyaura cross-coupling<sup>62</sup> (left) and low-pressure carbon dioxide reduction (right)<sup>63</sup>



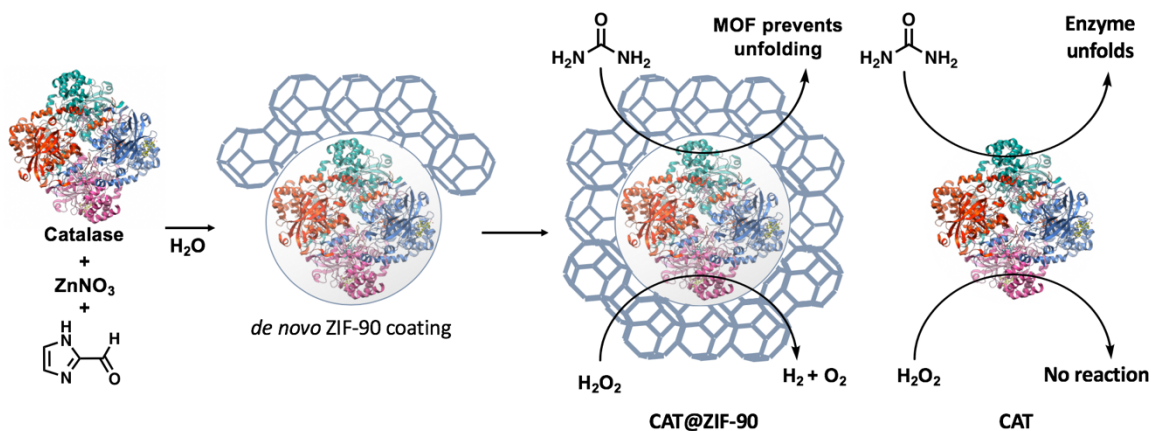
Guest attachment to a MOF can also be accomplished through the development of an entirely new structure rather than modification of an existing one, as is the case in the design of the catalytic “pincerMOFs,” developed by Wade and co-workers.<sup>65</sup> These pincerMOFs exhibit impressive selectivity in the intramolecular cyclization of o-alkynyl anilines, especially in the case of 2-ethynyl aniline.<sup>66</sup> PincerMOFs based on a PNPNP ligand also exhibited postsynthetic metal exchange that is inaccessible in analogous homogeneous pincer complexes without the formation of platinum or rhodium nanoparticles (Figure 1-10).<sup>67</sup> As the homogeneous analogues for these pincerMOFs either have not yet been synthesized or decompose rapidly in solution, this strategy offers the potential for the development of transition metal complexes that are entirely inaccessible in homogeneous form. These new, previously untested complexes could exhibit new, previously unobserved reactivity.



**Figure 1-10.** Post-synthetic metal exchange in “pincerMOFs” as described by Wade and co-workers<sup>67</sup>

### 1.2.2 Enzyme encapsulation in MOFs

While binding of a catalytic organometallic guest has been shown to be a successful method for catalyst heterogenization, significant strides have also been made in the internalization of enzymes in MOFs.<sup>68</sup> Enzyme encapsulation often results in improved stability and substrate selectivity, as was observed by Janiak and co-workers when they encapsulated a laccase enzyme within the zinc-imidazolate framework ZIF-8.<sup>69</sup> Similarly, Tsung and co-workers stabilized beta-glucosidase (BGL) through encapsulation in amino-functionalized UiO-66 (UiO-66-NH<sub>2</sub>) by mechanochemical synthesis, circumventing both the solvent and harsh solvothermal synthesis conditions that the enzyme is typically incompatible with.<sup>59</sup> This significantly improved the stability of the enzyme: BGL@UiO-66-NH<sub>2</sub> retained over 90% of its activity for the breakdown of  $\beta$ -D-glucopyranoside to 4-nitrophenol in the presence of protease as well as in acidic pH, which decreased the activity of free BGL. Other work in the Tsung group demonstrated that the encapsulation of catalase in ZIF-90 through “*de novo* encapsulation” protected the enzyme from unfolding in the presence of urea (Figure 1-11), maintaining activity for the encapsulated enzyme in harsher conditions than the free enzyme.<sup>70</sup> Enzyme stability was likewise improved by Farha and co-workers, who showed that the encapsulation of organophosphorus acid anhydrolase in the zirconium MOF PCN-128y engendered the enzyme with increased durability in both elevated temperatures and dry storage, retaining its activity for the breakdown of the nerve agent simulant diisopropyl fluorophosphate up to 70 °C and through three days of storage.<sup>71</sup>

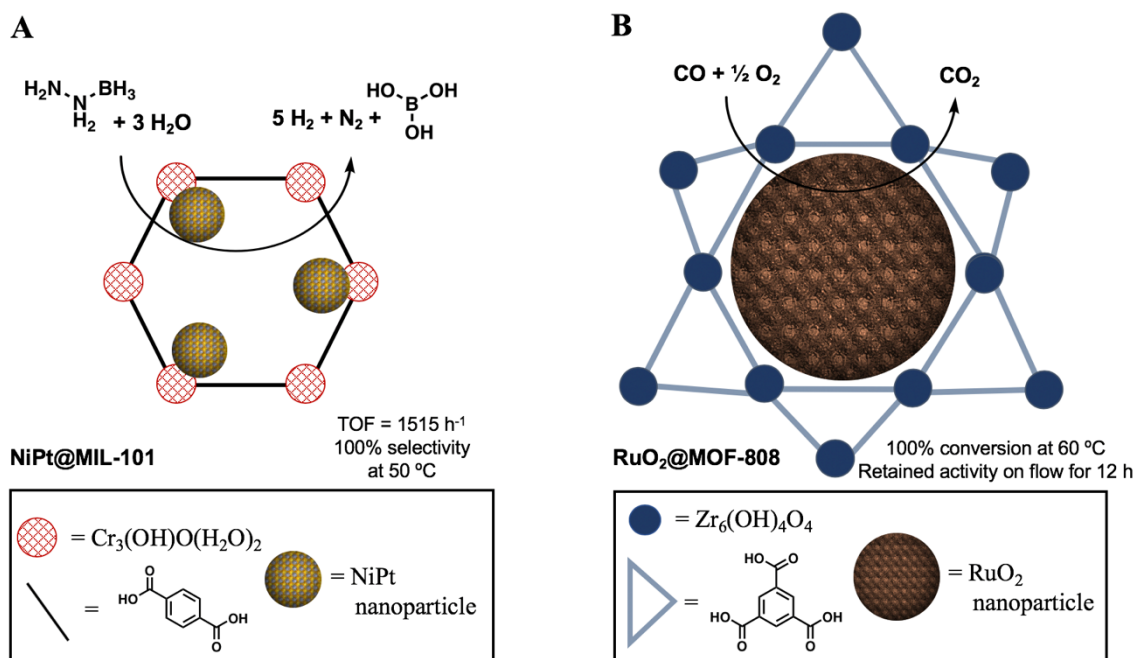


**Figure 1-11.** Prevention of enzyme denaturation by unfolding through encapsulation in ZIF-90<sup>72</sup>

### 1.2.3 MOF-Encapsulated Nanoparticles

While the encapsulation of enzymes primarily benefits their stability, the internalization of more stable guests such as nanoparticles can prove more beneficial to catalytic aspects such as selectivity. Huo and co-workers demonstrated this through the encapsulation of an array of nanoparticles formed from metals including gold, silver, and platinum in ZIF-8, all of which exhibited improved selectivity in olefin hydrogenation for hexene over cyclooctene resulting from MOF-afforded size exclusion.<sup>72</sup> They observed similar size-exclusion benefits for the hydrogenation of trans-stilbene upon the encapsulation of platinum nanoparticles in UiO-66-NH<sub>2</sub> functionalized post-synthetically with anhydrides of various sizes.<sup>73</sup> Separately, Lu and co-workers manipulated synergistic effects between the framework MIL-101 and nickel/platinum alloy nanoparticles to increase the rate of hydrogen evolution using hydrazine borane and hydrazine as feedstocks (Figure 1-12A), resulting in a very high turnover frequency (TOF) of 1515 h<sup>-1</sup> with 100% selectivity for hydrogen and no loss in activity over twenty cycles.<sup>74</sup> Smoukov and co-workers also observed improvements

to activity, with the encapsulation of ruthenium oxide nanoparticles in the zirconium-based MOF-808 (Figure 1-12B) leading to 100% conversion in carbon monoxide oxidation at low temperatures and retained activity on flow for over 12 hours.<sup>60</sup>

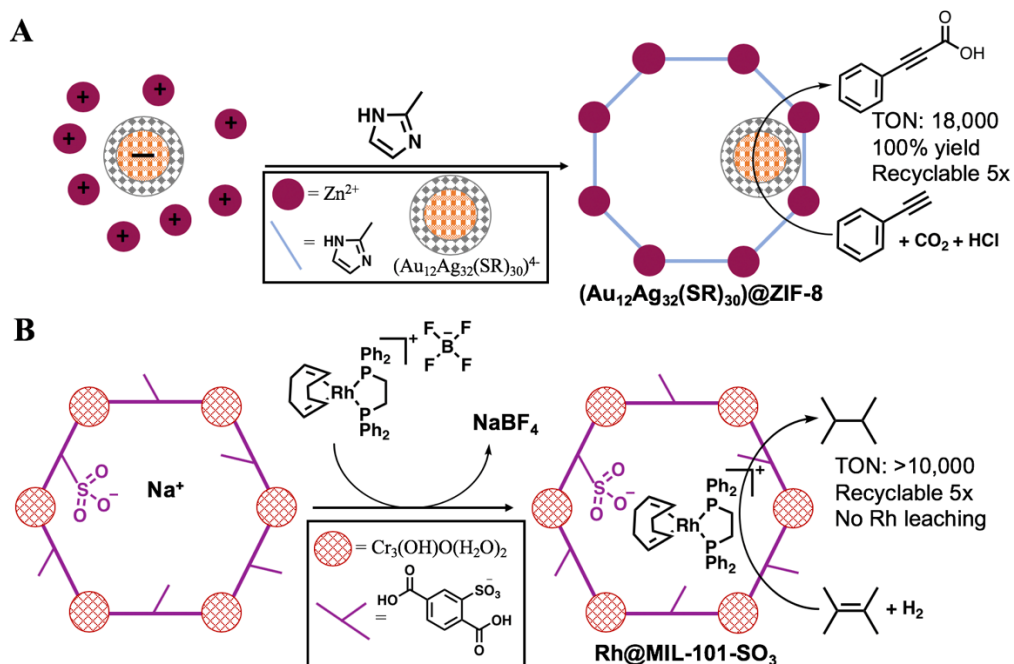


**Figure 1-12.** Activity of nanoparticle@MOF composites for A) hydrogen evolution from hydrazine borane<sup>74</sup> and B) carbon monoxide oxidation<sup>60</sup>

#### 1.2.4 Noncovalent Encapsulation of Molecular Catalytic Guests

Encapsulation of species such as enzymes and nanoparticles has led to a range of advantages in those catalytic constructs. However, a significant amount of promise also exists in the field of noncovalent encapsulation of molecularly defined catalysts in MOFs. This method of encapsulation circumvents the restriction of movement resulting from complex tethering, often leading to improvement in activity and selectivity. These noncovalent methods for encapsulation commonly involve the manipulation of electrostatic interactions to drive diffusion of guests into the MOF host. Such was the case in the work of Zhu and co-workers, who used these electrostatic

effects to form ZIF-8 around atomically-precise gold/silver nanoclusters, resulting in a turnover number (TON) of over 18,000 for the carboxylation of phenylacetylene (Figure 1-13A).<sup>75</sup> Sanford and co-workers employed cation exchange in the anionic MOFs ZJU-28 and MIL-101-SO<sub>3</sub> to encapsulate a cationic rhodium cyclooctadiene complex, imparting upon it size selectivity and improved recyclability for the hydrogenation of olefins (Figure 1-13B).<sup>61</sup> A similar cation exchange method was employed by Rosseinsky and co-workers to instead encapsulate a cationic iron complex in an indium-based MOF for the Diels-Alder reaction between isoprene and methyl vinyl ketone.<sup>76</sup> The resulting composite was continually active over the course of 48 hours and was recyclable and bench-stable for twelve days. In a more recent example of this cation exchange method, Ma and co-workers encapsulated a cationic trinuclear palladium complex in bio-MOF-100, increasing the longevity of the complex and allowing for recyclability that was inaccessible prior to encapsulation.<sup>77</sup> While most strategies for the noncovalent encapsulation of transition metal complexes in MOFs require an electrostatic driving force, a method has been developed for the encapsulation of catalytic guests within a MOF by taking advantage of “aperture-opening” linker dissociation events,<sup>54</sup> which imparts a ruthenium complex for the hydrogenation of carbon dioxide with several new, beneficial characteristics. This strategy will be discussed in detail in Chapter Two.



**Figure 1-13.** Representation of two different strategies for electrostatically driven catalyst encapsulation as employed by A) Zhu for the carboxylation of phenylacetylene<sup>75</sup> and B) Sanford for the hydrogenation of olefins<sup>61</sup>

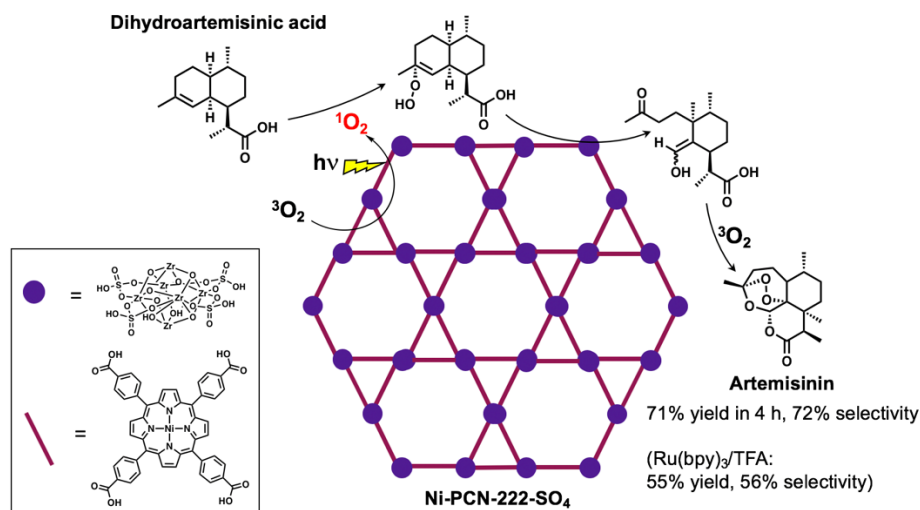
### 1.3 APPLYING HOST-GUEST CONSTRUCTS IN MULTICOMPONENT CATALYSIS

While the use of a single catalyst in a host-guest construct provides certain advantages, many valuable transformations can be synthetically demanding for a single catalytic component. Natural systems often make use of multiple catalytically active sites to affect more sophisticated transformations in a sequential manner, resulting in the conversion of simple substrates such as carbon dioxide and water to glucose during photosynthesis.<sup>12</sup> Significant advances have been made recently in MOF-based multicomponent catalysis, including the use of MOFs themselves as multifunctional catalysts,<sup>78</sup> coupling the activity of enzymes with other reactive species,<sup>79</sup> tandem

catalysis with encapsulated nanoparticles,<sup>80</sup> and cooperative and multicomponent transformations using immobilized molecular species.<sup>81</sup>

### 1.3.1 MOFs as Multicomponent Catalysts

Incorporation of a functional guest into a MOF for the formation of a multicomponent catalytic construct often imparts increased stability and selectivity to that guest. However, the frameworks themselves can be multifunctional as well.<sup>78</sup> For example, Han and co-workers incorporated the function of a covalent organic framework (COF) to form a core-shell MOF/COF hybrid composed of the Lewis acidic PCN-222 within the Brønsted acidic COF TpPa-1.<sup>82</sup> This recyclable hybrid catalyzed deacetylation and a Knoevenagel condensation in tandem in over 99% yield. In separate work pursuing pharmaceutical products, Zhou and co-workers employed an entirely MOF-based hybrid in their work toward the tandem semisynthesis of artemisinin (Figure 1-14).<sup>83</sup> Their construct was comprised of PCN-222-SO<sub>4</sub>H with Brønsted acid sites anchored to the framework that acted in tandem with a photocatalytic porphyrin-based linker to convert dihydroartemisinic acid to artemisinin in over 70% yield with improved recyclability and stability. Li and Zeng made use of a slightly different route to develop a multifunctional porous material: the surface coating of a functional MOF on functionalized silica.<sup>84</sup> By coating Ni-MOF-74 on Ni/SiO<sub>2</sub>, they formed a catalyst for the tandem imination of nitrobenzene with benzaldehyde with 100% selectivity, avoiding overreduction of the imine and retaining similar activity and selectivity through four cycles.



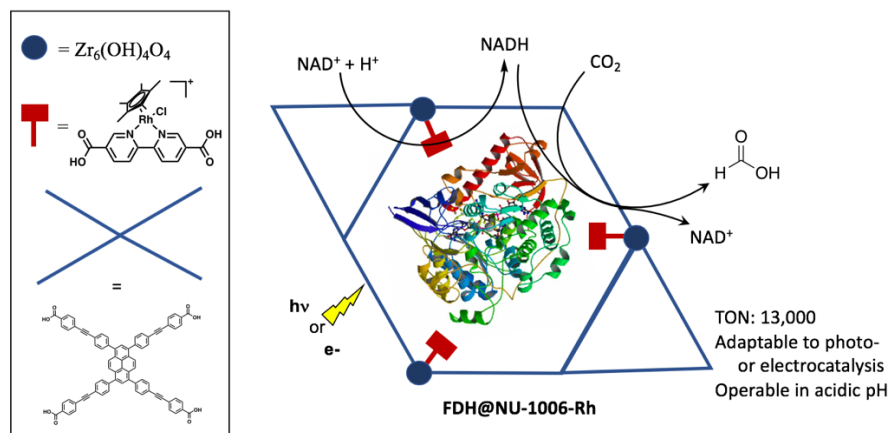
**Figure 1-14.** Use of linker/node tandem catalysis for the one-pot semisynthesis of artemisinin from dihydroartemisinic acid reported by Zhou and co-workers.<sup>83</sup>

### 1.3.2 Enzyme@MOF Composites in Tandem Catalysis

As previously described, the encapsulation of enzymes in MOFs allows access to previously restricted catalytic recyclability as a result of increased stability. Additionally, the encapsulation of enzymes in MOFs with catalytic functionality can result in constructs capable of conducting tandem catalysis. Wu and co-workers employed this strategy for the encapsulation of palladium nanoparticles and the enzyme *Candida Antarctica* lipase B in UiO-66-NH<sub>2</sub>, resulting in a composite that was capable of affecting the rapid, selective conversion of ethyl hexanoate and benzaldehyde to benzyl hexanoate.<sup>79</sup> Work conducted by Farha and co-workers showed that the encapsulation of formate dehydrogenase (FDH) in NU-1006 with a rhodium complex bound to the linker could be employed in either electricity-<sup>85</sup> or light-driven<sup>86</sup> conversion of carbon dioxide to formic acid with significant improvements to the stability of both catalytic components (Figure 1-15). In a more biological application,



Lei and co-workers coencapsulated catalase and black phosphorus quantum dots in MIL-101 nanoparticles to convert hydrogen peroxide through  $O_2$  to singlet oxygen.<sup>87</sup> This construct was found to be effective for therapy against hypoxic tumor cells while remaining compatible with healthy cells, further expanding the range of applications of tandem catalysis in MOFs.



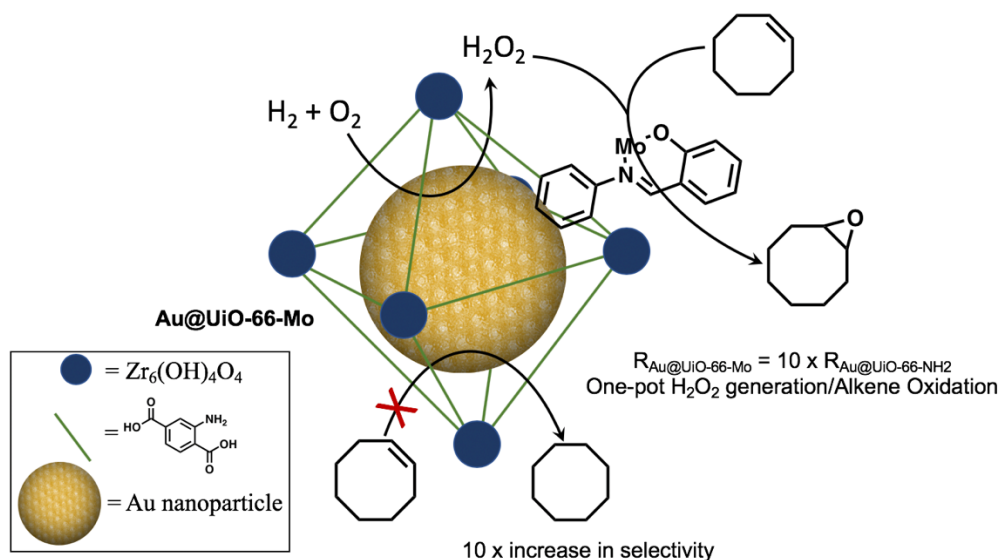
**Figure 1-15.** Representation of multicomponent electro-<sup>85</sup> or photocatalytic<sup>86</sup> conversion of carbon dioxide to formate using encapsulated FDH@NU-1006-Rh

Significant progress has also been made recently through the incorporation of glucose oxidase enzymes. In the work of Zheng and co-workers, encapsulation of glucose oxidase in the conductive copper MOF HKUST-1 and binding of the construct to copper foam allowed for the tandem electrocatalytic-biocatalytic conversion of glucose to gluconic acid with retention of activity after incubation at typically denaturing temperatures.<sup>88</sup> Zhu and co-workers took a different approach, immobilizing the enzyme through its interaction with the amine group of Fe-MIL-88B-NH<sub>2</sub> via amidation coupling, resulting in a construct that oxidized 3,3',5,5'-tetramethylbenzidine using the hydrogen peroxide produced from glucose oxidation and allowed for the colorimetric detection of glucose in solution.<sup>89</sup> Each one of these significant advances in enzyme catalysis was only accessible through the encapsulation

of an enzyme, allowing that enzyme to operate in the presence of a species with which it would otherwise be incompatible.

### 1.3.3 Multicomponent Catalysis in MOFs using NP@MOF Hybrids

The variety in possible active sites at the surface of metal nanoparticles can lead to unwanted byproducts. However, this active site variety can also be used to access unique catalytic transformations as it has been in the employment of nanoparticle@MOF (NP@MOF) hybrids in tandem catalysis. Jiang and co-workers developed a system using two different metals in alloy nanoparticles – palladium for activity and silver for selectivity – with the Lewis acidic MIL-101 as a host.<sup>80</sup> The composite catalyzed the multistep reductive amination of benzaldehyde with nitrobenzene in one vessel with 90% selectivity and 99% conversion. Huang and co-workers found that the encapsulation of platinum nanoclusters in UiO-66-NH<sub>2</sub> by wetness impregnation also led to tandem catalytic activity: the platinum clusters and the Lewis acidic MOF converted benzaldehyde and nitromethane to N-methyl- $\alpha$ -phenyl nitro compound with 98% selectivity at 99% conversion while avoiding byproducts from overreduction or condensation.<sup>90</sup> Similar improvements in selectivity were observed by Nguyen and co-workers, who made use of gold and palladium nanoparticles encapsulated within UiO-66-NH<sub>2</sub> decorated with a tethered molybdenum salicylaldehyde complex (Figure 1-16).<sup>91</sup> The construct catalyzed the epoxidation of alkenes by physically restricting the two catalytic components. Production of hydrogen peroxide from hydrogen and oxygen by the encapsulated nanoparticles occurred in proximity to the oxidation performed by the tethered molybdenum complex.

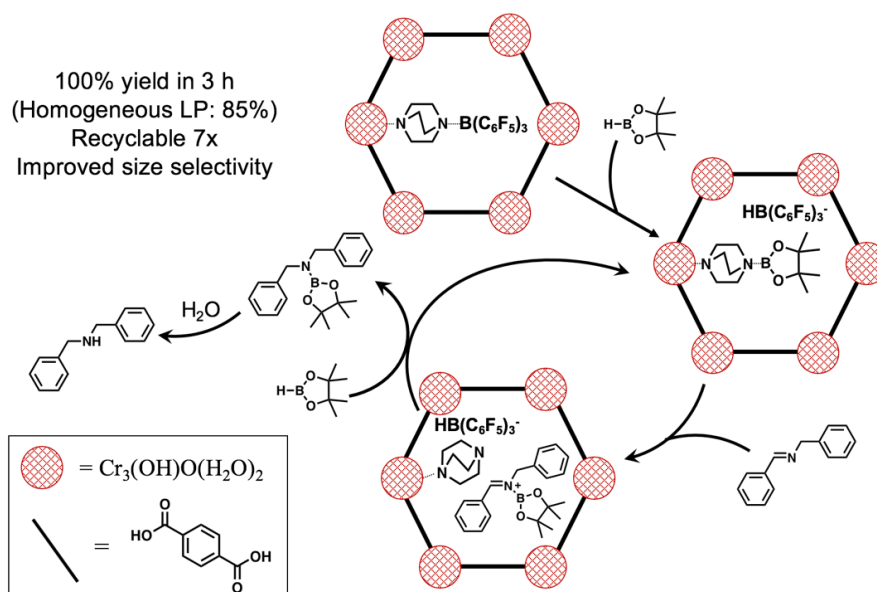


**Figure 1-16.** Representation of the tandem Au@MOF-Mo system developed by Nguyen and co-workers enabling conversion of cyclooctene to cyclooctene oxide selectively over alkene hydrogenation using oxygen as the source oxidant<sup>91</sup>

The proximity of active sites working in tandem can also be leveraged to positive effects within the MOF pores, as was observed by Olsbye and co-workers. In their system, carbon dioxide was hydrogenated to methanol using platinum nanoparticles encapsulated in UiO-67.<sup>92</sup> They found that the zirconium nodes nearby to the nanoparticle served as a Lewis acid catalyst to activate the substrate for hydrogenation, leading to improved selectivity by favoring formate as an intermediate over carbon monoxide or methane. Lin and co-workers separately developed a proximity-based tandem system comprised of palladium nanoparticles encapsulated in an aluminum-bipy based MOF.<sup>93</sup> In their system, location-controlled formation of nanoparticles within the MOF resulted in the proximity of nanoparticles to open aluminum sites, which acted as a Lewis acid catalyst to activate and convert alcohols to alkenes to be hydrogenated by palladium. They found in a separate study that coencapsulation of copper nanoparticles with a photoactive ruthenium complex in UiO-67-bipy allowed for the photocatalytic reduction of carbon dioxide to ethanol.<sup>94</sup>

### 1.3.4 Molecular Catalysts in MOF-Based Tandem Catalysis

Benefits that have been observed for the use of larger catalytic species in MOF-based tandem catalysis have also been exhibited by systems in which molecular catalysts operate cooperatively. Sanchez and co-workers demonstrated this tandem activity by tethering an iridium pincer complex to the amine-functionalized frameworks IRMOF-3 and UiO-66-NH<sub>2</sub>, combining the activity of that complex for hydrogenation and the Lewis acidity of the MOF. This construct converted nitrobenzene derivatives and aldehydes to a range of secondary amines by reductive amination with selectivity often exceeding 98% and greater than 99% conversion.<sup>81</sup> Using a similar strategy, Ma and co-workers anchored the Lewis base DABCO to the nodes of MIL-101 and subsequently introduced B(C<sub>6</sub>F<sub>5</sub>)<sub>3</sub> as a Lewis acid to form a MOF whose pores were interspersed with frustrated Lewis pairs (Figure 1-17).<sup>95</sup> This collocation allowed for the Lewis pair to catalyze the reduction of imines or malonates in tandem through seven cycles without loss in activity. Lin and co-workers have shown that tandem catalysis in MOFs employing molecular species can selectively convert carbon dioxide to ethanol. Copper centers bound to the Zr<sub>12</sub> node in a zirconium carboxylate MOF and a collocated cesium salt gave a yield of ethanol exceeding 6,000 mmol per gram of copper with greater than 99% selectivity.<sup>96</sup> While systems employing multiple transition metal complexes in tandem with MOF hybrids are not as common as those with catalysts such as nanoparticles or enzymes, one such system developed for the hydrogenation of carbon dioxide to methanol is detailed in Chapter Three.



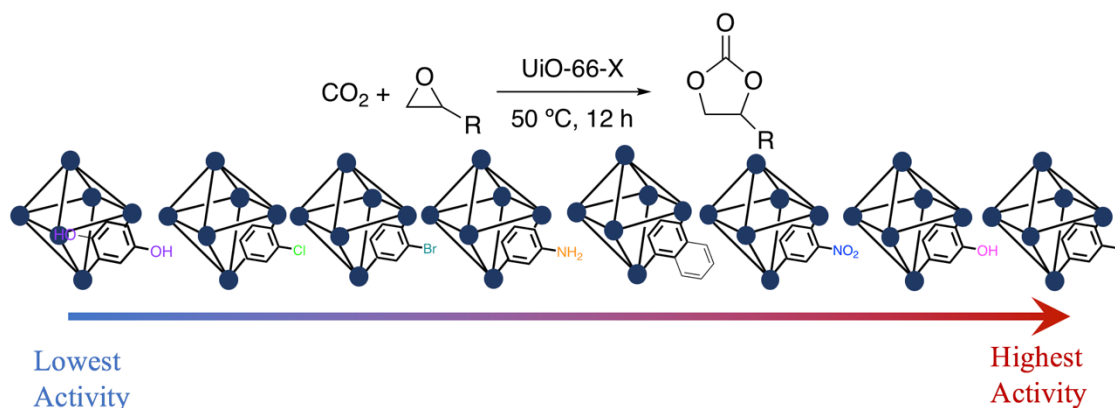
**Figure 1-17.** Representation of the FLP@MIL-101 cooperative system for imine reduction as described by Ma and co-workers.<sup>95</sup>

## 1.4 EMPLOYING HOST FUNCTIONALITY TOWARD NONCOVALENT INFLUENCE IN CATALYSIS

The active sites of natural systems are often precisely arranged to positively influence catalysis, dictating a certain geometric arrangement to favor a specific product.<sup>2</sup> These effects result from an enzyme's supramolecular structure fixing functionalities in very precise position so as to interact in the most constructive manner with a substrate. While much room for development in the use of such interactions in MOF-based host-guest constructs remains, the ability to easily modulate MOF pores has led to some intriguing findings. An increased understanding of the pore environment within MOFs and its effect on guests has recently yielded promising advances in catalysis and could even be leveraged to access new, previously inaccessible reactivity.

### 1.4.1 Introduction of functionality in MOFs to control pore environment

The variety in linkers and nodes that compose stable MOFs can be utilized for manipulation of their structures to achieve specific pore environments. As has been discussed, functional linkers have served as tethering points in catalytic constructs. These linkers can also influence the pore environment indirectly, through characteristics such as dielectric constant or the arrangement of internalized solvent molecules in a pore. Zhou and co-workers have demonstrated that the introduction of different linkers in PCN-700 doubled the nitrogen uptake capacity of the MOF when the installation of an unfunctionalized biphenyl dicarboxylate linker was compared to a bis-cyano- or bis-amino-functionalized analogue.<sup>97</sup> A different strategy, similar to that employed by Cohen and co-workers for the development of catalysts to break down nerve agent simulants,<sup>42</sup> was employed by Forgan and co-workers to install multiple different linkers in UiO-66 simultaneously.<sup>98</sup> This improved the uptake of anticancer drugs and led to high therapeutic activity toward MCF-7 breast cancer cells. Kim and co-workers conversely made use of the modularity of UiO-66 derivatives to synthesize a range of functionalized cages and perform a systematic study of the influence of linker functionality on those MOFs' catalytic activity toward carbon dioxide cycloaddition (Figure 1-18).<sup>99</sup> As the unfunctionalized MOF exhibited the highest activity at the lowest temperature, it is possible that the introduction of functionality via the linkers affected the pore environment in a manner that inhibited the reaction.

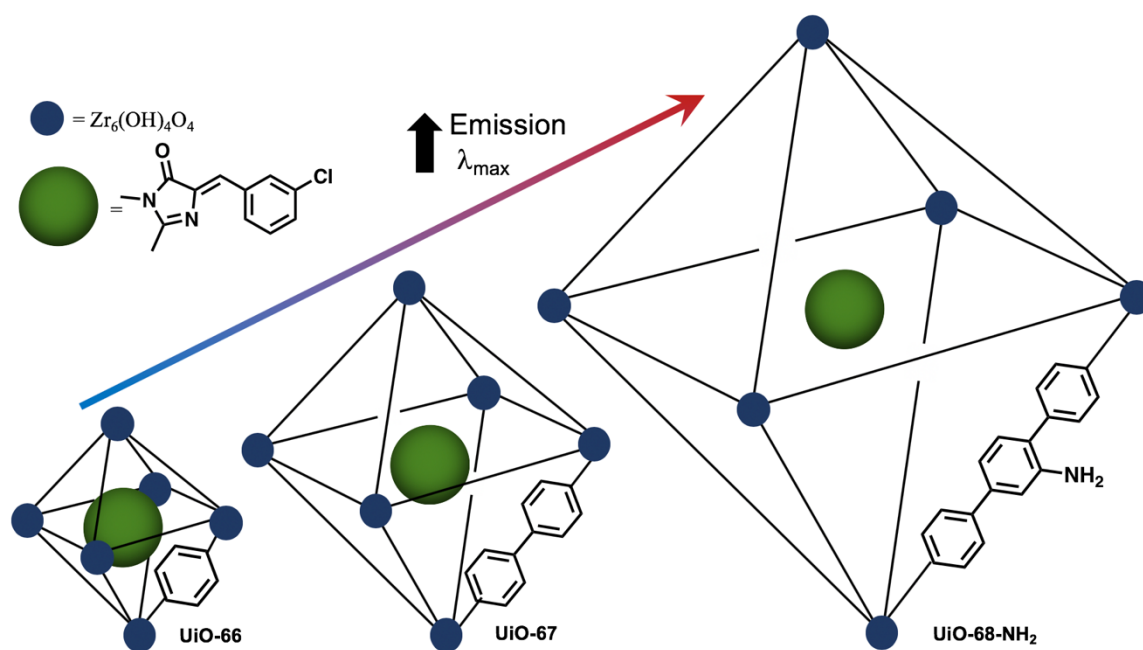


**Figure 1-18.** The effect of functional groups on MOF-based catalysis exemplified by the influence of UiO-66 substituent on carbon dioxide cycloaddition as reported by Kim and co-workers.<sup>99</sup>

#### 1.4.2 Effects of MOF pore environment on dye behavior

While some studies have indirectly suggested that changes in MOF functionality may affect an encapsulated guest, others have probed this effect more directly through the internalization of dyes and observation of corresponding changes in their behavior. In one such test, Wang and co-workers used 4-(dicyanomethylene)-2-methyl-6-(4-dimethylaminostyryl)-4H-pyran (DCM) dye to probe its two-color fluorescence as a function of encapsulation in stilbene- or naphthalene-based MOFs. They observed fluorescence changes from exposure to and evaporation of volatile solvents, which they linked to the role of confined solvent arrangement on the fluorescence of the internalized dye.<sup>100</sup> Mayers and Larsen observed pore environment influence more directly, noting a bathochromic shift in the fluorescence of both a ruthenium-tris-bipyridyl dye and a ruthenium-tris-phenanthroline dye when encapsulated in functionalized versus unfunctionalized UiO-66.<sup>101</sup> This corresponded to an effect on metal-ligand charge transfer in the dye, which might prove useful in an encapsulated catalyst. Shustova and co-workers conducted a more systematic study

involving guest confinement in a number of different hosts.<sup>102</sup> They investigated the effect of pore environment on guest reorganization and intramolecular hydrogen bonding as well as tethering of a guest dye to a rigid framework in the case of both a MOF and an analogous supramolecular cage as platforms. Interestingly, they found that progressively increasing MOF pore size resulted in correlated increase in the emission  $\lambda_{\text{max}}$  for the encapsulated 5-(3-chlorobenzylidene)-2,3-dimethyl-3,5-dihydro-4H-imidazol-4-one (Cl-BI) dye (Figure 1-19), with a bathochromic shift of 150 nm from dye confined in the largest pore compared to the smallest. These effects reflected the influence of guest mobility within porous structures on that guest's behavior and provided insights that could inform the study of confined catalytic guests in MOFs.



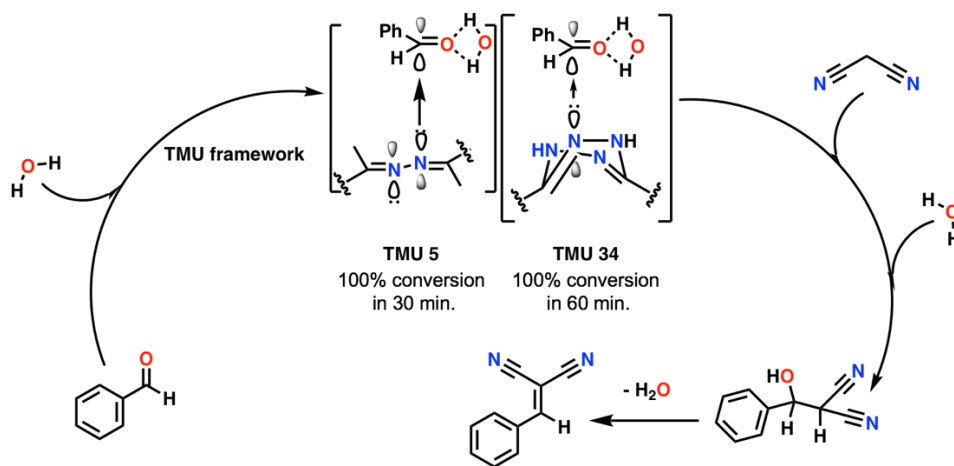
**Figure 1-19.** Representation of bathochromic shift in emission  $\lambda_{\text{max}}$  for CL-BI dye observed by Shustova and co-workers as a result of increasing MOF pore size<sup>102</sup>



### 1.4.3 Controlling catalytic behavior through MOF pore functionality

Through the knowledge gained from studying the influence of pore environment on probe molecules, unique benefits have been introduced to catalytic reactions in MOF-based host-guest systems. Long and co-workers observed a distinct effect on both activity and selectivity in cyclohexane oxidation that could be attributed to pore environment.<sup>103</sup> Using an iron-dioxo-benzenedicarboxylate (Fe-dobdc) MOF, they found that increasing the hydrophobicity of the pore environment led to a distinct increase in activity while simultaneously leading to increased selectivity for cyclohexanol over the overoxidized byproduct cyclohexanone. Huang and co-workers also observed an effect on selectivity resulting from changing pore functionality.<sup>104</sup> Palladium nanoparticles encapsulated in UiO-66-NH<sub>2</sub> favored different a product in the condensation of ethylene glycol with benzaldehyde than those encapsulated in UiO-66-OMe: the former gave 94% selectivity for the acetal product while the latter gave 97% selectivity for the benzyl ester, exemplifying the significant changes in reactivity that can result from small changes in pore environment. Studies by Doonan and co-workers showed that shifts in reactivity are not restricted to molecular species, as the activity of catalase enzymes for the decomposition of hydrogen peroxide differs significantly between the those encapsulated in the hydrophobic, methyl-functionalized ZIF-8 and those within aldehyde-functionalized ZIF-90, with the latter imparting thermal and chemical stability to the enzyme while the former almost entirely deactivates it.<sup>105</sup> In an investigation into the more fundamental causes of pore environment influence, Razavi and Morsali tested the difference in activity for a Knoevenagel condensation between the azine-methyl functionalized TMU-34 and the dihydro-tetrazine

functionalized TMU-5 and explored the cause of the latter's far-increased activity over the former (Figure 1-20). Their findings indicated that reagent-MOF molecular orbital interactions influenced activity, revealing valuable insight into possible reasons for pore environment influence on catalysts.<sup>106</sup> While each of these studies represents a significant advance in the field of catalysis, studies on the effects of pore environment on reactivity are still rare, especially in the case of encapsulated transition metal complexes. Chapter Four of this thesis details one such system that has been developed for the improvement of multicomponent carbon dioxide reduction to methanol.



**Figure 1-20.** Influence of functional group on reactivity in the Knoevenagel condensation as reported by Razavi and Morsali.<sup>115</sup>

## 1.5 THE SCOPE OF THIS DISSERTATION

Engineering multicomponent systems for catalysis holds significant promise for the improved synthesis of valuable products from simple reagents. While catalysts have been designed for these purposes, they are often either highly specialized or require harsh conditions for efficient turnover. The development of catalysts with hybrid

properties between homogeneous and heterogeneous is a promising route to address the limitations of previously existing systems while retaining their advantages. The second chapter of this thesis describes the aperture-opening encapsulation of a catalyst in a robust MOF to improve its recyclability and lifetime in the production of formate from carbon dioxide. This construct was then applied in the multicomponent conversion of carbon dioxide to methanol described in the third chapter, which was made possible by the separation of the encapsulated complex from an ester-reducing ruthenium complex in solution as well as the catalytic activity of the MOF nodes for esterification. The final chapter of this thesis describes work conducted to further increase this multicomponent system's activity for methanol production by altering the linker functionality in the framework in a systematic manner. The successful application of this strategy suggests promise for the development of similar systems for multicomponent transformations based on catalyst@MOF hybrids formed in a manner that does not require specific host-guest interactions for synthesis. The ability to further optimize activity based on insights into functional group effects suggests that other systems might be optimized with further variance in pore structure to more directly mimic enzyme active sites. Finally, the insights from these experiments suggest that such a catalyst system might be viable in an industrially relevant flow system or prove capable of stabilizing catalytic transition metal complexes that are unstable in solution, allowing access to reactivity that is inaccessible to homogeneous complexes.

## References

1. D. Rodríguez-Padrón, A. R. Puente-Santiago, A. M. Balu, M. J. Muñoz-Batista, R. Luque. Environmental Catalysis: Present and Future. *ChemCatChem*. **11**, 18-38. (2019).
2. P. K. Robinson. Enzymes: principles and biotechnological applications. *Essays Biochem*. **59**, 1-41. (2015).
3. M. L. Helm, M. P. Stewart, R. M. Bullock, M. R. DuBois, D. L. DuBois. A synthetic nickel electrocatalyst with a turnover frequency above 100,000 s<sup>-1</sup> for H<sub>2</sub> production. *Science*. **333**, 863-866. (2011).
4. J. Chen, X. Gong, J. Li, Y. Li, J. Ma, C. Hou, G. Zhao, W. Yuan, B. Zhao. Carbonyl catalysis enables a biomimetic asymmetric Mannich reaction. *Science*. **360**, 1438-1442. (2018).
5. E. Peris, R. H. Crabtree. Key factors in pincer ligand design. *Chem. Soc. Rev.* **47**, 1959-1968. (2018).
6. B. J. G. E. Pieters, M. B. van Eldijk, R. J. M. Nolte, J. Mécinović. Natural supramolecular protein assemblies. *Chem Soc. Rev.* **45**, 24-39. (2016).
7. H. Vardhan, M. Yusubov, F. Verpoort. Self-assembled metal-organic polyhedra: An overview of various applications. *Coordin. Chem. Rev.* **306**, 171-194. (2016).
8. M. Moshoeshe, M. S. Nadiye-Tabbiruka, V. Obuseng. A Review of the Chemistry, Structure, Properties, and Applications of Zeolites. *Am. J. Mater. Sci.* **7**, 196-221. (2017).
9. H. Furukawa, K. E. Cordova, M. O’Keefe, O. M. Yaghi, (2013). The chemistry and applications of metal-organic frameworks. *Science*. **341**, 1230444. DOI: 10.1126/science.1230444. (2013).
10. J.-J. Schneider, A. K. Yatsimirsky. Selectivity in host-guest complexes. *Chem. Soc. Rev.* **37**, 263-277. (2008).
11. A. Teepakakorn, T. Yamaguchi, M. Ogawa. The Improved Stability of Molecular Guests by the Confinement into Nanospaces. *Chem. Lett.* **48**, 398-409. (2019).
12. S. J. Benkovic, S. Hammes-Shiffer. A Perspective on Enzyme Catalysis. *Science*. **301**, 1196-1202. (2003).
13. O. Pàmies, J.-E. Bäckvall. Enzymatic Kinetic Resolution and Chemoenzymatic Dynamic Kinetic Resolution of  $\delta$ -Hydroxy Esters. An Efficient Route to Chiral  $\delta$ -Lactones. *J. Org. Chem.* **67**, 1261-1265. (2002).
14. S. Kobayashi, H. Uyama, S. Kimura. Enzymatic Polymerization. *Chem. Rev.* **101**, 3793-3818. (2001).
15. C. C. Farwell, J. A. McIntosh, T. K. Hyster, Z. J. Wang, F. H. Arnold. Enantioselective Imidation of Sulfides via Enzyme-Catalyzed Intermolecular Nitrogen Atom Transfer. *J. Am. Chem. Soc.* **136**, 8766-8771. (2014).
16. P. V. Iyer, L. Ananthanarayan. Enzyme stability and stabilization – Aqueous and non-aqueous environment. *Process Biochem.* **43**, 1019-1032. (2008).
17. F. H. Arnold. Directed evolution: bringing new chemistry to life. *Angew. Chem. Int. Ed.* **57**, 4143-4148. (2018).
18. L. Betancor, H. R. Luckarift. Bioinspired enzyme encapsulation for biocatalysis. *Trends Biotechnol.* **26**, 566-572. (2008).
19. C. J. Hastings, M. D. Pluth, R. G. Bergman, K. N. Raymond. Enzymelike Catalysis of the Nazarov Cyclization by Supramolecular Encapsulation. *J. Am. Chem. Soc.* **132**, 6938-6940. (2010).

20. H. Vardhan, F. Verpoort. Metal-Organic Polyhedra: Catalysis and Reactive Intermediates. *Adv. Synth. Catal.* **357**, 1351-1368. (2015).
21. D. Fiedler, H. van Halbeek, R. G. Bergman, K. N. Raymond. Supramolecular Catalysis of Unimolecular Rearrangements: Substrate Scope and Mechanistic Insights. *J. Am. Chem. Soc.* **128**, 10240-10252. (2006).
22. H. S. Lee, S. Lee, R. Kim, H.-T. Bui, B. Kim, J.-K. Kim, K. S. Park, W. Choi, W. Kim, K. M. Choi. A highly active, robust photocatalyst heterogenized in discrete cages of metal-organic polyhedra for CO<sub>2</sub> reduction. *Energy Environ. Sci.* **13**, 519-526. (2020).
23. S. S. Nurtila, W. Brenner, J. Mosquera, K. M. van Vliet, J. Nitschke, J. H. N. Reek. Size-Selective Hydroformylation by a Rhodium Catalyst Confined in a Supramolecular Cage. *Chem. Eur. J.* **25**, 609-620. (2019).
24. S. Mollick, S. Fajal, S. Mukherjee, S. K. Ghosh. Stabilizing Metal-Organic Polyhedra (MOP): Issues and Strategies. *Chem.-Asian J.* **14**, 3096-3108. (2019).
25. M. Dusselier, M. E. Davis. Small-Pore Zeolites: Synthesis and Catalysis. *Chem. Rev.* **118**, 5265-5329. (2018).
26. S. Wang, Y. Peng. Natural zeolites as adsorbents in water and wastewater treatment. *Chem. Eng. J.* **156**, 11-24. (2010).
27. S. Eckstein, P. H. Hintermeier, R. Zhao, E. Baráth, H. Shi, Y. Liu, J. A. Lercher. Influence of Hydronium Ions in Zeolites on Sorption. *Angew. Chem. Int. Edit.* **58**, 3450-3455. (2019).
28. N. Kosinov, J. Gascon, F. Kaptejin, E. J. M. Hensen. Recent developments in zeolite membranes for gas separation. *J. Membrane Sci.* **499**, 65-79. (2016).
29. G. Li, E. A. Pidko. The Nature and Catalytic Function of Cation Sites in Zeolites: a Computational Perspective. *ChemCatChem.* **11**, 134-156. (2018).
30. P. Eliášová, M. Opanasenko, P. S. Wheatley, M. Shamzhy, M. Mazur, P. Nachtigall, W. J. Roth, R. E. Morris, J. Čejka. The ADOR mechanism for the synthesis of new zeolites. *Chem. Soc. Rev.* **44**, 7177-7206. (2015).
31. B. Yilmaz, U. Müller. Catalytic Applications of Zeolites in Chemical Industry. *Top. Catal.* **52**, 888-895. (2009).
32. P. Z. Moghadam, A. Li, S. B. Wiggin, A. Tao, A. G. P. Maloney, P. A. Wood, S. C. Ward, D. Fairen-Jimenez. Development of a Cambridge Structural Database Subset: A Collection of Metal-Organic Frameworks for Past, Present, and Future. *Chem. Mater.* **29**, 2618-2625. (2017).
33. H. Li, K. Wang, Y. Sun, C. T. Lollar, J. Li, H.-C. Zhou. Recent advances in gas storage and separation using metal-organic frameworks. *Mater. Today.* **21**, 108-121. (2018).
34. W. Morris, C. J. Doonan, O. M. Yaghi. Postsynthetic Modification of a Metal-Organic Framework for Stabilization of a Hemiaminal and Ammonia Uptake. *Inorg. Chem.* **50**, 6853-6855. (2011).
35. L. Wang, M. Zheng, Z. Xie. Nanoscale metal-organic frameworks for drug delivery: a conventional platform with new promise. *J. Mater. Chem. B.* **6**, 707-717. (2018).
36. S. Wang, Y. Chen, S. Wang, P. Li, C. A. Mirkin, O. K. Farha. DNA-Functionalized Metal-Organic Framework Nanoparticles for Intracellular Delivery of Proteins. *J. Am. Chem. Soc.* **141**, 2215-2219. (2019).

37. Y. Chen, P. Li, J. A. Modica, R. J. Drout, O. K. Farha. Acid-Resistant Mesoporous Metal-Organic Framework toward Oral Insulin Delivery: Protein Encapsulation, Protection, and Release. *J. Am. Chem. Soc.* **140**, 5678-5681. (2018).
38. P. Kumar, A. Deep, K.-H. Kim. Metal-organic frameworks for sensing applications. *TrAC – Trend. Anal. Chem.* **73**, 39-53. (2015).
39. L. Ma, W. Lin. Designing metal-organic frameworks for catalytic applications. *Top. Curr. Chem.* **293**, 175-205. (2010).
40. F. G. Cirujano, A. Corma, F. X. Llabrés i Xamena. Conversion of levulinic acid into chemicals: synthesis of biomass derived levulinate esters over Zr-containing MOFs. *Chem. Eng. Sci.* **124**, 52-60. (2015).
41. S. Yuan, L. Zou, H. Li, Y.-P. Chen, J. Qin, Q. Zhang, W. Lu, M. B. Hall, H.-C. Zhou. Flexible Zirconium Metal-Organic Frameworks as Bioinspired Switchable Catalysts. *Angew. Chem. Int. Edit.* **55**, 10776-10780. (2016).
42. M. Kalaj, J. M. Palomba, K. C. Bentz, S. M. Cohen. Multiple functional groups in UiO-66 improve chemical warfare agent simulant degradation. *Chem. Commun.* **55**, 5367-5370. (2019).
43. J. Lyu, X. Zhang, K. Otake, X. Wang, P. Li, Z. Li, Z. Chen, Y. Zhang, M. C. Wasson, Y. Yang, P. Bai, X. Guo, T. Islamoglu, O. K. Farha. Topology and porosity control of metal-organic frameworks through linker functionalization. *Chem. Sci.* **10**, 1186-1192. (2019).
44. S. M. Cohen. The Postsynthetic Renaissance in Porous Solids. *J. Am. Chem. Soc.* **139**, 2855-2863. (2017).
45. Z. Yin, S. Wan, J. Yang, M. Kurmoo, M.-H. Zeng. Recent advances in post-synthetic modification of metal-organic frameworks: New types and tandem reactions. *Coord. Chem. Rev.* **378**, 500-512. (2019).
46. H.H. Mautschke, F. Drache, I. Senkovska, S. Kaskel, F. X. Llabrés I Xamena. Catalytic properties of pristine and defect-engineered Zr-MOF-808 metal organic frameworks. *Catal. Sci. Technol.* **8**, 3610-3616. (2018).
47. I. Agirrezabal-Telleria, I. Luz, M. A. Ortuño, M. Oregui-Bengoechea, I. Gandarias, N. López, M. A. Lail, M. Soukri. Gas reactions under intrapore condensation regime within tailored metal-organic framework catalysts. *Nat. Commun.* **10**, Article number: 2076. (2019).
48. U. Fluch, B. D. McCarthy, S. Ott. Post synthetic exchange enables orthogonal click chemistry in a metal organic framework. *Dalton Trans.* **48**, 45-49. (2019).
49. T. Li, M. T. Kozlowski, E. A. Doud, M. N. Blakely, N. L. Rosi. Stepwise Ligand Exchange for the Preparation of a Family of Mesoporous MOFs. *J. Am. Chem. Soc.* **135**, 11688-11691. (2013).
50. O. Karagiari, W. Bury, J. E. Mondloch, J. T. Hupp, O. K. Farha. Solvent-Assisted Linker Exchange: An Alternative to the De Novo Synthesis of Unattainable Metal-Organic Frameworks. *Angew. Chem. Int. Edit.* **53**, 4530-4540. (2014).
51. M. Taddei, R. J. Wakeham, A. Koutsianos, E. Andreoli, A. R. Barron. Post-Synthetic Ligand Exchange in Zirconium-Based Metal-Organic Frameworks: Beware of the Defects! *Angew. Chem. Int. Edit.* **57**, 11706-11710. (2018).

52. J. Marreiros, C. Caratelli, J. Hajek, A. Krajnc, G. Fleury, B. Bueken, D. E. De Vos, G. Mali, M. B. J. Roefsaers, V. Van Speybroeck, R. Ameloot. Active Role of Methanol in Post-Synthetic Linker Exchange in the Metal-Organic Framework UiO-66. *Chem. Mater.* **31**, 1359-1369. (2019).
53. D. T. Richens. Ligand Substitution Reactions at Inorganic Centers. *Chem. Rev.* **105**, 1961-2002. (2005).
54. J. V. Morabito, L.-Y. Chou, Z. Li, C. M. Manna, C. A. Petroff, R. J. Kyada, J. M. Palomba, J. A. Byers, C.-K. Tsung. Molecular encapsulation beyond the aperture size limit through dissociative linker exchange in metal-organic framework crystals. *J. Am. Chem. Soc.* **136**, 12540-12543. (2014).
55. J. Juan-Alcañiz, J. Gascon, F. Kaptejin. Metal-organic frameworks as scaffolds for the encapsulation of active species: state of the art and future perspectives. *J. Mater. Chem.* **22**, 10102-10118. (2012).
56. T. Drake, P. Ji, W. Lin. Site-Isolation in Metal-Organic Frameworks Enables Novel Transition Metal Catalysis. *Acc. Chem. Res.* **51**, 2129-2138. (2018).
57. N. Van Welthoven, S. Waitschat, S. M. Chavan, P. Liu, S. Smolders, J. Vercammen, B. Bueken, S. Bals, K. P. Lillerud, N. Stock, D. E. De Vos. Single-site metal-organic framework catalysts for the oxidative coupling of arenes via C-H/C-H activation. *Chem. Sci.* **10**, 3616-3622. (2019).
58. C. J. Doonan, W. Morris, H. Furukawa, O. M. Yaghi. Isoreticular Metalation of Metal-Organic Frameworks. *J. Am. Chem. Soc.* **131**, 9492-9493. (2009).
59. T.-H. Wei, S.-H. Wu, Y.-D. Huang, W.-S. Lo, B. P. Williams, S.-Y. Chen, H.-C. Yang, Y.-S. Hsu, Z.-Y. Lin, X.-H. Chen, P.-E. Kuo, L.-Y. Chou, C.-K. Tsung, F.-K. Shieh. Rapid mechanochemical encapsulation of biocatalysts into robust metal-organic frameworks. *Nat. Commun.* **10**, 5002. (2019).
60. T. Wang, L. Gao, J. Hou, S. J. A. Herou, J. T. Griffiths, W. Li, J. Dong, S. Gao, M.-M. Titirici, R. V. Kumar, A. K. Cheetham, X. Bao, Q. Fu, S. K. Smoukov. Rational approach to guest confinement inside MOF cavities for low-temperature catalyst. *Nat. Commun.* **10**, 1340. (2019).
61. D. T. Genna, L. Y. Pfund, D. C. Samblanet, A. G. Wong-Foy, A. J. Matzger, M. S. Sanford. Rhodium Hydrogenation Catalysts Supported in Metal Organic Frameworks: Influence of the Framework on Catalytic Activity and Selectivity. *ACS Catal.* **6**, 3569-3574. (2016).
62. X. Li, R. Van Zeeland, R. V. Maligal-Ganesh, Y. Pei, G. Power, L. Stanley, W. Huang. Impact of Linker Engineering on Catalytic Activity of Metal-Organic Frameworks Containing Pd(II)-Bipyridine Complexes. *ACS Catal.* **6**, 6324-6328. (2016).
63. B. An, L. Zeng, M. Jia, Z. Li, Z. Lin, Y. Song, Y. Zhou, J. Cheng, C. Wang, W. Lin. Molecular Iridium Complexes in Metal-Organic Frameworks Catalyze CO<sub>2</sub> Hydrogenation via Concerted Proton and Hydride Transfer. *J. Am. Chem. Soc.* **139**, 17747-17750. (2017).
64. J. S. Lee, E. A. Kapustin, X. Pei, S. Llopis, O. M. Yaghi, F. D. Toste. Architectural Stabilization of a Gold(III) Catalyst in Metal-Organic Frameworks. *Chem.* **6**, 142-152. (2020).

65. S. A. Burgess, A. Kassie, S. A. Baranowski, K. J. Fritzsche, K. Schmidt-Rohr, C. M. Brown, C. R. Wade. Improved Catalytic Activity and Stability of a Palladium Pincer Complex by Incorporation into a Metal-Organic Framework. *J. Am. Chem. Soc.* **138**, 1780-1783. (2016).
66. B. R. Reiner, A. A. Kassie, C. R. Wade. Unveiling reactive metal sites in a Pd pincer MOF: insights into Lewis acid and pore selective catalysis. *Dalton Trans.* **48**, 9588-9595. (2019).
67. A. A. Kassie, P. Duan, E. T. McClure, K. Schmidt-Rohr, P. M. Woodward, C. R. Wade. Postsynthetic Metal Exchange in a Metal-Organic Framework Assembled from Co(III) Diphosphine Pincer Complexes. *Inorg. Chem.* **58**, 3227-3236. (2019).
68. R. J. Drout, L. Robinson, O. K. Farha. Catalytic applications of enzymes encapsulated in metal-organic frameworks. *Coord. Chem. Rev.* **381**, 151-160. (2019).
69. T.-O. Knedel, E. Ricklefs, C. Schlüsener, V. B. Urlacher, C. Janiak. Laccase Encapsulation in ZIF-8 Metal-Organic Framework Shows Stability Enhancement and Substrate Selectivity. *Chem. Open.* **8**, 1337-1344. (2019).
70. F. S. Liao, W.-S. Lo, Y.-S. Hsu, C.-C. Wu, S.-C. Wang, F.-K. Shieh, J. V. Morabito, L.-Y. Chou, K. C.-W. Wu, C.-K. Tsung. Shielding against Unfolding by Embedding Enzymes in Metal-Organic Frameworks via a *de Novo* Approach. *J. Am. Chem. Soc.* **139**, 6530-6533. (2017).
71. P. Li, S.-Y. Moon, M. A. Guelta, S. P. Harvey, J. T. Hupp, O. K. Farha. Encapsulation of a Nerve Agent Detoxifying Enzyme by a Mesoporous Zirconium Metal-Organic Framework Engenders Thermal and Long-Term Stability. *J. Am. Chem. Soc.* **138**, 8052-8055. (2016).
72. G. Lu, S. Li, Z. Guo, O. K. Farha, B. G. Hauser, X. Qi, Y. Wang, X. Wang, S. Han, X. Liu, J. S. DuChene, H. Zhang, Q. Zhang, X. Chen, J. Ma, S. C. J. Loo, W. D. Wei, Y. Yang, J. T. Hupp, F. Huo. Imparting functionality to a metal-organic framework material by controlled nanoparticle encapsulation. *Nat. Chem.* **4**, 310-316. (2012).
73. Y. Liu, Y. Shen, W. Zhang, J. Weng, M. Zhao, T. Zhu, Y. R. Chi, Y. Yang, H. Zhang, F. Huo. Engineering channels of metal-organic frameworks to enhance catalytic selectivity. *Chem. Commun.* **55**, 11770-11773. (2019).
74. Z. Zhang, S. Zhang, Q. Yao, X. Chen, Z.-H. Lu. Controlled Synthesis of MOF-Encapsulated NiPt Nanoparticles toward Efficient and Complete Hydrogen Evolution from Hydrazine Borane and Hydrazine. *Inorg. Chem.* **56**, 11938-11945. (2017).
75. L. Sun, Y. Yun, H. Sheng, Y. Du, Y. Ding, P. Wu, P. Li, M. Zhu. Rational encapsulation of atomically precise nanoclusters into metal-organic frameworks by electrostatic attraction for CO<sub>2</sub> conversion. *J. Mater. Chem. A*, **6**, 15371-15376. (2018).
76. A. Grigoropoulos, G. F. S. Whitehead, N. Perret, A. P. Katsoulidis, F. M. Chadwick, R. O. Davies, A. Haynes, L. Brammer, A. S. Weller, J. Xiao, M. J. Rosseinsky. Encapsulation of an organometallic cationic catalyst by direct exchange into an anionic MOF. *Chem. Sci.* **7**, 2037-2050. (2016).



77. J. Ren, P. C. Lan, M. Chen, W. Zhang, S. Ma. Heterogenization of Trinuclear Palladium Complex into an Anionic Metal-Organic Framework through Postsynthetic Cation Exchange. *Organometallics*. **38**, 3460-3465. (2019).
78. Y.-B. Huang, J. Liang, X.-S. Wang, R. Cao. Multifunctional metal-organic framework catalysts: synergistic catalysis and tandem reactions. *Chem. Soc. Rev.* **46**, 126-157. (2017).
79. Y. Wang, N. Zhang, E. Zhang, Y. Han, Z. Qi, M. B. Ansorge-Schumacher, Y. Ge, C. Wu. Heterogeneous Metal-Organic Framework-Based Biohybrid Catalysts for Cascade Reactions in Organic Solvent. *Chem. Eur. J.*, **25**, 1716-1721. (2019).
80. Y.Z. Chen, Y.-X. Zhou, H. Wang, J. Lu, T. Uchida, Q. Xu, S.-H. Yu, H.-L. Jiang. Multifunctional PdAg@MIL-101 for One-Pot Cascade Reactions: Combination of Host-Guest Cooperation and Bimetallic Synergy in Catalysis. *ACS Catal.* **5**, 2062-2069. (2015).
81. M. Pintado-Sierra, A. M. Rasero-Almansa, A. Corma, M. Iglesias, F. Sanchez. Bifunctional iridium-(2-aminoterephthalate)-Zr-MOF chemoselective catalyst for the synthesis of secondary amines by one-pot three-step cascade reaction. *J. Catal.* **299**, 137-145. (2013).
82. M.-L. Gao, M.-H. Qi, L. Liu, Z.-B. Han. An exceptionally stable core-shell MOF/COF bifunctional catalyst for a highly efficient cascade deacetylation-Knoevenagel condensation. *Chem. Commun.* **55**, 6377-6380. (2019).
83. L. Feng, Y. Wang, S. Yuan, K.-Y. Wang, J.-L. Li, G. S. Day, D. Qiu, L. Cheng, W.-M. Chen, S. T. Madrahimov, H.-C. Zhou. Porphyrinic Metal-Organic Frameworks Installed with Brønsted Acid Sites for Efficient Tandem Semisynthesis of Artemisinin. *ACS Catal.* **9**, 5111-5118. (2019).
84. B. Li, H. C. Zeng, Synthetic Chemistry and Multifunctionality of an Amorphous Ni-MOF-74 Shell on a Ni/SiO<sub>2</sub> Hollow Catalyst for Efficient Tandem Reactions. *Chem. Mater.* **14**, 5320-5330. (2019).
85. Y. Chen, P. Li, H. Noh, C.-W. Kung, C. T. Buru, X. Wang, X. Zhang, O. K. Farha. Stabilization of Formate Dehydrogenase in a Metal-Organic Framework for Bioelectrocatalytic Reduction of CO<sub>2</sub>. *Angew. Chem. Int. Edit.* **58**, 7682-7686. (2019).
86. Y. Chen, P. Li, J. Zhou, C. T. Buru, L. Dordević, P. Li, X. Zhang, M. M. Cetin, J. F. Stoddart, S. I. Stupp, M. R. Wasielewski, O. K. Farha. Integration of Enzymes and Photosensitizers in a Hierarchical Mesoporous Metal-Organic Framework for Light-Driven CO<sub>2</sub> Reduction. *J. Am. Chem. Soc.* **142**, 1768-1773. (2020).
87. J. Liu, T. Liu, P. Du, L. Zhang, J. Lei. Metal-Organic Framework (MOF) Hybrid as a Tandem Catalyst for Enhanced Therapy against Hypoxic Tumor Cells. *Angew. Chem. Int. Edit.* **58**, 7808-7812. (2019).
88. X. Cheng, J. Zhou, J. Chen, Z. Xie, Q. Kuang, L. Zheng. One-step synthesis of thermally stable artificial multienzyme cascade system for efficient enzymatic electrochemical detection. *Nano Res.* **12**, 3031-3036. (2019).
89. W. Xu, L. Jiao, H. Yan, Y. Wu, L. Chen, W. Gu, D. Du, Y. Lin, C. Zhu. Glucose Oxidase-integrated Metal-organic Framework Hybrids as Biomimetic Cascade

- Nanozymes for Ultrasensitive Glucose Biosensing. *ACS Appl. Mater. Interfaces*. **11**, 22096-22101. (2019).
90. X. Li, B. Zhang, L. Tang, T.-W. Goh, S. Qi, A. Volkov, Y. Pei, Z. Qi, C.-K. Tsung, L. Stanley, W. Huang. Cooperative Multifunctional Catalysts for Nitron Synthesis: Platinum Nanoclusters in Amine-Functionalized Metal-Organic Frameworks. *Angew. Chem. Int. Edit.* **56**, 16371-16375. (2017).
  91. R. Limvorapitux, L.-Y. Chou, A. P. Young, C.-K. Tsung, S. T. Nguyen. Coupling Molecular and Nanoparticle Catalysts on Single Metal-Organic Framework Microcrystals for the Tandem Reaction of H<sub>2</sub>O<sub>2</sub> Generation and Selective Alkene Oxidation. *ACS Catal.* **7**, 6691-6698. (2017).
  92. E. S. Gutterød, A. Lazzarini, T. Fjermestad, G. Kaur, M. Manzoli, S. Bordiga, S. Svelle, K. P. Lillerud, E. Skúlason, S. Øien-Ødegaard, A. Nova, U. Olsbye. Hydrogenation of CO<sub>2</sub> to Methanol by Pt Nanoparticles Encapsulated in UiO-67: Deciphering the Role of the Metal-Organic Framework. *J. Am. Chem. Soc.* **142**, 999-1009. (2020).
  93. Y. Song, X. Feng, J. S. Chen, C. Brzezinski, Z. Xu, W. Lin. Multistep Engineering of Synergistic Catalysts in a Metal-Organic Framework for Tandem C-O Bond Cleavage. *J. Am. Chem. Soc.* **142**, 4872-4882. (2020).
  94. L. Zeng, Z. Wang, Y. Wang, J. Wang, Y. Guo, H. Hu, X. He, C. Wang, W. Lin. Photoactivation of Cu Centers in Metal-Organic Frameworks for Selective CO<sub>2</sub> Conversion to Ethanol. *J. Am. Chem. Soc.* **142**, 75-79. (2020).
  95. Z. Niu, W. D. C. B. Gunatilleke, Q. Sun, P. C. Lan, J. Perman, J.-G. Ma, Y. Cheng, B. Aguila, S. Ma. Metal-Organic Framework Anchored with Lewis Pair as a New Paradigm for Catalysis. *Chem.* **4**, 2587-2599. (2018).
  96. B. An, Z. Li, Y. Song, J. Zhang, L. Zheng, C. Wang, W. Lin. Cooperative copper centers in a metal-organic framework for selective conversion of CO<sub>2</sub> to ethanol. *Nature Catalysis*. **2**, 709-717. (2019).
  97. S. Yuan, Y.-P. Chen, J.-S. Qin, W. Lu, L. Zou, Q. Zhang, X. Wang, X. Sun, H.-C. Zhou. Linker Installation: Engineering Pore Environment with Precisely Placed Functionalities in Zirconium MOFs. *J. Am. Chem. Soc.* **138**, 8912-8919. (2016).
  98. I. A. Lázaro, C. J. R. Wells, R. S. Forgan. Multivariate Modulation of the Zr MOF UiO-66 for Defect-Controlled Combination Anticancer Drug Delivery. *Angew. Chem. Int. Edit.* **59**, 5211-5217. (2020).
  99. J. Noh, Y. Kim, H. Park, J. Lee, M. Yoon, M. H. Park, Y. Kim, M. Kim. Functional Group Effects on a Metal-Organic Framework Catalyst for CO<sub>2</sub> Cycloaddition. *J. Ind. Eng. Chem.* **64**, 478-481. (2018).
  100. D. Yan, Y. Tang, H. Lin, D. Wang. Tunable Two-color Luminescence and Host-guest Energy Transfer of Fluorescent Chromophores Encapsulated in Metal-Organic Frameworks. *Sci. Rep. - U. K.* **4**, Article number: 4337. (2015).
  101. J. M. Mayers, R. W. Larsen. Photophysical study of [Ru(2,2'-bipyridine)<sub>3</sub>]<sup>2+</sup> and [Ru(1,10-phenanthroline)<sub>3</sub>]<sup>2+</sup> encapsulated in the UiO-66-NH<sub>2</sub> metal organic framework. *Polyhedron*. **171**, 382-388. (2019).
  102. E. A. Dolgoplova, A. A. Berseneva, M. S. Faillace, O. A. Ejegbavwo, G. A. Leith, S. W. Choi, H. N. Gregory, A. M. Rice, M. D. Smith, M. Chruszcz, S. Garashchuck, K. Mythreye, N. B. Shustova. Confinement-Driven Photophysics

- in Cages, Covalent-Organic Frameworks, Metal-Organic Frameworks, and DNA. *J. Am. Chem. Soc.* **142**, 4769-4783. (2020).
103. D. J. Xiao, J. Oktawiec, P. J. Milner, J. R. Long. Pore Environment Effects on Catalytic Cyclohexane Oxidation in Expanded Fe<sub>2</sub>(dobdc) Analogues. *J. Am. Chem. Soc.* **138**, 14371-14379. (2016).
  104. X. Li, W. W. Goh, L. Li, C. Xiao, Z. Guo, X. C. Zeng, W. Huang. Controlling Catalytic Properties of Pd Nanoclusters through Their Chemical Environment at the Atomic Level Using Isorecticular Metal-Organic Frameworks. *ACS Catal.* **6**, 3461-3468. (2016).
  105. W. Liang, H. Xu, F. Carraro, N. K. Maddigan, Q. Li, S. G. Bell, D. M. Huang, A. Tarzia, M. B. Solomon, H. Amenitsch, L. Vaccari, C. J. Sumby, P. Falcaro, C. J. Doonan. Enhanced Activity of Enzymes Encapsulated in Hydrophilic Metal-Organic Frameworks. *J. Am. Chem. Soc.* **141**, 2348-2355. (2019).
  106. S. A. A. Razavi, A. Morsali. Function-Structure Relationship in Metal-Organic Frameworks for Mild, Green, and Fast Catalytic C-C Bond Formation. *Inorg. Chem.* **58**, 14429. (2019).

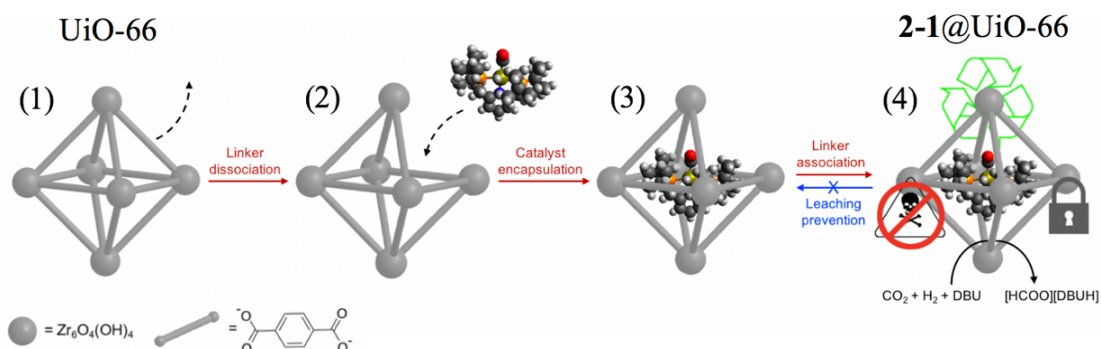
## 2.0 CHAPTER 2

### Aperture-Opening Encapsulation of a Transition Metal Catalyst in a Metal-Organic Framework for CO<sub>2</sub> Hydrogenation to Formic Acid

As discussed in Chapter 1, MOF-based host-guest composites have proven to be a versatile platform for a wide variety of applications including gas storage,<sup>1,2</sup> drug delivery,<sup>3</sup> chemical sensing,<sup>4</sup> and catalysis.<sup>5-9</sup> A number of methods have been developed to construct catalytically active MOF-based systems, including encapsulation of homogeneous catalysts during framework synthesis (i.e. *de novo* synthesis),<sup>10</sup> construction of molecular catalysts in the MOF pores after framework formation (i.e. ship-in-a-bottle synthesis),<sup>11,12</sup> functionalization of linkers with catalytically competent species,<sup>13-16</sup> and utilizing MOF nodes as active sites.<sup>17-19</sup>

A new approach to encapsulate guest molecules into MOFs was recently developed that circumvents lengthy synthetic sequences and incompatible reaction conditions.<sup>20</sup> In this approach, molecular guests larger than the aperture size of a MOF host can be encapsulated into the pores by taking advantage of aperture-opening events that occur as a result of dissociative linker exchange reactions. Discussed in this chapter is a demonstration of the highly solvent-dependent aperture-opening process in a robust MOF,<sup>21</sup> used to synthesize host-guest composites for chemical catalysis (Scheme 2-1). The encapsulation of catalysts and the conduction of catalytic reactions occurred under different conditions to optimize both loading and catalyst retention: solvents that favor

dissociative linker exchange were employed to promote encapsulation (e.g. (1) to (4), Scheme 2-1), while catalyst leaching from the MOF was prevented by carrying out catalytic reactions in solvents where dissociative linker exchange is slow (e.g. (4) to (3), Scheme 2-1).



**Scheme 2-1.** Representation of aperture-opening encapsulation of a transition metal complex and its application in catalysis

In this chapter, the successful implementation of this strategy is demonstrated with the encapsulation of a highly active homogeneous  $\text{CO}_2$  hydrogenation catalyst<sup>22-24</sup> into the robust metal-organic framework, UiO-66.<sup>25-27</sup> The encapsulated catalyst exhibited properties that were hybrid between homogeneous and heterogeneous catalysts, and evidence is provided that demonstrates that the majority of the active catalyst was encapsulated inside of the MOF rather than on its surface.

## 2.1 DETERMINING THE EFFECTIVENESS OF APERTURE-OPENING ENCAPSULATION IN UIO-66

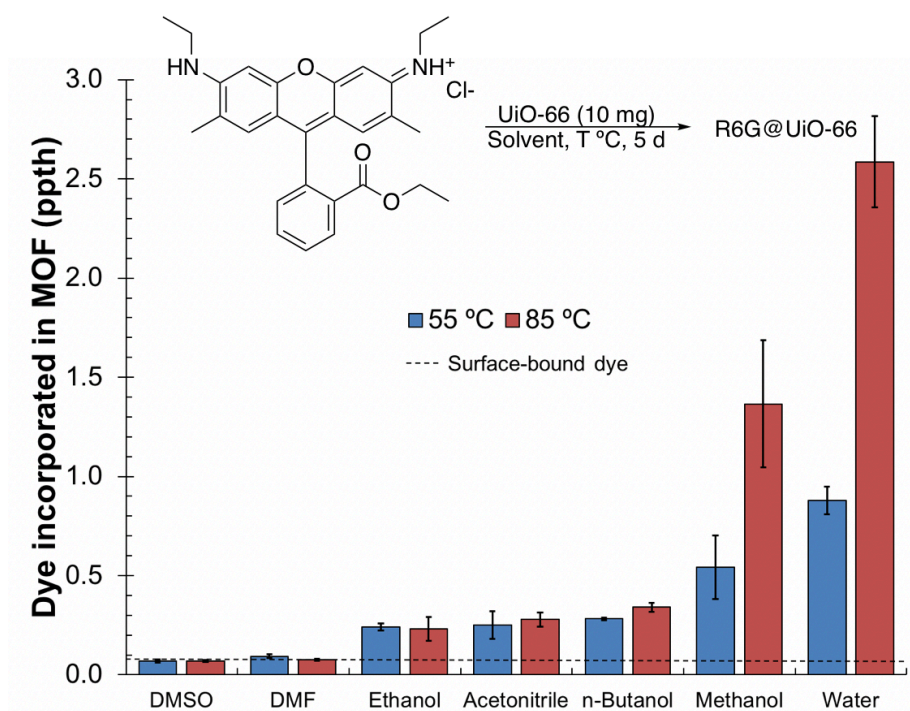
The remarkable stability the robust zirconium-terephthalate framework UiO-66 has been demonstrated in a variety of reaction conditions. As a result, UiO-66 was

selected as the host material to demonstrate the proposed aperture-opening catalyst encapsulation strategy. In order to verify that aperture-opening events in UiO-66 could be used to encapsulate guests in a manner similar to that previously observed in ZIF-8,<sup>20</sup> the fluorescent dye Rhodamine 6G (R6G) was used as a model guest molecule.

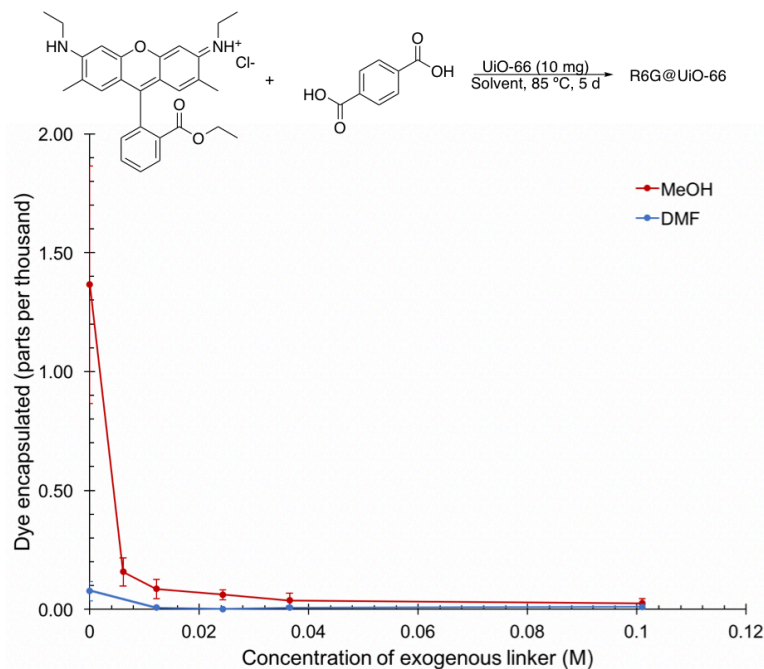
### **2.1.1 Encapsulating Dye via Aperture-Opening Pathways in UiO-66**

Dye encapsulation was found to be highest in polar protic solvents and acetonitrile and at high temperatures, consistent with the trends reported for ZIF-8 (Figure 2-1).<sup>20</sup> The observed solvent dependency was likely a result of the proposed mechanism for linker exchange in UiO-66<sup>28</sup> in the presence of protic solvents. Interestingly, the aprotic acetonitrile promoted dye encapsulation to a similar degree as ethanol or n-butanol. While the precise reason for this behavior is unknown, Adam Bensalah is currently conducting studies to better understand the role of acetonitrile as a viable aperture-opening encapsulation solvent. An increase in dye encapsulation with increasing temperature is consistent with linker dissociation being an endothermic process. MOF linkers that could not overcome the activation barrier to break the strong Zr-O bonds in UiO-66 and dissociate from the framework at lower temperatures are more likely to overcome that energetic barrier with increased energy input. As the likelihood of this activation barrier being overcome increases, a greater number of open apertures form, increasing the probability of the dye interacting with an opened aperture that leads to encapsulation. Encapsulation of R6G decreased in the presence of exogenous terephthalic acid (Figure 2-2B), suggesting the participation of the linker in the encapsulation process. The influence of the linker on the rate of dye encapsulation

was consistent with the process being a consequence of linker exchange. As R6G could only diffuse into the MOF pores under aperture-opened conditions, these results were consistent with aperture-opening being a consequence of linker exchange as well.<sup>20</sup> A solvent dependency was also observed in encapsulation in the presence of exogenous linker, suggesting that linker exchange occurred in aprotic solvents, but opened apertures in these solvents were too short-lived for encapsulation of the dye to occur.



**Figure 2-1.** Solvent and temperature dependency of encapsulation of R6G in UiO-66



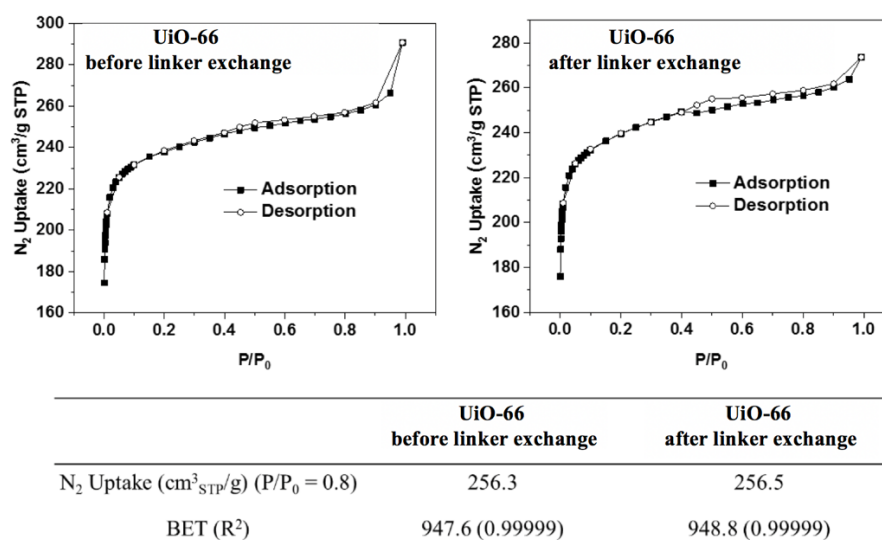
**Figure 2-2.** Effect increasing exogenous linker concentration on R6G encapsulation in methanol and DMF

The fluorescence intensity for encapsulated dye when normalized by total dye encapsulated (Table 2-1) was lower than that of surface-bound dye, suggesting that the dye incorporated in the structure was not simply bound to the external surface of the MOF. The dye could only be incorporated on the external surface or encapsulated within the MOF pores, so a difference in fluorescence intensity for the encapsulated sample with the same incorporated dye concentration as a surface-bound control further supported the hypothesis that the dye was immobilized within the framework. The surface area of UiO-66 obtained from nitrogen sorption (Figure 2-3) before (947.6 m<sup>2</sup>/g) and after exposure to aperture-opening conditions (948.8 m<sup>2</sup>/g) indicated that no additional defects were generated after exposure,<sup>26</sup> suggesting that encapsulation was not a consequence of defects in the MOF structure.



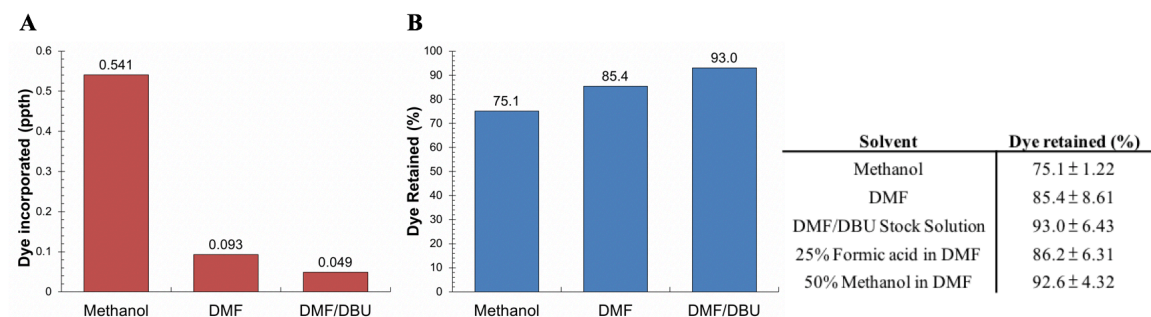
	R6G-on-UiO-66	R6G@UiO-66 (nBuOH, 85 °C)	R6G@UiO-66 (H <sub>2</sub> O, 55 °C)
Normalized I/A	1.00	0.318	0.081

**Table 2-1.** Fluorescence intensity for dye-incorporated samples normalized by the total amount of dye incorporated as measured by UV/Vis absorbance for R6G-on-UiO-66 (left) compared to that of R6G@UiO-66 formed by encapsulation in n-butanol at 85 °C (middle) or deionized water at 55 °C (right).



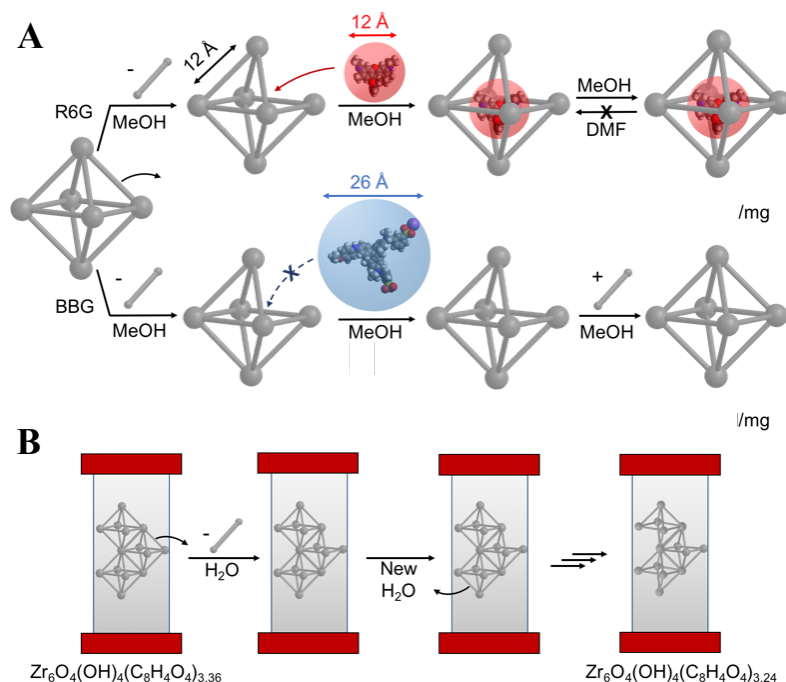
**Figure 2-3.** Nitrogen adsorption and desorption of UiO-66 before and after exposure to methanol at 55 °C for five days in the absence of guest

Next, similar dye encapsulation experiments (Figure 2-4) were used to identify the appropriate conditions required for encapsulation of a transition metal complex and to discern the orthogonal conditions needed to suppress leaching of the guest catalyst molecules during catalysis (Figure 2-5A, top). R6G encapsulation was highest at elevated temperatures in polar protic solvents (e.g., methanol) and did not occur to a large extent in most polar aprotic solvents (e.g., DMF) (Figure 2-4A). Similarly, in experiments that involved exposing R6G encapsulated in UiO-66 to various solvents, dye leaching into solution was highly suppressed in aprotic solvents compared to protic solvents (Figure 2-4B).

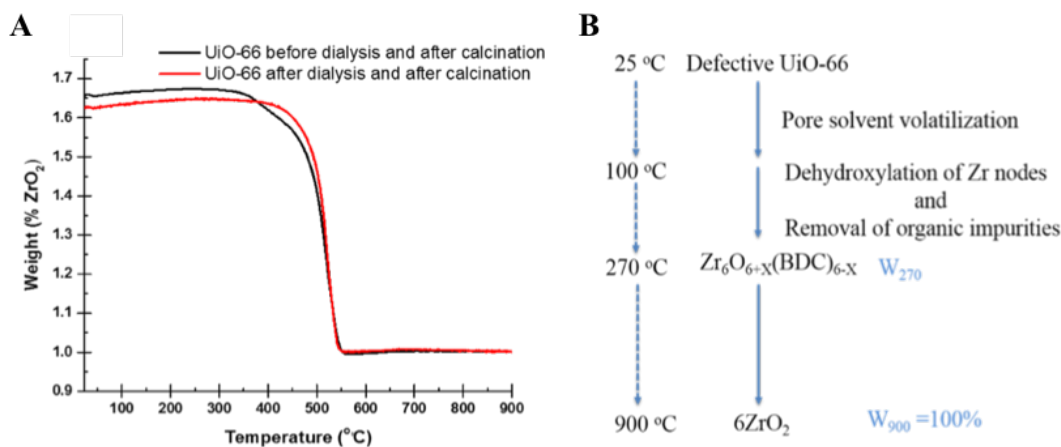


**Figure 2-4.** Dye encapsulation and leaching in various solvents. A) Amount of dye encapsulated in MOF in neat solvent at 55 °C for 5 days, B) percent of original encapsulated dye remaining in R6G@UiO-66 after exposure to solvents at 55 °C for 2 days represented in histogram and table form.

Due to the linker exchange reaction occurring at the solid-liquid interface and due to the transient nature of the intermediate involved, direct observation of the proposed aperture-opened intermediate (e.g., 2, Scheme 2-1) would be difficult. Therefore, to further probe the mechanism for guest encapsulation, Zhehui Li carried out two additional experiments (Figure 2-5A, bottom and 2-5B). She obtained evidence for the existence of the aperture-opened intermediate by subjecting UiO-66 to dialysis under conditions that were best for encapsulation (Figure 2-5B). Linkers dissociating from UiO-66 to form the aperture-opened intermediate could hypothetically then diffuse through the dialysis bag instead of reassociating with UiO-66. Periodic removal of water external to the dialysis bag would then ultimately result in UiO-66 that contained more missing terephthalic linkers. Zhehui observed results consistent with these expectations: thermogravimetric analysis (TGA) (Figure 2-6) revealed that the UiO-66 after dialysis in water for 18 days had less terephthalic acid linkers per zirconium node compared to UiO-66 before dialysis<sup>26</sup> ( $(\text{Zr}_6\text{O}_4(\text{OH})_4(\text{C}_8\text{H}_4\text{O}_4)_{3.36})$  and  $\text{Zr}_6\text{O}_4(\text{OH})_4(\text{C}_8\text{H}_4\text{O}_4)_{3.24}$  respectively).

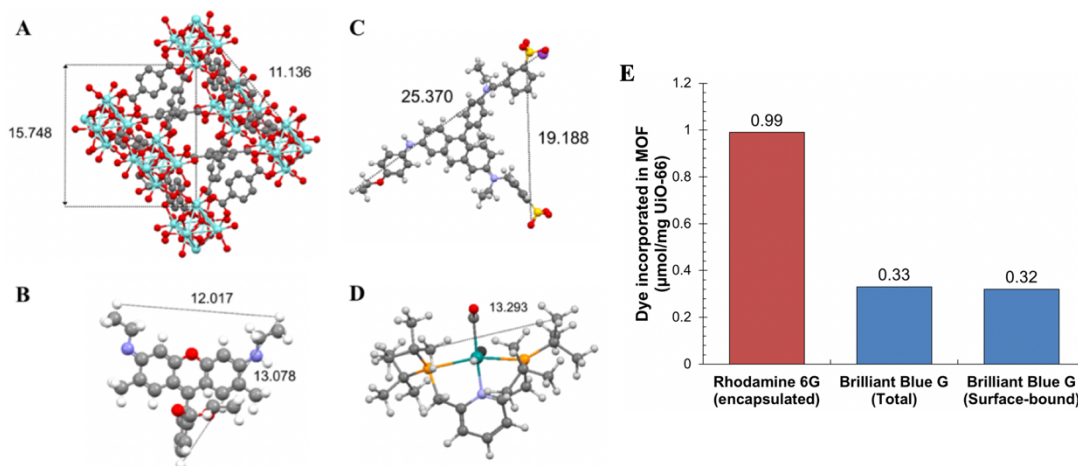


**Figure 2-5.** A) top: encapsulation of R6G in UiO-66; bottom: attempted encapsulation of Brilliant Blue G (BBG) in UiO-66. Both experiments conducted in methanol at 55 °C for five days. B) Dialysis experiment conducted by Zhehui Li with UiO-66 in water at 55 °C for 18 days; empirical formula for UiO-66 as determined from TGA analysis of MOF shown below corresponding dialysis bags.



**Figure 2-6.** Dialysis experiment carried out by Zhehui Li to probe dissociative linker exchange mechanism. A) TGA trace of UiO-66 before (black) and after after dialysis (red) after thermal activation; B) Diagram of species represented in each mass loss regime in the displayed TGA curve.

Next, to illustrate that encapsulation of guests requires properly-sized guest molecules for diffusion through opened apertures (e.g. 2  $\rightarrow$  3, Scheme 2-1), Zhehui subjected Brilliant Blue G (BBG) to the same encapsulation conditions (Figure 2-5A, bottom). BBG (26 Å, Figure 2-7C) is larger than the successfully encapsulated R6G (12 Å, Figure 2-7B) and the size of the opened apertures that would result upon dissociation of a terephthalic acid linker (12 Å, Figure 2-7A). Therefore, if aperture-opening was the key step for R6G encapsulation, BBG should not be encapsulated. Consistent with this rationale and unlike R6G, BBG demonstrated no appreciable incorporation (0.01  $\mu\text{mol}/\text{mg}$ ) beyond the amount adsorbed to the surface of the MOF (Figure 2-7E).



**Figure 2-7.** Comparison of molecular size between A) MOF host and B) Rhodamine 6G, C) Brilliant Blue G, or D)  $(^t\text{BuPNP})\text{Ru}(\text{CO})\text{HCl}$  (**2-1**); E) Comparison between R6G and BBG encapsulated in UiO-66 or on its surface.

## 2.2 APPLICATION OF A CATALYST@UIO-66 HYBRID FORMED BY APERTURE-OPENING ENCAPSULATION OF A TRANSITION METAL COMPLEX

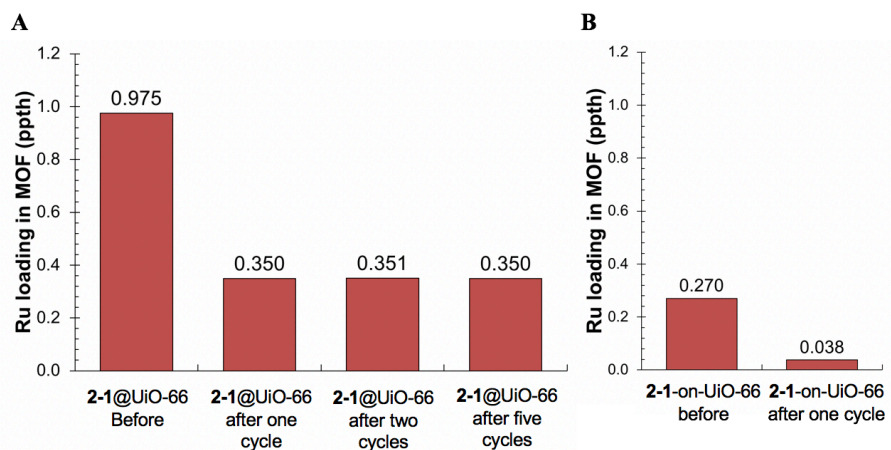
With aperture-opening in UiO-66 established as a viable synthetic method for guest encapsulation,  $(^t\text{BuPNP})\text{Ru}(\text{CO})\text{HCl}$  ( $^t\text{BuPNP}$  = 2,6-bis((di-*tert*-butylphosphino)methyl)pyridine) (**2-1**) was identified as an appropriate guest to demonstrate the developed in a catalytic application. This complex was popularized by Milstein<sup>29</sup> and explored extensively by Pidko and coworkers for CO<sub>2</sub> hydrogenation.<sup>23,30,31</sup> It was suitable as a guest molecule in UiO-66 because it is larger than the UiO-66 aperture size but smaller than its pore size (Figure 2-7D). It is also soluble and stable in methanol, and it is an active catalyst for CO<sub>2</sub> hydrogenation in DMF/1,8-diazabicyclo(5.4.0)undec-7-ene (DBU) mixtures.<sup>31</sup> Mixtures of DMF and DBU were found to be appropriate for catalysis, because R6G dye leaching was prevented with this mixture even upon prolonged heating of the host-guest system (Figure 2-4B).

### 2.2.1 Encapsulating a Ruthenium-PNP Complex in UiO-66

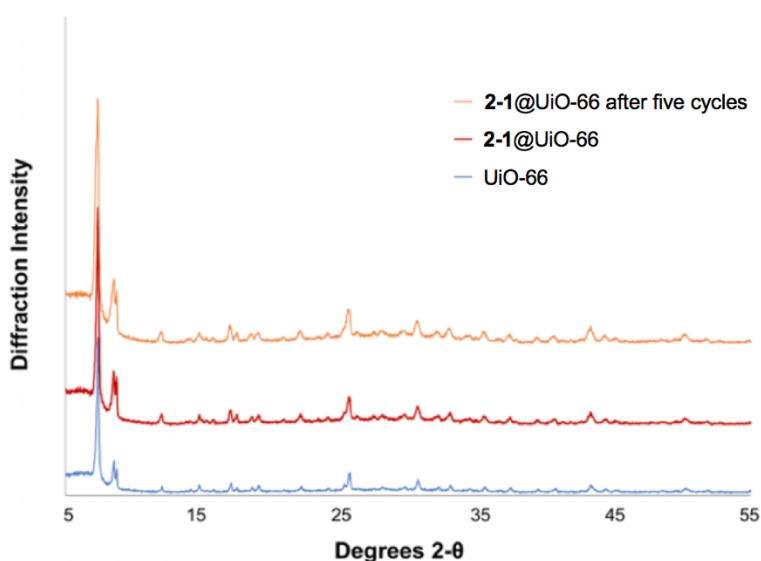
The encapsulated catalyst, henceforth referred to as **2-1**@UiO-66 in this chapter, was prepared by exposing UiO-66 to **2-1** in methanol at 55 °C for five days. catalyst loading was determined from analysis of the digested solid by inductively coupled plasma optical emission spectrometry (ICP-OES). From the Ru to Zr ratio, the loading of **2-1** in UiO-66 was initially determined to be 0.975 wt.%. When subjected to the reaction conditions described in the literature<sup>31</sup> (exposure to a solution of DBU

(15.50 mmol) in DMF (15 mL) to CO<sub>2</sub> (3 bar) and hydrogen (37 bar) at 129 °C for 45 minutes), the loading decreased to 0.35 wt.%, indicative of possible catalyst leaching (Figure 2-8A). However, when this sample was exposed to the same reaction conditions a second time, the ruthenium loading remained constant, suggesting that this exposure to harsh conditions removed **2-1** that was not encapsulated in the MOF pores from the construct rather than causing catalyst leaching. The P:Ru ratio was 2.1 for this sample both before and after these reactions, which suggested that the ligand did not dissociate from the ruthenium complex. <sup>1</sup>H-NMR analysis of **2-1** that remained in the supernatant indicated that it was unchanged during encapsulation, which further supported the absence of complex decomposition during the loading process. Powder X-ray diffraction (PXRD) analysis indicated that the crystal structure of UiO-66 was unchanged after encapsulation (Figure 2-9, red). Similar observations were made for a sample exposed to five total reaction cycles (Figure 2-8A and Figure 2-9, orange), so the first reaction cycle was then applied as a “pre-treatment” for all future samples.

For comparison, a sample in which the complex was adsorbed to the MOF crystals was also prepared, herein referred to as **2-1-on-UiO-66**. After pre-treatment of **2-1-on-UiO-66** as described above, the catalyst loading was determined to be nearly an order of magnitude lower ([**2-1**] = 0.0375 %) than the loading in **2-1@UiO-66** (Figure 2-8B). Subsequent to the studies described in this chapter, it was found that similar catalyst loadings for **2-1@UiO-66** could be achieved through exposure to encapsulation conditions in one day to those achieved in five days, so the encapsulation time was accordingly reduced.



**Figure 2-8.** Effect of pre-treatment on Ruthenium loading in **2-1@UiO-66** and **2-1-on-UiO-66**. A) Ruthenium concentration remaining in **2-1@UiO-66** before pretreatment, after pre-treatment, and after multiple exposures to reaction conditions. B) Ruthenium loading in **2-1-on-UiO-66** before and after exposure to reaction conditions.



**Figure 2-9.** PXRD of **UiO-66**, **2-1@UiO-66** and **2-1@UiO-66** after 5 cycles of CO<sub>2</sub> hydrogenation.

### 2.2.2 Assessing the Catalytic Behavior of **2-1@UiO-66**

Having determined that **2-1** remained intact during the encapsulation process, it was next necessary to compare the activity of **2-1@UiO-66** directly to that of the homogeneous complex. In order to properly compare the two catalysts, production of

formate could not be in excess of the DBU added to the reaction. In the hydrogenation of carbon dioxide to formate, the base additive serves to stabilize the formate product; after full consumption of the base, **2-1** can convert formic acid to carbon dioxide and hydrogen.<sup>31</sup> As this reversibility could lead to improper quantification of the total formate produced, it would complicate direct comparisons of activity between different catalytic species. To this end, reaction conditions were screened, beginning with the original conditions, until DBU was found not to be the limiting reagent (Table 2-2).

$$\begin{array}{c}
 \text{CO}_2 \quad + \quad \text{H}_2 \\
 (3 \text{ bar}) \quad (P \text{ bar})
 \end{array}
 \xrightarrow[\text{DMF (3 mL), DBU (3.30 mmol)}]{\text{2-1 (n mmol)} \atop T \text{ } ^\circ\text{C}, t \text{ min}}
 [\text{HCOO}^-][\text{DBUH}^+]$$

Entry	T (°C)	Catalyst loading (mmol)	Reaction time (min.)	P <sub>H<sub>2</sub></sub> (bar)	Formate produced (mmol)	Equivalents formate to DBU
1	129	9.98*10 <sup>-6</sup>	45	37	32.8	9.95
2	129	1.96*10 <sup>-13</sup>	45	37	21.5	6.52
3	80	1.96*10 <sup>-13</sup>	45	37	7.06	2.14
4	40	1.96*10 <sup>-13</sup>	45	37	6.14	1.86
5	35	1.96*10 <sup>-13</sup>	45	37	3.56	1.08
6	27	1.96*10 <sup>-13</sup>	45	37	3.47	1.05
7	27	9.98*10 <sup>-14</sup>	45	37	1.32	0.40
8	27	8.82*10 <sup>-9</sup>	45	37	19.9	6.03
9	27	8.82*10 <sup>-9</sup>	30	37	13.4	4.07
10	27	8.82*10 <sup>-9</sup>	10	37	12.5	3.79
11	27	8.82*10 <sup>-9</sup>	30	18	4.19	1.27
12	27	8.82*10 <sup>-9</sup>	30	12	2.07	0.63

**Table 2-2.** Determination of conditions under which the conversion of carbon dioxide to formate is not base-limited for **2-1**

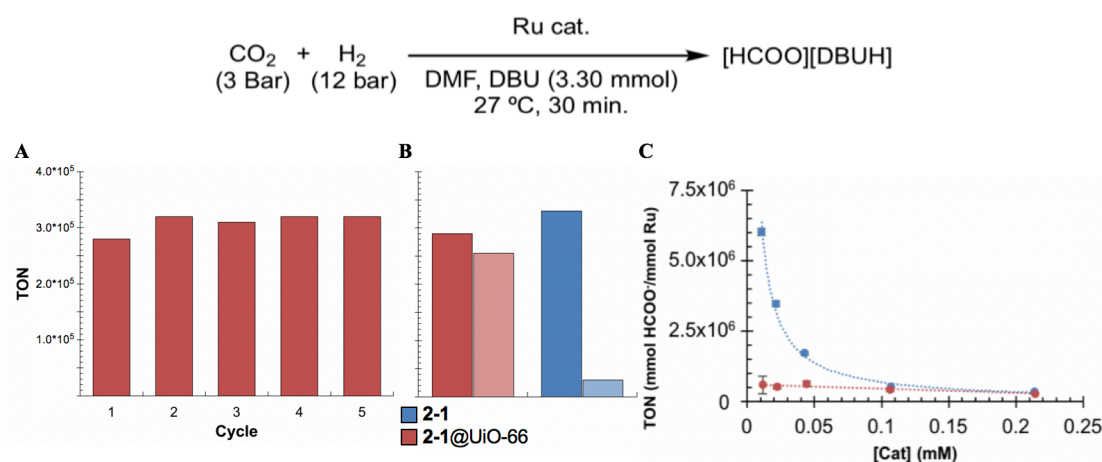


Under the reaction conditions described in the literature<sup>31</sup> (entry 1), nearly ten times as much formate was produced as base added, necessitating alteration of reaction conditions. Decreasing the catalyst loading led to a decrease in formate production, but the reaction remained base limited (entry 2). Reaction temperature was then reduced progressively (entries 3-6) until the reaction was conducted at room temperature. Though these conditions led to lower formate production as intended, a further decrease in catalyst loading was necessary to achieve conditions in which formate production did not exceed base loading (entry 7).

Unfortunately, the catalyst loading in this reaction was below the limit of detection for ICP-OES. Since proper comparison between the homogeneous and hybrid species required comparison at similar catalyst loadings, conditions had to be identified in which the reaction was not base limited while the catalyst loading was higher than the ICP-OES detection limit. At this increased catalyst loading (entry 8), the ratio of formate to DBU exceeded 6, thus reaction conditions had to be further altered. Consistent with this goal, the reaction time was decreased (entries 9 and 10). However, even at 10 minutes the reaction remained base-limited, suggesting that further change was necessary. Reduction in hydrogen pressure first to 18 bar (entry 11) then 12 bar (entry 12) at a 30-minute reaction time led to reaction conditions in which the reaction was not base limited: under the latter conditions, the ratio of formate to base was 0.63. The comparison of homogeneous **2-1** to **2-1@UiO-66** was thus possible under the conditions described in entry 12 without the complication of base limitation.

A key difference between the homogeneous **2-1** and **2-1@UiO-66** is the ability to recycle the catalyst. As shown in Figure 2-10A, **2-1@UiO-66** retained its activity

through five cycles. PXRD analysis after the fifth cycle (Figure 2-9, orange) and the absence of terephthalic acid in the  $^1\text{H}$ -NMR spectrum of the reaction supernatant provided support that the UiO-66 host maintained its integrity. The ruthenium loading in **2-1**@UiO-66 after the fifth cycle detected by ICP-OES was 0.35 wt.% with a P:Ru ratio of 2.4 (Figure 2-8A), which was similar to the catalyst composition prior to the first cycle. Additionally, the supernatant from reactions using **2-1**@UiO-66 was inactive for  $\text{CO}_2$  hydrogenation, further suggesting that catalyst leaching did not occur.



**Figure 2-10.** A) Activity of **2-1**@UiO-66 (TON = mmol HCOO<sup>-</sup>/mmol Ru) upon catalyst recycling. B) comparison of catalyst activity in first cycle (dark) to that upon addition of a second aliquot of DBU (light). C) Activity for **2-1** (blue) and **2-1**@UiO-66 (red) at different catalyst concentrations (mM).

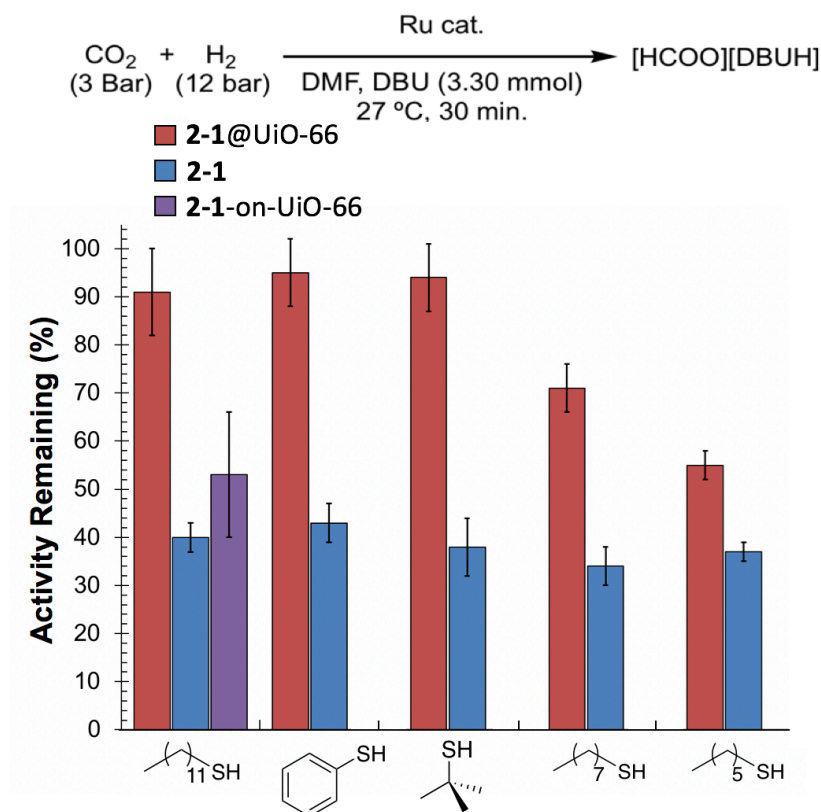
The recyclability and stability of the encapsulated catalyst were further evaluated by an alternative method: a second aliquot of DBU was added to reactions catalyzed by **2-1** and **2-1**@UiO-66, and the reaction mixtures were then re-subjected to the hydrogenation conditions. A significant decrease in activity was observed for the reaction catalyzed by **2-1**, whereas activity remained virtually the same for the reaction catalyzed by **2-1**@UiO-66 (Figure 2-8B). This outcome suggested that bimolecular decomposition limits the recyclability of the homogeneous catalyst, which is not the

case for **2-1**@UiO-66. Additional evidence that the homogeneous catalyst undergoes bimolecular catalyst deactivation more readily than the encapsulated catalyst was obtained by evaluating the activity of the two catalysts at different catalyst concentrations (Figure 2-8C). A polynomial decrease in turnover number with increasing catalyst loading was observed for **2-1**, which is characteristic of a catalyst that undergoes bimolecular catalyst deactivation. In contrast, turnover in **2-1**@UiO-66 was constant irrespective of catalyst loading, which is expected for a catalyst that does not undergo bimolecular decomposition. The large difference in turnover number between **2-1** and **2-1**@UiO-66 at low catalyst loadings is likely a result of size exclusion of the bulky DBU base by the MOF pores, as described by Zhehui Li in Chapter 4 of her thesis.<sup>32</sup>

To provide additional evidence that the ruthenium complex in **2-1**@UiO-66 was encapsulated in the MOF rather than on its surface, CO<sub>2</sub> hydrogenation reactions were carried out in the presence of thiols (Figure 2-11). Thiols are known poisons for many transition metal catalysts. As expected, when **2-1** was exposed to dodecanethiol, catalytic activity was reduced by 60% (blue). Additionally, **2-1**-on-UiO-66 was poisoned by dodecanethiol to a similar degree as the homogenous catalyst (purple). In contrast, when **2-1**@UiO-66 was exposed to dodecanethiol, catalytic activity was only reduced by 10% (red).

The susceptibility of the catalysts to poisoning was further probed by Zhehui Li by carrying out catalysis in the presence of a series of thiols (Figure 2-11). The activity of **2-1**@UiO-66 was unaffected by the presence of large and bulky thiols (e.g. dodecanethiol, and *tert*-butylthiol), supporting the hypothesis that the active species

was encapsulated in the framework rather than bound to the surface. Catalytic activity was higher in all cases for **2-1**@UiO-66 compared to **2-1** in the presence of the thiol poisons. Moreover, all reactions catalyzed by **2-1** were poisoned to approximately the same degree regardless to the identity of the thiol. In contrast, poisoning in reactions catalyzed by **2-1**@UiO-66 was dependent on thiol identity, with the most effective poisons being the least sterically demanding. These results were consistent with the catalyst being situated inside of the pores rather than on the surface of UiO-66 because more facile diffusion of the smaller thiols through the aperture of UiO-66 is expected, resulting in poisoning of the catalyst to a greater extent than with larger and more sterically bulky thiol poisons.<sup>33</sup>



**Figure 2-11.** Comparison of the activity of homogeneous (left) and encapsulated (right) catalysts in the presence of differently sized thiol poisons.

## 2.3 CONCLUSION

A new method was developed to form a MOF-based host-guest system by encapsulating a transition metal complex. This method takes advantage of solvent-dependent, aperture-opening events resulting from dissociative linker exchange reactions in UiO-66. The encapsulation of complex **2-1** separated individual active sites and prevented bimolecular deactivation, leading to recyclability not characteristic of its homogeneous counterpart. Isolation of the active site within the MOF also increased the resistance of the complex to poisoning during CO<sub>2</sub> hydrogenation as a result of size selectivity. Notably, the new method for encapsulation did not require engineering of the guest or host materials, decoupling the synthesis of the MOF from that of the transition metal complex and allowing for independent modification of each component. As a result, this method could be extended to the synthesis of host-guest composites that are suitable for a broader array of catalytic transformations.

In the following chapters, aperture-opening encapsulation is employed in the construction of multicomponent catalytic systems for the hydrogenation of CO<sub>2</sub> to methanol. The generality of the aperture-opening encapsulation method allows for the separation of two different transition metal complexes that are incompatible with each other, and a cascade transformation that was previously performed stepwise in multiple reaction vessels can consequently occur in one vessel. This leads to the observation of intriguing catalytic behavior that was not accessible in previous reports.

## Materials and Methods

### General Considerations:

Unless otherwise stated, all manipulations were carried out in air using standard analytical procedures. Catalytic carbon dioxide hydrogenation reactions were carried out in 5.0 mL ampules placed in a 450 mL stainless steel Parr reactor with stirring. Included with each reaction were positive and negative controls (using **2-1** and no catalyst, respectively) to ensure proper operation and to ensure that no cross contamination between ampules occurred. To ensure that all catalyst activity in the hybrid catalyst was coming from the encapsulated complex, a control reaction with virgin UiO-66 was carried out, which revealed only trace amounts of formate being formed. Experiments carried out in an air-free environment were conducted under a positive pressure of N<sub>2</sub> using standard glovebox or Schlenk line techniques.<sup>34</sup> UiO-66 was synthesized as previously described. **2-1** was synthesized following a procedure adapted from the literature.<sup>26</sup> All **2-1**@UiO-66 catalyst employed was pre-treated as noted and subjected to serial solid dilution with UiO-66 in a mortar and pestle to achieve sufficiently low catalyst loading so that the reactions were not base-limited. **2-1**-on-UiO-66 used in catalysis was subjected to solid dilution without pre-treatment because this procedure led to complete removal of catalyst from the surface of the MOF.

### *Materials*

2,6-lutidine (Aldrich), di-tert-butylchlorophosphine (Acros Organics), polyvinylpyrrolidone (TCI), and Rhodamine 6G (Sigma-Aldrich) were purchased from the indicated sources and used without further purification. Dialysis tubes were purchased

from BioDesignDialysis Tubing with 15.5 mm wet diameter, 1.91 ml/cm volume and 8000 MWCO. STA analysis was carried out in NETZSCH STA 449F. Powder X-ray diffraction traces were collected on a Bruker AXS diffractometer with Cu K $\alpha$  radiation ( $\lambda=1.5418$  Å).  $^1\text{H}$ -NMR and  $^{31}\text{P}\{^1\text{H}\}$ -NMR spectra were collected on a Varian Unity INOVA spectrometers (400 MHz, 500 MHz, or 600 MHz, as indicated), with all chemical shifts reported in ppm. Chemical shifts were reported in reference to tetramethylsilane and phosphoric acid for  $^1\text{H}$ -NMR and  $^{31}\text{P}$ -NMR spectra, respectively ( $\delta$  0.0 ppm for both). Formate production in catalysis was quantified using  $^1\text{H}$  NMR spectroscopy using benzene (10  $\mu\text{L}$ ) as an external standard in a mixture of  $\text{D}_2\text{O}$  (450  $\mu\text{L}$ ) and reaction mixture (250  $\mu\text{L}$ ).  $^1\text{H}$ -NMR spectra were acquired in 16 transients.  $^{31}\text{P}$ -NMR spectra were acquired in 160 transients. All centrifugation steps were performed at 4000 revolutions per minute for 10 minutes using a Thermo Scientific CL2 centrifuge unless otherwise noted. All UV-visible absorbance measurements were obtained using a refurbished Molecular Devices Spectramax M5 spectrometer. Inductively coupled plasma optical emission (ICP-OES) spectrometry was recorded in an Agilent 5100 instrument that was calibrated using known concentrations of standard solutions to quantify Zr, Ru, and P. Ru ( $1000\pm 4$  ppm), P ( $100.04\pm 0.55$  ppm), Zr ( $999\pm 5$  ppm) single elemental standards were purchased from Inorganic Ventures.

### *Procedures*

**Digestion of R6G/UiO-66 samples** Each dried solid sample (5 mg) was added to a 1.5-mL centrifugation tube. Dimethylsulfoxide (1.5 mL) was added to each sample. One drop of 15 wt% hydrofluoric acid was added to each sample, which was then left to digest

overnight. Each sample was then neutralized using excess sodium bicarbonate and subjected to centrifugation.

**Development of calibration curves** Rhodamine 6G was weighed directly in a 50-mL volumetric flask, which was then filled to the volumetric marking with the solvent to be tested. This solution was then distributed among as many 20-mL scintillation vials as necessary. 1 mL of each calibration solution was removed and diluted using a volumetric flask (10 mL or 50 mL) to yield various concentrations to be used to calibrate. The absorbance of each solution was taken at 530 nm and 25 °C using a compatible cuvette.

**Encapsulation of Rhodamine 6G in UiO-66, R6G@UiO-66.** Following a procedure similar to previously published procedure,<sup>20</sup> the intended encapsulation solvent (15 mL) was added to a 20-mL scintillation vial for each sample or to 20 mL crimp-sealed vials for reactions carried out at 85 °C. UiO-66 (15 mg) and Rhodamine 6G (14.8 mg) were added to the vial, which was then sealed and heated at the noted temperature (55 °C or 85 °C) for five days. Upon cooling, the solid sample was isolated by centrifugation, and then triturated by washing the solid with a 14 wt.% polyvinylpyrrolidone mixture in methanol followed by centrifugation. Trituration was carried out twice more and the samples were allowed to dry in air at room temperature overnight. The MOF material was digested using the above digestion procedure, and the absorbance of each resulting solution was collected at 530 nm and 25 °C in DMSO using a 0.7-mL VWR quartz cuvette. The concentration of the dye was determined by comparison to a standard curve, which was then related to the amount of digested MOF to determine the loading of Rhodamine 6G in UiO-66.

**Physical mixture control sample, R6G-on-UiO-66.** UiO-66 (15 mg in each vial) was weighed out in a 20-mL scintillation vial. Methanol (15 mL) was added to this vial,



which was subjected to sonication for approximately 10 minutes to disperse the solid. Rhodamine 6G (14.8 mg) was added to this vial, which was inverted twice, then immediately subjected to centrifugation. The supernatant was then decanted and the solids were obtained without further washing.

**I/A Measurements** A “Surface-bound dye” sample was prepared using the above procedure. This sample and all R6G@UiO-66 samples were added to separate 20 mL scintillation vials. All solids were dispersed in neat methanol and transferred to quartz cuvettes. The samples were excited at 530 nm and emission intensity measurements were obtained at 552 nm. The solids were then allowed to air-dry overnight. The solids were then digested using the above procedure and the absorbance of each resulting solution at 530 nm and 25 °C was obtained using a 0.7-mL VWR quartz cuvette in dimethyl sulfoxide. These readings were normalized by mass and analyzed to find a ratio of fluorescence intensity to absorbance of the solution. The most representative data are listed in Table S2. Consistent with previous similar measurements made with ZIF-8,<sup>20</sup> R6G@UiO-66 had a different I/A value than did R6G@UiO-66 or R6G in solution, which is an indicator that the aperture opening procedure led to the encapsulation of R6G in UiO-66.

**Influence of exogenous terephthalic acid linker concentration on dye encapsulation in R6G@UiO-66.** The general procedure used for encapsulating Rhodamine 6G was used as described above except different amounts of terephthalic acid (30.3 mg, 60.6 mg, 90.9 mg, or 250.9 mg) were also added to the reaction and an additional washing step using N,N'-dimethylformamide in place of the PVP/methanol solution. Analysis of dye encapsulation was carried out in an analogous fashion as described above.

**Rhodamine 6G leaching studies from R6G@UiO-66.** Solid samples of R6G@UiO-66 (encapsulated in water at 55 °C, 5 mg each) were weighed out in separate 20 mL scintillation vials and dried for three days in a vacuum oven at 130 °C to remove residual water. Solvent (5.0 mL) was added to each of these vials, which were then sealed and heated for two days at either 55 °C or 85 °C. The solid from the samples were isolated by centrifugation, washed three times with a mixture of polyvinylpyrrolidone (PVP) in methanol (14 wt %), then allowed to dry in air overnight at room temperature. The dye concentration was then determined as described above. The resulting dye loading values were compared to loadings from R6G@UiO-66 obtained from the same source directly after its synthesis.

**Synthesis of 2,6-bis((di-*tert*-butylphosphino)methyl)pyridine (<sup>t</sup>BuPNP).** The synthesis of this species was adapted from a literature procedure.<sup>29</sup> On a Schlenk line under nitrogen atmosphere, a solution of 2,6-lutidine (0.54 mL, 4.7 mmol) in diethyl ether (1.96 mL) was prepared in a 50-mL two-neck flask, then cooled to 0 °C. *n*-Butyl lithium in hexanes (2.0 M, 4.8 mL, 9.6 mmol) was added slowly by syringe to this cooled solution, which resulted in the homogeneous reaction mixture to turn a dark maroon-red color. The reaction mixture was allowed to warm to room temperature and heated to 40 °C for fifteen hours. After cooling to room temperature, the reaction mixture was brought -78 °C where di-*tert*-butylchlorophosphine (1.85 mL, 9.74 mmol) was added dropwise to the reaction mixture via syringe. The reaction mixture was allowed to warm to room temperature where it reacted for one hour, retaining its deep red coloration. The reaction mixture was quenched with degassed methanol (40 mL), resulting in a color change to light-yellow. The reaction mixture was left without stirring for one hour to allow the resulting lithium salt to settle.

The liquid product mixture was transferred by cannula filtration to another two-necked flask, and the lithium salt was washed twice with diethyl ether. The solvent mixture was removed by vacuum at 55 °C resulting in an off-white solid. This solid was transferred to the glovebox and extracted in diethyl ether, then recrystallized in diethyl ether at -40 °C. The clear-white crystalline product was recovered and washed with cold diethyl ether (492.8 mg, 53% yield).  $^{31}\text{P}\{^1\text{H}\}$  NMR ( $\text{C}_6\text{D}_6$ ): 37.60 (s).  $^1\text{H}$  NMR ( $\text{C}_6\text{D}_6$ ): 1.13 (d,  $^3J_{\text{PH}}$ ) 10.8 Hz, 36H,  $\text{PC}(\text{CH}_3)_3$ , 3.09 (d,  $^2J_{\text{PH}}$ ) 2.4 Hz, 4H,  $\text{CH}_2\text{P}$ ), 7.17 (d,  $^3J_{\text{HH}}$ ) 7.5 Hz, 2H, pyridine-H3,5), 7.25 (t,  $^3J_{\text{HH}}$ ) 7.8 Hz, 1H, pyridine-H4).  $^{13}\text{C}\{^1\text{H}\}$  NMR ( $\text{C}_6\text{D}_6$ ): 29.68 (d,  $^2J_{\text{PC}}$ ) 54.0 Hz,  $\text{PC}(\text{CH}_3)_3$ , 31.69 (d,  $^1J_{\text{PC}}$ ) 94.2 Hz,  $\text{CH}_2\text{P}$ ), 32.23 (d,  $^1J_{\text{PC}}$ ) 103.8 Hz,  $\text{CH}_2\text{P}$ ), 120.64 (d,  $^3J_{\text{PC}}$ ) 36.6 Hz, pyridine-C3,5), 135.68 (s, pyridine-C4), 161.40 (d,  $^2J_{\text{PC}}$ ) 59.4 Hz, pyridine-C2,5).  $^1\text{H}$  and  $^{31}\text{P}$ -NMR spectra matched literature precedents<sup>29</sup>

**Synthesis of ( $^t\text{BuPNP}$ )Ru(CO)HCl. (2-1) (Adapted from literature)<sup>23</sup>** In an inert atmosphere glove box,  $\text{RuHCl}(\text{PPh}_3)_3(\text{CO})$  (257.7 mg, 0.2707 mmol) was suspended in tetrahydrofuran (10 mL) in a 100 mL Schlenk tube.  $^t\text{BuPNP}$  (110.2 mg, 0.2786 mmol) was added to this suspension. The solution was diluted with THF (20 mL). This reaction mixture was sealed and removed from the glovebox, then heated at 65 °C for 3 hours. The resulting mixture was returned to the glove box and filtered through celite on a coarse fritted funnel. The remaining THF was removed *en vacuo*. The resultant oily yellow solid was dissolved in THF (0.5 mL), and precipitated into pentane to give a yellow solid. This solid was then washed with pentane (50 mL), and the crude product was recrystallized in pentane at -40 °C. The recrystallized product (87.3 mg, 0.155 mmol, 57.4% yield)  $^1\text{H}$ -NMR (500 MHz,  $\text{C}_6\text{D}_6$ )  $\delta$ : -14.52 (t,  $J = 20.0$  Hz, 1H), 1.13 (t,  $J = 8.0$  Hz, 18H), 1.52 (t,  $J = 8.0$  Hz, 18H), 2.87 (dt,  $J = 16.0$  Hz,  $J = 4.0$  Hz, 2H), 3.77 (dt,  $J = 16.0$  Hz,  $J = 4.0$  Hz, 2H), 6.46

(d,  $J = 8.0$  Hz, 2H), 6.79 (t,  $J = 8.0$  Hz, 1H) ppm.  $^{31}\text{P}\{^1\text{H}\}$ -NMR (202 MHz,  $\text{C}_6\text{D}_6$ )  $\delta$ : 90.8 (s) ppm. This spectral data was consistent with the literature reported spectral data.<sup>23</sup>

**Synthesis of UiO-66.** This synthesis was adapted from the literature<sup>26</sup>  $\text{N,N'}$ -dimethylformamide (DMF) (25 mL) was added to a 45 mL Teflon-lined steel autoclave. Zirconium tetrachloride (241.4 mg, 1.036 mmol) and terephthalic acid (342.8 mg, 2.063 mmol) and concentrated hydrochloric acid (180  $\mu\text{L}$ ) was added to the autoclave, which was then sealed and heated at 220  $^\circ\text{C}$  for 20 hours. The reaction mixture was then allowed to cool to room temperature and agitated to suspend the solid. This solid was isolated by centrifugation, then washed with DMF (15 mL) and left to soak in this solvent overnight. This solid was isolated again by centrifugation and washed twice with methanol (15 mL), then left to soak overnight in methanol. The solid was isolated by centrifugation and dried in a vacuum chamber overnight, then dried overnight in an oven at 70  $^\circ\text{C}$ . Powder X-Ray diffraction traces matched literature precedents.<sup>26</sup>

**Synthesis of 2-1@UiO-66.** In an inert atmosphere glovebox, methanol (10 mL) was added to a 20-mL crimp-sealed vial in a glovebox. UiO-66 (200 mg) and 2-1 (5.0 mg, 5.3  $\mu\text{mol}$ ) were added to the vial, which was then sealed. This mixture was heated at 55  $^\circ\text{C}$  for five days, and then allowed to cool to room temperature. The resulting mixture was brought into a glovebox. The vial was unsealed, and the resultant mixture was transferred to a 20 mL scintillation vial and subjected to centrifugation. Trituration was achieved by decanting the supernatant from this mixture, which was set aside for NMR analysis. The remaining solid was further triturated three times with methanol (10 mL) each time using centrifugation to ensure quantitative mass transfer. After three washing cycles, 188 mg of a pale yellow solid (94%) was obtained. This solid was dried overnight in a vacuum

chamber. A portion of this material (100 mg) was suspended in 15 mL of degassed DMF, and then transferred as a slurry to a 20 mL ampule containing a stir bar using a 9" glass pipet. 1,8-diazabicyclo[5.4.0]undec-7-ene (DBU) (2.465 mL, 2.505 g, 15.50 mmol) was added to this ampule. The ampule was added to a 450-mL stainless steel Parr reactor. The vessel was purged with carbon dioxide for 5 minutes and then pressurized to 42 psi. The vessel was then pressurized with hydrogen gas to achieve a total pressure of 542 psi at room temperature. The reactor was heated to 129 °C and left to react for 45 minutes. The heating mantle was removed, the reactor was cooled using a room-temperature water bath, and the pressure was released slowly from the vessel. The vessel was opened and the ampule was removed. The reaction mixture was transferred as a slurry to a 20-mL scintillation vial and subjected to centrifugation at 3000 revolutions per minute for 15 min, after which the supernatant was decanted. The solid was triturated twice with methanol (20 mL) followed by centrifugation and dried overnight in a vacuum chamber to give a pale yellow powder (93 mg, 93%). The loading of catalyst in the MOF was determined by ICP-OES (see "Preparation of **2-1** stock solutions" and "Digestion of UiO-66 for ICP-OES analysis", below). The structural integrity of the solid was confirmed by powder x-ray diffraction.

**Procedure for preparing 2-1-on-UiO-66.** In an inert atmosphere glovebox, methanol (10 mL) was added to a 20-mL scintillation vial. UiO-66 (100 mg) and **2-1** (5.0 mg, 5.3  $\mu$ mol) were added to the vial, which was then sealed. This mixture was agitated by shaking for several seconds, then immediately subjected to centrifugation. Trituration was achieved by decanting the supernatant from this mixture. The remaining solid was further triturated three times with methanol (10 mL) each time using centrifugation to ensure

quantitative mass transfer and dried overnight in a vacuum chamber. After three washing, 92 mg of a pale yellow solid (92%) was obtained and used without further manipulation in catalysis. This solid was dried overnight in a vacuum chamber and the loading of catalyst in the MOF was determined by ICP-OES (see “Preparation of **2-1** stock solutions” and “Digestion of UiO-66 for ICP-OES analysis”, below). The structural integrity of the solid was confirmed by powder x-ray diffraction.

**Preparation of 2-1 stock solutions.** **2-1** (5.0 mg, 5.3  $\mu\text{mol}$ ) was added to a 20 mL scintillation vial. Degassed N,N'-dimethylformamide (DMF) (3.0 mL) was added to this vial. From this solution, 1.0 mL was extracted and diluted to 5.0 mL in a class A 10-mL volumetric flask using DMF. Further serial dilution was achieved by removing 1.0 mL of this solution and diluting to 10 mL in a class A 10-mL volumetric flask. The catalytic solution (0.033  $\mu\text{M}$ ) was transferred to a 20-mL scintillation vial, sealed, and stored at -40  $^{\circ}\text{C}$  in a glovebox. Solutions were allowed to warm to room temperature before use in catalysis

**General Procedure for the hydrogenation of carbon dioxide.** For homogeneous catalysis, a stock solution (3.0 mL) of **2-1** in DMF was prepared as previously noted and added to a 5.0-mL ampule using a 9” glass pipet. For the heterogeneous catalyst, unless otherwise noted, the solid was suspended in 3 mL of degassed DMF, and then transferred as a slurry to 5-mL ampules using a 9” glass pipet. 1,8-diazabicyclo[5.4.0]undec-7-ene (DBU) (0.493 mL, 0.501 g, 3.30 mmol) was added to each ampule with a stir bar. These ampules were arranged in a 450 mL stainless steel Parr reactor that contained a thermocouple to ensure thermostated reactions. The vessel was placed on a Parr instrument stand atop a stir plate and surrounded by a heating mantle. The reaction vessel was purged

with carbon dioxide for 5 minutes and then pressurized to 42 psi. The vessel was pressurized with hydrogen to a total pressure of 212 psi, and the reactions were allowed to react at room temperature for 30 minutes. Upon conclusion of the reaction, the heating mantle was removed and the pressure was released slowly from the vessel. The vessel was opened and the ampules were removed. The colorless slurry obtained from reactions involving heterogeneous catalysis were transferred to 20 mL scintillation vials and subjected to centrifugation, after which the supernatant was decanted. The homogeneous reactions were removed from the ampules and the supernatant was analyzed as described below without further manipulation. A 0.25 mL aliquot of the supernatant was removed and combined with benzene (0.01 mL) and D<sub>2</sub>O (0.45 mL) in 4.0-mL vials. These mixtures were then transferred to individual NMR tubes and quantitative <sup>1</sup>H NMR was used to determine the yield of formate by integration of the formate peak in reference to benzene.

**Digestion of UiO-66 for ICP-OES analysis.** Solid MOF material (5.00 mg) was weight out into a 1.5 mL Teflon vial. DMSO (300  $\mu$ L) and 1 drop of 15 wt.% aqueous hydrofluoric acid solution were added in sequence. The mixture was sonicated for 1 minute and left to digest for 1 hour. The digested samples then heated to approximately 150  $^{\circ}$ C overnight in a sand bath open to the air to remove solvent. The resulting solid was dissolved and transferred to a 20 mL glass scintillation vial using a mixture (10% v/v) of hydrochloric acid in deionized water (300  $\mu$ L). Each sample was diluted with additional deionized water (3.7 mL) and analyzed by ICP-OES.

**ICP-OES Standard preparation.** Four standards were prepared by dilution from commercially available zirconium ( $999 \pm 5$  ppm), ruthenium ( $999 \pm 5$  ppm), and phosphorus ( $100.04 \pm 0.55$  ppm) standards using serial dilution in grade A volumetric

glassware to cover the expected concentration ranges. The standards were then employed in a calibration curve to determine the loading of catalyst in a tested solid. These standards consisted of Zr/Ru/P concentrations in ppm at the proportions: 250/5/5, 150/2/2, 25/0.5/0.5, 2.5/0.05/0.05

**Procedure for carbon dioxide hydrogenation recycling studies using 2-1@UiO-66.** Carbon dioxide hydrogenation was carried out using the “general procedure for carbon dioxide hydrogenation” at 5x scale in a 20-mL ampule. The solid was washed twice with methanol (20 mL) and dried overnight in a vacuum chamber between cycles.

**Procedure for carbon dioxide hydrogenation in the presence of thiols.** Carbon dioxide hydrogenation was carried out using the “general procedure for carbon dioxide hydrogenation” with the addition of different thiols. 1-dodecanethiol (0.15 mL, 0.63 mmol), 1-hexanethiol (0.09 mL, 0.63 mmol), 1-octanethiol (0.11 mL, 0.627 mmol), benzenethiol (0.064 mL, 0.63 mmol), 2-ethylhexanethiol (0.11 mL, 0.63 mmol), or tert-butyl thiol (0.07 mL, 0.63 mmol) was added to the reaction mixture in a fume hood. These ampules were added to a 450 mL stainless steel Parr reactor. Upon conclusion of the reaction, the heating mantle was removed and the pressure was released slowly from the vessel into a fume hood. The vessel was brought to a fume hood and opened and the ampules were removed. The ampules and reactor were cleaned after the reaction with a solution of bleach (20%) in water.

**Procedure for carbon dioxide hydrogenation to test catalyst deactivation.** Carbon dioxide hydrogenation was carried out using the “general procedure for carbon dioxide hydrogenation”. After the first cycle, an aliquot of reaction mixture (0.25 mL) was removed from the ampule set aside in a small vial. DBU (0.493 mL, 3.30 mmol) was added



to each ampule, and the ampules were again subjected to reaction conditions. Catalyst deactivation was determined as the difference between formate production in the first and second reactions.

**Procedure for BET measurement:** The samples “UiO-66” and “UiO-66 after linker exchange” (with no catalyst being added) were incubated in methanol for 7 days with solvent replaced every twelve hours. The solids were isolated by centrifugation and dried, then activated by first ramping the temperature to 200 °C at a rate of 5 °C/min, remaining constant for 10 minutes, then ramping to 270 °C and remaining constant for twelve hours. The nitrogen gas adsorption-desorption was carried out on quodrasorb evo provided by ShanghaiTech University.

**Procedure for UiO-66 dialysis experiment:** A dialysis tube was soaked in water first for 5 minutes until it was fully solvated. One side of the tube was clamped tightly and UiO-66 (200 mg) and deionized water (3 mL) were added to the tube, and then the other side was clamped. The dialysis tube was placed in a 1-L beaker and suspended in water (1 L) with stirring at 55 °C for 18 days. The external water was refreshed daily, and water removed was collected and concentrated by heating for LC-MS analysis.

**Procedure for STA analysis.** Prior to STA analysis, all samples were dried under vacuum and heat at 150 °C to ensure the complete dryness before the TGA measurement. Analysis was carried out in an Al<sub>2</sub>O<sub>3</sub> crucible on NETZSCH STA 449F1. Samples were thermally activated in air by STA with first ramping to 270 °C with 10 °C/min and stay isotherm at 270 °C for 12 hours and cool back down to room temperature. After the thermal acitivation to get rid of any residue solvent and organic impurities, the samples were ran

from room temperature to 900 °C at 5 °C/min in air. Unless otherwise stated, all the measurements were carried out using air as carrier gas and nitrogen as the protection gas.

**Calculation of missing linkers from TGA data<sup>26</sup>.** The number of missing linkers (x) per Zr<sub>6</sub>-oxo cluster of the defective UiO-66 was calculated by Zhehui Li using the following formula :

$$X = 6 - \frac{W_{270} - W_{900}}{(W_{theo.270} - W_{900})/6} = 6 - \frac{W_{270} - W_{900}}{(220.2\% - 100\%)/6} = 6 - \frac{W_{270} - 100\%}{20.03\%}$$

Where the final weight W<sub>900</sub> (6 ZrO<sub>2</sub>) was normalized to 100%. W<sub>theo.270</sub> is the ideal weight of a defect-free UiO-66, Zr<sub>6</sub>O<sub>4</sub>(OH)<sub>4</sub>(BDC)<sub>6</sub>, after the normalization which equals to 220.2%. W<sub>270</sub> is the actual normalized weight at 270 °C detected from TGA trace of the sample.

**Encapsulation of Brilliant Blue G in UiO-66, Dye-at-UiO-66.** Following a procedure similar to previously published procedure,<sup>20</sup> methanol (15 mL), UiO-66 (15 mg) and Brilliant blue G (15 mg) were added to a 20-mL scintillation vial. The vial was then sealed and heated at 55 °C for five days. Upon cooling, the solid sample was isolated by centrifugation, and then triturated by washing the solid with a 14 wt.% polyvinylpyrrolidone mixture in methanol followed by centrifugation. Trituration was carried out twice more and the samples were allowed to dry in air at room temperature overnight. The MOF material was digested using the above digestion procedure, and the absorbance was collected at 624 nm and 25 °C in DMSO using a 0.7-mL VWR quartz cuvette. The concentration of the dye was determined by comparison to a standard curve.

**Physical mixture control sample, dye-on-UiO-66.** UiO-66 was weighed out in a 20-mL scintillation vial. Methanol (15 mL) was added to this vial, which was subjected to sonication for approximately 10 minutes to disperse the solid. Brilliant Blue G (15 mg)

was added to this vial, which was inverted twice, then immediately subjected to centrifugation. The supernatant was then decanted and the solids were obtained without further washing.

**Detection of formate by mass spectrometry.** A carbon dioxide hydrogenation product mixture (3 mL) was placed in a 50-mL round-bottom flask and hooked up to an air-free manifold. This flask was put under vacuum and heated at 120 °C for three hours. The mixture was allowed to cool to room temperature and transferred to a 20-mL scintillation vial. Methanol (5 mL) was then added to this mixture, and the product formate was detected using Direct Analysis in Real Time in the negative ion mode on a JEOL AccuTOF 4G LC-Plus. ( $\text{CH}_2\text{O}_2$  expected: 45.017 g/mol; found: 45.000 g/mol)

**Procedure for testing pre-treated homogeneous catalyst mixture for catalytic activity** A solution of **2-1** (7.0 mg, 0.013 mmol) in DMF was prepared and added to a 5.0-mL ampule, then subjected to pre-treatment as described above. The supernatant was concentrated by rotary evaporation and evaluated by  $^{31}\text{P}$ -NMR to observe the speciation of the homogeneous catalyst. Carbon dioxide hydrogenation was carried out using the “general procedure for carbon dioxide hydrogenation”. This experiment was run simultaneously with a sample of **2-1** that had not been pre-treated to properly observe the effect of pre-treatment on the homogeneous catalyst. The reaction containing the homogeneous complexes that had undergone the pretreatment procedure demonstrated evidence for catalyst decomposition as is evidenced by multiple peaks in the  $^{31}\text{P}$  NMR spectrum including free ligand. Consistent with this hypothesis was that no activity for  $\text{CO}_2$  hydrogenation was observed when the pretreated solution was exposed to the reaction conditions.

**Procedure for testing pre-treated supernatant and UiO-66 for catalytic activity.** UiO-66 (10 mg) and **2-1** (7.4 mg, 0.013 mmol) were mixed together in a 5.0-mL glass ampule and subjected to pre-treatment as described above. The solid and supernatant were then separated by centrifugation. The solid was washed once with methanol and dried overnight in a vacuum chamber. The supernatant was concentrated by rotary evaporation and evaluated by  $^{31}\text{P}$ -NMR to observe the speciation of the homogeneous catalyst. Carbon dioxide hydrogenation was carried out using the “general procedure for carbon dioxide hydrogenation” for each of these species. These experiments were run simultaneously with a sample of **2-1@UiO-66** to ensure the activity of the hybrid species in the absence of activity for the pre-treated UiO-66 and supernatant. The reaction containing the homogeneous complexes and UiO-66 that had undergone the pretreatment procedure demonstrated evidence for catalyst decomposition as is evidenced by multiple peaks in the  $^{31}\text{P}$  NMR spectrum including free ligand. Consistent with this hypothesis was that no activity for  $\text{CO}_2$  hydrogenation was observed when the pretreated solution was exposed to the reaction conditions.

## References:

1. K. Sumida, D. L. Rogow, J. A. Mason, T. M. McDonald, E. D. Bloch, Z. R. Herm, T.-H. Bae, J. R. Long. Carbon Dioxide Capture in Metal-Organic Frameworks. *Chem. Rev.* **112**, 724-781. (2012).
2. J.-R. Li, R. J. Kuppler, H.-C. Zhou. Selective gas adsorption and separation in metal-organic frameworks. *Chem. Soc. Rev.* **38**, 1477-1504. (2009).
3. P. Horcajada, R. Gref, T. Baati, P. K. Allan, G. Maurin, P. Couvreur, G. Férey, R. E. Morris, C. Serre. Metal-Organic Frameworks in Biomedicine. *Chem. Rev.* **112**, 1232-1268. (2012).
4. L. E. Kreno, K. Leong, O. K. Farha, M. Allendorf, R. P. Van Duyne, J. T. Hupp. Metal-Organic Framework Materials as Chemical Sensors. *Chem. Rev.* **112**, 1105-1125. (2012).
5. J. Lee, O. K. Farha, J. Roberts, K. A. Scheidt, S. T. Nguyen, J. T. Hupp. Metal-organic framework materials as catalysts. *Chem. Soc. Rev.* **38**, 1450-1459. (2009).
6. P. Hu, J. V. Morabito, C.-K. Tsung. Core-Shell Catalysts of Metal Nanoparticle Core and Metal-Organic Framework Shell. *ACS Catal.* **4**, 4409-4419. (2014).
7. J. Liang, Z. Liang, R. Zou, Y. Zhao. Heterogeneous Catalysis in Zeolites, Mesoporous Silica, and Metal-Organic Frameworks. *Adv. Mater.* **29**, 1701139 (2017).
8. K. Manna, P. Ji, Z. Lin, F. X. Greene, A. Urban, N. C. Thacker, W. Lin. Chemoselective single-site Earth-abundant metal catalysts at metal-organic framework nodes. *Nat. Commun.* **7**, 12610. (2016).
9. H. Furukawa, K. E. Cordova, M. O’Keeffe, O. M. Yaghi. The Chemistry and Applications of Metal-Organic Frameworks. *Science.* **341**, 1230444. (2013).
10. F.-S. Liao, W. S. Lo, Y.-S. Hsu, C.-C. Wu, S.-C. Wang, F.-K. Shieh, J. V. Morabito, L.-Y. Chou, K. C. W. Wu, C.-K. Tsung. Shielding against Unfolding by Embedding Enzymes in Metal-Organic Frameworks via a de Novo Approach. *J. Am. Chem. Soc.* **139**, 6530-6533. (2017).
11. T. Gadzikwa, O. K. Farha, K. L. Mulfort, K. J. T. Hupp, S. T. Nguyen. A Zn-based, pillared paddlewheel MOF containing free carboxylic acids via covalent post-synthesis elaboration. *Chem. Commun.* 3720-3722. (2009).
12. B. Li, Y. Zhang, D. Ma, T. Ma, Z. Shi, S. Ma. Metal-Cation-Directed de Novo Assembly of a Functionalized Guest Molecule in the Nanospace of a Metal-Organic Framework. *J. Am. Chem. Soc.* **136**, 1202-1205. (2014).
13. S. Jung, Y. Kim, S.-J. Kim, T.-H. Kwon, S. Huh, S. Park. Bio-functionalization of metal-organic frameworks by covalent protein conjugation. *Chem. Commun.* **47**, 2904-2906. (2011).
14. S. A. Burgess, A. Kassie, S. A. Baranowski, K. J. Fritzsche, K. Schmidt-Rohr, C. M. Brown, C. R. Wade. Improved Catalytic Activity and Stability of a Palladium Pincer Complex by Incorporation into a Metal-Organic Framework. *J. Am. Chem. Soc.* **138**, 1780-1783. (2016).
15. S. M. Cohen, Z. Zhang, J. A. Boissonnault. Toward “metalloMOFzymes”: Metal-Organic Frameworks with Single-Site Metal Catalysts for Small Molecule Transformations. *Inorg. Chem.* **55**, 7281. (2016).

16. C.-D. Wu, W. Lin. Heterogeneous asymmetric catalysis with homochiral metal-organic frameworks: network-structure-dependent catalytic activity. *Angew. Chem. Int. Ed.* **46**, 1075. (2007).
17. H. D. Park, M. Dincă, Y. Román-Leshkov. Heterogeneous Epoxide Carbonylation by Cooperative Ion-Pair Catalysis in  $\text{Co}(\text{CO})_4^-$  - Incorporated Cr-MIL-101. *ACS Cent. Sci.* **3**, 444-448. (2017).
18. A. Corma, H. García, F. X. Llabrés i Xamena. Engineering Metal-Organic Frameworks for Heterogeneous Catalysis. *Chem. Rev.* **110**, 4606-4655. (2010).
19. C. Caratelli, J. Hajek, F. G. Cirujano, M. Waroquier, F. X. Llabrés i Xamena, V. Van Speybroeck. Nature of active sites on UiO-66 and beneficial influence of water in the catalysis of Fischer esterification. *J. Catal.* **352**, 401-414. (2017).
20. J. V. Morabito, L.-Y. Chou, Z. Li, C. M. Manna, C. A. Petroff, R. J. Kyada, J. M. Palomba, J. A. Byers, C.-K. Tsung. Molecular encapsulation beyond the aperture size limit through dissociative linker exchange in metal-organic framework crystals. *J. Am. Chem. Soc.* **136**, 12540-12543. (2014).
21. J. V. Morabito, Z. Li, J. A. Byers, C.-K. Tsung. Boston College, Chestnut Hill, MA, Unpublished work, 2017.
22. G. A. Filonenko, M. P. Conley, C. Copéret, M. Lutz, E. J. M. Hensen, E. A. Pidko. The impact of Metal-Ligand Cooperation in Hydrogenation of Carbon Dioxide Catalyzed by Ruthenium PNP Pincer. *ACS Catal.* **3**, 2522-2526. (2013).
23. G. A. Filonenko, E. J. M. Hensen, E. A. Pidko. Mechanism of  $\text{CO}_2$  hydrogenation to formates by homogeneous Ru-PNP pincer catalyst: from a theoretical description to performance optimization. *Catal. Sci. Technol.* **4**, 3474-3485. (2014).
24. H. Ge, Y. Jing, X. Yang. Computational Design of Cobalt Catalysts for Hydrogenation of Carbon Dioxide and Dehydrogenation of Formic Acid. *Inorg. Chem.* **55**, 12179-12184. (2016).
25. J. H. Cavka, S. Jakobsen, U. Olsbye, N. Guillou, C. Lamberti, S. Bordiga, K. P. Lillerud. A New Zirconium Inorganic Building Brick Forming Metal Organic Frameworks with Exceptional Stability. *J. Am. Chem. Soc.* **130**, 13850-13851. (2008).
26. G. C. Shearer, S. Chavan, J. Ethiraj, J. G. Vitillo, S. Svelle, U. Olsbye, C. Lamberti, S. Bordiga, K. P. Lillerud. Tuned to Perfection: Ironing Out the Defects in Metal-Organic Framework UiO-66. *Chem. Mater.* **26**, 4068-4071. (2014).
27. L. Valenzano, B. Civalieri, S. Chavan, S. Bordiga, M. H. Nilsen, S. Jakobsen, K. P. Lillerud, C. Lamberti. Disclosing the Complex Structure of UiO-66 Metal Organic Framework: A Synergic Combination of Experiment and Theory. *Chem. Mater.* **23**, 1700-1718. (2011).
28. J. Marreiros, C. Caratelli, J. Hajek, A. Krajnc, G. Fleury, B. Bueken, D. E. De Vos, G. Mali, M. B. J. Roelofs, V. Van Speybroeck, R. Ameloot. Active Role of Methanol in Post-Synthetic Linker Exchange in the Metal-Organic Framework UiO-66. *Chem. Mater.* **31**, 1359-1369. (2019).
29. D. Hermann, M. Gandelman, H. Rozenberg, L. J. W. Shimon, D. Milstein. Synthesis, structure, and reactivity of new rhodium and iridium complexes, bearing a highly electron-donating PNP system. Iridium-mediated vinylic C-H bond activation. *Organometallics*. **21**, 812-818. (2002).
30. G. A. Filonenko, D. Smykowski, B. M. Szyja, G. Li, J. Szczygieł, E. J. M. Hensen, E. A. Pidko. Catalytic Hydrogenation of  $\text{CO}_2$  to Formates by a Lutidine-Derived Ru-CNC

- Pincer Complex: Theoretical Insight into the Unrealized Potential. *ACS Catal.* **5**, 1145-1154. (2015).
31. G. A. Filonenko, R. Van Putten, E. N. Schulpen, E. J. M. Hensen, and E. A. Pidko. Highly efficient reversible hydrogenation of carbon dioxide to formates using a ruthenium PNP-pincer catalyst. *ChemCatChem.* **6**. 1526-1530. (2014).
  32. Z. Li. Design of a Host-guest Hybrid Catalytic System Through Aperture-opening Encapsulation Using Metal-Organic Framework. PhD Thesis, Boston College, Chestnut Hill, MA.
  33. G. Dinelli, L. Civitano, M. Rea. Industrial experiments on pulse corona simultaneous removal of NO<sub>x</sub> and SO<sub>2</sub> from flue gas. *IEEE Transactions on Industry Applications.* **26**, 535-541. (1990).
  34. B. J. Burger, J. E. Bercaw. Vacuum Line Techniques for Handling Air-Sensitive Organometallic Compounds. In *Experimental Organometallic Chemistry*; A. L. Wayda, and M. Y. Darensbourg. Eds.; ACS Symposium Series 357; American Chemical Society: Washington D.C. 1987, 79-115.

### 3.0 CHAPTER 3

## A Bioinspired Multicomponent Catalytic System for Converting Carbon Dioxide into Methanol

As discussed in Chapter 1, biological organisms have evolved complex networks of chemical reactions that are necessary for their survival. For example, the Calvin cycle employs a series of redox and condensation reactions to convert carbon dioxide into glyceraldehyde-3-phosphate (G3P), a precursor to the sugars that organisms use as fuel (Figure 3-1A).<sup>1</sup> The Calvin cycle involves multiple catalytic transformations precisely controlled by supramolecular assemblies that traffic substrates between isolated active sites. This strategy allows biological systems to overcome inherent limitations to selectivity, reactivity, and compatibility. Many bioinspired synthetic catalytic systems have been developed in pursuit of similar activity and selectivity, some of which rival their natural analogs.<sup>2-7</sup> For example, Dubois and co-workers developed a nickel electrocatalyst inspired by [FeFe] hydrogenase that exceeds the activity of the enzyme that it is based on.<sup>5</sup> However, most of these systems primarily mimic the coordinative environment in enzyme active sites.<sup>8</sup> Synthetic systems that mimic the arrangement of multiple active sites by supramolecular protein assemblies could capitalize on pathways that could otherwise benefit from multistep processes.<sup>9-11</sup>



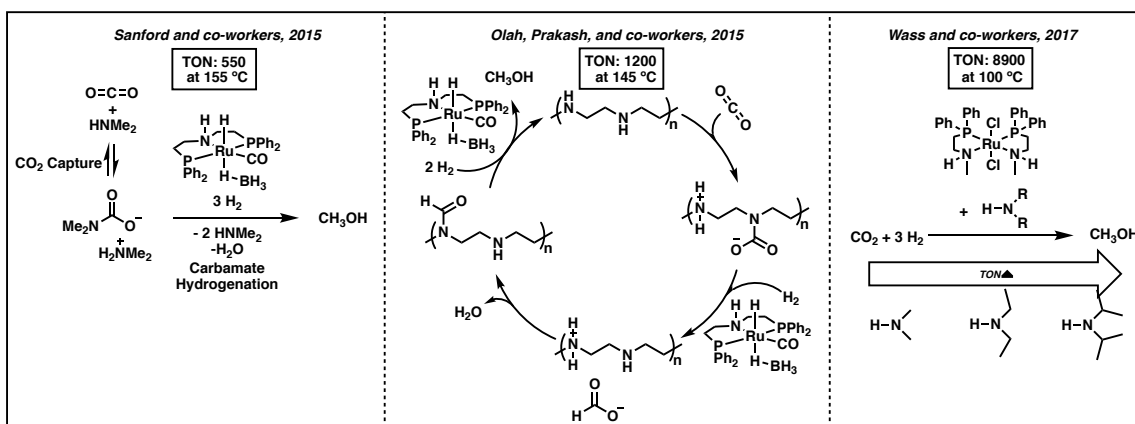


### 3.1 DEVELOPING AND OPTIMIZING A MULTICOMPONENT SYSTEM FOR CO<sub>2</sub> HYDROGENATION TO METHANOL

Coupled with catalytic water splitting,<sup>16</sup> the hydrogenation of carbon dioxide to methanol is a promising method to selectively obtain easily transportable, energy-dense fuel from readily available, renewable resources.<sup>17-20</sup> While heterogeneous catalysts are industrially employed for this transformation,<sup>17</sup> reactions are carried out at high temperatures and pressures. In addition, the ill-defined active sites inherent to most heterogeneous catalysts adversely affect reaction selectivity.<sup>21</sup> Homogeneous molecular catalysts have also been developed for carbon dioxide hydrogenation.<sup>22-26</sup> These catalysts feature well-defined active sites amenable to logical optimization and beneficial for reaction selectivity. However, few examples of homogeneous catalysts are known for the hydrogenation of carbon dioxide to methanol, and none of the reported systems are recyclable.<sup>13-15,27-31</sup> All catalysts for this transformation face a formidable challenge in traversing four different oxidation states of carbon, each thermodynamically uphill until the final reduction of formaldehyde to methanol.<sup>33</sup>

The most efficient molecular catalysts for carbon dioxide hydrogenation reported to date involve combining a ruthenium-based catalyst with superstoichiometric amounts of amine additives (Scheme 3-1).<sup>27-29</sup> This combination aids with methanol formation by first converting formic acid to a formamide or carbamate intermediate. While this approach increased catalyst turnover compared to previous homogeneous molecular catalysts, the stability of the intermediate often led to mixtures of methanol and formamide.<sup>28</sup> Subsequent work improved product separation by using a polyamine,<sup>29</sup> or by using sterically encumbered amine additives that force the reaction to proceed through a

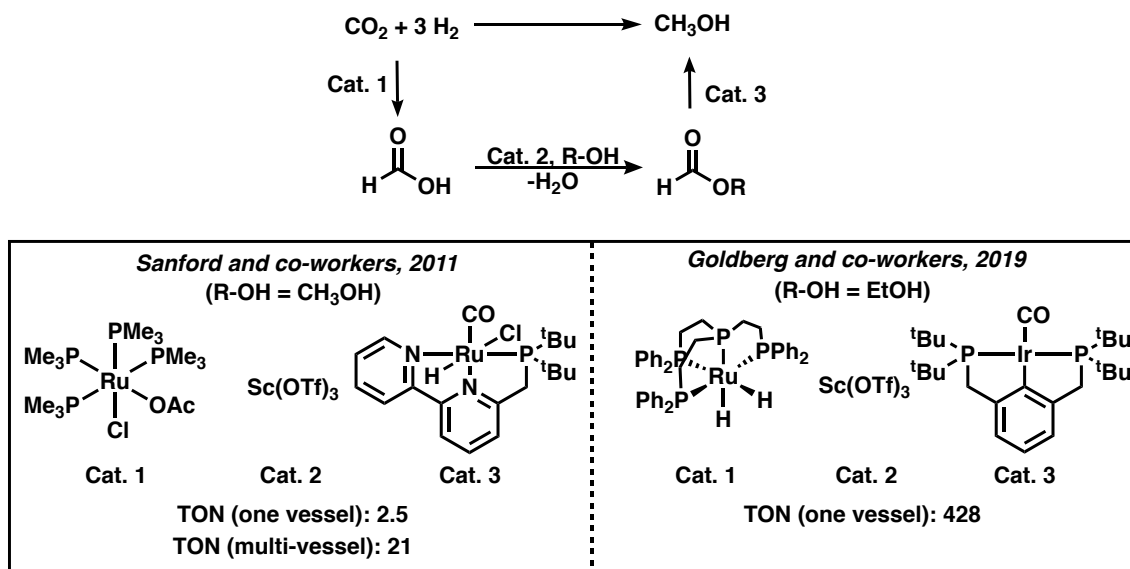
thermodynamically less stable and therefore more reactive formamide intermediate, which resulted in a turnover number (TON) that exceeded that for any other transition metal complex at the time it was reported.<sup>13</sup> Despite these developments, all iterations of this strategy require superstoichiometric amine additives. There is one example of a molecular homogeneous catalyst that does not require any additives for catalytic turnover,<sup>30</sup> but this cationic ruthenium-based catalyst is less active and requires higher temperature than the systems that utilize amines as additives.



**Scheme 3-1.** Strategies employed by Sanford, Olah and Prakash, and Wass in the hydrogenation of carbon dioxide to methanol with amine additives

An alternative that has been less extensively explored is the use of multiple catalysts to affect the conversion of carbon dioxide to methanol via a cascade of chemical reactions (Scheme 3-2). Sanford and coworkers demonstrated that such an approach is feasible.<sup>31</sup> In this approach, a ruthenium-based hydrogenation catalyst was first used to convert carbon dioxide to formic acid. Next, a Lewis acid catalyst incorporated the methanol solvent to convert formic acid into methyl formate. After the first two steps, methyl formate was distilled to a second reactor containing another ruthenium-based catalyst that reduced methyl formate to methanol. This reaction engineering by catalyst separation was

necessary to address catalyst incompatibility that led to low catalyst activity. Goldberg and coworkers have built upon this concept using more stable homogeneous complexes by employing catalysts with improved stability, resulting in a twenty-fold further increase in activity.<sup>32</sup>



**Scheme 3-2.** Previous examples of cascade hydrogenation of carbon dioxide to methanol through formic acid and ester intermediates reported by Sanford<sup>31</sup> and Goldberg<sup>32</sup>

The activity of these three-component systems was admittedly lower than when amines were used as additives. However, carbon dioxide hydrogenation reactions that proceed through a formate ester rather than a formamide intermediate are potentially beneficial because esters are less thermodynamically stable than amides.<sup>33</sup> Additionally, autocatalytic behavior is possible if the reactions could be carried out in a single reaction vessel because the methanol product can be used as a reactant to drive the esterification. High turnover of carbon dioxide to methanol is hypothetically achievable if reactor separation could be circumvented so that the three steps of the cascade occur within a single reaction vessel. Inspired by the efficacy of protein superstructures used in biological systems, a catalyst system for the cascade hydrogenation of carbon dioxide to methanol

was pursued that involved isolating multiple active sites in a nanostructured assembly (Figure 3-1B).

### 3.1.1 Separating Active Components to Achieve Cascade Catalysis

The utility of MOFs as attractive platforms for host-guest constructs and the benefits that they can impart on a catalytic guest have been described at length in Chapters 1 and 2.<sup>8,34-39</sup> As a further demonstration of the promise of using MOFs in catalysis, the effective separation of multiple catalysts was possible through the aperture-opening encapsulation approach described in Chapter 2.<sup>36,40-42</sup> The host-guest construct described in the previous chapter (**3-1@UiO-66**) was an excellent catalyst for the hydrogenation of carbon dioxide to formate. However, that transformation did not require the simultaneous operation of multiple catalysts hypothesized to be necessary for the conversion of carbon dioxide to methanol.

To extend this method to the three-step cascade hydrogenation of carbon dioxide to methanol, catalysts for the other two steps in the cascade transformation were evaluated. First, the Lewis acidic zirconium oxide nodes of UiO-66<sup>43</sup> were tested as a catalyst to convert formic acid to a formate ester in the presence of an alcohol additive (Table 3-1).<sup>44</sup> The MOF was found to be an effective catalyst for this esterification reaction in the presence of methanol (entries 1 and 2), ethanol (entries 3 and 4), 2,2,2-trifluoroethanol (TFE) (entries 5 and 6), and 2-nitroethanol (entries 7 and 8) in both 1,4-dioxane and N,N'-dimethylformamide (DMF). For reactions conducted in dioxane, between 55% and 60% of the formic acid was converted to formate ester after four hours, depending on the alcohol additive employed. Conversion in DMF was even greater, ranging from 80% with

trifluoroethanol to 88% with ethanol. The superior performance of the MOF for esterification in DMF was promising, as **3-1@UiO-66** was highly effective in the reduction of carbon dioxide to formate in the same solvent. Access to optimal reaction rates for both of the first two steps in the cascade transformation allowed for solvent selection without detrimental effects on the rate of either of the first two reactions.

$$\text{H}-\overset{\text{O}}{\parallel}{\text{C}}-\text{OH} \xrightarrow[\text{Solvent, 80 } ^\circ\text{C, 4 h}]{\text{UiO-66 (10 mg)} \atop \text{R-OH (10 mmol)}} \text{H}-\overset{\text{O}}{\parallel}{\text{C}}-\text{OR}$$

Entry	R-OH	Solvent	Conversion (%)
1	MeOH	Dioxane	58
2	MeOH	DMF	83
3	EtOH	Dioxane	63
4	EtOH	DMF	88
5	CF <sub>3</sub> CH <sub>2</sub> OH (TFE)	Dioxane	58
6	CF <sub>3</sub> CH <sub>2</sub> OH (TFE)	DMF	80
7	NO <sub>2</sub> CH <sub>2</sub> CH <sub>2</sub> OH	Dioxane	54
8	NO <sub>2</sub> CH <sub>2</sub> CH <sub>2</sub> OH	DMF	86

**Table 3-1.** Esterification of formic acid to formate ester using UiO-66 as Lewis acid catalyst

The third step in the cascade transformation was reduction of the formate ester intermediate to methanol and the alcohol additive introduced in the esterification. Two ruthenium pincer catalysts were selected as possible candidates for this transformation: (<sup>t</sup>BuPNN)RuH(CO)Cl (**3-2**), employed previously by Sanford and co-workers in ester reduction, and Ru-MACHO<sup>29</sup> (**3-3**), employed previously in multiple examples of amide reduction. Preliminary tests for the reduction of carbon dioxide using **3-3** in tandem with **3-1@UiO-66** produced methanol in the presence of hydrogen and carbon dioxide. This methanol, however, was formed through the reduction of DMF rather than the formate ester, evident from the formation of dimethyl amine.

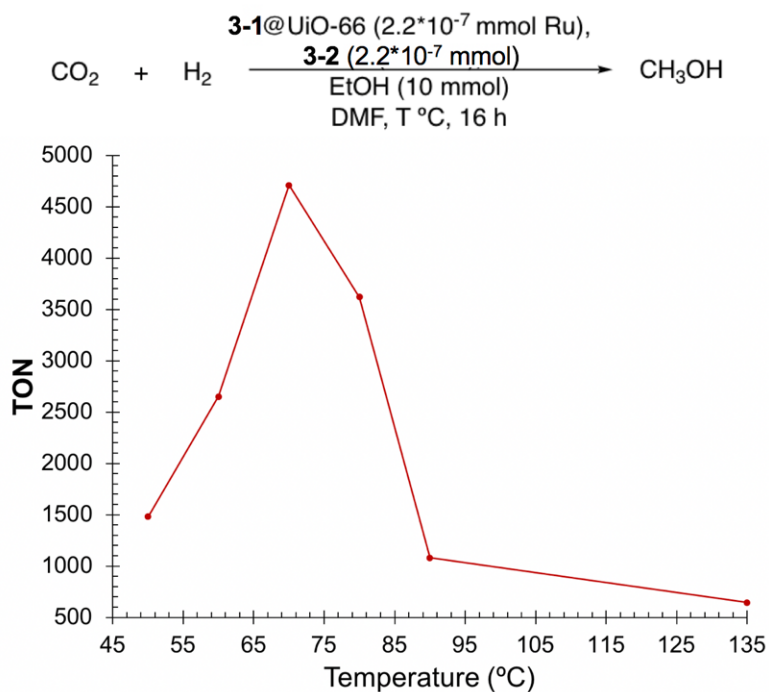
Complex **3-2** was then used for ester reduction (Table 3-2), with initial tests conducted in conditions similar to those reported by Sanford and co-workers.<sup>31</sup> These reactions employed a hydrogen pressure of 30 bar and a carbon dioxide pressure of 10 bar. However, optimal activity for the system employed in this chapter was found at 37 bar hydrogen and 3 bar carbon dioxide (entries 1-3). A ratio of **3-1** to **3-2** of 1:1 was found to give optimal TON based on the highest catalyst loading between the two transition metal complexes (entries 4-7). The most surprising and significant jump in activity occurred with manipulation of temperature: activity increased as temperature decreased, with TON only decreasing after the reaction temperature had been reduced past 70 °C from 135 °C (Entries 8-12 and Figure 3-2)).

$$\text{CO}_2 + \text{H}_2 \xrightarrow[\text{DMF, T } ^\circ\text{C, 16 h}]{\begin{array}{c} \text{3-1@UiO-66 (2.2*10}^{-7}\text{ mmol Ru),} \\ \text{3-2 (n mmol),} \\ \text{EtOH (10 mmol)} \end{array}} \text{CH}_3\text{OH}$$

Entry	mmol 2	P <sub>CO2</sub> (bar)	P <sub>H2</sub> (bar)	T (°C)	TON <sup>a</sup>
1	0.0126	10	30	135	21
2	0.0126	3	37	135	244
3	0.0126	3	45	135	13
4	3.8*10 <sup>-6</sup>	3	37	135	209
5	2.3*10 <sup>-6</sup>	3	37	135	250
6	9.7*10 <sup>-7</sup>	3	37	135	536
7	2.2*10 <sup>-7</sup>	3	37	135	644
8	2.2*10 <sup>-7</sup>	3	37	90	1080
9	2.2*10 <sup>-7</sup>	3	37	80	3620
10	2.2*10 <sup>-7</sup>	3	37	70	4710
11	2.2*10 <sup>-7</sup>	3	37	60	2650
12	2.2*10 <sup>-7</sup>	3	37	50	1480

**Table 3-2.** Table detailing optimization of carbon dioxide conversion to methanol using the described multicomponent system. <sup>a</sup>TON calculated based on highest loading between **3-1** and **3-2**

Increased activity at lower temperature is atypical for catalytic reactions. However, the observed maximum activity at 70 °C could be reasonably attributed to several causes. The conversion of four gas molecules – one of carbon dioxide and three of hydrogen – to two liquid molecules in the form of methanol and water is entropically disfavored, and this entropic contribution factors into the overall energy of the reaction to a greater degree at higher temperatures. As a result, the overall transformation is more exergonic at lower temperatures. However, reaction temperatures above 70 °C may be necessary to overcome the energetic barriers for the reaction, thus an optimal temperature at which entropic contributions are minimized but energy barriers can be overcome might lead to maximized activity. Alternatively, the solubility of gases such as carbon dioxide and hydrogen in solution typically increases with decreasing temperature. As such, a balance between energy input and reagent solubility may be the reason for the observed trend.

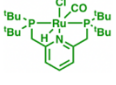

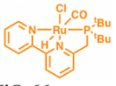
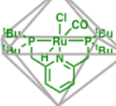


**Figure 3-2.** Graphical representation of the dependence of TON for the hydrogenation of carbon dioxide to methanol on reaction temperature



Having determined optimal reaction conditions for the production of methanol, it was necessary to confirm that this methanol was the only product formed and that it was formed as a result of the hypothesized multistep transformation (Table 3-3). The combination of catalysts and ethanol (10 mmol) described above produced methanol as the only detectable product with a TON of  $4,710 \pm 150$  (entry 1). No other liquid products were observed in this reaction by  $^1\text{H}$  NMR spectroscopy. Additionally, analysis of the reactor headspace by GC revealed trace amounts of carbon monoxide ( $1.9 \pm 1.1$  ppm), which was not statistically distinct from the background production of CO in the absence of catalyst ( $1.2 \pm 0.6$  ppm) with no other gaseous products formed. This was possibly a consequence of the reverse water-gas shift reaction on the stainless-steel reactor surface, which has a similar thermodynamic driving force as the hydrogenation of carbon dioxide to methanol.

The necessity for each component in this cascade reaction was then evaluated by carrying out reactions under otherwise identical conditions using each component individually (entries 2-5). In these control experiments, **3-1**, UiO-66, and **3-2** were found to be inactive when used independently for the hydrogenation of carbon dioxide. Moreover, all combinations of **3-1**, **3-2**, and UiO-66 resulted in similar inactivity, including a combination of all three components in solution (entries 6-9). This last control experiment highlighted the benefits of the site isolation achieved by encapsulating at least one catalyst precursor in the MOF: prevention of bimolecular decomposition pathways between catalysts **3-1** and **3-2** that would hinder the productivity of the homogeneous system.

		$\text{CO}_2 \text{ (3 bar)} + \text{H}_2 \text{ (37 Bar)} \xrightarrow[\text{DMF, EtOH (10 mmol), 70 }^\circ\text{C, 16h}]{\text{(Catalysts)}} \text{CH}_3\text{OH}$								
Entry	Catalyst	1	2	3	4	5	6	7	8	9
3-1		-	✓	-	-	-	✓	✓	-	✓
UiO-66		-	-	✓	-	-	✓	-	✓	✓
3-2		✓	-	-	✓	-	-	✓	✓	✓
3-1@UiO-66		✓	-	-	-	✓	-	-	-	-
TON		4710	0	0	0	0	0	0	0	0

**Table 3-3.** Activity of carbon dioxide hydrogenation reactions under using various catalytic components: **3-1** ( $2.23 \times 10^{-7}$  mmol) or **3-1@UiO-66** (10 mg,  $[\text{Ru}] = 2.23 \times 10^{-7}$  mmol), UiO-66 (10 mg), and **3-2** ( $2.23 \times 10^{-7}$  mmol). Check marks indicate which species are present in each reaction. Reaction mixtures analyzed by  $^1\text{H}$  NMR spectroscopy, Error in entry 1 ( $\text{TON} \pm 150$ ) is the average error of 3 runs (Figure 3-3).

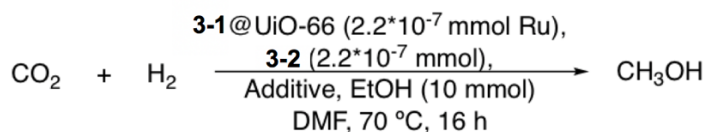
Next, different additives were evaluated (Table 3-4). The first of these manipulations was the addition of base, which facilitates carbon dioxide conversion to formate. The addition of base shut down conversion to methanol, instead resulting in the observation of formate as the only product (entries 1 and 2). Interestingly, the observed TON for formate in the presence of DBU was lower than that observed in Chapter 2. An approximately 2.5 mmol decrease in the ethanol present in the reaction by  $^1\text{H}$ -NMR suggested that this was as a result of the base deprotonating the alcohol additive, decreasing the effective base loading. A similar decrease in dissolved ethanol was observed with the addition of triethylamine, suggesting similar behavior. The production of formate supported the role of **3-1** as a catalyst for carbon dioxide hydrogenation but prohibited the

use of base to drive forward the first reaction in the cycle. No turnover was observed when formic acid was added instead of the alcohol additive (entry 3 and Figure 3-4), underlining the importance of the ester intermediate in the operative mechanistic pathway and confirming that methanol was not being produced from the direct reduction of formic acid.

Turnover was identical to standard conditions when formic acid was added as a feedstock in place of carbon dioxide (entry 4). While the introduction of an intermediate directly to the reaction might be expected increase TON, the observation of identical activity could be a result of more rapid decomposition of **3-2**. Under typical reaction conditions, it is believed that only a trace amount of formic acid is produced before it is converted to ester. Shift in bulk solution pH would therefore be negligible. The addition of 10 mmol of formic acid leads to much harsher, more acidic conditions. The observed identical TON could then be a result of serendipity rather than identical behavior to that under the original reaction conditions.

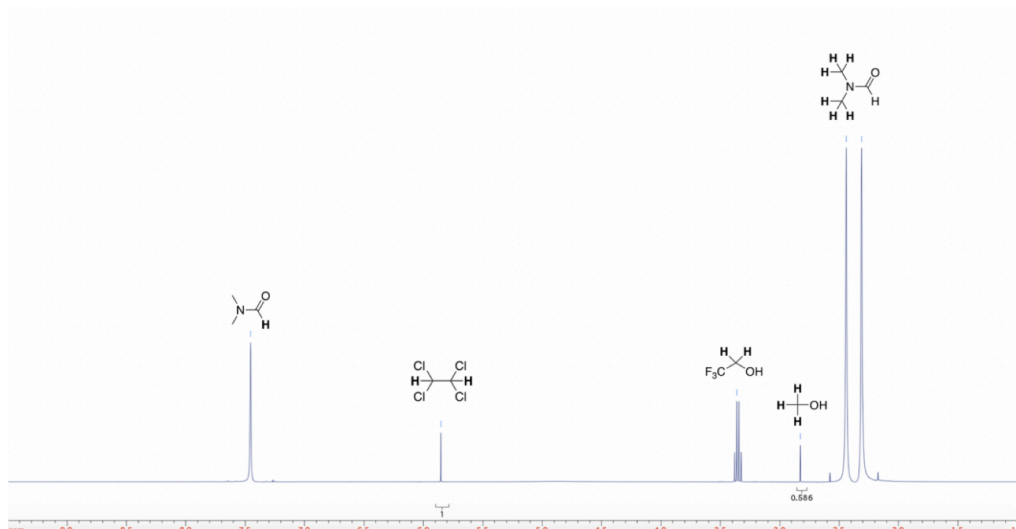
Finally, the defect content and identity of the metal ion in the host node were altered. This was accomplished by encapsulating **3-1** in UiO-66 derivatives synthesized under altered conditions. The synthesis of high-defect “30-Benz” and “40-Benz” UiO-66 was conducted as reported in the literature<sup>45</sup> in the presence of 30 and 40 equivalents of benzoic acid as a modulator, respectively. During MOF synthesis, this modulator binds to the MOF nodes competitively with terephthalic acid, resulting in the formation of a greater number of missing linker defects than are observed under typical synthesis conditions. Hafnium-UiO-66 (Hf-UiO-66) was synthesized under typical UiO-66 synthesis conditions with the substitution of equimolar hafnium tetrachloride for zirconium tetrachloride. Such a substitution leads to an isostructural UiO-66 analogue with nodes composed of hafnium

oxide instead of zirconium oxide. Neither of these structural alterations to UiO-66 resulted in changes in turnover to methanol (entries 5-7). Addition of exogenous UiO-66 similarly did not increase turnover.



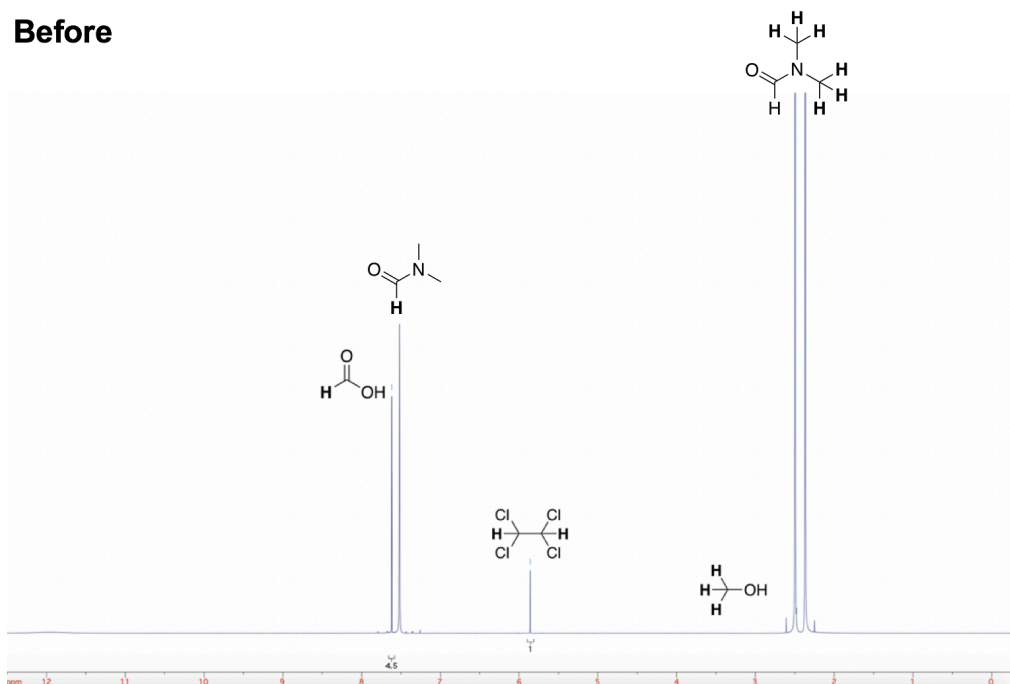
Entry	P <sub>CO2</sub> (bar)	P <sub>H2</sub> (bar)	Additive	Additive loading	TON
1	3	37	DBU	3.30 mmol	0 <sup>a</sup>
2	3	37	NEt <sub>3</sub>	3.30 mmol	0 <sup>a</sup>
3 <sup>b</sup>	3	37	HCOOH <sup>b</sup>	10.0 mmol	0 <sup>b</sup>
4	0	37	HCOOH	10.0 mmol	4700
5 <sup>c</sup>	3	37	-	-	4680 <sup>c</sup>
6 <sup>d</sup>	3	37	-	-	4720 <sup>d</sup>
7 <sup>e</sup>	3	37	-	-	4730 <sup>e</sup>

**Table 3-4.** Assessment of cascade reaction through alterations intended to affect a single step. (<sup>a</sup>Formate product observed, TON(DBU):1.5\*10<sup>6</sup>, TON(NEt<sub>3</sub>): 8.3\*10<sup>5</sup>; <sup>b</sup>no EtOH; <sup>c</sup>**3-1**@“30-benz”-UiO-66; <sup>d</sup>**3-1**@“40-benz”-UiO-66; <sup>e</sup>**3-1**@Hf-UiO-66)

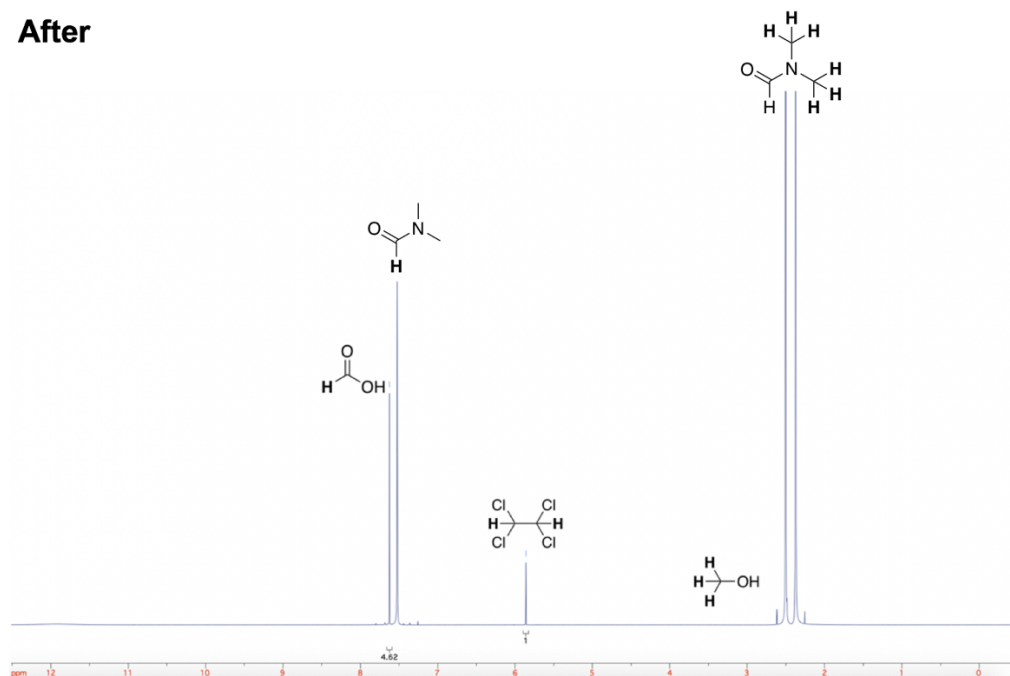


**Fig. 3-3.** Representative <sup>1</sup>H-NMR spectrum for cascade production of methanol from CO<sub>2</sub>, with methanol CH<sub>3</sub> peak (δ = 2.827 ppm) integrated against tetrachloroethane standard peak (δ = 5.852 ppm), displaying the absence of any peaks for formate ester or formic acid

**Before**



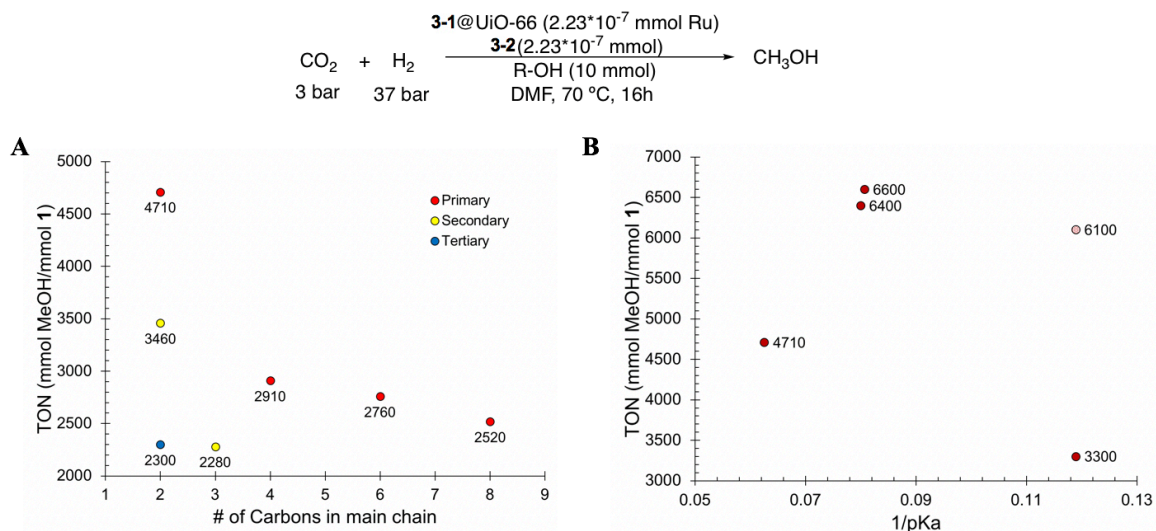
**After**



**Figure 3-4.** <sup>1</sup>H-NMR Spectra from before (top) and after (bottom) control reactions showing no conversion of formic acid ( $\delta = 5.86$  ppm) to methanol ( $\delta = 2.83$  ppm) in the absence of alcohol additive.

### 3.1.2 Improving Activity by Manipulating Alcohol Additive Identity

The identity of the alcohol additive was next evaluated to further improve catalyst activity. Results from these reactions revealed three factors important to catalyst performance: the length of the alcohol, the degree of branching in the alcohol, and the acidity of the alcohol (Figure 3-5A). When linear alcohols were used, a modest decrease in TON was observed with increasing chain length (Figure 3-5A, red). Compared to linear alcohols, branched alcohols led to lower turnover for analogues of the same molecular weight (Figure 3-5A, blue and yellow). Finally, significant increase in activity was observed when the acidity of the alcohol was increased (Figure 3-5B). In particular, greatly increased TON was observed with 2,2,2-trifluoroethanol (TFE) leading to the highest turnover of any alcohol employed (TON = 6,600).

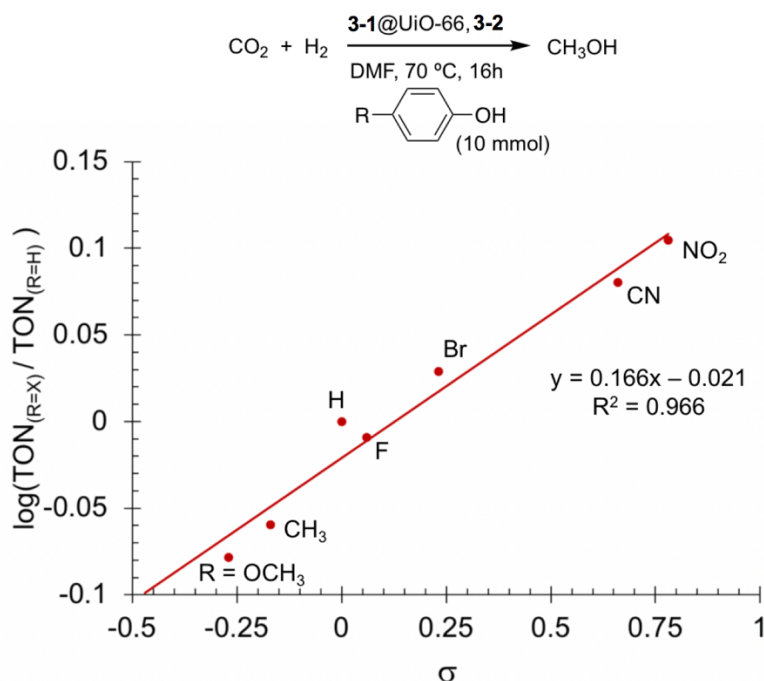


**Figure 3-5.** A) The length of linear alcohols or the degree of branching and B) the  $pK_a$  of the alcohol (red) affected activity. Light red circle denotes TON to or through formate ester.

Slower reaction rates with increasing alcohol size and branching suggested that mass transport was important for the steps involving the alcohol additive. The faster

reaction rates observed for more acidic alcohols is consistent with a mechanism that proceeds through an ester intermediate because the electrophilic formate ester formed is expected to be more reactive. Interestingly, when 2-nitroethanol was used as an additive, a significant amount of the formate ester intermediate was observed, which was not observed using any other additive (MeOH/ester = 1.2:1). This intermediate was likely observed due to atypical formate ester stability.<sup>46</sup> In this case, turnover to or through the formate ester was similar to the two other substituted ethanols tested ( $\text{TON}_{\text{ester}} = 6,100$ ).

While a direct correlation between  $\text{pK}_a$  and TON was not observed with the aliphatic alcohols, the size differences for these alcohol additives is likely also important, as described above. To better understand the electronic effects of the alcohol on the reaction and to minimize the influence from steric bulk, reactions were carried out using para-substituted phenols as additives. Consistent with the results obtained with aliphatic alcohols, electron deficient phenols resulted in higher catalytic turnover. A Hammett plot was generated from these results, revealing a good correlation between TON and the Hammett  $\sigma$ -value (Figure 3-6). A  $\rho$ -value of +0.166 was obtained from the slope of the line relating TON to  $\sigma$ , which suggested buildup of negative charge in the rate determining step of the process. In contrast, Hammett plots previously obtained for Fischer esterification reactions have a negative  $\rho$ -value,<sup>47</sup> suggesting that the rate-limiting step in the three-step cascade hydrogenation reaction was likely not esterification.



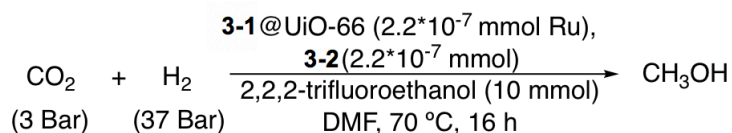
**Figure 3-6.** A Hammett plot for carbon dioxide hydrogenation reactions carried out with various *para*-substituted aromatic alcohols suggests negative charge buildup ( $\rho = 0.166$ ) during the rate-determining step (Conditions for all reactions:  $2.23 \times 10^{-7}$  mmol Ru per catalyst, 10 mmol alcohol additive, 37 bar  $\text{H}_2$ , 3 bar  $\text{CO}_2$ , 70  $^\circ\text{C}$ , 16 h).

In order to ensure that the methanol product observed was a product of the cascade reduction rather than any other process involved in synthesis, encapsulation, or isolation, several control experiments were performed (Table 3-5). To rule out the reduction of DMF solvent as the source of the observed methanol, the reaction was carried out in the absence of alcohol additive and carbon dioxide, resulting in no methanol production by  $^1\text{H-NMR}$  (entry 1). Methanol adsorbed to the MOF was next eliminated as a source of the observed product by a reaction conducted in the presence of only **3-1@UiO-66**, which resulted in no methanol production by  $^1\text{H-NMR}$  (entry 2). Next, a sample of **3-1@UiO-66** was prepared using  $\text{CD}_3\text{OD}$  in place of methanol for encapsulation and washing steps at all stages, resulting in a TON of 6600 when employed at optimal conditions. Since no decrease in TON resulted from the removal of  $\text{CH}_3\text{OH}$  from the process, these preparation steps were



not the source of methanol (entry 3). Catalysis using constructs dried rigorously in a rotating glass oven under vacuum at 150 °C resulted in no decrease in TON (entry 4), further ruling out MOF-adsorbed methanol as the source of the observed product. In order to rule out methanol already present in solvents used in synthesis, washing, catalysis, and gathering of NMR spectra, samples of each of these solvents were tested by <sup>1</sup>H-NMR, with no methanol observed in any sample.

When an increased catalyst loading was used (entry 5), methanol production increased, whereas methanol coming from MOF synthesis would have resulted in the same amount of methanol produced rather than a more than ten-fold increase. Although the production of methanol increased, the TON for the reaction decreased. This was likely a consequence of the increased concentration of **3-2** leading to bimolecular deactivation pathways like those described in Chapter 2. The prevention of these bimolecular deactivation pathways and improvement of the catalyst lifetime could be accomplished through encapsulation of **3-2**.



Entry	Alteration to Standard Conditions	TON
1	No 2,2,2-trifluoroethanol or CO <sub>2</sub>	0
2	No <b>3-2</b>	0
3	<b>3-1@UiO-66</b> prepared with CD <sub>3</sub> OD in place of CH <sub>3</sub> OH at all stages of synthesis	6600
4	<b>3-1@UiO-66</b> dried in a rotating glass oven at 150 °C in addition to typical drying	6600
5	2.0*10 <sup>-5</sup> mmol Ru loading each for <b>3-1@UiO-66</b> and <b>3-2</b>	800

**Table 3-5.** Summary of catalysis results with alterations to standard conditions listed in reaction scheme

## 3.2 IMPROVING CATALYST LIFETIME THROUGH HETEROGENIZATION

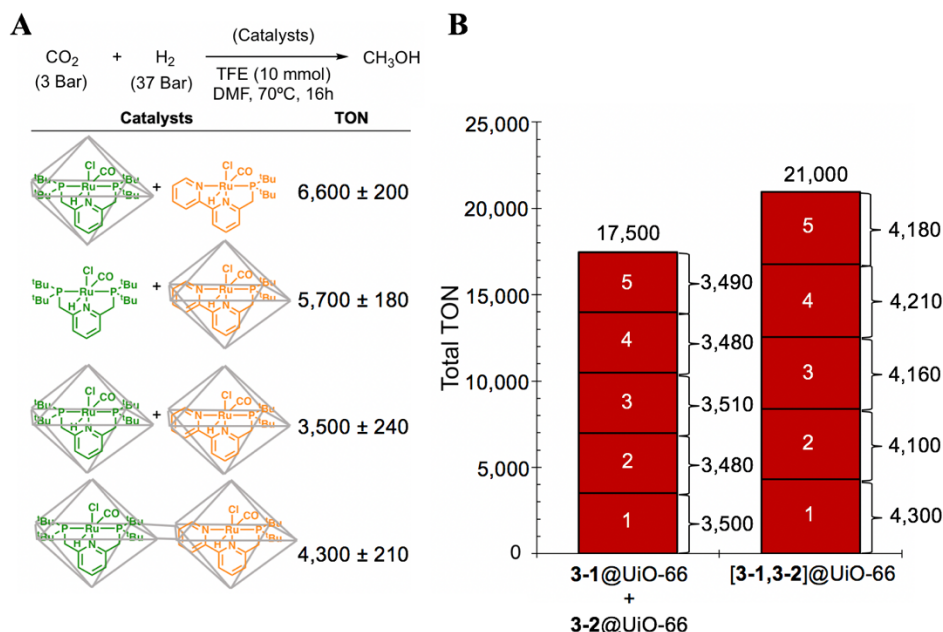
While the observed catalytic activity of this multicomponent system resulting from logical modulation was encouraging, there were still routes through which improvements could be accessed. To this end, tests were conducted to evaluate substrate diffusion effects and the effect of heterogeneity on catalyst longevity and recyclability. This was accomplished by manipulating the identity of encapsulated catalyst and taking note of changes in the activity of the system that resulted (Figure 3-7).

### 3.2.1 Imparting Recyclability Through Full Heterogenization

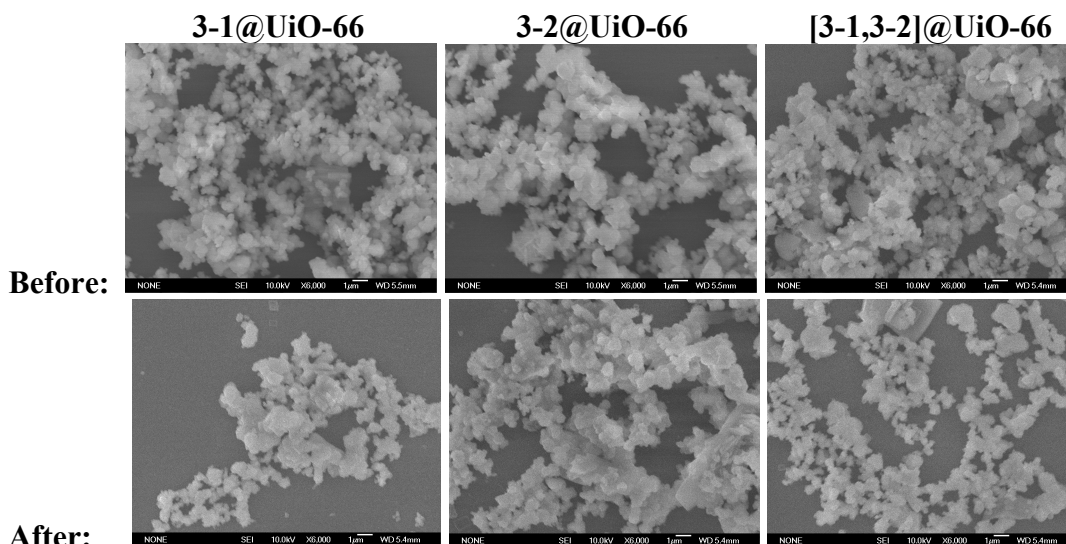
The heterogenized ester reduction catalyst **3-2@UiO-66** was synthesized through a similar aperture-opening encapsulation used for **3-1@UiO-66**, with the goal of applying both heterogeneous constructs in catalysis to access previously inaccessible recyclability. Due to the instability of **3-2** in neat methanol, acetonitrile was employed for the synthesis of **3-2@UiO-66**. When tested for loading by ICP-OES, loadings were lower than those observed in **3-1@UiO-66**, likely because acetonitrile is not as fast a solvent for aperture-opening encapsulation as methanol. A P:Ru ratio of approximately 1.0 was observed as well, consistent with the pincer complex maintaining its structural integrity during encapsulation. Similarly to **3-1@UiO-66**, a pre-treatment step was necessary to ensure that catalyst bound to the surface of the MOF was removed, but the P:Ru ratio remained approximately 1.0, consistent with catalyst stability to encapsulation.

When **3-2@UiO-66** and **3-1** were utilized in tandem with TFE as the additive, a turnover of 5,700 was observed, which was lower than when **3-1@UiO-66** and **3-2** were

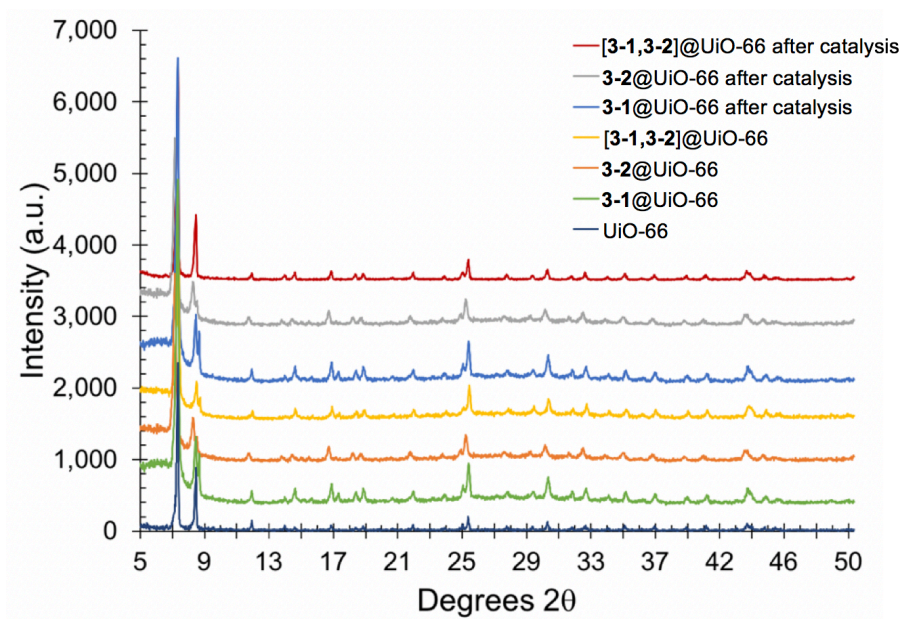
used in the reaction (rows 1 and 2, Figure 3-7A). The application of two separately-encapsulated constructs at once, manipulated to give equimolar ruthenium loadings for **3-1** and **3-2**, was next tested to determine the effect of full heterogenization on the reaction. When the two heterogenized constructs were used together, a TON of 3,500 was observed, which was just over half the turnover achieved by **3-1@UiO-66** and **3-2** or **3-2@UiO-66** and **3-1** (row 3, Figure 3-7A). The combination of mass transport limitations and the reversibility of the esterification step likely led to lower catalyst turnover in this scenario. Nevertheless, the fully heterogeneous system was advantageous because it could be readily recycled (Figure 3-7B, left). No appreciable loss in activity was observed over 5 cycles, leading to an effective TON of approximately 17,500. Analysis of the catalyst construct by SEM (Figure 3-8) and powder XRD (Figure 3-9) showed no degradation or significant change in the morphology of the MOF host, and analysis of the supernatant by inductively coupled plasma optical emission spectroscopy (ICP-OES) revealed no detectable ruthenium. Moreover, the ruthenium loadings within the MOF were similar before (4.55 ppm) and after recycling (4.52 ppm).



**Figure 3-7.** A) Turnover number (TON) observed for reactions using either or both of **3-1** and **3-2** encapsulated in UiO-66. TON is expressed as mmol methanol per mmol **3-1** and represents an average of three reactions (error expressed as average error). B) Recyclability studies for five cycles in the two fully heterogenized systems, **3-1@UiO-66** + **3-2@UiO-66** and **[3-1,3-2]@UiO-66**. Each cycle denoted by a black outlined box and numbered in white. Turnover number for each reaction is represented to the right of each column.



**Fig. 3-8.** SEM images of the samples before (top) and after (bottom) subjection to reaction conditions

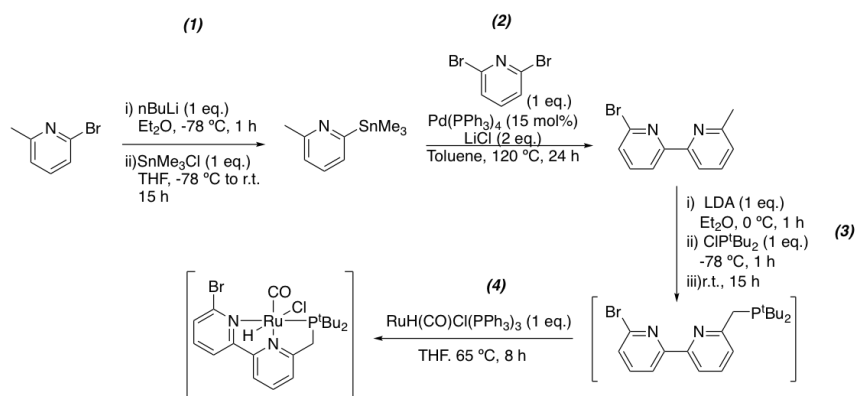


**Fig. 3-9.** Crystallinity of the catalysts before and after the reactions as shown by powder X-ray diffraction patterns

Finally, the case in which both pincer catalysts are encapsulated within the same framework was evaluated (Figure 3-7A, bottom). As complex **3-1** is incompatible with acetonitrile and **3-2** is incompatible with neat methanol, the co-encapsulated construct **[3-1,3-2]@UiO-66** was synthesized using sequential encapsulation involving encapsulation of **3-1** in methanol followed by encapsulation of **3-2** in acetonitrile (Table 3-4). Although the synthesis of **[3-1,3-2]@UiO-66** is straightforward, a unique analytical challenge exists in ensuring that **3-1** does not leach from **3-1@UiO-66** during encapsulation of **3-2**. Two methods were pursued to address this challenge, one featuring the use of an analogue to **3-2** with a distinguishable functional group installed on the <sup>t</sup>BuPNN ligand and the other employing an alternative metal center bound by the same <sup>t</sup>BuPNP ligand as **3-1**.

The first potential method for distinguishing co-encapsulated complexes was the installation of a bromine substituent on one of the aromatic rings of the <sup>t</sup>BuPNN ligand. This

synthesis was attempted through the Stille coupling of two differently substituted pyridines, followed by deprotonation of a methyl group and nucleophilic attack on the phosphine substituent (Scheme 3-3). While stannylation (**1**) and coupling (**2**) were successful, the final construction of the ligand (**3**) proved to be difficult due to significantly increased sensitivity of the phosphine moiety to oxygen with the introduction of the bromine substituent. Thus, this method was not pursued further.



**Scheme 3-3.** Procedures for the synthesis of Ru-<sup>t</sup>BuPNN-Br

The quantification of guests in a co-encapsulated construct was successfully carried out using the second method: synthesis of the complex (<sup>t</sup>BuPNP)Ir(CO)<sub>2</sub>H (**3-4**) which is similar in size to **3-1** but contains iridium instead of ruthenium. Accessed by metalating the <sup>t</sup>BuPNP ligand with iridium rather than ruthenium, **3-4** could serve as a reasonable proxy for **3-1** so that leaching could be evaluated during the encapsulation of **3-2** (Table 3-6). The iridium loading in **3@UiO-66** was found to be the same as **3-1@UiO-66**, which validated that **3-4** could serve as a viable proxy for **3-1**.

An ideal construct for the purpose of differentiating two co-encapsulated complexes would be both distinguishable from its counterpart by a rigorous characterization method and active in the reaction that the construct was intended to

catalyze. Unfortunately, no methanol was observed when **3-4**@UiO-66 was substituted for **3-1**@UiO-66 in CO<sub>2</sub> hydrogenation to methanol. Nevertheless, the iridium in **3-4** and the ruthenium in **3-2** were easily distinguishable by ICP-OES, so this model complex allowed for the assessment of complex leaching was occurring during the second step of the sequential encapsulation strategy.

Synthesis of [**3-4,3-2**]@UiO-66 was achieved in the same manner as the synthesis of [**3-1,3-2**]@UiO-66 by exposing **3-4**@UiO-66 to **3-2** in acetonitrile. ICP-OES analysis of [**3-4,3-2**]@UiO-66 showed the presence of ruthenium (16 ppm) and a nearly equal amount of iridium (73 ppm) as analyzed in **3-4**@UiO-66. The phosphorous concentration (162.1 ppm) was also consistent with the ruthenium and iridium concentrations expected for organometallic complexes that do not break down during encapsulation. These results demonstrated that there is neither leaching of **3-4** during the synthesis of [**3-4,3-2**]@UiO-66 nor is there destruction of either catalyst. Since similar increases in total metal concentration and P:Ru ratio were observed in the synthesis of [**3-1,3-2**]@UiO-66, leaching of **3-1** likely also does not occur during the synthesis of [**3-1,3-2**]@UiO-66.

$$\begin{array}{c} \text{3-1@UiO-66} \xrightarrow[\text{MeOH (10 mL), 55 }^\circ\text{C, 1d}]{\text{UiO-66 (100 mg)}} \text{3-1@UiO-66} \xrightarrow[\text{MeCN (10 mL), 55 }^\circ\text{C, 2d}]{\text{3-2 (5 mg)}} [\text{3-1,3-2}]@UiO-66 \\ \text{3-4@UiO-66} \xrightarrow[\text{MeOH (10 mL), 55 }^\circ\text{C, 1d}]{\text{UiO-66 (100 mg)}} \text{3-4@UiO-66} \xrightarrow[\text{MeCN (10 mL), 55 }^\circ\text{C, 2d}]{\text{3-2 (5 mg)}} [\text{3-4,3-2}]@UiO-66 \end{array}$$

Species	P:Ir Ratio	P:Ru Ratio	Ir/UiO-66	Ru/UiO-66	$\Delta[\text{cat.}]@UiO-66$
<b>3-1</b> @UiO-66	-	2.01	-	$6.81 \cdot 10^{-5}$	$6.81 \cdot 10^{-5}$
[ <b>3-1,3-2</b> ]@UiO-66	-	1.81	-	$8.42 \cdot 10^{-5}$	$1.61 \cdot 10^{-5}$
<b>3-4</b> @UiO-66	2.22	-	$7.26 \cdot 10^{-5}$	-	$7.26 \cdot 10^{-5}$
[ <b>3-4,3-2</b> ]@UiO-66	2.65	10.10	$7.30 \cdot 10^{-5}$	$1.60 \cdot 10^{-5}$	$1.62 \cdot 10^{-5}$

**Table 3-6.** Comparative test by ICP-OES for the loading of **3-4** complex in place of **3-1** to determine relative loading of **3-1** and **3-2** within [**3-1,3-2**]@UiO-66.

The activity of [3-1,3-2]@UiO-66 was notably higher compared to mixtures of 3-1@UiO-66 and 3-2@UiO-66 (Row 4, Figure 3-6A) but lower than both of the partially homogeneous combinations. As was the case with the mixtures of 3-1@UiO-66 and 3-2@UiO-66, [3-1,3-2]@UiO-66 could be recycled through 5 cycles with no appreciable decrease in activity or loss in ruthenium loading, leading to a cumulative TON of 21,000 (Figure 3-6B, right).

### 3.2.2 Observing Network Autocatalytic Behavior at Low Additive Loadings

The most commonly accepted mechanism for the conversion of carbon dioxide to methanol by the path described in this chapter involves three steps: 1) hydrogenation of carbon dioxide to formic acid, 2) conversion of formic acid to formate ester aided by the alcohol additive, and 3) hydrogenation of the formate ester to give methanol and reform the alcohol additive. As mentioned previously, since both products from the third step of the reaction can serve as reactants in the second step of the reaction, the overall transformation can exhibit autocatalytic behavior.

Autocatalytic behavior is defined slightly differently in biology,<sup>48</sup> polymer chemistry,<sup>49</sup> and asymmetric catalysis,<sup>50</sup> but commonly refers to reactions in which one of the products can accelerate the same reaction or a coupled reaction isothermally.<sup>51</sup> The simplest example of this is a single-catalyst reaction  $A + B \xrightarrow{C} C$  in which the product acts as a catalyst for its own formation. This self-catalysis is specifically defined as “direct autocatalysis” and is based on the Frank model.<sup>50</sup> Direct autocatalysis is exemplified by the Soai alkylation<sup>52</sup> (Figure 3-10A) that leads to amplified enantiomeric enrichment from



only slightly enantioenriched feedstocks. In this specific example, an aldehyde is reacted with stoichiometric amounts of diisopropyl zinc, giving an alcohol product and forming a stereocenter where the isopropyl group is added. This reaction proceeds slowly and gives racemic product without an enantiomerically enriched alcohol catalyst present. Introduction of the alcohol product formed from this reaction resulted in increased reaction rates, which accelerate over time, and amplification of the enantiopurity introduced from the exogenous alcohol product. These effects were a result of the product itself directly acting as a catalyst to activate the dialkylzinc reagent and control the stereoselectivity of the reaction.

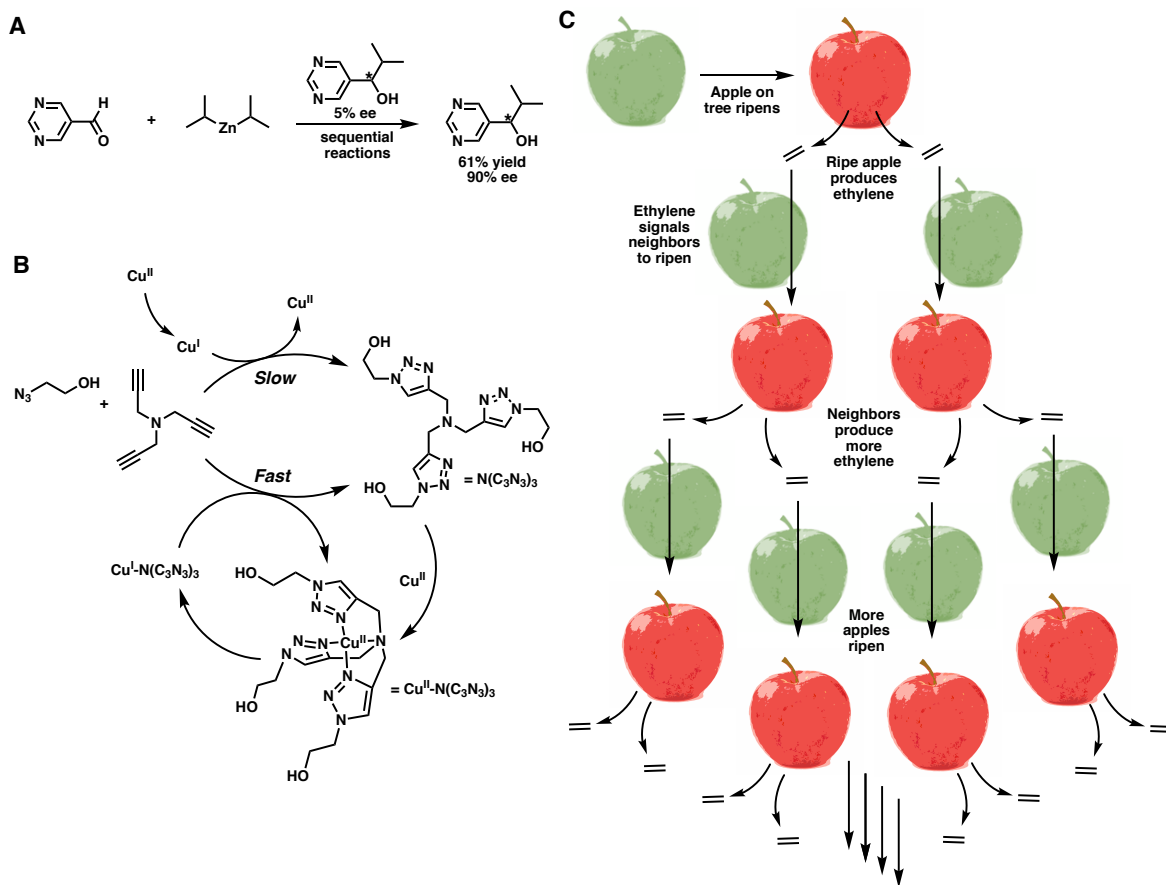
Although direct autocatalysis best fits the strictest definition of the term, autocatalytic behavior has also been observed in more complex systems that are not strictly self-catalyzed. The behavior of some or all of a multicomponent system could be described as autocatalytic even if the product itself does not act directly as a catalyst.<sup>53</sup> While in such a case the product-forming step of the reaction is not itself autocatalytic, the system as a whole could be said to exhibit “network autocatalysis”. Network autocatalysis occurs in systems where a product can accelerate its own production indirectly.<sup>54,55</sup>

Representative examples of such network autocatalysis in transition metal-catalyzed processes have been published recently by Whitesides and co-workers.<sup>56,57</sup> In the most recent case, the product of a copper-catalyzed azide-alkyne cycloaddition served as a ligand for a copper complex that catalyzes that same cycloaddition reaction at a higher rate (Figure 3-10B). They observed that the rate of the reaction accelerated over time and that the initial slow turnover period was shortened by addition of exogenous  $N(C_3N_3)_3$ . Thus,

while the product did not directly catalyze its own formation, its formation resulted in an increased reaction rate, consistent with indirect network autocatalysis.

Although the behavior described by Whitesides and co-workers highlights the promise of network autocatalysis in organometallic systems, network autocatalytic behavior most similar to that possible in the hydrogenation of carbon dioxide to methanol can be found in biological systems. For example, the ripening of fruit is accelerated by ethylene, which is itself produced by ripe fruits (Figure 3-10C).<sup>58</sup> The ethylene produced by the ripe fruits increases the rate at which neighboring fruits ripen, and these ripened neighboring fruits produce ethylene at an accelerated rate themselves. Thus, ethylene increases the rate of fruit ripening, which in turn increases the rate of ethylene production. In this loop, ethylene indirectly increases the rate of its own formation and could then be said to participate in network autocatalysis.

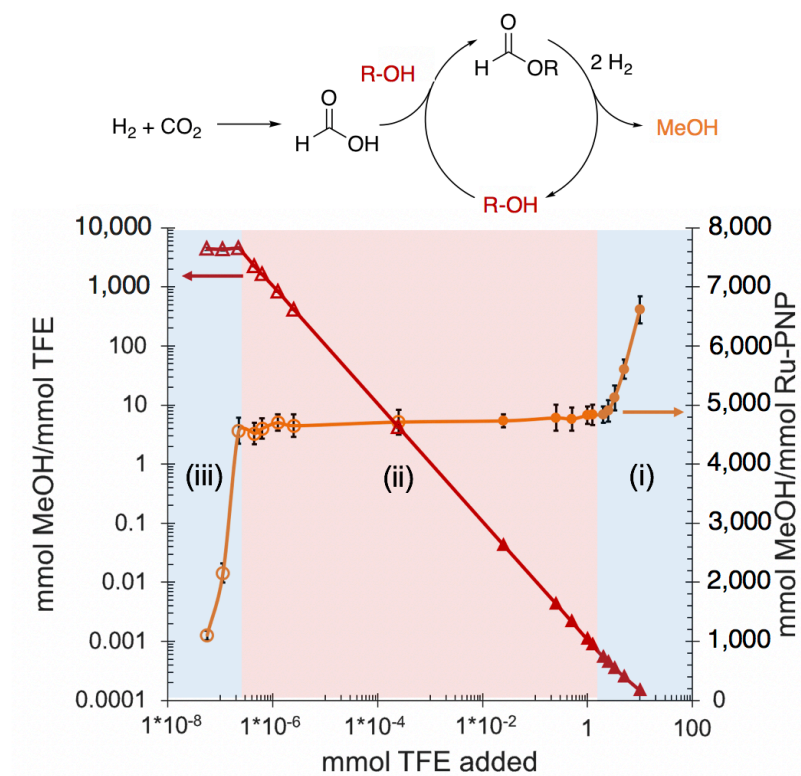
This type of network autocatalytic feature was previously unobservable in the hydrogenation of carbon dioxide to methanol because the reactions were performed in two separate vessels<sup>31</sup> or proceeded through a reaction mechanism where autocatalysis is not possible.<sup>13,14,28-30</sup> While Goldberg and co-workers circumvented both of these obstacles, they did not report tests for such behavior. Their system could lead to network autocatalysis, though this might be complicated by the fully homogeneous nature of their catalyst selection.



**Figure 3-10.** Comparison of observed examples of A) direct autocatalysis in the Soai reaction resulting in amplified enantioenrichment,<sup>52</sup> B) network autocatalysis observed by Whitesides and co-workers in azide-alkyne cyclization with accelerated rate over time through catalysis promoted more effectively by product-ligated copper species,<sup>57</sup> and C) network autocatalysis in production of ethylene during fruit ripening<sup>58</sup>

To interrogate the possibility for network autocatalysis, carbon dioxide hydrogenation reactions were carried out at progressively decreasing loadings of TFE using **3-1@UiO-66** and **3-2** as the multicomponent system (Figure 3-11). Turnover with respect to **3-1@UiO-66** decreased initially from 6,600 to 4,500 when TFE loading was decreased from 10 mmol to 1 mmol (section i). However, as TFE loading was decreased further from 1 mmol to  $2.2 \times 10^{-7}$  mmol, no appreciable change in TON was observed (section ii). In this range, productivity of methanol with respect to TFE increased by six orders of magnitude from  $1.08 \times 10^{-3}$  to 4,500 mmol of product methanol per mmol of TFE added, making the

reaction catalytic in TFE. Below TFE loadings of  $2.2 \times 10^{-7}$  mmol, TON with respect to **3-1@UiO-66** began to decrease (section iii), while productivity of methanol with respect to TFE remained constant.



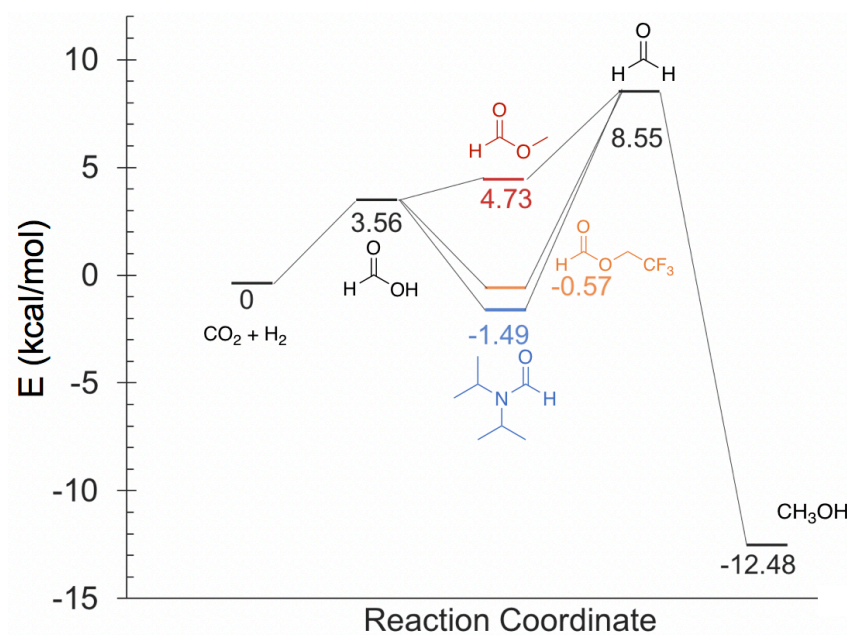
**Figure 3-11.** Effect of varying the concentration of TFE additive on catalyst productivity with respect to ruthenium (orange) and TFE (red). Data points collected when the reaction is catalytic in TFE are denoted with an open marker. Data is represented as an average of three runs and error bars represent average error.

These three regimes reflect complex behavior in the multicomponent system that can be explained by considering the reaction mechanism. At high TFE loadings (section i), the additive comprised a major percentage of the solvent (19% to 2% v/v), which significantly changes the solvent polarity. Solvent dielectric is expected to be an important contributor to the rate of the reaction considering that negative charge build-up occurs during the rate limiting step of the transformation (Figure 3-6). At intermediate TFE concentrations (section ii), the amount of methanol produced remained constant regardless

to the amount of TFE added. However, the amount of methanol produced with respect to the TFE added steadily increased as TFE decreased until  $[\text{TFE}] < 7.3 \times 10^{-5} \text{ mM}$ . Network autocatalysis is indicated by this observation because above a critical TFE concentration, enough methanol can be produced so that the reaction proceeds predominately through a methyl formate intermediate. In such a scenario, the reaction would not depend on the amount of TFE, thereby allowing the additive to be used in catalytic quantities. Finally, at very low TFE loadings (section iii), the decrease in TON as TFE is decreased and the constant amount of methanol produced with respect to TFE are evidence that at these low TFE concentrations, the rate determining step changes so that the esterification reaction becomes rate-limiting.

The observed network autocatalytic behavior highlights a unique advantage of the system reported in this chapter compared to reactions that proceed through a formamide intermediate. The major difference between these systems stems from the thermodynamic stability and (presumably) kinetically controlled reactivity of the ester and amide intermediates (Figure 3-12). The behavior of the multicomponent catalytic system described in this chapter is most consistent with the conversion of the ester or amide to formaldehyde being rate-limiting (when  $[\text{TFE}] > 2.23 \times 10^{-7} \text{ mmol}$ ). Thermodynamically, the pathway through 2,2,2-trifluoroethyl formate (orange path) and N,N'-diisopropylformamide (blue path) differ by nearly 1 kcal, with the latter being more stable. The difference favors faster reactions at lower temperatures through the formate ester compared to the formamide. This thermodynamic preference is likely further magnified in the transition state (not shown) for ester hydrogenation compared to the amide reduction due to the latter's greater steric bulk and the expected greater electrophilicity of the former.

Compounding the thermochemical and kinetic advantages, the transformation reported here benefits from access to a second pathway through a methyl ester intermediate inaccessible to reactions requiring formation of an amide (red path, Figure 3-12). While methyl formate is thermodynamically uphill relative to carbon dioxide and hydrogen, the barrier can be overcome with sufficient buildup of methanol, which ultimately results in network autocatalysis.



**Figure 3-12.** Reaction coordinate diagram for converting carbon dioxide to methanol proceeding through a N,N'-diisopropylformamide (blue path), 2,2,2-trifluoroethyl formate ester (orange path), or methyl formate ester (red path) intermediate. Energies shown are enthalpic heats of reaction ( $\Delta H_{\text{rxn}}$ , kcal/mol), which were obtained directly from thermochemical data or calculated using Benson group increments.<sup>46</sup>

The nanostructured assembly of three catalysts reported here for cascade hydrogenation of carbon dioxide to methanol is among the most active systems reported to date. It was thus necessary to compare it directly to the most active transition metal complex catalyst reported for the reaction. To this end, trans-[RuCl<sub>2</sub>(dppea)<sub>2</sub>] (**3-5**) was synthesized and its activity (TON<sub>(3-5)</sub>) was compared directly against that of the

multicomponent system developed in this chapter ( $\text{TON}_{(\text{MC})}$ ) in various conditions (Table 3-7). While the activity of **3-5** was higher under conditions that were optimized for it<sup>13</sup> (entry 1),  $\text{TON}_{(3-5)}$  and  $\text{TON}_{(\text{MC})}$  became equal upon decreasing reaction temperature to 70 °C (entry 2). When reagent pressures were altered to those optimized for the multicomponent system,  $\text{TON}_{(\text{MC})}$  was greater than twice  $\text{TON}_{(3-5)}$  (entry 3). This superior activity persisted at extended reaction times, where  $\text{TON}_{(\text{MC})}$  exceeded  $\text{TON}_{(3-5)}$  by 3650 (entry 4). Excitingly,  $\text{TON}_{(\text{MC})}$  also exceeded  $\text{TON}_{(3-5)}$  at reduced additive loading, which was especially impressive because the additive loading for the multicomponent system was six orders of magnitude lower than that for **3-5**. It was thus concluded that the multicomponent catalytic system developed in this chapter compared favorably to the state-of-the-art homogeneous catalyst under the majority of conditions tested.

$$\text{CO}_2 + \text{H}_2 \longrightarrow \text{CH}_3\text{OH}$$

Entry	$\text{P}_{\text{CO}_2}$	$\text{P}_{\text{H}_2}$	T (°C)	t (h)	$\text{TON}_{(3-5)}$	$\text{TON}_{(\text{MC})}$
1	10	30	100	2	8800*	4920
2	10	30	70	2	5270	5270
3	3	37	70	2	1630	3700
4	3	37	70	16	2950	6600*
5	10	30	100	2	1160 <sup>a</sup>	-
6	3	37	70	2	-	1420 <sup>a</sup>

**Table 3-7.** Comparison between turnover number for **3-5** ( $\text{TON}_{(3-5)}$ ) and the multicomponent system of **3-1@UiO-66** and **3-2** developed in this chapter ( $\text{TON}_{(\text{MC})}$ ) at various pressures, temperatures, and reaction times in conditions otherwise optimized for that catalyst. Optimal conditions for **3-5**: **3-5** ( $5 \times 10^{-5}$  mmol),  $i\text{Pr}_2\text{NH}$  (3.5 mmol),  $\text{NaOEt}$  (0.15 mmol), toluene (3 mL). Optimal conditions for **3-1@UiO-66** + **3-2**: **3-1@UiO-66** ( $2.2 \times 10^{-7}$  mmol Ru), **3-2** ( $2.2 \times 10^{-7}$  mmol), TFE (10 mmol), DMF (3 mL). \* = TON at optimized conditions, <sup>a</sup> = TON at reduced additive loading (0.35 mmol  $i\text{Pr}_2\text{NH}$  for **3-5**,  $2.2 \times 10^{-7}$  mmol TFE for **3-1@UiO-66** + **3-2**)

### 3.4 CONCLUSION

In this chapter, aperture-opening encapsulation was employed to construct a multicomponent catalytic system for the tandem conversion of carbon dioxide to methanol. The system is particularly active at low temperatures and with substoichiometric amounts of TFE additive where it exhibits network autocatalysis. Moreover, because multiple physically separated and individually tunable catalysts are used in this system, a step in the transformation could be independently optimized without significantly affecting the activity of the catalysts used for other steps of the transformation. Access to new behavior through multicomponent catalysis is particularly exciting for the discovery of reactivity that has previously remained dormant due to the focus of research on single catalysts for complex reactions that has predominated synthetic catalyst design.

The advances described in this chapter represent a significant step forward from those in Chapter 2 in several regards. First, methanol synthesis from carbon dioxide is much more challenging than the synthesis of formate: while both are thermodynamically downhill, carbon must only be reduced once in the latter while three reduction steps are required for the former. Furthermore, the use of two previously incompatible catalysts in a single reaction vessel is extremely rare. The manner in which this was accomplished in this chapter is analogous to reactor engineering on a molecular scale, which is potentially groundbreaking for other one-pot multi-catalyst systems. Finally, the aperture-opening encapsulation method allows for even further system modularity. Described in Chapter 4 is the use of such modularity to further optimize the system described in this chapter, resulting in even greater improvements through logical design and systematic screening.



## Materials and Methods

### General Considerations

Unless otherwise stated, all manipulations were carried out in air using standard analytical procedures. Catalytic carbon dioxide hydrogenation reactions were carried out in 5.0 mL ampules each containing a stir bar, placed in a 450 mL stainless steel Parr reactor. Included with each reaction were positive and negative controls (using an active combination of the three catalysts and no catalyst, respectively) to ensure proper operation and to ensure that no cross contamination between ampules occurred. Experiments carried out in an air-free environment were conducted under a positive pressure of nitrogen using standard glovebox or Schlenk line techniques.<sup>59</sup> All catalysts employed were pre-treated as described below.

### *Materials*

N,N'-dimethylformamide (Acros Organics), ethanol (Fisher), 2,2,2-trifluoroethanol (Alfa Aesar), trichloroethanol (Acros), 2-nitroethanol (Aldrich), isopropanol (Fisher), 1-butanol (Fisher), 2-butanol (Aldrich), 2-methyl-2-propanol (Aldrich), hexanol (Aldrich), octanol (Acros), phenol (Aldrich), 4-bromophenol (TCI), 4-cyanophenol (TCI), 4-fluorophenol (Acros), 4-methoxyphenol (Acros), 4-nitrophenol (Acros), 4-cresol (TCI), zirconium tetrachloride (Aldrich), terephthalic acid (Aldrich), concentrated hydrochloric acid (Fisher), 2,2'-bipyridyl (TCI), 1,1,2,2-tetrachloroethane (Beantown Chemical Co.), 2,6-lutidine (Aldrich), Ru-MACHO (**3-3**) (Strem) and di-tert-

butylchlorophosphine (Acros Organics) were purchased from the indicated sources and used without further purification.

#### *Instrumentation.*

Powder X-ray diffraction traces were collected on a Bruker AXS diffractometer with Cu K $\alpha$  radiation ( $\lambda=1.5418$  Å).  $^1\text{H}$ -NMR and  $^{31}\text{P}\{^1\text{H}\}$ -NMR spectra were collected on Varian Unity INOVA spectrometers (400 MHz, 500 MHz, or 600 MHz, as indicated.  $^{31}\text{P}\{^1\text{H}\}$ -NMR spectra were collected at 202 MHz, with all chemical shifts reported in ppm. Chemical shifts were reported in reference to tetramethylsilane and phosphoric acid for  $^1\text{H}$ -NMR and  $^{31}\text{P}$ -NMR spectra, respectively ( $\delta = 0.0$  ppm for both).

Formate production in catalysis was quantified using  $^1\text{H}$  NMR spectroscopy using tetrachloroethane (10  $\mu\text{L}$ ) as an external standard in a mixture of  $\text{CDCl}_3$  (450  $\mu\text{L}$ ) and reaction mixture (250  $\mu\text{L}$ ).  $^1\text{H}$ -NMR spectra were acquired in 16 transients.  $^{31}\text{P}\{^1\text{H}\}$ -NMR spectra were acquired in 160 transients. All centrifugation steps were performed at 3000 revolutions per minute for 10 minutes using a Thermo Scientific CL2 centrifuge unless otherwise noted. Inductively coupled plasma optical emission (ICP-OES) spectrometry was recorded on an Agilent 5100 instrument that was calibrated using known concentrations of standard solutions to quantify Zr, Ru, Ir, and P. Ru ( $1000 \pm 4$  ppm), Ir ( $999 \pm 3$  ppm), P ( $100.04 \pm 0.55$  ppm), Zr ( $999 \pm 5$  ppm) single elemental standards were purchased from Inorganic Ventures. Gas Chromatography data was collected on an SRI Instruments Multiple Gas Analyzer #5 using a 2 meter Molesieve 5A column, nitrogen as carrier gas, and a Flame Ionization Detector equipped with a methanizer. Quantification

was performed on 0.5-mL samples using prepared 1 ppm, 10 ppm, and 50 ppm standards of carbon monoxide in nitrogen.

### *Procedures*

**Synthesis of 2,6-bis((di-tert-butylphosphino)methyl)pyridine (<sup>t</sup>BuPNP).** This synthesis was adapted from a literature procedure.<sup>60</sup> On a Schlenk line under nitrogen atmosphere, a solution of 2,6-lutidine (0.54 mL, 4.7 mmol) in diethyl ether (1.96 mL) was prepared in a 50-mL two-neck flask, then cooled to 0 °C. n-Butyl lithium in hexanes (2.0 M, 4.8 mL, 9.6 mmol) was added slowly by syringe to this cooled solution, which resulted in the homogeneous reaction mixture to turn a dark maroon-red color. The reaction mixture was allowed to warm to room temperature and heated to 40 °C for fifteen hours. After cooling to room temperature, the reaction mixture was brought to -78 °C where di-tert-butylchlorophosphine (1.9 mL, 9.7 mmol) was added dropwise to the reaction mixture via syringe. The reaction mixture was allowed to warm to room temperature where it reacted for one hour, retaining its deep red coloration. The reaction mixture was quenched with degassed methanol (40 mL), resulting in a color change to light-yellow. The reaction mixture was left without stirring for one hour to allow the resulting lithium salt to settle. The liquid product mixture was transferred by cannula filtration to another two-necked flask, and the lithium salt was washed twice with diethyl ether. The solvent mixture was removed by vacuum at 55 °C resulting in an off-white solid. This solid was transferred to a nitrogen-filled glovebox and extracted in diethyl ether (10 mL), then recrystallized in diethyl ether at -40 °C. The clear-white crystalline product was recovered and washed with cold diethyl ether. (490 mg, 2.5 mmol, 53% yield). <sup>1</sup>H NMR (500 MHz, C<sub>6</sub>D<sub>6</sub>) δ: 1.13 (d,

$J = 10.8$  Hz, 36H), 3.09 (d,  $2J = 2.4$  Hz, 4H), 7.17 (d,  $J = 7.5$  Hz, 2H), 7.25 (t,  $J = 7.8$  Hz, 1H) ppm.  $^{31}\text{P}\{^1\text{H}\}$  NMR (202 MHz,  $\text{C}_6\text{D}_6$ )  $\delta$ : 37.60 (s) ppm. This spectral data was consistent with the literature reported spectral data.<sup>60</sup>

**Synthesis of  $(^t\text{BuPNP})\text{Ru}(\text{CO})\text{HCl}$  (3-1).** This synthesis was adapted from a literature procedure.<sup>61</sup> In a nitrogen-filled glove box,  $\text{RuHCl}(\text{PPh}_3)_3(\text{CO})$  (260 mg, 0.27 mmol) was suspended in tetrahydrofuran (THF) (10 mL) in a 100 mL Schlenk tube.  $^t\text{BuPNP}$  (110 mg, 0.28 mmol) was added to this suspension. The solution was diluted with THF (20 mL). This reaction mixture was sealed and removed from the glovebox, then heated at 65 °C for 3 hours. The resulting mixture was returned to the glove box and filtered through celite on a coarse fritted funnel. The remaining THF was removed *en vacuo*. The resultant oily yellow solid was dissolved in THF (0.50 mL), and precipitated into pentane to give a yellow solid. This solid was then washed with pentane (50 mL), and the crude product was recrystallized in pentane at -40 °C. The recrystallized product was a yellow solid (87 mg, 16 mmol, 57% yield).  $^1\text{H}$ -NMR (500 MHz,  $\text{C}_6\text{D}_6$ )  $\delta$ : -14.52 (t,  $J = 20.0$  Hz, 1H), 1.13 (t,  $J = 8.0$  Hz, 18H), 1.52 (t,  $J = 8.0$  Hz, 18H), 2.87 (dt,  $J = 16.0$  Hz,  $J = 4.0$  Hz, 2H), 3.77 (dt,  $J = 16.0$  Hz,  $J = 4.0$  Hz, 2H), 6.46 (d,  $J = 8.0$  Hz, 2H), 6.79 (t,  $J = 8.0$  Hz, 1H) ppm.  $^{31}\text{P}\{^1\text{H}\}$ -NMR (202 MHz,  $\text{C}_6\text{D}_6$ )  $\delta$ : 90.8 (s) ppm. This spectral data was consistent with the literature reported spectral data.<sup>61</sup>

**Synthesis of 6-methyl-2,2'-bipyridyl.** The synthesis of this compound was adapted from a literature procedure.<sup>62</sup> Methyllithium in diethyl ether (4.0 mL, 1.6 M, 6.4 mmol) was added dropwise to a diethyl ether solution (40 mL) containing 2,2'-bipyridine (1.0 g, 6.4 mmol) at 0 °C. After complete addition, the resulting brown solution was gently refluxed for 3 h under  $\text{N}_2$ . It was then allowed to cool to room temperature and water was

added with stirring, resulting in a biphasic yellow solution. The aqueous layer was separated from the organic layer and extracted three times with diethyl ether. The combined organic layers were washed twice with brine (20 mL) followed by addition of anhydrous  $\text{Na}_2\text{SO}_4$  to remove residual water. The solution was then decanted into a round-bottom flask and the ether was removed by rotary evaporation. The resulting orange oil was oxidized with a saturated  $\text{KMnO}_4$ /acetone solution (100 mL) until formation of  $\text{MnO}_2$  ceased. The  $\text{MnO}_2$  was removed by vacuum filtration through celite. The filtrate was placed in a round-bottom flask and acetone was removed by rotary evaporation. Purification of the crude product by column chromatography (heptane/EtOAc 1/1 on silica) gave the desired product. (810 mg, 4.8 mmol, 74% yield).  $^1\text{H}$ -NMR (500 MHz,  $\text{CDCl}_3$ )  $\delta$ : 2.61 (s, 3H), 7.13 (d,  $J$  = 7.80 Hz, 1H), 7.26-7.27 (m, 1H), 7.57 (t,  $J$  = 7.80 Hz, 1H), 7.74-7.79 (m, 1H), 8.17 (d,  $J$  = 7.50 Hz, 1H), 8.40 (d,  $J$  = 8.10 Hz, 1H), 8.64-8.67 (m, 1H). This spectral data was consistent with the literature reported spectral data.<sup>62</sup>

**Synthesis of 6-di-tert-butylphosphinomethyl-2,2'-bipyridyl ( $^t\text{BuPNN}$ ).** The synthesis of this compound was adapted from a literature procedure.<sup>63</sup> An oven-dried 500 mL two-necked round bottom flask with a stirring bar, dropping funnel and one rubber septum was cooled under a stream of nitrogen. A solution of 6-methyl-2,2'-bipyridine (3.4 g, 20 mmol) in dry ether (80 mL) was added to this flask. The solution was cooled to 0 °C and lithium diisopropylamide (LDA) (1.8 M, 13 mL, 24 mmol) in diethyl ether was added dropwise via addition funnel. The resulting brown colored mixture was stirred for 1 hr at 0 °C and then cooled to -78 °C. A solution of di-tertbutylchlorophosphine (4.3 g, 24 mmol) in dry ether (30 mL) was added dropwise to this mixture. The stirring was continued for 1 hr at -78 °C and the mixture was allowed to slowly warm to room temperature and stirred

overnight. The supernatant was transferred by cannula to a round-bottom flask, then exposed to vacuum. The resulting solid was purified by recrystallization in pentane to yield 6-di-tertbutylphosphinomethyl-2,2'-bipyridine (<sup>t</sup>BuPNN) as a white solid. (3.3 g, 10 mmol, 52% yield). <sup>1</sup>H NMR (C<sub>6</sub>D<sub>6</sub>) δ: 1.19 (d, J = 11.0 Hz, 18H), 3.10 (d, J = 3.3 Hz, 2H), 7.25 (ddd, J = 7.5 Hz, J = 4.8 Hz, J = 1.2 Hz, 1H), 7.38 (td, J<sub>HH</sub> = 7.8 Hz, J = 1.0 Hz, 1H), 7.65 (t, J = 7.8 Hz, 1H), 7.74 (dt, J = 7.8 Hz, J = 1.8 Hz, 1H), 8.14 (br d, J = 7.8 Hz, 1H), 8.41 (td, J = 8.0 Hz, J = 1.0 Hz, 1H), 8.60-8.62 (m, 1H). <sup>31</sup>P{<sup>1</sup>H}-NMR (C<sub>6</sub>D<sub>6</sub>) δ: 37.5 (s). This spectral data was consistent with the literature reported spectral data.<sup>63</sup>

**Synthesis of (<sup>t</sup>BuPNN)Ru(CO)HCl (3-2).** This synthesis of this compound was adapted from a literature procedure.<sup>63</sup> <sup>t</sup>BuPNN (100 mg, 0.33 mmol), RuHCl(CO)(PPh<sub>3</sub>)<sub>3</sub> (300 mg, 0.32 mmol), and 12 mL dry THF were added to an oven-dried 25-mL Schlenk tube in a nitrogen-filled glove box. The vessel was sealed and brought out of the glovebox. On a Schlenk line under nitrogen, the reaction was heated at 65 °C for 8 hrs with stirring, then cooled to room temperature to give a red-brown solid. The reaction mixture was brought into the glove box, and the solvent was decanted and the solid thus obtained was washed with ether (3 × 3.0 mL), then dried under vacuum to give pure complex (130 mg, 0.27 mmol, 85% yield). <sup>1</sup>H-NMR (500 MHz, C<sub>6</sub>D<sub>6</sub>) δ: -15.3 (d, 2 J = 24.6 Hz, 1H), 1.27 (d, J = 13.2 Hz, 9H), 1.47 (d, J<sub>PH</sub> = 13.8 Hz, 9H), 3.02-3.72 (m, 2H), 7.45-7.47 (m, 1H), 7.59 (d, J = 7.8 Hz, 1H), 7.81-7.88 (m, 2H), 7.95 (d, J = 8.1 Hz, 1H), 8.06 (d, J = 7.8 Hz, 1H), 9.11-9.15 (br m, 1H). <sup>31</sup>P{<sup>1</sup>H}-NMR (202 MHz, C<sub>6</sub>D<sub>6</sub>) δ: 107.1 (s). This spectral data was consistent with the literature reported spectral data.<sup>63</sup>

**Synthesis of (<sup>t</sup>BuPNP)IrH<sub>2</sub>Cl (3-4).** The synthesis of this compound was adapted from a literature procedure.<sup>60</sup> In a nitrogen-filled glove box, [Ir(coe)<sub>2</sub>Cl]<sub>2</sub> (29 mg, 0.033

mmol) was suspended in tetrahydrofuran (5.0 mL) in a 20 mL scintillation vial. <sup>t</sup>BuPNP (26 mg, 0.065 mmol) was added to this suspension. The solution was diluted with THF (10 mL). This mixture was transferred to a 20-mL ampule and placed inside a 450-mL stainless steel autoclave, which was sealed and removed from the glovebox. The autoclave was pressurized with hydrogen (25 bar) and heated at 90 °C for 12 hours. The autoclave was depressurized to 3 bar and returned to the glove box, then filtered through celite on a coarse fritted funnel. The remaining THF was removed *en vacuo*. The resulting red solid was dissolved in THF (0.50 mL) and precipitated into pentane to give a transparent red solid. This solid was then washed with pentane (25 mL), and the crude product was recrystallized in pentane at -40 °C to give the recrystallized product (23 mg, 0.036 mmol, 55% yield). <sup>1</sup>H-NMR (C<sub>6</sub>D<sub>6</sub>, 500 MHz) δ: 7.51 (dd, J = 8 Hz, 1H), 7.21 (d, J = 8 Hz, 2H), 3.85 (d, br, 2 J = 16 Hz, 2H), 3.37 (d, br, 2 J = 17 Hz, 2H), 1.37 (s, br, 18H), 1.10 (brs, 18H), -19.49 (dt, 2 J = 7 Hz, 2 J = 13 Hz, 1H), -23.69 (dt, 2 J = 7 Hz, 2 J = 14 Hz, 1H); <sup>31</sup>P{<sup>1</sup>H}-NMR (C<sub>6</sub>D<sub>6</sub>, 202 MHz) δ: 59.5 This spectral data was consistent with the literature reported spectral data.<sup>60</sup>

**Synthesis of Sodium diphenylphosphide.** Sodium hydride (0.50 g, 21 mmol) was suspended in THF (15 mL) in a 20-mL scintillation vial with a stir bar, Diphenylphosphine (3.6 mL, 18 mmol) was added to this vessel, which was then capped. The mixture was stirred overnight with intermittent venting until the mixture appeared homogeneous. The product (3.5 g, 16 mmol, 87% yield) was precipitated in pentane. The supernatant was decanted and residual solvent was removed by vacuum. The product was washed three times with pentane and stored in a 20-mL scintillation vial. <sup>31</sup>P{<sup>1</sup>H}-NMR (202 MHz, C<sub>6</sub>D<sub>6</sub>) δ: -58.2 (s).

**Synthesis of  $\text{HN}(\text{Me})(\text{CH}_2)_2\text{Cl}\cdot\text{HCl}$ .** This procedure was adapted from that performed in the literature.<sup>64</sup> 2-(Methylamino)ethanol (15 mL, 190 mmol) was dissolved in  $\text{CHCl}_3$  (180 mL), and the solution was cooled to 0 °C. Thionyl chloride (14 mL, 200 mmol) was added, and the resulting suspension was stirred at room temperature overnight. The volume of  $\text{CHCl}_3$  was reduced by 50 mL and EtOH was added (~50 mL) to quench the excess of thionyl chloride. The solvent was removed in vacuo, and the resulting off-white solid was recrystallized twice with an  $\text{Et}_2\text{O}$  and EtOH mixture (20:80) at 4 °C. Colorless crystals of  $\text{HN}(\text{Me})(\text{CH}_2)_2\text{Cl}\cdot\text{HCl}$  so obtained were washed with cold EtOH and dried (9.2 g, 71 mmol, 39% yield).  $^1\text{H}$ -NMR (500 MHz,  $\text{CDCl}_3$ )  $\delta$ : 9.81 (s, br, 2H), 3.95 (t,  $J$  = 6.2 Hz, 2H), 3.29 (p,  $J$  = 6.2 Hz, 2H), 2.75 (t,  $J$  = 5.6 Hz, 3H). This spectral data was consistent with the literature reported spectral data.<sup>64</sup>

**Synthesis of 2-(diphenylphosphino)-N-methylethanamine (dppea).** This procedure was adapted from that performed in the literature.<sup>64</sup> A solution of NaOH (88 mg, 2.2 mmol) in THF (10 mL) was prepared in a 25-mL round-bottom flask.  $\text{HN}(\text{Me})(\text{CH}_2)_2\text{Cl}\cdot\text{HCl}$  (0.26 g, 2.0 mmol) was added to this solution and left for 2 hours. A THF solution (10 mL) of  $\text{NaPPh}_2$  (1.1 g, 5.0 mmol) was stirred for 30 min at room temperature. The second solution was added to the first and heated at reflux overnight, whereby the dark red color turned milky white. The solvent was removed under reduced pressure, and the residue was stirred with 10%  $\text{HCl}(\text{aq})$  (10 mL) and washed with diethyl ether (20 mL). The aqueous solution was washed with 10%  $\text{NaOH}(\text{aq})$  (10 mL) and extracted with diethyl ether (20 mL). The organic solution was washed with brine (10 mL), dried over anhydrous  $\text{MgSO}_4$ , and evaporated. The residue was passed through a short alumina plug to give  $\text{HN}(\text{Me})(\text{CH}_2)_2\text{PPh}_2$  as a colorless oil (0.22 g, 0.90 mmol, 74% yield).



This product was dried overnight and brought into the glovebox.  $^1\text{H}$  NMR (500 MHz,  $\text{CDCl}_3$ )  $\delta$ : 7.40 (m, 10H), 2.69 (q,  $J = 8.5$  Hz, 2H), 2.35 (s, 3H), 2.21 (t,  $J = 7.3$  Hz, 2H), 1.07 (s, br, 1H).  $^{31}\text{P}\{^1\text{H}\}$ -NMR (202 MHz,  $\text{CDCl}_3$ )  $\delta$ : -23.6 (s). This spectral data was consistent with the literature reported spectral data.<sup>64</sup>

**Synthesis of trans-[RuCl<sub>2</sub>(dppea)<sub>2</sub>] (3-5).** This procedure was adapted from that performed in the literature.<sup>65</sup> A solution of  $\text{HN}(\text{Me})(\text{CH}_2)_2\text{PPh}_2$  (0.52 g, 2.2 mmol) in toluene (1.5 mL) was added to a stirred mixture of tris(triphenylphosphine)ruthenium(II) dichloride (1.00 g, 1.00 mmol) in toluene (5.0 mL). The mixture was stirred at 100 °C for 6 h, after which time the resulting suspension was allowed to cool and then filtered. The solid was washed with toluene (4 x 20 mL), until the filtrate was colorless, and dried under reduced pressure to give complex trans-[RuCl<sub>2</sub>(dppea)<sub>2</sub>] (0.41 g, 0.60 mmol, 60% yield) as an orange solid.  $^1\text{H}$ -NMR (500 MHz,  $\text{C}_6\text{D}_6$ )  $\delta$ : 7.25–6.95 (m, ArH, 20H), 4.03 (s, br, 2H), 3.40–3.25 (m, 2H), 2.78–2.74 (m, 12 H);  $^{31}\text{P}\{^1\text{H}\}$ -NMR (202 MHz,  $\text{C}_6\text{D}_6$ )  $\delta$ : 60.1 (minor, s) 58.7 (major, s). This spectral data was consistent with the literature reported spectral data.<sup>65</sup>

**Synthesis of 6-Methyl-2-(trimethylstannyl)pyridine.** This procedure was adapted from that performed in the literature.<sup>66</sup> To a dry  $\text{Et}_2\text{O}$  solution of 2-bromo-6-methylpyridine (1.6 mmol, 0.275 g) at -78 °C under nitrogen, a 2.2 M solution of *n*-butyllithium in hexanes (1.6 mmol, 0.727 mL) was added dropwise. The reaction mixture was stirred at -78 °C for 1 h, then a 1 M solution of  $\text{Me}_3\text{SnCl}$  in dry THF was added dropwise (1.7 mmol, 1.7 mL), and the reaction mixture was allowed to warm up to room temperature and was stirred overnight. The solvent was evaporated and the crude reaction mixture was rinsed with diethyl ether; the solid ( $\text{LiCl}$ ) was filtered and the solvent removed

under vacuum to give a pale yellow oil that was used in the next step without further purification (401 mg, 98% yield).  $^1\text{H}$  NMR (500 MHz,  $\text{CDCl}_3$ ):  $\delta$  = 7.78 (t, 1H, H4,  $J$  = 6.1 Hz), 7.50 (m, 2H, H2,H5), 0.24 (s, 9H,  $\text{CH}_3$ ). This spectral data was consistent with the literature reported spectral data.<sup>66</sup>

**Synthesis of 6-bromo-6'-methyl-2,2'-bipyridine.** This procedure was adapted from that performed in the literature.<sup>66</sup> 6-Methyl-2-(trimethylstannyl)pyridine (0.326 g, 1.27 mmol) and degassed toluene (4.5 mL) were added consecutively by syringe to a mixture of 2,6-dibromopyridine (0.301g, 1.27 mmol), LiCl (0.1 g, 2.35 mmol) and  $\text{Pd}(\text{PPh}_3)_4$  (0.23 g, 0.2 mmol), under a nitrogen atmosphere. The reaction was refluxed for 24 h, and the toluene evaporated under reduced pressure. The residue was then purified by column-chromatography on silica gel and eluted with dichloromethane, to afford pale yellow powder (0.203 g, 64% yield).  $^1\text{H}$  NMR (500 MHz,  $\text{CDCl}_3$ ):  $\delta$  = 8.41 (d, 1H, H3,  $J$  = 7.6 Hz), 8.20 (d, 1H, H3',  $J$  = 7.6 Hz), 7.68 (m, 2H, H4, H4',  $J$ =8.8 Hz), 7.48 (d, 1H, H5,  $J$  = 7.3 Hz), 7.20 (d, 1H, H5',  $J$  = 7.0 Hz), 2.53 (s, 3H,  $\text{CH}_3$ ). This spectral data was consistent with the literature reported spectral data.<sup>66</sup>

**Synthesis of UiO-66.** This procedure was adapted from a literature procedure.<sup>67</sup> N,N'-dimethylformamide (DMF) (25 mL) was added to a 45 mL Teflon-lined steel autoclave. Zirconium tetrachloride (241.4 mg, 1.036 mmol) and terephthalic acid (342.8 mg, 2.063 mmol) and concentrated hydrochloric acid (180  $\mu\text{L}$ ) was added to the autoclave, which was then sealed and heated at 220  $^\circ\text{C}$  for 20 hours. The reaction mixture was then allowed to cool to room temperature and agitated to suspend the solid. This solid was isolated by centrifugation, then washed with DMF (15 mL) and left to soak in this solvent overnight. This solid was isolated again by centrifugation and washed twice with methanol

(15 mL), then left to soak overnight in methanol. The solid was isolated by centrifugation and dried in a vacuum chamber overnight, then dried overnight in an oven at 70 °C. Powder X-Ray diffraction traces matched literature precedents.<sup>67</sup>

**Synthesis of “30Benz” and “40Benz” UiO-66.** This synthesis was adapted from literature.<sup>68</sup> The two defective UiO-66 samples (named 30Benz and 40Benz) were synthesized by the same method with different amounts of benzoic acid as a modulator (26.42 g, 216.34 mmol for 30Benz and 35.226 g, 288.45 mmol for 40Benz). ZrCl<sub>4</sub> (1.680 g, 7.209 mmol), deionized water (0.173 mL, 9.603 mmol), benzoic acid (listed above), and terephthalic acid (1.198g, 7.211 mmol) were added to a 1 L Erlenmeyer flask containing warm (ca. 70 °C) N,N'-dimethylformamide (413.2 mL, 5336 mmol) under constant magnetic stirring. Once the reagents had fully dissolved, the stir bars were removed and watch glasses were placed over the mouths of the flasks as a loose cover. The covered synthesis solutions were then placed in an oven preheated to 120 °C and were allowed to react over a period of 24 h. The resulting microcrystalline powder precipitates were separated from their synthesis solutions via centrifugation and soaked overnight in 80 mL of fresh DMF. This was repeated three times at a duration of 2 hours per wash for cycles subsequent to the first before the washed products were separated by centrifugation, dried overnight at 70 °C, and ground with a mortar and pestle.

**Synthesis of Hf-UiO-66.** N,N'-dimethylformamide (DMF) (25 mL) was added to a 45 mL Teflon-lined steel autoclave. Hafnium tetrachloride (331.8 mg, 1.036 mmol) and terephthalic acid (342.8 mg, 2.063 mmol) and concentrated hydrochloric acid (180 µL) was added to the autoclave, which was then sealed and heated at 220 °C for 20 hours. The reaction mixture was then allowed to cool to room temperature and agitated to suspend the

solid. This solid was isolated by centrifugation, then washed with DMF (15 mL) and left to soak in this solvent overnight. This solid was isolated again by centrifugation and washed twice with methanol (15 mL), then left to soak overnight in methanol. The solid was isolated by centrifugation and dried in a vacuum chamber overnight, then dried overnight in an oven at 70 °C. Powder X-Ray diffraction traces matched literature precedents.<sup>65</sup>

**Synthesis of 3-1@UiO-66.** In a nitrogen-filled glovebox, methanol (10 mL) was added to a 20-mL scintillation vial. UiO-66 (200 mg) and **3-1** (5.0 mg, 5.3  $\mu$ mol) were added to the vial, which was then sealed. The vial was brought out of the glovebox and heated at 55 °C with stirring for 24 h, and then allowed to cool to room temperature. The resulting mixture was brought into a glovebox, and the resulting mixture was transferred to a 20 mL scintillation vial and subjected to centrifugation. Trituration was achieved by decanting the supernatant from this mixture, which was set aside for NMR analysis. The remaining solid was further triturated three times with methanol (10 mL), each time using centrifugation to ensure quantitative mass transfer. After three washing cycles, 188 mg of a pale yellow solid (94%) was obtained. This solid was dried overnight in a vacuum chamber. A portion of this material (100 mg) was suspended in 15 mL of degassed DMF, and then transferred as a slurry to a 20 mL ampule containing a stir bar using a 9" glass pipet. 1,8-diazabicyclo[5.4.0]undec-7-ene (DBU) (2.465 mL, 2.505 g, 15.50 mmol) was added to this ampule. The ampule was added to a 450-mL stainless steel Parr reactor. The vessel was purged with carbon dioxide for 5 minutes and then pressurized to 42 psi. The vessel was then pressurized with hydrogen gas to achieve a total pressure of 560 psi at room temperature. The reactor was heated to 129 °C and left to react for 45 minutes. The

heating mantle was removed, the reactor was cooled using a room-temperature water bath, and the pressure was released slowly from the vessel. The vessel was opened and the ampule was removed. The reaction mixture was transferred as a slurry to a 20-mL scintillation vial and subjected to centrifugation at 3000 revolutions per minute for 15 min, after which the supernatant was decanted. The solid was triturated twice with methanol (20 mL) followed by centrifugation and dried overnight in a vacuum chamber to give a pale yellow powder (93 mg, 93%). The loading of catalyst in the MOF was determined by ICP-OES (68 ppm Ru, P/Ru = 2.01, see “Digestion of UiO-66 for ICP-OES analysis”, below). The structural integrity of the solid was confirmed by powder x-ray diffraction.

**Synthesis of 3-2@UiO-66.** In an inert atmosphere glovebox, acetonitrile (10 mL) was added to a 20-mL scintillation vial in a glovebox. UiO-66 (200 mg) and **3-2** (3.0 mg, 6.1  $\mu$ mol) were added to the vial, which was then sealed. This mixture was heated at 55 °C with stirring for five days, and then allowed to cool to room temperature. The resulting mixture was brought into a glovebox. The vial was unsealed, and the resultant mixture was transferred to a 20 mL scintillation vial and subjected to centrifugation. Trituration was achieved by decanting the supernatant from this mixture, which was set aside for NMR analysis. The remaining solid was further triturated three times with methanol (10 mL) each time using centrifugation to ensure quantitative mass transfer. After three washing cycles, 190 mg (95%) of a pale orange solid was obtained. This solid was dried overnight in a vacuum chamber. A portion of this material was suspended in 15 mL of degassed DMF, and then transferred as a slurry to a 20 mL ampule containing a stir bar using a 9” glass pipet. Ethanol (2.92 mL, 50.0 mmol) was added to this ampule. The ampule was added to a 450-mL stainless steel Parr reactor. The vessel was purged with carbon dioxide

for 5 minutes and then pressurized to 42 psi. The vessel was then pressurized with hydrogen gas to achieve a total pressure of 560 psi at room temperature. The reactor was heated to 135 °C and left to react for 16 hours. The heating mantle was removed, the reactor was cooled using a room-temperature water bath, and the pressure was released slowly from the vessel. The vessel was opened and the ampule was removed. The reaction mixture was transferred as a slurry to a 20-mL scintillation vial and subjected to centrifugation at 3000 revolutions per minute for 10 minutes, after which the supernatant was decanted. The solid was triturated twice with methanol (20 mL) followed by centrifugation and dried overnight in a vacuum chamber to give a pale orange powder. The loading of catalyst in the MOF was determined by ICP-OES (84 ppm Ru, P/Ru = 1.81, see Table S2 and “Digestion of UiO-66 for ICP-OES analysis”, below). The structural integrity of the solid was confirmed by powder x-ray diffraction.

**Synthesis of [3-1,3-2]@UiO-66.** In an inert atmosphere glovebox, acetonitrile (10 mL) was added to a 20-mL scintillation vial in a glovebox. **3-1@UiO-66** (100 mg) and **3-2** (3.0 mg, 6.1  $\mu$ mol) were added to the vial, which was then sealed. This mixture was heated at 55 °C with stirring for five days, and then allowed to cool to room temperature. The resulting mixture was brought into a glovebox. The vial was unsealed, and the resulting mixture was transferred to a 20 mL scintillation vial and subjected to centrifugation. Trituration was achieved by decanting the supernatant from this mixture, which was set aside for NMR analysis. The remaining solid was further triturated three times with methanol (10 mL), each time using centrifugation to ensure quantitative mass transfer. After three washing cycles, 180 mg (90%) of a pale beige solid was obtained. This solid was dried overnight in a vacuum chamber. A portion of this material was suspended in 15

mL of degassed DMF, and then transferred as a slurry to a 20 mL ampule containing a stir bar using a 9" glass pipet. Ethanol (2.92 mL, 50.0 mmol) was added to this ampule. The ampule was added to a 450-mL stainless steel Parr reactor. The vessel was purged with carbon dioxide for 5 minutes and then pressurized to 42 psi. The vessel was then pressurized with hydrogen gas to achieve a total pressure of 560 psi at room temperature. The reactor was heated to 135 °C and left to react for 16 hours. The heating mantle was removed, the reactor was cooled using a room-temperature water bath, and the pressure was released slowly from the vessel. The vessel was opened and the ampule was removed. The reaction mixture was transferred as a slurry to a 20-mL scintillation vial and subjected to centrifugation at 3000 revolutions per minute for 10 minutes, after which the supernatant was decanted. The solid was triturated twice with methanol (20 mL) followed by centrifugation and dried overnight in a vacuum chamber to give a pale orange powder. The loading of catalyst in the MOF was determined by ICP-OES (28 ppm Ru, P/Ru = 1.06, see "Digestion of UiO-66 for ICP-OES analysis", below). The structural integrity of the solid was confirmed by powder x-ray diffraction.

**Synthesis of 3-4@UiO-66.** In an inert atmosphere glovebox, methanol (10 mL) was added to a 20-mL scintillation vial in a glovebox. UiO-66 (100 mg) and (<sup>t</sup>BuPNP)IrH<sub>2</sub>Cl (**3**) (5.57 mg, 8.9 μmol) were added to the vial, which was then sealed. This mixture was heated at 55 °C with stirring for 24 h, and then allowed to cool to room temperature. The resulting mixture was brought into a glovebox. The vial was unsealed, and the resultant mixture was transferred to a 20 mL scintillation vial and subjected to centrifugation. Trituration was achieved by decanting the supernatant from this mixture, which was set aside for NMR analysis. The remaining solid was further triturated three times with

methanol (10 mL) each time using centrifugation to ensure quantitative mass transfer. After three washing cycles, 192 mg of a pale red solid (96%) was obtained. This solid was dried overnight in a vacuum chamber. A portion of this material (100 mg) was suspended in 15 mL of degassed DMF, and then transferred as a slurry to a 20 mL ampule containing a stir bar using a 9" glass pipet. 1,8-diazabicyclo[5.4.0]undec-7-ene (DBU) (2.465 mL, 2.505 g, 15.50 mmol) was added to this ampule. The ampule was added to a 450-mL stainless steel Parr reactor. The vessel was purged with carbon dioxide for 5 minutes and then pressurized to 42 psi. The vessel was then pressurized with hydrogen gas to achieve a total pressure of 560 psi at room temperature. The reactor was heated to 129 °C and left to react for 45 minutes. The heating mantle was removed, the reactor was cooled using a room-temperature water bath, and the pressure was released slowly from the vessel. The vessel was opened and the ampule was removed. The reaction mixture was transferred as a slurry to a 20-mL scintillation vial and subjected to centrifugation at 3000 revolutions per minute for 15 min, after which the supernatant was decanted. The solid was triturated twice with methanol (20 mL) followed by centrifugation and dried overnight in a vacuum chamber to give a pale red powder (95 mg, 95%). The loading of catalyst in the MOF was determined by ICP-OES (73 ppm Ir, P/Ir = 2.2, see Table S2 and "Digestion of UiO-66 for ICP-OES analysis", below). The structural integrity of the solid was confirmed by powder x-ray diffraction.

**Synthesis of [3-4,3-2]@UiO-66.** In an inert atmosphere glovebox, acetonitrile (10 mL) was added to a 20-mL scintillation vial in a glovebox. **3**@UiO-66 (100 mg) and **2** (3.0 mg, 6.1  $\mu$ mol) were added to the vial, which was then sealed. This mixture was heated at 55 °C with stirring for five days, and then allowed to cool to room temperature. The



resulting mixture was brought into a glovebox. The vial was unsealed, and the resultant mixture was transferred to a 20 mL scintillation vial and subjected to centrifugation. Trituration was achieved by decanting the supernatant from this mixture, which was set aside for NMR analysis. The remaining solid was further triturated three times with methanol (10 mL) each time using centrifugation to ensure quantitative mass transfer. After three washing cycles, 180 mg (90%) of a pale beige solid was obtained. This solid was dried overnight in a vacuum chamber. A portion of this material was suspended in 15 mL of degassed DMF, and then transferred as a slurry to a 20 mL ampule containing a stir bar using a 9" glass pipet. Ethanol (2.92 mL, 50.0 mmol) was added to this ampule. The ampule was added to a 450-mL stainless steel Parr reactor. The vessel was purged with carbon dioxide for 5 minutes and then pressurized to 42 psi. The vessel was then pressurized with hydrogen gas to achieve a total pressure of 560 psi at room temperature. The reactor was heated to 135 °C and left to react for 16 hours. The heating mantle was removed, the reactor was cooled using a room-temperature water bath, and the pressure was released slowly from the vessel. The vessel was opened and the ampule was removed. The reaction mixture was transferred as a slurry to a 20-mL scintillation vial and subjected to centrifugation at 3000 revolutions per minute for 10 minutes, after which the supernatant was decanted. The solid was triturated twice with methanol (20 mL) followed by centrifugation and dried overnight in a vacuum chamber to give a pale orange powder. The loading of catalyst in the MOF was determined by ICP-OES (73 ppm Ir, 16 ppm Ru, P/Ir = 2.22, P/Ru = 10.10, see Table S2 and "Digestion of UiO-66 for ICP-OES analysis", below). The structural integrity of the solid was confirmed by powder x-ray diffraction.

**Digestion of UiO-66 for ICP-OES analysis.** Solid MOF material (5.00 mg) was weighed into a 1.5 mL Teflon vial. DMSO (300  $\mu$ L) and 1 drop of 15 wt.% aqueous hydrofluoric acid solution were added in sequence. The mixture was sonicated for 1 minute and left to digest for 1 hour. The digested samples then heated to approximately 150 °C overnight in a sand bath open to the air to remove solvent. The resulting solid was dissolved and transferred to a 20 mL glass scintillation vial using a mixture (10% v/v) of hydrochloric acid in deionized water (300  $\mu$ L). Each sample was diluted with additional deionized water (3.7 mL) and analyzed by ICP-OES.

**ICP-OES Standard preparation.** Five standards were prepared by dilution from commercially available zirconium ( $999 \pm 5$  ppm), ruthenium ( $999 \pm 5$  ppm), iridium ( $999 \pm 3$  ppm), and phosphorus ( $100.04 \pm 0.55$  ppm) standards using serial dilution in grade A volumetric glassware to cover the expected concentration ranges. The standards were then employed in a calibration curve to determine the loading of catalyst in a tested solid. These standards consisted of Zr/Ru/Ir/P concentrations in ppm at the proportions: 250/5/5/5, 150/2/2/2, 25/0.5/0.5/0.5, 2.5/0.05/0.05/0.05.

**Esterification of Formic acid using UiO-66 as a Lewis acid catalyst.** UiO-66 (10 mg) was weighed out and added to a 20-mL scintillation vial. Anhydrous N,N'-dimethylformamide or 1,4-dioxane (3 mL) was added to this vial. Formic acid (0.337 mL, 10.0 mmol) and alcohol additive (10.0 mmol) were added to this mixture. The vial was sealed and heated at 80 °C for 4 h. The supernatant was separated by centrifugation. An aliquot of the reaction mixture (0.25 mL), 1,1,2,2-tetrachloroethane (0.01 mL), and  $\text{CDCl}_3$  (0.45 mL) were each added to a small vial. This mixture was then added to an NMR tube

using a 9" glass pipet. Percent conversion was determined by  $^1\text{H}$ -NMR using 1,1,2,2-tetrachloroethane as an external standard.

**General procedure for cascade hydrogenation of  $\text{CO}_2$  to methanol.**

Encapsulated catalyst (10 mg) was weighed out and added to a 20-mL scintillation vial. Exogenous catalyst ( $2.23 \times 10^{-7}$  mmol, diluted on bench with anhydrous DMF) was weighed out in a glovebox and added to a 4-mL scintillation vial. These vials were sealed and removed from the glovebox. Anhydrous N,N'-dimethylformamide (3 mL) was added to the 4-mL vial. The hybrid catalyst was suspended in this solution and wet-transferred to a 5-mL ampule using a glass 9" pipet. Alcohol additive (10.0 mmol) was added to this ampule. The ampule was added to a 450-mL stainless steel Parr instrument pressure vessel. The vessel was purged with  $\text{CO}_2$  for 5 minutes and then pressurized to 42 psi, then pressurized with  $\text{H}_2$  to 560 psi at room temperature. The reactor was heated slowly to  $70^\circ\text{C}$  and left to react for 16 hours. Upon conclusion of the reaction, the heating mantle was removed, the reactor was cooled using a room-temperature water bath, and the pressure was released slowly from the vessel. The vessel was opened and the ampules were removed. The reaction mixtures were wet-transferred to 20-mL scintillation vials and subjected to centrifugation at 3000 revolutions per minute for 10 min, after which the supernatants were decanted and set aside. An aliquot of the reaction mixture (0.25 mL), tetrachloroethane (0.01 mL), and  $\text{CDCl}_3$  (0.45 mL) were each added to a small vial. This mixture was then added to an NMR tube using a 9" glass pipet. TON was determined by  $^1\text{H}$ -NMR using tetrachloroethane as an external standard.

**$\text{CO}_2$  hydrogenation with 3-5.** This procedure was adapted from that performed in the literature.<sup>13</sup> In a glove box, **3-5** (0.80 mg,  $1.3 \mu\text{mol}$ ) and sodium ethoxide (2.5 mg,  $0.040$

mmol) were weighed in a 7-mL scintillation vial in a glovebox. Toluene (2.5 mL) was added and the contents were transferred into an oven-dried 5-mL glass ampule. Diisopropylamine (0.5 mL) was then added to the ampule. This was repeated two additional times. The ampules were added to a 450-mL stainless steel Parr instrument pressure vessel. The vessel was then pressurized with CO<sub>2</sub> to the specified pressure, then pressurized with H<sub>2</sub> to the specified pressure at room temperature. The reactor was heated slowly to the specified temperature and left to react for the specified time period. Upon conclusion of the reaction, the heating mantle was removed, the reactor was cooled using a room-temperature water bath, and the pressure was released slowly from the vessel. The vessel was opened and the ampules were removed. The reaction mixtures were transferred to 4-mL scintillation vials. An aliquot of each reaction mixture (0.25 mL), tetrachloroethane (0.01 mL), and CDCl<sub>3</sub> (0.45 mL) were each added to separate small vials. These mixtures were then added to NMR tubes using 9" glass pipets. TON was determined by <sup>1</sup>H-NMR using tetrachloroethane as an external standard.

**Exposure of formic acid to hydrogenation conditions in the absence of additive.** Encapsulated catalyst (10 mg) was weighed out and added to a 20-mL scintillation vial. Exogenous catalyst ( $2.23 \times 10^{-7}$  mmol, diluted on bench with anhydrous DMF) was weighed out in a glovebox and added to a 4-mL scintillation vial. These vials were sealed and removed from the glovebox. Anhydrous N,N'-dimethylformamide (3 mL) was added to the 4-mL vial. The hybrid catalyst was suspended in this solution and wet-transferred to a 5-mL ampule using a glass 9" pipet. Formic acid (10.0 mmol) was added to this ampule. The ampule was added to a 450-mL stainless steel Parr instrument pressure vessel. The vessel was purged with CO<sub>2</sub> for 5 minutes and then pressurized to 42 psi, then

pressurized with H<sub>2</sub> to 560 psi at room temperature. The reactor was heated slowly to 70 °C and left to react for 16 hours. Upon conclusion of the reaction, the heating mantle was removed, the reactor was cooled using a room-temperature water bath, and the pressure was released slowly from the vessel. The vessel was opened and the ampules were removed. The reaction mixtures were wet-transferred to 20-mL scintillation vials and subjected to centrifugation at 3000 revolutions per minute for 10 min, after which the supernatants were decanted and set aside. An aliquot of the reaction mixture (0.25 mL), tetrachloroethane (0.01 mL), and CDCl<sub>3</sub> (0.45 mL) were each added to a small vial. This mixture was then added to an NMR tube using a 9" glass pipet and analyzed.

**Quantification of byproducts in reaction headspace.** **3-1@UiO-66** (10 mg) was weighed out and added to a 20-mL scintillation vial. **3-2** ( $2.23 \times 10^{-7}$  mmol, diluted on bench with anhydrous DMF) was weighed out in a glovebox and added to a 4-mL scintillation vial. This vial was sealed and removed from the glovebox. Anhydrous N,N'-dimethylformamide (3 mL) was added to the 4-mL vial. The hybrid catalyst was suspended in this solution and wet-transferred to a 5-mL ampule using a glass 9" pipet. 2,2,2-trifluoroethanol (10.0 mmol) was added to this ampule. The ampule was added to a 450-mL stainless steel Parr instrument pressure vessel. The vessel was purged with CO<sub>2</sub> for 5 minutes and then pressurized to 42 psi, then pressurized with H<sub>2</sub> to 560 psi at room temperature. The reactor was heated slowly to 70 °C and left to react for 16 hours. Upon conclusion of the reaction, the heating mantle was removed and the reactor was cooled using a room-temperature water bath. The pressure in the reactor was released through airtight rubber tubing into a two-necked flask under vacuum equipped with a 180-degree joint. This headspace was sampled using a gastight syringe (0.5 mL) and was analyzed

using a Gas Chromatograph equipped with a methanizer and FID detector and quantified based on standards of 1 ppm, 10 ppm, and 50 ppm of carbon monoxide in nitrogen and compared to the headspace from exposure of the empty reactor to reaction conditions. The Parr vessel was opened and the ampule was removed. The reaction mixture was transferred to a 4-mL scintillation vial. An aliquot of the reaction mixture (0.25 mL), tetrachloroethane (0.01 mL), and  $\text{CDCl}_3$  (0.45 mL) was added to this vial. This mixture was then added to an NMR tube using a 9" glass pipet. TON was determined by  $^1\text{H}$ -NMR using tetrachloroethane as an external standard. This experiment was repeated three times for the determination of average error

**Recycling of 3-1@UiO-66 + 3-2@UiO-66.** 3-1@UiO-66 ( $5.60 \times 10^{-7}$  mmol Ru) and 3-2@UiO-66 ( $5.60 \times 10^{-7}$  mmol Ru) were weighed out separately. Carbon dioxide hydrogenation was carried out using the "general procedure for cascade hydrogenation of  $\text{CO}_2$  to methanol" at 5x scale in a 20-mL ampule. The solid was washed twice with methanol (20 mL) and dried overnight in a vacuum chamber between cycles.

**Recycling of [3-1,3-2]@UiO-66.** [3-1,3-2]@UiO-66 was weighed out in a 20-mL scintillation vial. Carbon dioxide hydrogenation was carried out using the "general procedure for cascade hydrogenation of  $\text{CO}_2$  to methanol" at 5x scale in a 20-mL ampule. The solid was washed twice with methanol (20 mL) and dried overnight in a vacuum chamber between cycles.

## References:

1. M. Calvin. The photosynthetic cycle. *Bull. Soc. Chim. Biol.* **38**, 1233–1244. (1956).
2. J. Chen, X. Gong, J. Li, Y. Li, J. Ma, C. Hou, G. Zhao, W. Yuan, B. Zhao. Carbonyl catalysis enables a biomimetic asymmetric Mannich reaction. *Science*. **360**, 1438-1442. (2018).
3. S. M. Morrow, I. Colomer, S. P. Fletcher. A chemically fuelled self-replicator. *Nat. Commun.* **10**, Article number:1011. DOI: 10.1038/s41467-019-08885-9. (2019).
4. C. Liu, B. E. Colón, P. A. Silver, D. G. Nocera. Solar-powered CO<sub>2</sub> reduction by a hybrid biological/inorganic system. *J. Photoch. Photobio. A*. **358**, 411-415. (2018).
5. M. L. Helm, M. P. Stewart, R. M. Bullock, M. R. DuBois, D. L. DuBois. A synthetic nickel electrocatalyst with a turnover frequency above 100,000 s<sup>-1</sup> for H<sub>2</sub> production. *Science*. **333**, 863-866. (2011).
6. S. A. Chabolla, C. W. Machan, J. Yin, E. A. Dellamary, S. Sahu, N. C. Gianneschi, M. K. Gilson, F. A. Tezcan, C. P. Kubiak. Bio-inspired CO<sub>2</sub> reduction by a rhenium tricarbonyl bipyridine-based catalyst appended to amino acids and peptidic platforms: incorporating proton relays and hydrogen-bonding functional groups. *Faraday Discuss.* **198**, 279-300. (2017).
7. S. L. Foster, S. I. P. Bakovic, R. D. Duda, S. Maheshwari, R. D. Milton, S. D. Minter, M. J. Janik, J. N. Renner, L. F. Greenlee. Catalysts for nitrogen reduction to ammonia. *Nat. Catal.* **1**, 490-500. (2018).
8. B. An, Z. Li, Y. Song, J. Zhang, L. Zeng, C. Wang, W. Lin. Cooperative copper centres in a metal-organic framework for selective conversion of CO<sub>2</sub> to ethanol. *Nat. Catal.* **2**, 709–717. (2019).
9. C. G. S. Lima, N. M. Moreira, M. W. Paixão, A. G. Corrêa. Heterogenous green catalysis: application of zeolites on multicomponent reactions. *Curr. Opin. Green Sustain. Chem.* **15**, 7-12. (2019).
10. M. J. Climent, A. Corma, S. Iborra. Homogeneous and heterogeneous catalysts for multicomponent reactions. *RSC Adv.* **2**, 16-69. (2012).
11. A. Bruggink, R. Schoevaart, T. Kieboom. Concepts of nature in organic synthesis: cascade catalysis and multistep conversions in concert. *Org. Process Res. Dev.* **5**, 622-640. (2003).
12. H. Furukawa, K. E. Cordova, M. O’Keefe, O. M. Yaghi. (2013). The chemistry and applications of metal-organic frameworks. *Science*. **341**, 1230444. DOI: 10.1126/science.1230444. (2013).
13. M. Everett, D. F. Wass. Highly productive CO<sub>2</sub> hydrogenation to methanol – a tandem catalytic approach via amide intermediates. *Chem. Commun.* **53**, 9502-9504. (2017).
14. S. Kar, R. Sen, J. Kothandaraman, A. Goeppert, R. Chowdhury, S. B. Munoz, R. Haiges, G. K. S. Prakash. Mechanistic insights into ruthenium-pincer-catalyzed

- amine-assisted homogeneous hydrogenation of CO<sub>2</sub> to methanol. *J. Am. Chem. Soc.* **141**, 3160-3170. (2019).
15. A. P. C. Ribeiro, L. M. D. R. S. Martins, A. J. L. Pombeiro. Carbon dioxide-to-methanol single-pot conversion using a C-scorpionate iron(II) catalyst. *Green Chem.* **19**, 4811-4815. (2017).
  16. S. Chu, W. Li, Y. Yan, T. Hamann, I. Shih, D. Wang, Z. Mi. Roadmap on solar water splitting: current status and future prospects. *Nano Futures.* **1**, 022001. DOI: 10.1088/2399-1984/aa88a. (2017).
  17. G. A. Olah, A. Goeppert, G. K. S. Prakash. Chemical recycling of carbon dioxide to methanol and dimethyl ether: from greenhouse gas to renewable, environmentally carbon neutral fuels and synthetic hydrocarbons. *J. Org. Chem.* **74**, 487-498. (2009).
  18. B. M. Tackett, E. Gomez, J. G. Chen. Net reduction of CO<sub>2</sub> via its thermocatalytic and electrocatalytic transformation reactions in standard and hybrid processes. *Nat. Catal.* **2**, 381-386. (2019).
  19. W.-H. Wang, Y. Himeda, J. T. Muckerman, G. F. Manbeck, E. Fujita. CO<sub>2</sub> hydrogenation to formate and methanol as an alternative to photo- and electrochemical CO<sub>2</sub> reduction. *Chem. Rev.* **115**, 12936-12973. (2015).
  20. S. Roy, A. Cherevotan, S. C. Peter. Thermochemical CO<sub>2</sub> Hydrogenation to single carbon products: scientific and technological challenges. *ACS Energy Lett.* **3**, 1938-1966. (2018).
  21. M. R. Gogate. Methanol synthesis revisited: reaction mechanisms in CO/CO<sub>2</sub> hydrogenation over Cu/ZnO and DFT analysis. *Pet. Sci. Technol.* **37**, 603-610. (2019).
  22. J. E. Heimann, W. H. Bernskoetter, N. Hazari. Understanding the individual and combined effects of solvent and Lewis acid on CO<sub>2</sub> insertion into a metal hydride. *J. Am. Chem. Soc.* **141**, 10520-10529. (2019).
  23. R. Tanaka, M. Yamashita, K. Nozaki. Catalytic hydrogenation of carbon dioxide using Ir(III) pincer complexes. *J. Am. Chem. Soc.* **131**, 14168-14169. (2009).
  24. H. Valdés, M. A. García-Eleno, D. Canseco-Gonzalez, D. Morales-Morales. Recent advances in catalysis with transition-metal pincer compounds. *ChemCatChem.* **10**, 3136-3172. (2018).
  25. E. S. Wiedner, J. C. Linehan. Making a splash in Homogeneous CO<sub>2</sub> hydrogenation: elucidating the impact of solvent on catalytic mechanisms. *Chem Eur. J.* **24**, 16964-16971. (2018).
  26. G. A. Filonenko, R. Van Putten, E. N. Schulpen, E. J. M. Hensen, E. A. Pidko. Highly efficient reversible hydrogenation of carbon dioxide to formates Using a ruthenium PNP-pincer catalyst. *ChemCatChem.* **6**, 1526-1530. (2014).
  27. S. Kar, J. Kothandaraman, A. Goeppert, G. K. S. Prakash. Advances in catalytic homogeneous hydrogenation of carbon dioxide to methanol. *J. CO<sub>2</sub> Util.* **23**, 212-218. (2018).



28. N. M. Rezayee, C. A. Huff, M. S. Sanford. Tandem amine and ruthenium-catalyzed hydrogenation of CO<sub>2</sub> to methanol. *J. Am. Chem. Soc.* **137**, 1028-1031. (2015).
29. J. Kothandaraman, A. Goeppert, M. Czaun, G. A. Olah, G. K. S. Prakash. Conversion of CO<sub>2</sub> from air into methanol using a polyamine and a homogeneous ruthenium catalyst. *J. Am. Chem. Soc.* **138**, 778-781. (2016).
30. S. Wesselbaum, V. Moha, M. Meuresch, S. Brosinski, K. M. Thenert, J. Kothe, T. vom Stein, U. Englert, M. Hölscher, J. Klankermeyer, W. Leitner. Hydrogenation of carbon dioxide to methanol using a homogeneous ruthenium–triphos catalyst: from mechanistic investigations to multiphase catalysis. *Chem. Sci.* **6**, 693-704. (2014).
31. C. A. Huff, M. S. Sanford. Cascade catalysis for the homogeneous hydrogenation of CO<sub>2</sub> to methanol. *J. Am. Chem. Soc.* **133**, 18122-18125. (2011).
32. W.-Y. Chu, Z. Culakova, B.-T. Wang, K. I. Goldberg. Acid-Assisted Hydrogenation of CO<sub>2</sub> to Methanol in a Homogeneous Catalytic Cascade System. *ACS Catal.* **9**, 9317-9326. (2019).
33. K. Ahmad, S. Upadhyayula. Greenhouse gas CO<sub>2</sub> hydrogenation to fuels: a thermodynamic analysis. *Environ. Prog. Sustain.* **38**, 98-111. (2018).
34. Y.-B. Huang, J. Liang, X.-S. Wang, R. Cao. Multifunctional metal-organic framework catalysts: synergistic catalysis and tandem reactions. *Chem. Soc. Rev.* **46**, 126-157. (2017).
35. L. Chen, Q. Xu. Metal-organic framework composites for catalysis. *Matter.* **1**, 57-89. (2019).
36. Z. Li, T. M. Rayder, L. Luo, J. A. Byers, C.-K. Tsung. Aperture-opening encapsulation of a transition metal catalyst in a metal–organic framework for CO<sub>2</sub> hydrogenation. *J. Am. Chem. Soc.* **140**, 8082-8085. (2018).
37. M. Mon, R. Adam, J. Ferrando-Soria, A. Corma, D. Armentano, E. Pardo, A. Leyva Pérez. Stabilized Ru[(H<sub>2</sub>O)<sub>6</sub>]<sup>3+</sup> in Confined Spaces (MOFs and Zeolites) Catalyzes the Imination of Primary Alcohols under Atmospheric Conditions with Wide Scope. *ACS Catal.* **8**, 10401-10406. (2018).
38. J.-S. Qin, S. Yuan, C. Lollar, J. Pang, A. Alsalme, H.-C. Zhou. Stable metal-organic frameworks as a host platform for catalysis and biomimetics. *Chem. Commun.* **54**, 4231-4249. (2018).
39. C. T. Buru, M. C. Wasson, O. K. Farha. H<sub>5</sub>PV<sub>2</sub>Mo<sub>10</sub>O<sub>40</sub> Polyoxometalate Encapsulated in NU-1000 Metal-Organic Framework for Aerobic Oxidation of a Mustard Gas Simulant. *ACS Appl. Nano Mater.* **3**, 658-664. (2020).
40. M. Kim, J. F. Cahill, H. Fei, K. A. Prather, S. M. Cohen. Postsynthetic ligand and cation exchange in robust metal–organic frameworks. *J. Am. Chem. Soc.* **134**, 18082-18088. (2012).
41. J. V. Morabito, L.-Y. Chou, Z. Li, C. M. Manna, C. A. Petroff, R. J. Kyada, J. M. Palomba, J. A. Byers, C.-K. Tsung. Molecular encapsulation beyond the aperture size limit through dissociative linker exchange in metal-organic framework crystals. *J. Am. Chem. Soc.* **136**, 12540-12543. (2014).

42. O. Karagiari, W. Bury, J. E. Mondloch, J. T. Hupp, O. K. Farha. Solvent-assisted linker exchange: an alternative to the de novo synthesis of unattainable metal-organic frameworks. *Angew. Chem. Int. Edit.* **53**, 4530-4540. (2014).
43. J. H. Cavka, S. Jakobsen, U. Olsbye, N. Guillou, C. Lamberti, S. Bordiga, K. P. Lillerud. A new zirconium inorganic building brick forming metal organic frameworks with exceptional stability. *J. Am. Chem. Soc.*, **130**, 13850-13851. (2008).
44. F. G. Cirujano, A. Corma, F. X. Llabres i Xamena. Conversion of levulinic acid into chemicals: synthesis of biomass derived levulinate esters over Zr-containing MOFs. *Chem. Eng. Sci.* **124**, 52-60. (2015).
45. C. Atzori, G. C. Shearer, L. Maschio, B. Civalieri, F. Bonino, C. Lamberti, S. Svelle, K. P. Lillerud, S. Bordiga. Effect of Benzoic Acid as a Modulator in the Structure of UiO-66: An Experimental and Computational Study. *J. Phys. Chem. C* **121**, 9312-9324. (2017)
46. E. S. Domalski, E. D. Hearing. Estimation of the thermodynamic properties of C-H-N-O-S-halogen compounds at 298.15 K. *J. Phys. Chem. Ref. Data.* **22**, 805-1159. (1993).
47. J. B. Smith, H. Byrd, S. E. O'Donnell, W. Davis. Hammett parameter and molecular-modeling correlations of substituent effects on esterification kinetics. *J. Chem. Educ.* **87**, 845-847. (2010).
48. W. Hordijk, M. Steel, S. A. Kauffman. Molecular Diversity Required for the Formation of Autocatalytic Sets. *Life*, **9**, 23-36. (2019).
49. A.O. Konuray, X. Fernández-Francos, X. Ramis. Analysis of the reaction mechanism of the thiol-epoxy addition initiated by nucleophilic tertiary amines. *Polym. Chem.* **8**, 5934-5947. (2017).
50. F. C. Frank. On spontaneous asymmetric synthesis. *Biochim. Biophys. Acta.* **11**, 459-463. (1953).
51. J. W. Moore, R.G. Pearson. *Kinetics and Mechanism*. p.26. Wiley. (1981).
52. K. Soai, T. Shibata, H. Morioka, K. Choji. Asymmetric autocatalysis and amplification of enantiomeric excess of a chiral molecule. *Nature*, **378**, 767-768. (1995).
53. J. I. Steinfeld, J. S. Francisco, W. L. Hase. *Chemical Kinetics and Dynamics*. 2nd ed., Prentice-Hall. p.151. (1999).
54. R. Plasson, A. Brandenburg, L. Jullien, H. Bersini. Autocatalyses. *J. Phys. Chem. A*. **115**, 8073-8085. (2011).
55. A. J. Bissette, S. P. Fletcher. Mechanisms of Autocatalysis. *Angew. Chem. Int. Ed.* **52**, 12800-12826. (2013).
56. S. N. Semenov, L. J. Kraft, A. Ainla, M. Zhao, M. Baghbanzadeh, C. E. Campbell, K. Kang, J. M. Fox, G. M. Whitesides. Autocatalytic, bistable, oscillatory networks of biologically relevant organic reactions. *Nature*. **537**, 656-660. (2016).
57. S. N. Semenov, L. Belding, B. J. Cafferty, M. P. S. Mousavi, A. M. Finogenova, R. S. Cruz, E. V. Skorb, G. M. Whitesides. Autocatalytic Cycles in a Copper-Catalyzed Azide-Alkyne Cycloaddition Reaction. *J. Am. Chem. Soc.* **140**, 10221-10232. (2018).
58. E. J. McMurchie, W. McGlasson, I. Eaks. Treatment of Fruit with Propylene gives Information about the Biogenesis of Ethylene. *Nature*. **237**, 235-236. (1972).

59. B. J. Burger, J. E. Bercaw. "Vacuum line techniques for handling air-sensitive organometallic compounds" in *Experimental Organometallic Chemistry*, A. L. Wayda, M. Y. Darensbourg. Eds. (ACS). ACS Symposium Series 357, pp 79-115. (1987).
60. D. Hermann, M. Gandelman, H. Rozenberg, L. J. W. Shimon, D. Milstein. Synthesis, structure, and reactivity of new rhodium and iridium complexes, bearing a highly electron-donating PNP System. Iridium-mediated vinylic C–H bond activation. *Organometallics*. **21**, 812-818. (2002).
61. B. Gnanaprakasam, J. Zhang, D. Milstein. Direct synthesis of imines from alcohols and amines with liberation of H<sub>2</sub>. *Angew. Chem., Int. Ed.* **49**, 1468-1471. (2010).
62. T. Garber, S. V. Wallendacl, D. P. Rillema, M. Kirk, W. Hatfield, J. H. Welch, P. Singh. A novel copper(II) complex containing the ligand 1,2-bis(2,2'-bipyridyl-6-yl)ethane: structural, magnetic, redox, and spectral properties. *Inorg. Chem.* **29**, 2863-2868. (1990).
63. E. Balaraman, B. Gnanaprakasam, L. J. W. Shimon, D. Milstein. Direct hydrogenation of amides to alcohols and amines under mild conditions. *J. Am. Chem. Soc.*, **132**, 16756-16758. (2010).
64. Y. Shaikh, J. Gurnham, K. Albahily, S. Gambarotta, I. Korobkov. Aminophosphine-based chromium catalysts for selective ethylene tetramerization. *Organometallics*. **31**, 7427-7433. (2012).
65. R. L. Wingad, E. J. E. Bergström, M. Everett, K. J. Pellowa, D. F. Wass. Catalytic conversion of methanol/ethanol to isobutanol – a highly selective route to an advanced biofuel. *Chem. Commun.* **52**, 5202-5204. (2016).
66. V. Patroniak, M. Kubicki, A. R. Stefankiewicz, A. M. Grochowska. Preparation of new heterotopic ligands. *Tetrahedron*, **61**, 5475-5480. (2005).
67. G. C. Shearer, S. Chavan, J. Ethiraj, J. G. Vitillo, S. Svelle, U. Olsbye, C. Lamberti, S. Bordiga, K. P. Lillerud. Tuned to Perfection: Ironing Out the Defects in Metal–Organic Framework UiO-66. *Chem. Mater.* **26**, 4068-4071. (2014).
68. C. Atzori, G. C. Shearer, L. Maschio, B. Civalieri, F. Bonino, C. Lamberti, S. Svelle, K. P. Lillerud, S. Bordiga. Effect of Benzoic Acid as a Modulator in the Structure of UiO-66: An Experimental and Computational Study. *J. Phys. Chem. C* **121**, 9312-9324. (2017).

## 4.0 CHAPTER 4

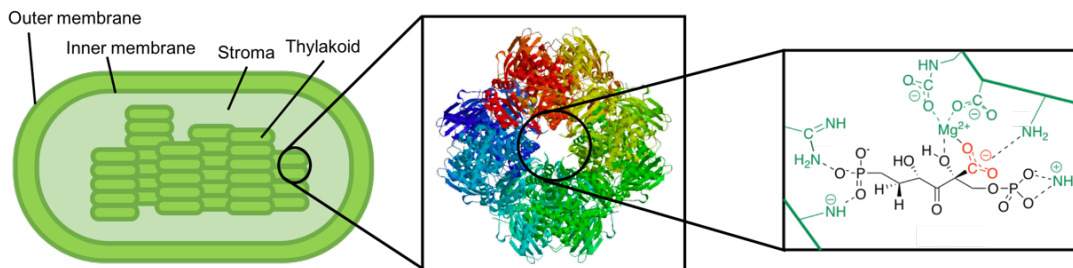
### Manipulation of Noncovalent Host-Guest Interactions in a Catalyst@MOF Hybrid for Unprecedented Activity in CO<sub>2</sub> Hydrogenation to Methanol

As described in previous chapters, the high activity and selectivity of catalytic processes in natural systems frequently inspires the development of synthetic catalysts.<sup>1</sup> Some of this inspiration is taken from the specific interactions between enzyme and substrate that have significant impact on the activity and selectivity of enzymatic transformations.<sup>2</sup> However, bestowing synthetic catalysts with the same activity and selectivity as enzymes still presents a significant challenge.<sup>3-5</sup> Though synthetic chemists have developed excellent tools for control over direct catalyst interaction with substrates, control over the indirect interactions characteristic of enzymes has not been as extensively explored, restricting the applicable degree of control over these systems.

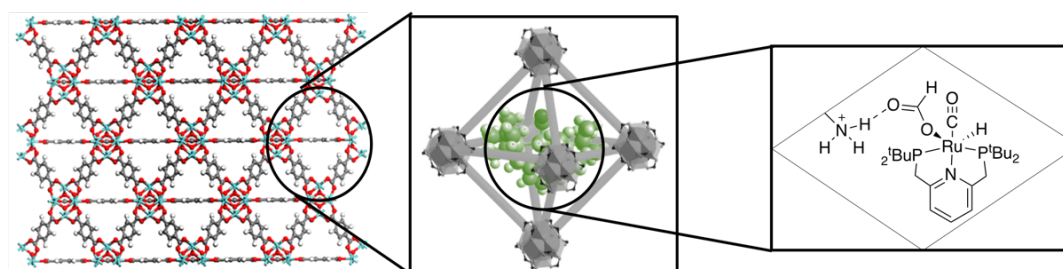
The protein superstructures present in enzymes have served as templates for host-guest systems in their immobilization of active sites and control of active site geometry (Scheme 4-1, top). Some catalytic host-guest systems have been developed from these templates, with hosts including supramolecular cages,<sup>6</sup> zeolites,<sup>7</sup> and MOFs.<sup>8</sup> Previous developments made toward active site sequestration<sup>9</sup> and multicomponent catalytic transformations<sup>10</sup> in MOFs are described in this thesis in Chapters 2 and 3, respectively. However, most catalytic systems are optimized based entirely on inner sphere effects on the active site. Noncovalent interactions can precisely control the geometry of enzyme

active sites,<sup>11</sup> and control over analogous interactions in synthetic host-guest systems offers an additional handle for optimization.<sup>12-15</sup>

**Natural system: RuBisCo**



**This work: [Ru-PNP]@UiO-66-NH<sub>2</sub><sup>±</sup>**

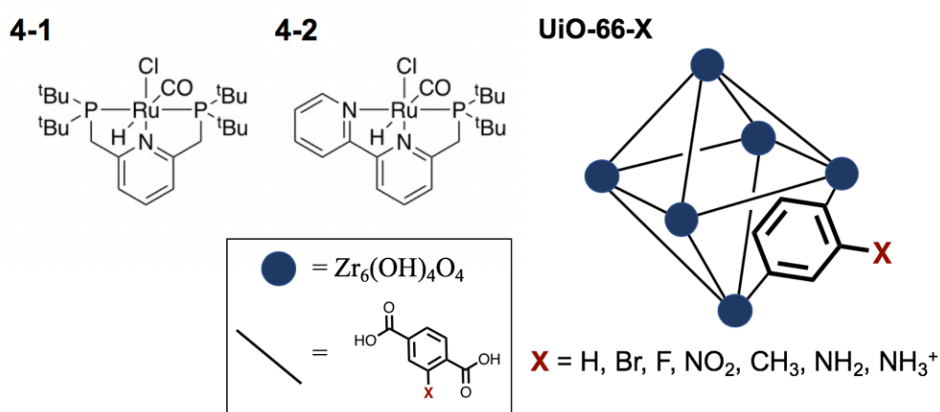


**Scheme 4-1.** Comparison of natural system for CO<sub>2</sub> reduction to fuel (top) to the developed system (bottom)

While noncovalent interactions have been manipulated in molecular catalysts by modulating ligand design,<sup>16-18</sup> this can be synthetically demanding and can negatively affect the steric and electronic influences of the ligand on the coordinated transition metal. Alternatively, these interactions have been explored for a range of applications in porous hosts. In supramolecular cages, the most successful example of outer-sphere control resulted in increased enantioselectivity.<sup>19</sup> Outer-sphere influence has also been explored for photocatalysis in zeolites,<sup>20</sup> but most cases where noncovalent interactions are manipulated in zeolites are in pursuit of novel adsorption properties.<sup>21</sup> Furthermore, the necessary modifications to these hosts in order to screen their properties systematically is synthetically demanding: modifications to supramolecular cages require bottom-up

synthesis of new organic ligands<sup>22</sup> and zeolite modification is often restricted by the strong bonding between the components comprising the porous aluminosilicate superstructure.<sup>23</sup>

MOFs offer a promising alternative to these hosts, with a variety of organic functionalities comprising the library of linkers present in stable structures.<sup>24</sup> Additionally, some MOFs can be modified post-synthetically, allowing for further modulation.<sup>25</sup> In particular, many functionalized analogues of the zirconium-terephthalate framework UiO-66 have been reported,<sup>26</sup> with improved catalytic properties accessible through the introduction of functionalized terephthalic acid derivatives.<sup>27</sup> Furthermore, the structural stability of these derivatives allows for additional modification after functionality has been introduced, including cross-linking of separate MOF structures with polymers<sup>28</sup> and the tethering of organometallic complexes to the ligands.<sup>29</sup>



**Scheme 4-2.** Diagram of components used in catalysis in this work

This modularity was utilized to develop a range of functionalized catalyst@MOF hybrids and assess the effect of outer-sphere functionality on catalytic conversion of carbon dioxide to methanol (Scheme 4-1, bottom). The catalytic system studied here (Scheme 4-2) employs the same components utilized in Chapter 3: ruthenium-PNP complex **4-1** for carbon dioxide hydrogenation, UiO-66 for esterification, and ruthenium PNN complex **4-**

**2** for ester reduction in order to affect the cascade hydrogenation of CO<sub>2</sub> to methanol. This systematic study takes advantage of the modularity of the aperture-opening encapsulation method described in Chapter 2 to test the effect of functional derivatives (UiO-66-X) on the activity of the multicomponent system. Such a study is not feasible in hosts where functional modification is more synthetically demanding. As a result, component manipulation could be applied based on an in-depth understanding of the mechanism of each catalytic cycle in the reaction. With this mechanistic understanding, optimal activity was achieved using the construct **4-1@UiO-66-NH<sub>3</sub><sup>+</sup>**, which exhibited the highest reported turnover number and turnover frequency for hydrogenation of CO<sub>2</sub> to methanol involving a homogeneous catalyst.<sup>30,31</sup> Further improvement was made through full heterogenization, demonstrating recyclability through ten cycles and an unprecedented turnover number achieved as a result of iterative logical optimization of the multicomponent catalytic system.

#### **4.1 IMPROVING CATALYTIC ACTIVITY BY INTRODUCING OUTER- SPHERE FUNCTIONALITY**

In order to improve catalytic activity using noncovalent effects, it is important to understand the nature of these effects and the identity of functionalities that can have such an influence. While the multicomponent nature of such a system obscures the identification of the exact operative functional group, understanding can be gained through interpretation of the catalytic behavior resulting from systematic changes. Previous results illustrated that a functional group introduced in the UiO-66 cage can influence the fluorescence properties

of an encapsulated dye.<sup>32</sup> The same introduced functionality might also have an effect on catalytic turnover. As such, it was necessary to determine whether the activity of the cascade system changed when different functionalities were introduced to the MOF host. Varying the functionalized linker used in the synthesis of UiO-66-X (X = H, Br, F, 4F, CH<sub>3</sub>, NO<sub>2</sub>, NH<sub>2</sub>, NHMe, NMe<sub>2</sub>, NH<sub>3</sub><sup>+</sup>, NH<sub>2</sub>Me<sup>+</sup>, NHMe<sub>2</sub><sup>+</sup>, (NH<sub>3</sub><sup>+</sup>)<sub>2</sub>) in the cascade reduction of carbon dioxide to methanol, the potential for improvement in catalytic performance through modulation of functionality was probed and specific trends in activity that arose were further investigated.

#### 4.1.1 Investigating the effect of linker functionality on catalytic activity

Previous reports indicated that functionality introduced to the host framework might improve catalytic turnover. This hypothesis was first tested by application of a range of functionalized hosts to the full cascade reaction. To this end, **4-1** was encapsulated in various UiO-66 derivatives and tested in the cascade production of methanol from carbon dioxide in tandem with **4-2** in solution (Table 4-1, entries 1-8). In addition to unfunctionalized UiO-66 (entry 1), frameworks bore the functionalities of -CH<sub>3</sub>, -F (and perfluorinated), -Br, -NO<sub>2</sub>, and -NH<sub>2</sub> (entries 2-7). With the exception of -NH<sub>2</sub>, there was no significant change in TON with the functionality installed on the terephthalic acid linker. When this amine-functionalized hybrid catalyst was treated with HCl in DMSO and applied in the cascade reaction, the resulting catalyst **4-1@UiO-66-NH<sub>3</sub><sup>+</sup>** exhibited the highest activity of any construct tested (entry 8).

The positive influence of both basic (-NH<sub>2</sub>) and acidic (-NH<sub>3</sub><sup>+</sup>) functionality on catalytic turnover required further investigation and clarification. It was possible that the



basic amine functionality was protonated *in situ* by the acidic TFE additive, meaning that the functional group leading to an increase in activity in both cases was actually  $\text{-NH}_3^+$ . Ethanol, a less acidic additive, was used in similar tests in place of TFE to determine if this was the case (Table 4-1, entries 9-11). In these reactions, the increase in TON that had been observed for **1@UiO-66-NH<sub>2</sub>** in the presence of TFE was no longer observed (Entry 10), while a significant activity increase was still observed for **4-1@UiO-66-NH<sub>3</sub><sup>+</sup>**. Taken together, these results supported the hypothesized *in situ* amine protonation as the reason for the original increase in activity for **4-1@UiO-66-NH<sub>2</sub>**.

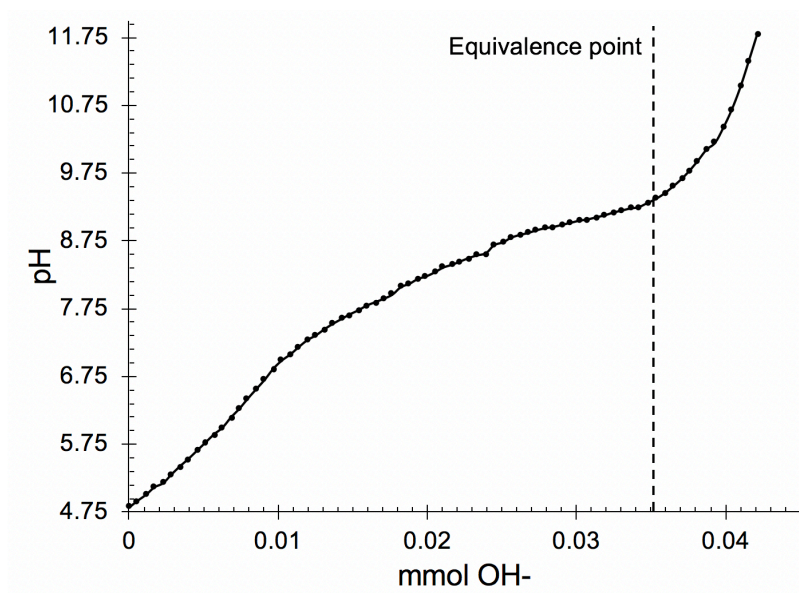
				$\text{4-1@UiO-66-X}$ ( $2.2 \times 10^{-7}$ mmol Ru) $\text{4-2}$ ( $2.2 \times 10^{-7}$ mmol) R-OH (10 mmol) DMF, 70 °C, 2h			
$\text{CO}_2$	+	$\text{H}_2$					$\text{CH}_3\text{OH}$
(3 Bar)		(37 Bar)					
Entry	X	R-OH	TON	Entry	X	R-OH	TON
1	H	TFE	6900	7	NH <sub>2</sub>	TFE	8700
2	CH <sub>3</sub>	TFE	6900	8	NH <sub>3</sub> <sup>+</sup>	TFE	10900
3	4F	TFE	6800	9	H	EtOH	6000
4	F	TFE	6900	10	NH <sub>2</sub>	EtOH	6200
5	Br	TFE	7300	11	NH <sub>3</sub> <sup>+</sup>	EtOH	8900
6	NO <sub>2</sub>	TFE	6600				

**Table 4-1.** Effect of host functionality on cascade production of methanol from carbon dioxide

#### 4.1.2 Characterizing the Ammonium Functionality

Having determined that the ammonium functionality was operative in increasing turnover, it followed to ensure that the effect of this functionality would be present in any pore of the framework in which a catalyst may be encapsulated. While it was assumed that every amine functional group was protonated during acid treatment, it was necessary to experimentally test this assumption. Two different titration methods were employed: the

first was potentiometric and the second a  $^1\text{H}$ -NMR method employed previously for the investigation of ammonium functionality in UiO-66.<sup>33</sup>

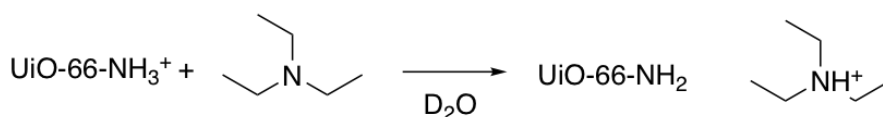


**Figure 4-1.** Potentiometric titration of UiO-66-NH<sub>3</sub><sup>+</sup> with NaOH

Potentiometric titration (Figure 4-1) led to a gradual increase in pH before molar equivalency between the added hydroxide and the linker present in the MOF, which was followed by a rapid increase in pH after the equivalence point. This behavior was atypical for a potentiometric titration but was consistent with many functional groups with slightly different  $\text{pK}_a$  being deprotonated at slightly different pH, leading to a gradual pH increase. For a MOF in which every amine group was protonated, it is likely that increasing concentration of charge within the host would lower the  $\text{pK}_a$  as charge-charge repulsion increases. The observation of a gradual increase in pH with increasing addition of base and the rapid increase in pH after the base-to-linker equivalence point were thus both consistent with every linker in the MOF being protonated.

Tests by NMR titration against triethylamine (Table 4-2) similarly suggested that the MOF linkers were fully protonated. In these tests, the protonated MOF was exposed to

different equivalents of triethylamine relative to the number of possible protonated linkers. The resulting shift in  $^1\text{H}$ -NMR signal for the N-H proton of triethylammonium in deuterium oxide was then measured against a calibration curve, which was developed from the same  $^1\text{H}$ -NMR peak shift for different equivalents of triethylamine relative to a known amount of hydrochloric acid.<sup>33</sup> Three different equivalents of proton to base were found when MOF was titrated against three different amounts of triethylamine, each consistent with approximately 100% of the MOF linkers being protonated. Thus, both titration methods supported the assumption that protonation of amine-based functionality would take place throughout the entire host under the employed acid treatment conditions.

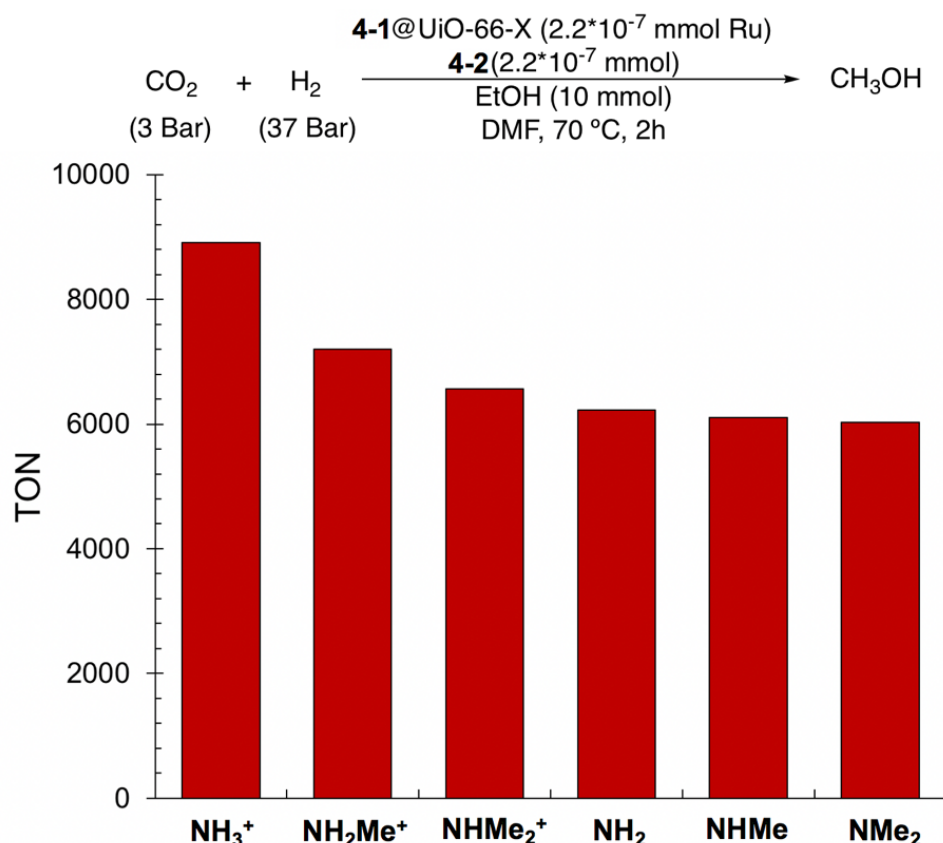


Equivalents NEt <sub>3</sub> added	% linkers protonated
5.6	101.5
2.9	97.7
2.0	99.2

**Table 4-2.** NMR titration of UiO-66-NH<sub>3</sub><sup>+</sup> against triethylamine.

#### 4.1.3 Exploring the role of the ammonium functionality in catalysis

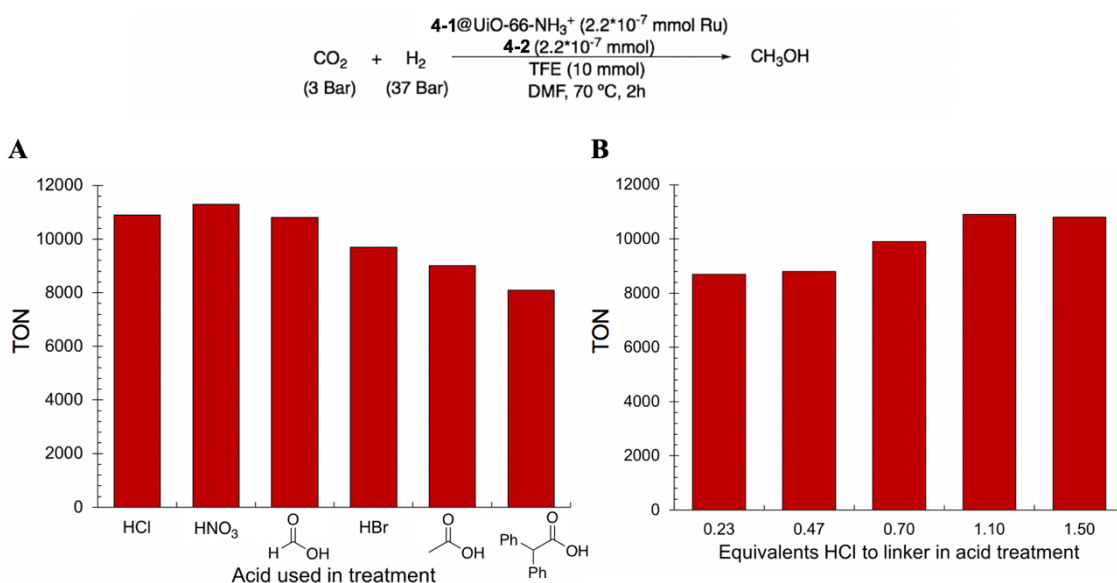
As the effect of a functional group appended to the terephthalic acid linker of the host was only observed with a protonated amine, it was likely that the acidity of the ammonium group influenced catalytic turnover. It was unclear, however, whether this influence was from cooperative effects between the functional group and the encapsulated catalyst or discrete donation of a proton from the functional group to an intermediate. The reaction was then probed using ethanol as an additive to ensure that functionality did not change in the course of the reaction (Figure 4-2).



**Figure 4-2.** Hydrogenation of carbon dioxide to methanol in the presence of ethanol as an additive with different amine-based substitutions on the host framework

The activity of the composite for the cascade reaction iteratively decreased when the functional group of **4-1@UiO-66-X** was altered from  $\text{X} = \text{NH}_3^+$  to  $\text{X} = \text{NH}_2\text{Me}^+$  and further to  $\text{X} = \text{NHMe}_2^+$ . Deprotonating these functional groups using an excess of triethylamine led to a decrease in activity from that observed for the protonated functionalities. This decrease resulted in equal activity for each of the three catalysts. Use of MOFs synthesized with the deprotonated functional groups in their original structure ( $\text{X} = \text{NH}_2$ ,  $\text{X} = \text{NHMe}$ , and  $\text{X} = \text{NMe}_2$ ) likewise exhibited no difference in activity. These findings were consistent with the hypothesis that protonation of the functional group was critical to increasing the activity of the system.

The effect of acid treatment method was also investigated using acids with different  $pK_a$  (Figure 4-3A) and with different amounts of HCl (Figure 4-3B). When compared to the standard treatment conditions (“HCl”), treatment with HBr ( $pK_a = -9.0$ ) resulted in a significant decrease in activity, as did treatment with acetic acid ( $pK_a = 4.76$ ) and its sterically hindered diphenyl derivative ( $pK_a = 4.43$ ). When treated with nitric ( $pK_a = -1.3$ ) or formic acid ( $pK_a = 3.77$ ), the activity of the construct was similar to that for standard conditions. As the  $pK_a$  of HCl is  $-8.0$ , there was no discernible trend relating the activity of the system to  $pK_a$ . In cases where the amount of HCl used in treatment was varied (Figure 4-3B), activity increased with increasing acid concentration, but did not increase beyond the activity achieved with the original acid treatment protocol. These findings supported the hypothesis that, while there was no direct correlation of  $pK_a$  of the acid used in acid treatment to increased activity, the degree to which the host was protonated directly affected activity and the acidic ammonium protons thus had a direct role in the reaction.



**Figure 4-3.** Effect of acid treatment conditions on the hydrogenation of carbon dioxide to methanol: A) acid identity and B) amount of HCl added

The direct involvement of the functional group installed on the terephthalic acid linker was further probed by testing the effect of pore confinement on activity. Previous studies correlated a larger bathochromic shift in the emission  $\lambda_{\text{max}}$  of rhodamine 6G dye to confinement in closer proximity to a functional group.<sup>32</sup> By similar logic, closer proximity of the functional group to the guest catalyst could lead to a more significant impact of that functional group on catalysis (Table 4-3). To test this hypothesis, **4-1** was encapsulated in UiO-67-NH<sub>2</sub>, an isomorph of UiO-66-NH<sub>2</sub> with larger cages. Mild acid treatment was then performed on the composite to give **4-1@UiO-67-NH<sub>3</sub><sup>+</sup>**. The new composite (entry 1), exhibited a much lower TON than **4-1@UiO-66-NH<sub>3</sub><sup>+</sup>** (entry 2), although an increase in TON was observed when compared to **4-1@UiO-67** (entry 3). However, this increase in activity was less significant than that observed for **4-1@UiO-66-NH<sub>3</sub><sup>+</sup>** compared to the unfunctionalized **4-1@UiO-66** (entry 4).

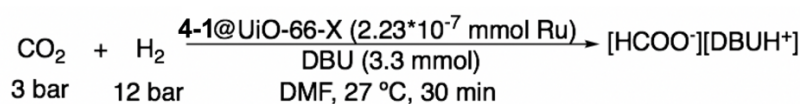
When **4-1@UiO-66** was employed in a DMF solution of ammonium chloride (entries 5 and 6), the resulting TON was far less than that observed for **4-1@UiO-66-NH<sub>3</sub><sup>+</sup>**. Additionally, there was no increase in turnover when 2,6-diisopropyl anilinium chloride was used as an ammonium source (entries 7 and 8). The absence of any effect on TON was likely due to steric bulk preventing its interaction with the encapsulated catalyst, underlining the importance of proximity between the encapsulated catalyst and ammonium functionality. These confinement effects suggested that activity might increase with an increasing concentration of ammonium functionality in the MOF pores. Although such an improvement in activity was observed for a construct with two ammonium groups per linker (entry 9), this increase was not as significant as that observed with the introduction of the first ammonium group.

Tests in which the ammonium functionality was deuterated (entry 10) further suggested the direct involvement of the functional group in catalytic turnover. The observed TON of 8300 gave a difference in TON between **4-1@UiO-66-NH<sub>3</sub><sup>+</sup>** and **4-1@UiO-66-ND<sub>3</sub><sup>+</sup>** of 2600 and a TON<sub>H</sub>/TON<sub>D</sub> ratio of 1.31. A difference in activity of that magnitude is consistent with a direct isotope effect, which would typically be observed in cases where a hydrogen directly involved in the operative mechanistic pathway is replaced by the heavier deuterium. This direct involvement is consistent with both the observed importance of functional group proximity to the encapsulated catalyst and protonated amine functional groups being the only introduced functionality to lead to increased activity.

$\text{CO}_2 + \text{H}_2 \xrightarrow[\text{DMF, 70 } ^\circ\text{C, 2 h}]{\begin{array}{c} \text{4-1@UiO-66-X (2.23*10}^{-7} \text{ mmol Ru)} \\ \text{4-2 (2.23*10}^{-7} \text{ mmol Ru)} \\ \text{TFE (10 mmol)} \\ \text{Additive (n mmol)} \end{array}} \text{CH}_3\text{OH}$ 3 bar    37 bar			
Entry	Host	Additive	TON
1	UiO-67-NH <sub>3</sub> <sup>+</sup>	-	8300
2	UiO-66-NH <sub>3</sub> <sup>+</sup>	-	10900
3	UiO-67	-	7100
4	UiO-66	-	6900
5	UiO-66	NH <sub>4</sub> Cl <sup>a</sup>	7500
6	UiO-66	NH <sub>4</sub> Cl <sup>b</sup>	8300
7	UiO-66	2,6-Diisopropyl Anilinium Chloride <sup>a</sup>	6700
8	UiO-66	2,6-Diisopropyl Anilinium Chloride <sup>b</sup>	6800
9	UiO-66-(NH <sub>3</sub> <sup>+</sup> ) <sub>2</sub>	-	11800
10	UiO-66-ND <sub>3</sub> <sup>+</sup>	-	8300

**Table 4-3.** Effect of confinement and direct interaction between encapsulated catalyst and functionality on TON. Entries in which no additive is specified do not include an additive. (<sup>a</sup>10 mmol, <sup>b</sup>50 mmol)

While these tests suggested that the ammonium functionality played a direct mechanistic role in catalytic turnover, the nature of this involvement was still not entirely clear. As described in Chapter 2, the hybrid construct **4-1@UiO-66** was originally developed for the first step of the cascade transformation: hydrogenation of carbon dioxide to formate. While no change in activity had previously been observed for this reaction with the introduction of a functional group to **4-1@UiO-66**, it was necessary to test **4-1@UiO-66-NH<sub>3</sub><sup>+</sup>** for this purpose (Table 4-4).



Entry	Host	TON
1	UiO-66	325,000 ± 15,000
2	UiO-66-NH <sub>2</sub>	335,000 ± 20,000
3	UiO-66-NH <sub>3</sub> <sup>+</sup>	340,000 ± 15,000

**Table 4-4.** Effect of host functional group on the hydrogenation of carbon dioxide to formate

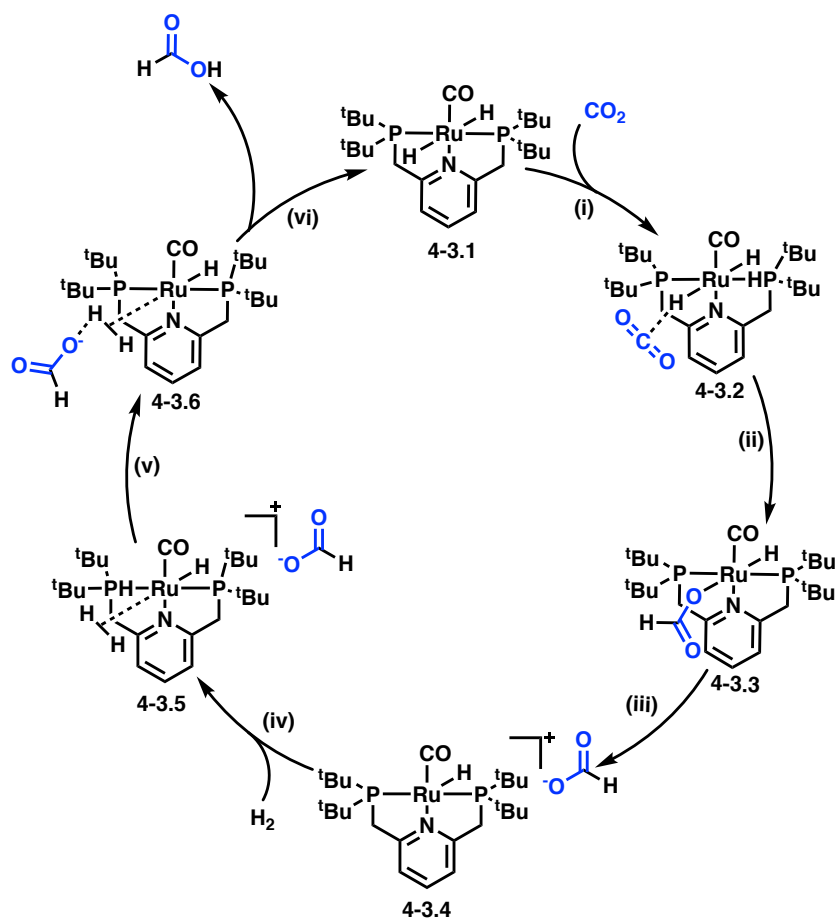
When compared to the unfunctionalized construct (entry 1), neither **4-1@UiO-66-NH<sub>2</sub>** (entry 2) nor **4-1@UiO-66-NH<sub>3</sub><sup>+</sup>** showed a statistically significant increase in activity, consistent with previous observations. Importantly, the absence of an activity increase between entries 2 and 3 could be evidence that the excess of base in the reaction deprotonated the acidic ammonium functionality, supporting the importance of the acidic ammonium proton and its direct mechanistic role in the reaction.



#### 4.1.4 Investigating the mechanistic role of the ammonium functionality

An investigation into the nature of the ammonium functional group's role in the reaction mechanism could allow for more informed and efficient optimization of the multicomponent system. This investigation was conducted by altering the reaction conditions to determine functional group influence on a specific reaction cycle. Understanding the individual steps of the mechanism for the cascade reaction described posed a significant challenge as the mechanistic pathway for the reaction is hypothesized to involve three simultaneously occurring catalytic cycles (Schemes 4-3 through 4-5).

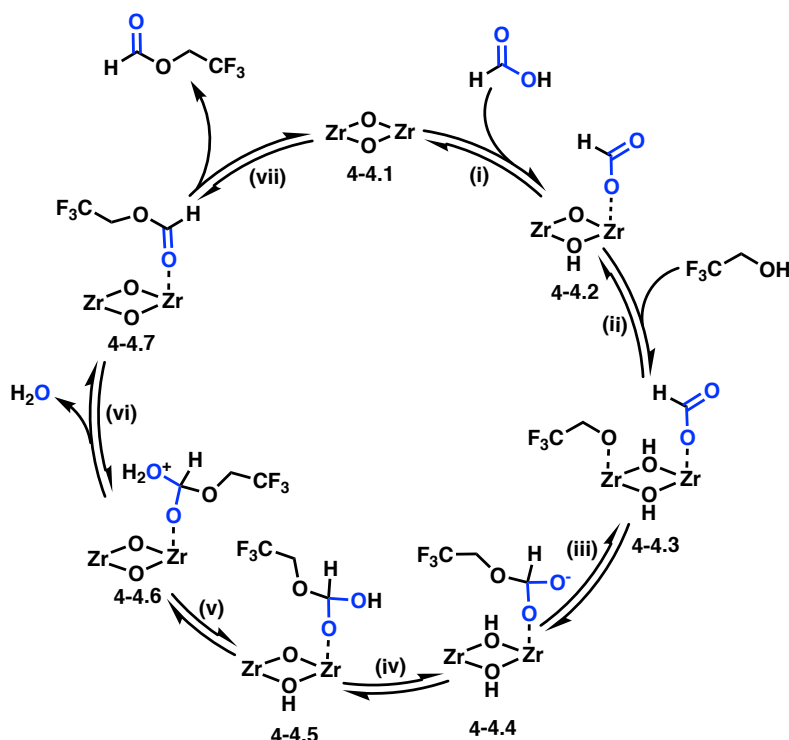
The first of these is the hydrogenation of carbon dioxide to formic acid by **4-1** (Scheme 4-3), studied experimentally and computationally by Pidko and co-workers.<sup>34</sup> In the absence of base, the catalytic cycle is believed to proceed through a six-step mechanism: after coordination of CO<sub>2</sub> (i) to the active species 4-3.1 to form intermediate 4-3.2, the nucleophilic attack of a hydride ligand (ii) on the electron-deficient carbon of CO<sub>2</sub> forms the formate-bound intermediate 4-3.3. This formate then dissociates (iii) in the rate-limiting step of the reaction to give the coordinatively unsaturated intermediate 4-3.4, allowing for the coordination of dihydrogen to the metal center (iv) and formation of intermediate 4-3.5, after which deprotonation of dihydrogen (intermediate 4-3.6) by formate (v,vi), forms formic acid and active species 4-3.1.



**Scheme 4-3.** Catalytic cycle for CO<sub>2</sub> reduction to formic acid<sup>34</sup>

This product is then subjected to Lewis acid-catalyzed esterification at the nodes of UiO-66, represented as 4-4.1, as described by Llabres i Xamena and co-workers (Scheme 4-4).<sup>35</sup> This is initiated by deprotonation and coordination of formic acid to one zirconium of a coordinatively unsaturated node (i), forming intermediate 4-4.2. The alcohol additive is then likewise deprotonated and coordinated to an adjacent zirconium site (ii) to give the coordinatively saturated intermediate 4-4.3. The rate-determining nucleophilic attack of the alkoxide on the carbonyl carbon (iii) leads to intermediate 4-4.4. The resulting tetrahedral intermediate is then protonated twice, first (iv) to give intermediate 4-4.5, then (v) to form water as a more favorable leaving group than hydroxide. Intermediate 4-4.6 subsequently undergoes elimination (vi), giving water and intermediate 4-4.7 as products.

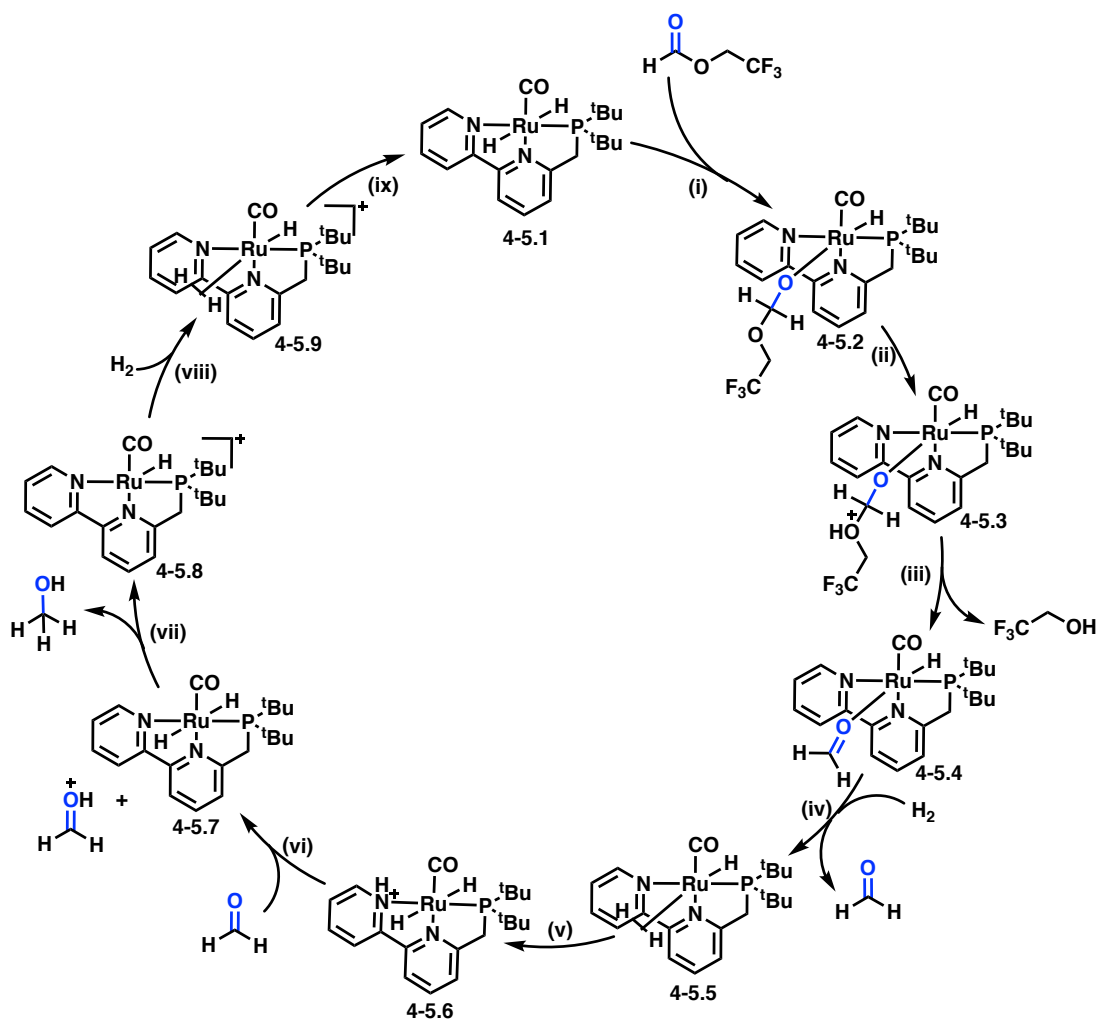
Dissociation of the ester from intermediate 4-4.7 (vii) returns the active site to its initial coordinatively unsaturated state 4-4.1. Control of the water formed in this cycle is extremely important, as water present in the system can drive the equilibrium of esterification back toward formic acid and inhibit the overall cascade transformation.



**Scheme 4-4.** Catalytic cycle for formic acid esterification<sup>35</sup>

The ester then interacts with catalyst **4-2** as reported by Miller and co-workers<sup>36</sup> (Scheme 4-5). Beginning with the active catalyst 4-5.1, an initial hydride attack on the electrophilic carbon of the ester (i) gives intermediate 4-5.2. Subsequent protonation (ii) to form intermediate 4-5.3 and the rate-determining elimination of the alcohol additive (iii) forms formaldehyde complex 4-5.4, which then undergoes ligand exchange with the substitution of dihydrogen (iv) to release formaldehyde and form intermediate 4-5.5. This dihydrogen dissociates heterolytically (v) to form intermediate 4-5.6, allowing for protonation of the formaldehyde and leading to intermediate 4-5.7 (vi). Methanol is then

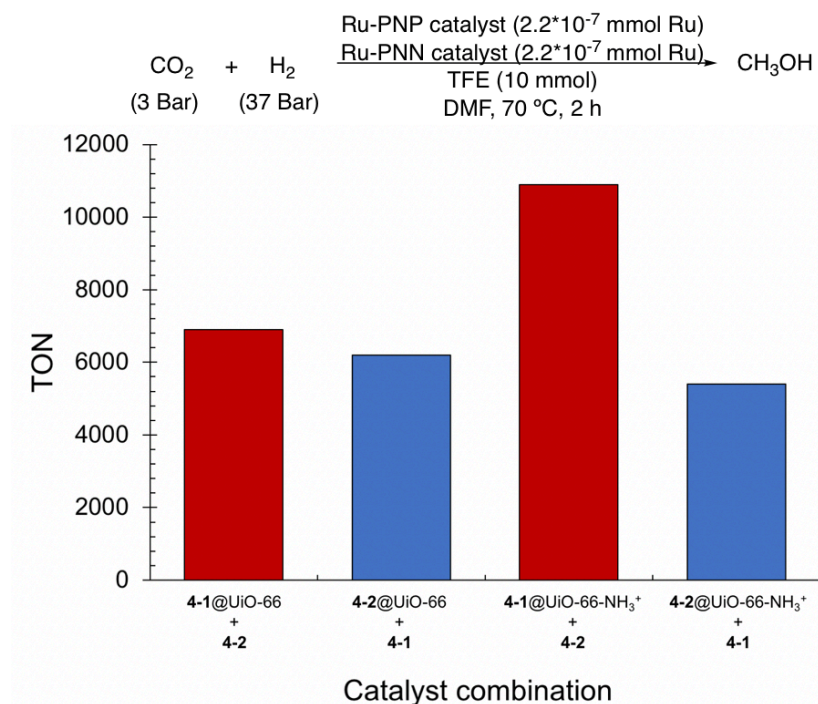
formed by nucleophilic hydride addition (vii), leaving the coordinatively unsaturated intermediate 4-5.8. Coordination of a second equivalent of hydrogen (viii) to give intermediate 4-5.9 and subsequent deprotonation (ix) regenerate the active species 4-5.1 and complete the catalytic cycle.



**Scheme 4-5.** Catalytic cycle for ester reduction to methanol<sup>36</sup>

It was necessary to determine experimentally which of these cycles the ammonium functionality most likely affected so that targeted alterations could be made for efficient improvement in catalytic activity. First, the established system (**4-1**@UiO-66, **4-2** in solution) was compared to an orthogonal system in which **4-2** was encapsulated and **4-1**

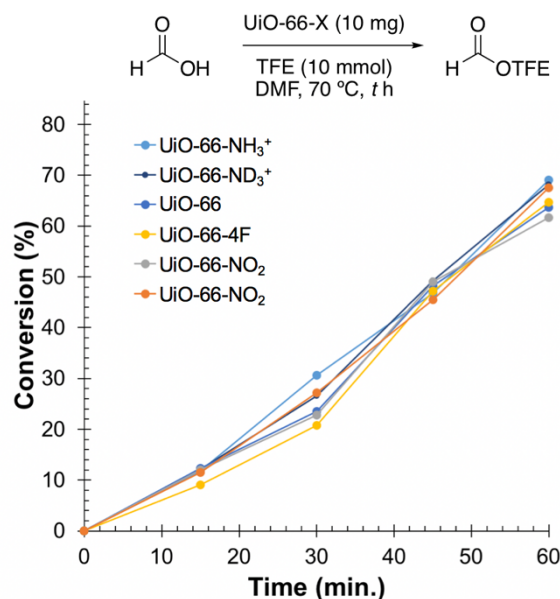
was in solution (Figure 4-4). No increase in TON was observed in the latter case, suggesting that the influence of the ammonium functional group did not affect the rate of the ester reduction step of the reaction (Scheme 4-5).



**Figure 4-4.** Catalytic activity in the cascade reduction of  $\text{CO}_2$  to methanol with **4-1** (red) or **4-2** (blue) as the heterogeneous species in a partially homogeneous reaction

Various functionalized derivatives of UiO-66 were then tested for the esterification of formic acid (Scheme 4-4) with no observable difference in reaction rate resulting from changing functionality (Figure 4-5). The esterification was also not likely shifting from a Lewis acid catalyzed process to a Bronsted acid catalyzed process, as the rate of esterification by UiO-66-ND<sub>3</sub><sup>+</sup> was identical to that for UiO-66-NH<sub>3</sub><sup>+</sup>. Based on the described experiments, it could be concluded that neither the esterification nor the ester reduction was directly affected by the introduced functional group. It could thus be concluded that the ammonium functionality affected the rate at which carbon dioxide hydrogenation to formic acid (Scheme 4-3) occurred. The rate-determining step of this

cycle is believed to be the dissociation of formate (Scheme 4-3, step iii) to give a coordinatively unsaturated complex 4-3.4, so it could be reasonably hypothesized that the positively charged ammonium functionality provides a driving force for the anionic formate to dissociate in this step.



**Figure 4-5.** Esterification of formic acid to 2,2,2-trifluoroethyl formate using differently functionalized UiO-66 derivatives

## 4.2 INCREASING METHANOL PRODUCTION THROUGH FULL CATALYST HETEROGENIZATION

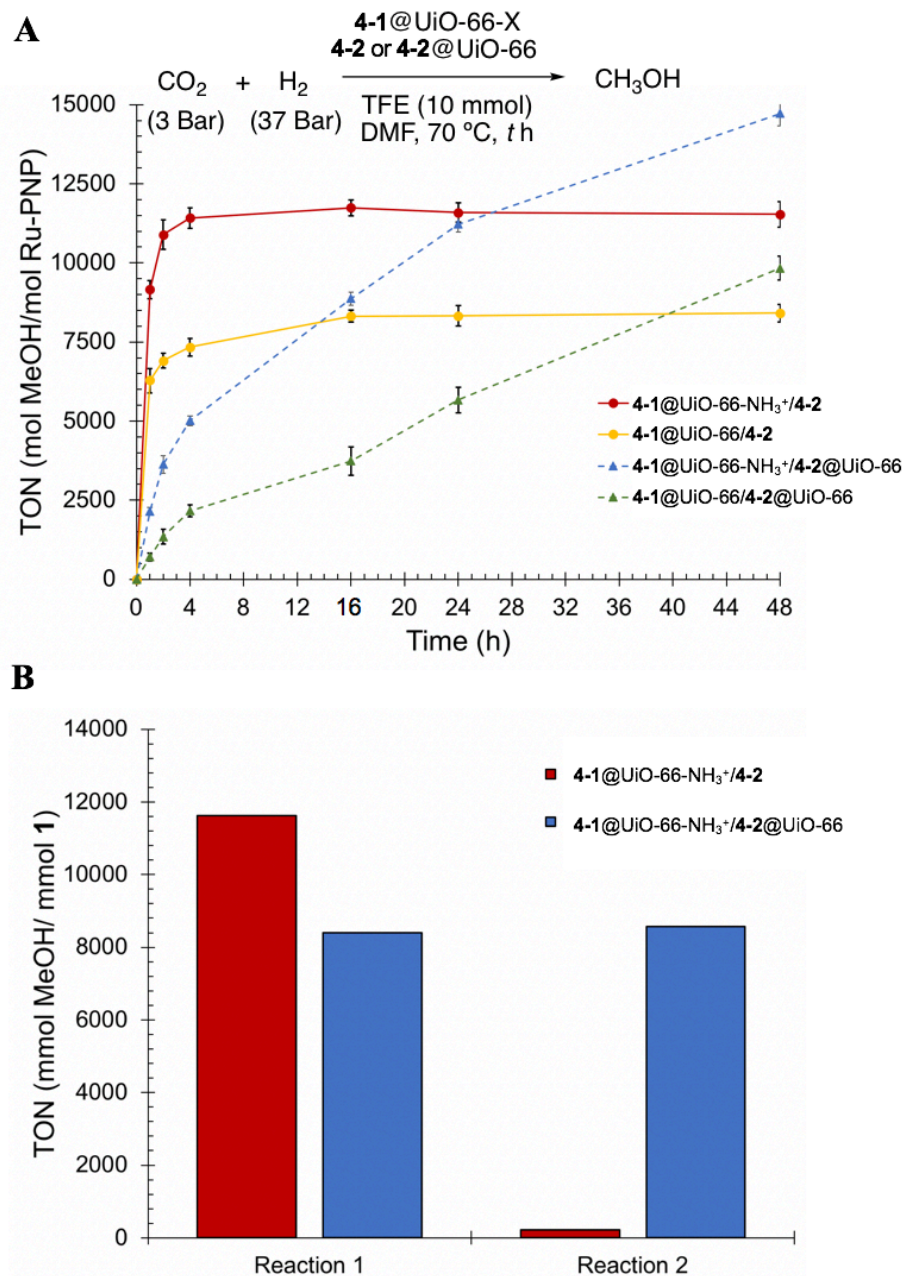
The developed mechanistic and structural understanding allowed for further optimization through encapsulation of both transition metal complexes. The fully heterogeneous nature of the resulting system led to distinct behavior in turnover rate with respect to time and recyclability when compared to the partially homogeneous system. Full heterogenization also allowed for the observation of behavior previously complicated by

the instability of molecular homogeneous catalysts. Further optimization led to previously unreported activity and catalyst lifetime for carbon dioxide reduction to methanol with transition metal complexes.

#### 4.2.1 Improving catalyst lifetime through heterogenization

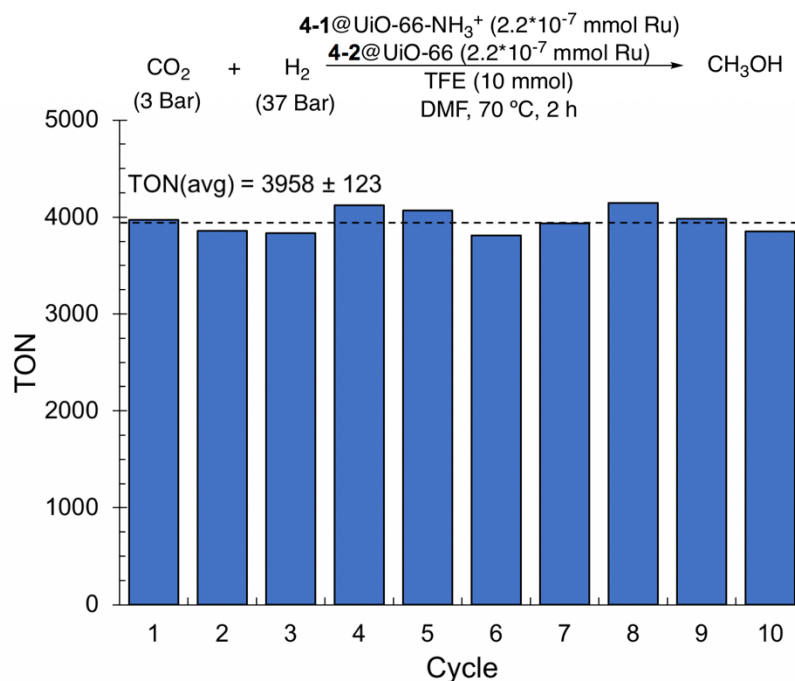
The behavior of the original multicomponent system was tested as a function of time (Figure 4-6A, solid lines) in order to better understand the difference in turnover between **4-1**@UiO-66 and **4-1**@UiO-66-NH<sub>3</sub><sup>+</sup>. The observed difference in activity could be attributed to a much higher initial turnover rate, though both systems ceased to turn over after four hours. While the partially homogeneous system exhibited high initial turnover followed by a rapid decrease in reaction rate, systems where both **4-1** and **4-2** were encapsulated (Figure 4-6A, dotted lines) turned over more slowly at initial time points compared to systems where **4-2** was unencapsulated but continued to turn over at a similar, constant rate thereafter regardless of framework functionality.

The behavior of the partially homogeneous system was likely a result of the decomposition of **4-2**, as the mixture gave no significant increase in methanol production when resubjected to reaction conditions after an initial 16-hour reaction (Figure 4-6B, red). Conversely, the fully heterogeneous system exhibited almost identical turnover upon resubjection to reaction conditions (Figure 4-6B, blue), suggesting that both catalysts survived the initial reaction. The advantage in increased catalyst lifetime provided by full heterogenization also extended to recyclability, allowing for negligible change in activity through ten cycles (Figure 4-7) and a cumulative TON of almost 40,000 at a cumulative reaction time of 20 hours, far exceeding any TON observed in a single-reaction setting.



**Figure 4-6.** Comparison of partially homogeneous (solid lines) and fully heterogeneous (dotted lines) systems for the conversion of CO<sub>2</sub> to methanol A) as a function of time and B) after resubjecting the same catalysts to reaction conditions as listed for 16 hours

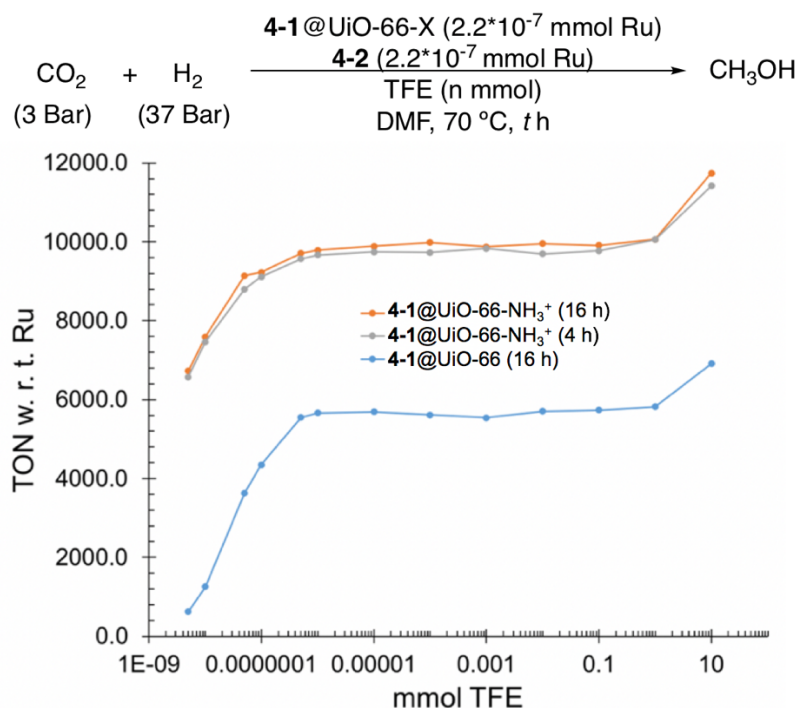




**Figure 4-7.** Recycling of the fully heterogeneous cascade system over ten cycles

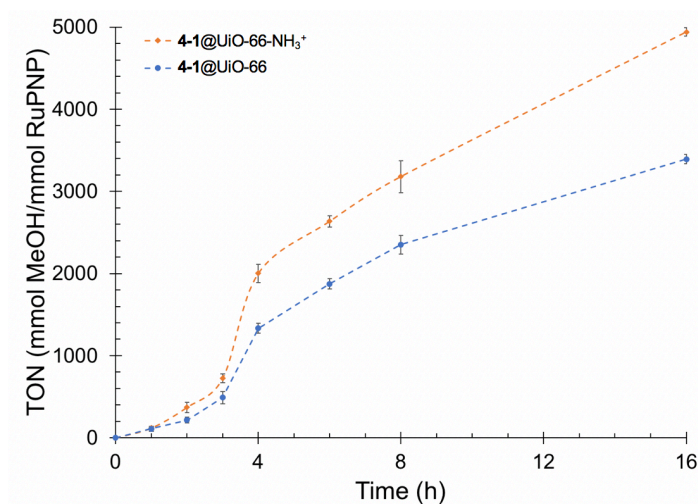
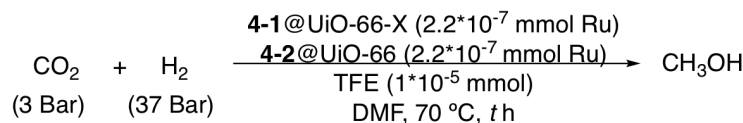
#### 4.2.2 Tuning Network Autocatalytic Behavior in a Fully Heterogeneous System

Complete heterogenization of the catalyst system also allowed for the observation of network autocatalytic characteristics previously suspected for this reaction pathway (Figure 4-8) without the added complication of catalyst decomposition. The same network autocatalytic behavior was observed in a functionalized partially homogeneous system (orange and grey) as reported for the unfunctionalized system described in Chapter 3 (blue), with no increase in turnover between four hours (grey) and sixteen hours (orange) at all additive loadings. This finding suggested that prevention of catalyst decomposition was necessary in order to observe the hypothesized rate increase with time that is typically associated with autocatalysis.



**Figure 4-8.** Effect of additive amount on turnover number at 4 hours and 16 hours for **4-1@UiO-66** (blue) and **4-1@UiO-66-NH<sub>3</sub><sup>+</sup>** (grey and orange)

Encapsulation of **4-2** as described above and application of the resulting construct in tandem with **4-1@UiO-66-NH<sub>3</sub><sup>+</sup>** (Figure 4-9, orange) or **4-1@UiO-66** (Figure 4-9, blue) allowed for the observation of network autocatalytic behavior in the absence of catalyst deactivation. A low turnover rate was observed at low TFE loadings, followed by a rapid increase in turnover frequency as the overall additive fraction became more methanol-rich, consistent with the hypothesized network autocatalysis. This rapid turnover period also seemed to be the main differentiating factor in between functionalized and unfunctionalized systems, with turnover frequency being comparable with or without ammonium functionality outside of this range. However, the increase in reaction rate spanned only a short time period. Since the recyclability of the system suggested that neither transition metal complex was decomposing, an alternative explanation for this reduction in reaction rate was necessary.



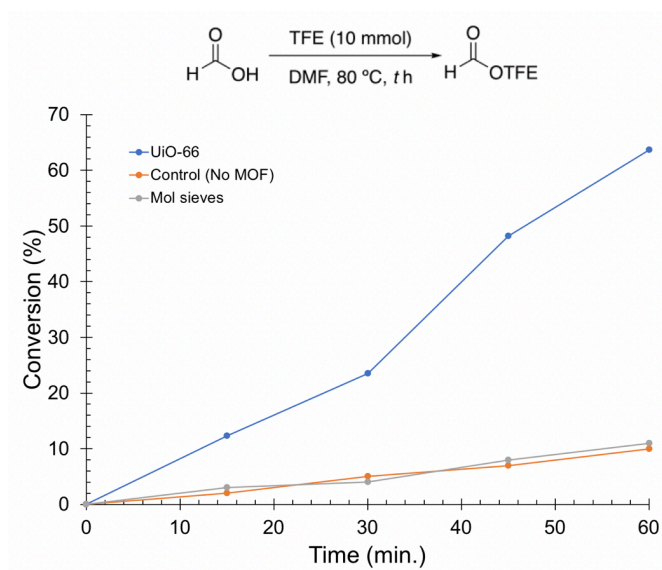
**Figure 4-9.** Turnover number as a function of time in the cascade hydrogenation of carbon dioxide to methanol with a fully heterogeneous multicomponent system

One potential cause was the inhibition of one or both of the complexes by carbon monoxide produced via the reverse water-gas shift reaction on the internal reactor surface. However, the fraction of this carbon monoxide in the bulk reactor space observed in Chapter 3 was very low when compared to hydrogen or carbon dioxide, suggesting that both complexes were far more likely to interact with a substrate that would lead to productive catalysis than carbon monoxide. While the role of carbon monoxide as a reversible inhibitor could not be fully ruled out, the recyclability of the multicomponent system suggested that it was not binding irreversibly and deactivating an encapsulated catalyst. Since carbon monoxide was likely not the major inhibitory factor that resulted in turnover frequency at longer time points, it was necessary to determine another possible explanation for this behavior.

The buildup of water, which forms as a byproduct of each turnover and inhibits esterification (Scheme 4-4, step vi) could lead to such a turnover frequency decrease.

Washing the catalyst after each reaction likely removes this water between cycles, allowing for the observed recyclability while still inhibiting the reaction within a single cycle. Furthermore, water production is a feature of the mechanistic pathway and would be operative within the same vessel, increasing the likelihood of its involvement in catalysis.

With the likely cause of reaction inhibition identified, a method for the removal of water from the reaction was necessary in order to increase the time period in which high turnover rates were observed. The introduction of a desiccant was believed to be a viable method for accomplishing this task. To this end, the previously described tests for autocatalysis were performed in the presence of an excess of 3 Å molecular sieves. These molecular sieves did not participate in the esterification reaction (Figure 4-10) and served as a superior desiccant to functionalized or unfunctionalized UiO-66 (Table 4-5). These findings, in addition to the adsorptive selectivity of the molecular sieves for water over methanol, allowed for the assumption that the only role of the sieves in the cascade transformation would be to remove water as it was produced.



**Figure 4-10.** Determination of activity for the conversion of formic acid to trifluoroethyl formate by UiO-66 (blue) or 3 Å molecular sieves (grey)

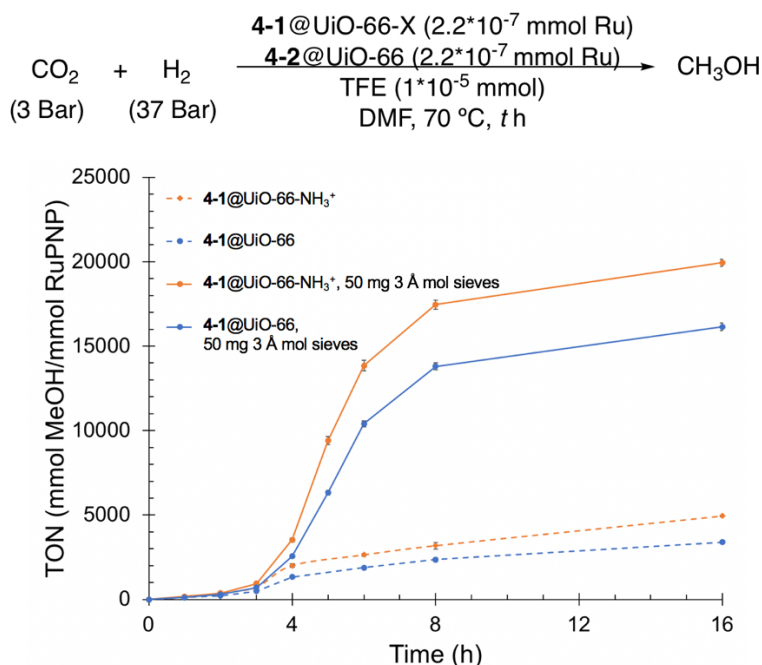
$\text{H}_2\text{O} + \text{CH}_3\text{OH} \xrightarrow[\text{DMF, 70 } ^\circ\text{C, 16 h}]{\text{Desiccant}} \text{H}_2\text{O} + \text{CH}_3\text{OH}$ <p style="text-align: center;">1 : 1</p>		
Desiccant	H <sub>2</sub> O adsorbed (%)	MeOH adsorbed (%)
3 Å sieves	75 ± 8	5 ± 3
UiO-66	10 ± 3	4 ± 3
UiO-66-NH <sub>2</sub>	8 ± 4	3 ± 2
UiO-66-NH <sub>3</sub> <sup>+</sup>	11 ± 3	4 ± 3

**Table 4-5.** Comparison of desiccant capabilities and selectivity for water over methanol for different porous solids used in the described cascade transformation. Quantification was performed by <sup>1</sup>H-NMR in CDCl<sub>3</sub> using tetrachloroethane as an external standard.

The addition of molecular sieves to the reaction mixture for cascade hydrogenation (Figure 4-11) led to an approximately fourfold increase in turnover for the ammonium-functionalized system. A similar low-turnover period was observed in methanol-deficient regimes to that described above. The rapid turnover period that followed was extended from two hours to six hours, leading to a large increase in overall TON and resulting in an even larger difference in TON between functionalized and unfunctionalized systems. Surprisingly, a decrease in turnover frequency at longer time points was still observed despite the amount of water produced being far below the desiccant capacity of the added molecular sieves.

The difference in turnover frequency between functionalized and unfunctionalized species during the observed rapid turnover period supported the hypothesis that functionalized and unfunctionalized systems were primarily differentiated when the additive fraction becomes methanol-rich, as the turnover rate for both systems was similar during lower-activity timeframes even with the addition of molecular sieves. The persistence of these low-turnover rate periods was puzzling considering the adsorptive capacity of the added molecular sieves far exceeded the amount of water produced during

the reaction. As previously mentioned, it was not likely that carbon monoxide was causing this inhibition due to the observed recyclability, suggesting that another inhibitory factor must be present.



**Figure 4-11.** Network autocatalytic behavior as a function of time in the cascade hydrogenation of carbon dioxide to methanol using a fully heterogeneous multicomponent system with (solid lines) or without (dotted lines) the addition of 3 Å molecular sieves

Both the functionalized and unfunctionalized MOFs showed a degree of desiccant capability (Table 4-5), so it was hypothesized that water trapped within the MOF pores could inhibit turnover even in the presence of molecular sieves. Thus, several control experiments were conducted. The first control tested catalyst subjected to reaction conditions for 16 hours and resubjected without washing, leading to residual water within the MOF pores. This sample showed a decrease in TON from 4900 to 3800 upon resubjection to reaction conditions, suggesting that some inhibitory species remained after the first reaction cycle. When a sample of catalyst saturated with deionized water was employed, the observed turnover number decreased further to 1200, less than 25% of the

activity of the dry species. Another sample of catalyst was likewise saturated with deionized water, then subjected to standard washing procedures. This catalyst gave a TON of 4800, consistent with water being removed from the pores by washing between cycles and confirming that water's role as an inhibitory factor. Taken together, these tests supported the hypothesis that water formed as a byproduct of the reaction was trapped in the MOF pores and inhibited conversion of carbon dioxide to methanol by altering the equilibrium of the esterification step. This inhibition could, however, be easily circumvented by washing the catalyst between cycles to give consistent and reproducible turnover.

#### 4.3 CONCLUSION

Through a fundamental understanding of each component of a multicomponent catalytic system and application of logical design based on this understanding, activity not previously observed in the hydrogenation of carbon dioxide to methanol was achieved. While most introduced functional groups had no effect on catalyst activity, an ammonium functionality was found to significantly increase turnover. Insight into its specific mechanistic function allowed for further optimization. An investigation into the behavior of the system with time and the effect that full heterogenization has on this behavior revealed recyclability and increased catalyst lifetime compared to a partially homogeneous system. Removal of inhibitory byproducts further increased the activity of the system to the point of previously unreported TON values.

Efforts toward optimizing reactions catalyzed by transition metal complexes are presently focused primarily on the design and modification of ligands to influence the electronic and steric environment directly interacting with the active metal center. The developments described in this chapter represent an example of catalyst design through manipulation of noncovalent interactions in a host-guest system, resulting in significant improvements to catalyst lifetime and activity. The method used for catalyst encapsulation could allow for heterogenization of a wide range of transition metal complex catalysts, and a similar variety exists in the functionality that can be installed on the MOF linker. Such modularity lays the foundation for similar studies in a variety of other catalytic systems, with the potential for logical design and optimization based both on the selection of catalyst for a targeted reaction and the desired noncovalent influence and could allow access to reactivity inaccessible through manipulations of inner-sphere steric and electronic interactions. Such catalytic systems could be a significant step toward enzyme-like activity and selectivity in synthetic catalysts.



## Materials and Methods:

### General Considerations:

Unless otherwise stated, all manipulations were carried out in air using standard analytical procedures. Catalytic carbon dioxide hydrogenation reactions were carried out in 5.0 mL ampules placed in a 450 mL stainless steel Parr reactor with stirring. Experiments carried out in an air-free environment were conducted under a positive pressure of N<sub>2</sub> using standard glovebox or Schlenk line techniques.<sup>37</sup> All [Ru]@UiO-66 catalysts employed were pre-treated as noted.

### Materials

Tetrafluoroterephthalic acid (Aldrich), 2-fluoroterephthalic acid (Aldrich), 2-nitroterephthalic acid (Aldrich), 2-aminoterephthalic acid (Aldrich), 2-bromoterephthalic acid (ThermoFisher), 2,6-lutidine (Aldrich) and di-tert-butylchlorophosphine (Acros Organics) were purchased and used without further purification. 2-N-methylaminoterephthalic acid and 2-N,N'-dimethylaminoterephthalic acid were synthesized by Adam Bensalah as described in his thesis. Powder X-ray diffraction traces were collected on a Bruker AXS diffractometer with Cu K $\alpha$  radiation ( $\lambda=1.5418$  Å). <sup>1</sup>H-NMR and <sup>31</sup>P{<sup>1</sup>H}-NMR spectra were collected on a Varian Unity INOVA spectrometers (400 MHz, 500 MHz, or 600 MHz, as indicated), with all chemical shifts reported in ppm. Chemical shifts were reported in reference to tetramethylsilane and phosphoric acid for <sup>1</sup>H-NMR and <sup>31</sup>P-NMR spectra, respectively ( $\delta$  0.0 ppm for both). Formate production in catalysis was quantified using <sup>1</sup>H NMR spectroscopy using tetrachloroethane (10  $\mu$ L) as an external standard in a mixture of CDCl<sub>3</sub> (450  $\mu$ L) and reaction mixture (250  $\mu$ L). <sup>1</sup>H-

NMR spectra were acquired in 16 transients.  $^{31}\text{P}$ -NMR spectra were acquired in 160 transients. All centrifugation steps were performed at 3000 revolutions per minute for 10 minutes using a Thermo Scientific CL2 centrifuge unless otherwise noted. Inductively coupled plasma optical emission (ICP-OES) spectrometry was recorded in an Agilent 5100 instrument that was calibrated using known concentrations of standard solutions to quantify Zr, Ru, and P. Ru ( $1000 \pm 4$  ppm), P ( $100.04 \pm 0.55$  ppm), Zr ( $999 \pm 5$  ppm) single elemental standards were purchased from Inorganic Ventures.

### *Procedures*

All procedures reflect the final developed protocols for a given process. Systematic changes to initially used procedures (e.g. alteration of  $\text{CO}_2$  hydrogenation temperature, reaction time, and  $\text{H}_2$  pressure) to optimize proper data comparison are not described in these general procedures. All catalytic reactions included both positive and negative controls to ensure proper operation. Experiments in an air-free environment were conducted under a positive pressure of  $\text{N}_2$ . All catalyst loadings were determined by ICP-OES spectroscopy using prepared standards.

**Synthesis of UiO-66.** The synthesis of UiO-66 was adapted from a literature procedure.<sup>38</sup>  $\text{N,N}'$ -dimethylformamide (DMF) (25 mL) was added to a 45 mL Teflon-lined steel autoclave. Zirconium tetrachloride (240 mg, 1.0 mmol) and terephthalic acid (340 mg, 2.1 mmol) and concentrated hydrochloric acid (180  $\mu\text{L}$ ) was added to the autoclave, which was then sealed and heated at 220  $^\circ\text{C}$  for 20 hours. The reaction mixture was then allowed to cool to room temperature and agitated to suspend the solid. The solid was isolated by centrifugation, then washed with DMF (15 mL) and left to soak in this solvent

overnight. The solid was isolated again by centrifugation and washed twice with methanol (15 mL), then left to soak overnight in methanol. The solid was isolated by centrifugation and dried in a vacuum chamber overnight, then dried overnight in an oven at 70 °C to give a white crystalline solid. (280 mg, 0.99 mmol, 95% yield). Powder X-Ray diffraction traces matched literature precedence and confirmed the structure of UiO-66.<sup>38</sup>

**General synthesis of functionalized UiO-66-X derivatives.** This synthesis was adapted from literature procedures.<sup>39</sup> ZrCl<sub>4</sub> (18.64 mg, 0.08 mmol) and functionalized terephthalic acid (varied masses, 0.08 mmol) were weighed out in a 20-mL scintillation vial. N,N'-dimethylformamide (10 mL) was added to this vial, followed by acetic acid (1.378 mL, 24 mmol). This vessel was sealed and heated at 120 °C for 24 hours in an oil bath. The product was collected by centrifugation at 3000 rpm for 10 minutes. The solid precipitate was triturated by decanting the DMF supernatant then re-suspended with fresh DMF (10 mL) overnight. This mixture was then subjected to centrifugation and the solid was washed with methanol, then suspended in methanol overnight. This solvent was removed through centrifugation and trituration. The residual solvent was removed from the isolated solids in a vacuum oven at 100 °C overnight.

**Synthesis of 2,6-bis((di-*tert*-butylphosphino)methyl)pyridine (<sup>t</sup>BuPNP).** The synthesis of this ligand was adapted from a literature procedure.<sup>40</sup> On a Schlenk line under nitrogen atmosphere, a solution of 2,6-lutidine (0.54 mL, 4.7 mmol) in diethyl ether (1.96 mL) was prepared in a 50-mL two-neck flask, then cooled to 0 °C. *n*-Butyl lithium in hexanes (2.0 M, 4.8 mL, 9.6 mmol) was added slowly by syringe to this cooled solution, which resulted in the homogeneous reaction mixture to turn a dark maroon-red color. The reaction mixture was allowed to warm to room temperature and heated to 40 °C for fifteen

hours. After cooling to room temperature, the reaction mixture was brought -78 °C where di-tert-butylchlorophosphine (1.9 mL, 9.7 mmol) was added dropwise to the reaction mixture via syringe. The reaction mixture was allowed to warm to room temperature where it reacted for one hour, retaining its deep red coloration. The reaction mixture was quenched with degassed methanol (40 mL), resulting in a color change to light-yellow. The reaction mixture was left without stirring for one hour to allow the resulting lithium salt to settle. The liquid product mixture was transferred by cannula filtration to another two-necked flask, and the lithium salt was washed twice with diethyl ether. The solvent mixture was removed by vacuum at 55 °C resulting in an off-white solid. This solid was transferred to a nitrogen-filled glovebox and extracted in diethyl ether (10 mL), then recrystallized in diethyl ether at -40 °C. The clear-white crystalline product was recovered and washed with cold diethyl ether. (490 mg, 2.5 mmol, 53% yield). <sup>1</sup>H NMR (500 MHz, C<sub>6</sub>D<sub>6</sub>) δ: 1.13 (d, J = 10.8 Hz, 36H), 3.09 (d, 2J = 2.4 Hz, 4H), 7.17 (d, J = 7.5 Hz, 2H), 7.25 (t, J = 7.8 Hz, 1H) ppm. <sup>31</sup>P{<sup>1</sup>H} NMR (202 MHz, C<sub>6</sub>D<sub>6</sub>) δ: 37.60 (s) ppm. This spectral data was consistent with the literature reported spectral data.<sup>40</sup>

**Synthesis of (tBuPNP)Ru(CO)HCl (4-1).** The synthesis of this complex was adapted from a literature procedure.<sup>41</sup> In a nitrogen-filled glove box, RuHCl(PPh<sub>3</sub>)<sub>3</sub>(CO) (260 mg, 0.27 mmol) was suspended in tetrahydrofuran (THF)(10 mL) in a 100 mL Schlenk tube. tBuPNP (110 mg, 0.28 mmol) was added to this suspension. The solution was diluted with THF (20 mL). This reaction mixture was sealed and removed from the glovebox, then heated at 65 °C for 3 hours. The resulting mixture was returned to the glove box and filtered through celite on a coarse fritted funnel. The remaining THF was removed en vacuo. The resultant oily yellow solid was dissolved in THF (0.50 mL), and precipitated

into pentane to give a yellow solid. This solid was then washed with pentane (50 mL), and the crude product was recrystallized in pentane at -40 °C. The recrystallized product was a yellow solid (87 mg, 16 mmol, 57% yield). <sup>1</sup>H-NMR (500 MHz, C6D6) δ: -14.52 (t, J = 20.0 Hz, 1H), 1.13 (t, J = 8.0 Hz, 18H), 1.52 (t, J = 8.0 Hz, 18H), 2.87 (dt, J = 16.0 Hz, J = 4.0 Hz, 2H), 3.77 (dt, J = 16.0 Hz, J = 4.0 Hz, 2H), 6.46 (d, J = 8.0 Hz, 2H), 6.79 (t, J = 8.0 Hz, 1H) ppm. <sup>31</sup>P{<sup>1</sup>H}-NMR (202 MHz, C6D6) δ: 90.8 (s) ppm. This spectral data was consistent with the literature reported spectral data.<sup>41</sup>

**Synthesis of 6-methyl-2,2'-bipyridyl.** The synthesis of this compound was adapted from a literature procedure.<sup>42</sup> Methyllithium in diethyl ether (4.0 mL, 1.6 M, 6.4 mmol) was added dropwise to a diethyl ether solution (40 mL) containing 2,2'-bipyridine (1.0 g, 6.4 mmol) at 0 °C. After complete addition, the resulting brown solution was gently refluxed for 3 h under N<sub>2</sub>. It was then allowed to cool to room temperature and water was added with stirring, resulting in a biphasic yellow solution. The aqueous layer was separated from the organic layer and extracted three times with diethyl ether. The combined organic layers were washed twice with brine (20 mL) followed by addition of anhydrous Na<sub>2</sub>SO<sub>4</sub> to remove residual water. The solution was then decanted into a round-bottom flask and the ether was removed by rotary evaporation. The resulting orange oil was oxidized with a saturated KMnO<sub>4</sub>/acetone solution (100 mL) until formation of MnO<sub>2</sub> ceased. The MnO<sub>2</sub> was removed by vacuum filtration through celite. The filtrate was placed in a round-bottom flask and acetone was removed by rotary evaporation. Purification of the crude product by column chromatography (heptane/EtOAc 1/1 on silica) gave the desired product. (810 mg, 4.8 mmol, 74% yield). <sup>1</sup>H-NMR (500 MHz, CDCl<sub>3</sub>) δ: 2.61 (s, 3H), 7.13 (d, J = 7.80 Hz, 1H), 7.26-7.27 (m, 1H), 7.57 (t, J = 7.80 Hz, 1H), 7.74-7.79 (m,

1H), 8.17 (d, J = 7.50 Hz, 1H), 8.40 (d, J = 8.10 Hz, 1H), 8.64-8.67 (m, 1H). This spectral data was consistent with the literature reported spectral data.<sup>42</sup>

**Synthesis of 6-di-*tert*-butylphosphinomethyl-2,2'-bipyridyl (<sup>t</sup>BuPNN).** The synthesis of this compound was adapted from a literature procedure.<sup>43</sup> An oven-dried 500 mL two-necked round bottom flask with a stirring bar, dropping funnel and one rubber septum was cooled under a stream of nitrogen. A solution of 6-methyl-2,2'-bipyridine (3.4 g, 20 mmol) in dry ether (80 mL) was added to this flask. The solution was cooled to 0 °C and lithium diisopropylamide (LDA) (1.8 M, 13 mL, 24 mmol) in diethyl ether was added dropwise via addition funnel. The resulting brown colored mixture was stirred for 1 hr at 0 °C and then cooled to -78 °C. A solution of di-*tert*butylchlorophosphine (4.3 g, 24 mmol) in dry ether (30 mL) was added dropwise to this mixture. The stirring was continued for 1 hr at -78 °C and the mixture was allowed to slowly warm to room temperature and stirred overnight. The supernatant was transferred by cannula to a round-bottom flask, then exposed to vacuum. The resulting solid was purified by recrystallization in pentane to yield 6-di-*tert*butylphosphinomethyl-2,2'-bipyridine (<sup>t</sup>BuPNN) as a white solid. (3.3 g, 10 mmol, 52% yield). <sup>1</sup>H NMR (C<sub>6</sub>D<sub>6</sub>) δ: 1.19 (d, J = 11.0 Hz, 18H), 3.10 (d, J = 3.3 Hz, 2H), 7.25 (ddd, J = 7.5 Hz, J = 4.8 Hz, J = 1.2 Hz, 1H), 7.38 (td, J<sub>HH</sub> = 7.8 Hz, J = 1.0 Hz, 1H), 7.65 (t, J = 7.8 Hz, 1H), 7.74 (dt, J = 7.8 Hz, J = 1.8 Hz, 1H), 8.14 (br d, J = 7.8 Hz, 1H), 8.41 (td, J = 8.0 Hz, J = 1.0 Hz, 1H), 8.60-8.62 (m, 1H). <sup>31</sup>P{<sup>1</sup>H-NMR (C<sub>6</sub>D<sub>6</sub>) δ: 37.5 (s). This spectral data was consistent with the literature reported spectral data.<sup>43</sup>

**Synthesis of (<sup>t</sup>BuPNN)Ru(CO)HCl (4-2).** This synthesis of this compound was adapted from a literature procedure.<sup>43</sup> <sup>t</sup>BuPNN (100 mg, 0.33 mmol), RuHCl(CO)(PPh<sub>3</sub>)<sub>3</sub> (300 mg, 0.32 mmol), and 12 mL dry THF were added to an oven-dried 25-mL Schlenk

tube in a nitrogen-filled glove box. The vessel was sealed and brought out of the glovebox. On a Schlenk line under nitrogen, the reaction was heated at 65 °C for 8 hrs with stirring, then cooled to room temperature to give a red-brown solid. The reaction mixture was brought into the glove box, and the solvent was decanted and the solid thus obtained was washed with ether ( $3 \times 3.0$  mL), then dried under vacuum to give pure complex (130 mg, 0.27 mmol, 85% yield).  $^1\text{H}$ -NMR (500 MHz,  $\text{C}_6\text{D}_6$ )  $\delta$ : -15.3 (d, 2 J = 24.6 Hz, 1H), 1.27 (d, J = 13.2 Hz, 9H), 1.47 (d, JPH = 13.8 Hz, 9H), 3.02-3.72 (m, 2H), 7.45-7.47 (m, 1H), 7.59 (d, J = 7.8 Hz, 1H), 7.81-7.88 (m, 2H), 7.95 (d, J = 8.1 Hz, 1H), 8.06 (d, J = 7.8 Hz, 1H), 9.11-9.15 (br m, 1H).  $^{31}\text{P}\{^1\text{H}\}$ -NMR (202 MHz,  $\text{C}_6\text{D}_6$ )  $\delta$ : 107.1 (s). This spectral data was consistent with the literature reported spectral data.<sup>43</sup>

**Synthesis of 4-1@UiO-66-X.** In an inert atmosphere glovebox, methanol (10 mL) was added to a 20-mL scintillation vial in a glovebox. UiO-66-X (200 mg) and ( $^t\text{BuPNP}$ )Ru(CO)HCl (5.0 mg, 5.3  $\mu\text{mol}$ ) were added to the vial, which was then sealed. This mixture was heated at 55 °C for 24 h, and then allowed to cool to room temperature. The resulting mixture was brought into a glovebox. The vial was unsealed, and the resultant mixture was transferred to a 20 mL scintillation vial and subjected to centrifugation. Trituration was achieved by decanting the supernatant from this mixture, which was set aside for NMR analysis. The remaining solid was further triturated three times with methanol (10 mL) each time using centrifugation to ensure quantitative mass transfer. After three washing cycles, 190 mg of a pale yellow solid (96%) was obtained. This solid was dried overnight in a vacuum chamber. A portion of this material (100 mg) was suspended in 15 mL of degassed DMF, and then transferred as a slurry to a 20 mL ampule containing a stir bar using a 9" glass pipet. 1,8-diazabicyclo[5.4.0]undec-7-ene (DBU) (2.465 mL,

2.505 g, 15.50 mmol) was added to this ampule. The ampule was added to a 450-mL stainless steel Parr reactor. The vessel was purged with carbon dioxide for 5 minutes and then pressurized to 42 psi. The vessel was then pressurized with hydrogen gas to achieve a total pressure of 560 psi at room temperature. The reactor was heated to 129 °C and left to react for 45 minutes. The heating mantle was removed, the reactor was cooled using a room-temperature water bath, and the pressure was released slowly from the vessel. The vessel was opened and the ampule was removed. The reaction mixture was transferred as a slurry to a 20-mL scintillation vial and subjected to centrifugation at 3000 revolutions per minute for 15 min, after which the supernatant was decanted. The solid was triturated twice with methanol (20 mL) followed by centrifugation and dried overnight in a vacuum chamber to give a pale yellow powder (93 mg, 93%). The loading of catalyst in the MOF was determined by ICP-OES (see “Digestion of UiO-66-X for ICP-OES analysis”, below). The structural integrity of the solid was confirmed by powder x-ray diffraction

**Acid treatment of 4-1@UiO-66-NH<sub>2</sub>.** 4-1@UiO-66-NH<sub>2</sub> (20 mg) was weighed out in a 20-mL scintillation vial. Dimethyl sulfoxide (10 mL) was added to this vial, followed by concentrated aqueous hydrochloric acid (0.350 mL, 1 equiv. to linker). This mixture was stirred at room temperature overnight. The resulting solid was isolated by centrifugation and washed once with methanol (10 mL), then dried in a vacuum oven overnight. This solid (4-1@UiO-66-NH<sub>3</sub><sup>+</sup>) was confirmed to have maintained crystallinity by powder x-ray diffraction and catalyst retention was confirmed by ICP-OES spectroscopy.

**Synthesis of 4-2@UiO-66-X and 4-2@UiO-67-NH<sub>2</sub>.** In an inert atmosphere glovebox, acetonitrile (10 mL) was added to a 20-mL scintillation vial in a glovebox. UiO-



66 (200 mg) and (<sup>t</sup>BuPNN)Ru(CO)HCl (3.0 mg, 6.1 μmol) were added to the vial, which was then sealed. This mixture was heated at 55 °C for five days, and then allowed to cool to room temperature. The resulting mixture was brought into a glovebox. The vial was unsealed, and the resultant mixture was transferred to a 20 mL scintillation vial and subjected to centrifugation. Trituration was achieved by decanting the supernatant from this mixture, which was set aside for NMR analysis. The remaining solid was further triturated three times with methanol (10 mL) each time using centrifugation to ensure quantitative mass transfer. After three washing cycles, 190 mg (95%) of a pale orange solid was obtained. This solid was dried overnight in a vacuum chamber. A portion of this material was suspended in 15 mL of degassed DMF, and then transferred as a slurry to a 20 mL ampule containing a stir bar using a 9" glass pipet. Ethanol (2.92 mL, 50.0 mmol) was added to this ampule. The ampule was added to a 450-mL stainless steel Parr reactor. The vessel was purged with carbon dioxide for 5 minutes and then pressurized to 42 psi. The vessel was then pressurized with hydrogen gas to achieve a total pressure of 560 psi at room temperature. The reactor was heated to 135 °C and left to react for 16 hours. The heating mantle was removed, the reactor was cooled using a room-temperature water bath, and the pressure was released slowly from the vessel. The vessel was opened and the ampule was removed. The reaction mixture was transferred as a slurry to a 20-mL scintillation vial and subjected to centrifugation at 3000 revolutions per minute for 10 minutes, after which the supernatant was decanted. The solid was triturated twice with methanol (20 mL) followed by centrifugation and dried overnight in a vacuum chamber to give a pale orange powder. The loading of catalyst in the MOF was determined by ICP-

OES (see “Digestion of UiO-66 for ICP-OES analysis”, below). The structural integrity of the solid was confirmed by powder x-ray diffraction.

**Digestion of UiO-66-X for ICP-OES analysis.** Solid MOF material (5.00 mg) was weight out into a 1.5 mL Teflon vial. DMSO (300  $\mu$ L) and 1 drop of 15 wt.% aqueous hydrofluoric acid solution were added in sequence. The mixture was sonicated for 1 minute and left to digest for 1 hour. The digested samples then heated to approximately 150 °C overnight in a sand bath open to the air to remove solvent. The resulting solid was dissolved and transferred to a 20 mL glass scintillation vial using a mixture (10% v/v) of hydrochloric acid in deionized water (300  $\mu$ L). Each sample was diluted with additional deionized water (3.7 mL) and analyzed by ICP-OES.

**ICP-OES Standard preparation.** Five standards were prepared by dilution from commercially available zirconium ( $999 \pm 5$  ppm), ruthenium ( $999 \pm 5$  ppm), and phosphorus ( $100.04 \pm 0.55$  ppm) standards using serial dilution in grade A volumetric glassware to cover the expected concentration ranges. The standards were then employed in a calibration curve to determine the loading of catalyst in a tested solid. These standards consisted of Zr/Ru/P concentrations in ppm at the proportions: 250/5/5, 150/2/2, 25/0.5/0.5, 2.5/0.05/0.05

**General procedure for cascade hydrogenation of CO<sub>2</sub> to methanol.** Encapsulated catalyst (10 mg) was weighed out and added to a 20-mL scintillation vial. Exogenous catalyst ( $2.23 \times 10^{-7}$  mmol, diluted from greater mass on bench) was weighed out in a glovebox and added to a 4-mL scintillation vial. These vials were sealed and removed from the glovebox. Anhydrous N,N'-dimethylformamide (3 mL) was added to the 4-mL vial. The hybrid catalyst was suspended in this solution and wet-transferred to a

5mL ampule using a glass 9" pipet. 2,2,2-trifluoroethanol (0.720 mL, 10.0 mmol) was added to this ampule. The ampule was added to a 450-mL stainless steel Parr instrument pressure vessel. The vessel was purged with CO<sub>2</sub> for 5 minutes and then pressurized to 42 psi, then pressurized with H<sub>2</sub> to 560 psi at room temperature. The reactor was heated to 70 °C and left to react for 2 hours. Upon conclusion of the reaction, the heating mantle was removed, the reactor was cooled using a room-temperature water bath, and the pressure was released slowly from the vessel. The vessel was opened and the ampules were removed. The reaction mixtures were wet-transferred to 20-mL scintillation vials and subjected to centrifugation at 3000 revolutions per minute for 10 min, after which the supernatants were decanted and set aside. An aliquot of the reaction mixture (0.25 ml), tetrachloroethane (0.01 mL), and CDCl<sub>3</sub> (0.45 mL) were each added to a small vial. This mixture was then added to an NMR tube using a 9" glass pipet. TON was determined by <sup>1</sup>H-NMR using tetrachloroethane as an external standard.

**General procedure for esterification.** UiO-66-X (10 mg) was weighed out and added to a 20-mL scintillation vial. Anhydrous N,N'-dimethylformamide (3 mL) was added to this vial. Formic acid (0.337 mL, 10.0 mmol) and alcohol additive (10.0 mmol) were added to this mixture. The vial was sealed and heated at 70 °C for the denoted time. The supernatant was separated by centrifugation. An aliquot of the reaction mixture (0.25 ml), tetrachloroethane (0.01 mL), and CDCl<sub>3</sub> (0.45 mL) were each added to a small vial. This mixture was then added to an NMR tube using a 9" glass pipet. Percent conversion was determined by <sup>1</sup>H-NMR using tetrachloroethane as an external standard.

**Recycling of 4-1@UiO-66-NH<sub>3</sub><sup>+</sup> + 4-2@UiO-66.** 4-1@UiO-66-NH<sub>3</sub><sup>+</sup> (5.60\*10<sup>-7</sup> mmol Ru) and 4-2@UiO-66 (5.60\*10<sup>-7</sup> mmol Ru) were weighed out separately. Carbon

dioxide hydrogenation was carried out using the “general procedure for cascade hydrogenation of CO<sub>2</sub> to methanol” at 5x scale in a 20-mL ampule. The solid was washed twice with methanol (20 mL) and dried overnight in a vacuum chamber between cycles.

**Digestion of R6G@UiO-66-X.** R6G@UiO-66-X (5 mg) was added to a 1.5-mL centrifuge tube. Dimethylsulfoxide (1.5 mL) was added to each sample. One drop of 15 wt% aqueous hydrofluoric acid was added to each sample, which was then left to digest overnight. Each sample was then neutralized using excess sodium bicarbonate and subjected to centrifugation. Fluorescence measurements were taken in quartz cuvettes with excitation at 530 nm.

**Deuterium exchange for 4-1@UiO-66-ND<sub>3</sub><sup>+</sup>.** 4-1@UiO-66-NH<sub>2</sub> (10 mg) was weighed out in a 20-mL scintillation vial. Methanol-d<sub>4</sub> (4 mL) was added to this vial, which was then sonicated for 10 seconds and left to sit for 5 minutes. The mixture was then subjected to centrifugation and the supernatant was removed. This process was repeated four times. The solid was dried overnight in a vacuum chamber. A solution of DCl (350 μL) in DMSO-d<sub>6</sub> (10 mL) was added to the vial, which was left to stir overnight. This mixture was subjected to centrifugation and the supernatant was removed. The solid was washed three times with methanol-d<sub>4</sub> (2 mL), then left to dry overnight in a vacuum chamber.

**Potentiometric titration of UiO-66-NH<sub>3</sub><sup>+</sup>.** UiO-66-NH<sub>3</sub><sup>+</sup> (10 mg) was added to a 20-mL scintillation vial. Deionized water (10 mL) was added to this vial. The initial pH of the mixture was recorded using a potentiometer. A solution of sodium hydroxide in deionized water was added in 10-μL increments from a buret, with potentiometer readings recorded after readings stabilized for ten seconds.

**NMR titration of UiO-66-NH<sub>3</sub><sup>+</sup>.** This procedure was adapted from literature<sup>33</sup> UiO-66-NH<sub>3</sub><sup>+</sup> was added to a 4-mL scintillation vial. D<sub>2</sub>O (450 μL) was added to this vial. Triethylamine was added in amounts noted. The number of equivalents of Bronsted acid present was determined by <sup>1</sup>H-NMR based on a calibration curve developed with known equivalents of acid to triethylamine. The resulting value was compared to the value obtained from potentiometric titration to confirm full linker protonation.

**Hydrogenation of carbon dioxide to formate by 4-1@UiO-66-X.** 4-1@UiO-66-X was suspended in 3 mL of degassed DMF, and then wet-transferred to 5-mL ampules using a glass 9" pipet. 1,8-diazabicyclo[5.4.0]undec-7-ene (DBU) (0.493 mL) was added to each ampule. These ampules were added to a 450-mL stainless steel Parr instrument pressure vessel. The vessel was placed on a Parr instrument stand atop a stir plate and surrounded by a heating mantle, then purged with CO<sub>2</sub> for 5 minutes and then pressurized to 42 psi, then pressurized with H<sub>2</sub> to 212 psi at room temperature. The mixtures were left to react for 30 minutes. Upon conclusion of the reaction, the heating mantle was removed and the pressure was released slowly from the vessel. The vessel was opened and the ampules were removed. The heterogeneous catalysis mixtures were wet-transferred to 20-mL scintillation vials and subjected to centrifugation, after which the supernatant was decanted. An aliquot of each reaction mixture (0.25 mL), Benzene (0.01 mL), and D<sub>2</sub>O (0.45 mL) were each added to small vials. These mixtures were then added to individual NMR tubes using 9" glass pipets. <sup>1</sup>H NMR was used to determine the yield of formate via integration of the formate peak in reference to benzene.

## References

1. S. D. Brown, P. C. Babbitt. New insights about enzyme evolution from large scale studies of sequence and structure relationships. *J. Biol. Chem.* **289**, 30221-30228. (2014).
2. S. M. Cuesta, S. A. Rahman, N. Furnham, J. M. Thornton. The classification and evolution of enzyme function. *Biophysical Journal*. **109**, 1082-1086. (2015).
3. Z. Li, D. Wang, Y. Wu, Y. Li. Recent advances in the precise control of isolated single-site catalysts by chemical methods. *National Science Review*. **5**, 673–689. (2018).
4. X.-M. Liu, G. Q. Lu, Z.-F. Yan, J. Beltramini. Recent advances in catalysts for methanol synthesis via hydrogenation of CO and CO<sub>2</sub> *Ind. Eng. Chem. Res.* **42**, 6518-6530. (2003).
5. H. Valdés, M. A. García-Eleno, D. Canseco-Gonzalez, D. Morales-Morales. Recent advances in catalysis with transition-metal pincer compounds. *ChemCatChem*. **10**, 3136-3172. (2018).
6. D. M. Dalton, S. R. Ellis, E. M. Nichols, R. A. Mathies, F. D. Toste, R. G. Bergman, K. N. Raymond. Supramolecular Ga<sub>4</sub>L<sub>6</sub><sup>12-</sup> cage photosensitizes 1,3-rearrangement of encapsulated guest via photoinduced electron transfer. *J. Am. Chem. Soc.* **137**, 10128-10131. (2015).
7. A. Corma, H. Garcia. Supramolecular host-guest systems in zeolites prepared by ship-in-a-bottle synthesis. *European Journal of Inorganic Chemistry*. **6**, 1143-1164. (2004).
8. T. Wang, L. Gao, J. Hou, S. J. A. Herou, J. T. Griffiths, W. Li, J. Dong, S. Gao, M.-M. Titirici, R. V. Kumar, A. K. Cheetham, X. Bao, Q. Fu, S. K. Smoukov. Rational approach to guest confinement inside MOF cavities for low-temperature catalysis. *Nature Communications*. **10**, Article number: 1340. (2019).
9. Z. Li, T. M. Rayder, L. Luo, J. A. Byers, C.-K. Tsung. Aperture-opening encapsulation of a transition metal catalyst in a metal–organic framework for CO<sub>2</sub> hydrogenation. *J. Am. Chem. Soc.* **140**, 8082-8085. (2018).
10. T. M. Rayder, E. H. Adillon, J. A. Byers, C.-K. Tsung. A Bioinspired Multicomponent Catalytic System for Converting Carbon Dioxide into Methanol Autocatalytically. *Chem. In Press*. (2020). DOI: 10.1016/j.chempr.2020.04.008
11. P. K. Robinson. Enzymes: principles and biotechnological applications. *Essays Biochem.* **59**, 1-41. (2015).
12. D. J. Xiao, J. Oktawiec, P. J. Milner, J. R. Long. Pore Environment Effects on Catalytic Cyclohexane Oxidation in Expanded Fe<sub>2</sub>(dobdc) Analogues. *J. Am. Chem. Soc.* **138**, 14371-14379. (2016).
13. X. Li, W. W. Goh, L. Li, C. Xiao, Z. Guo, X. C. Zeng, W. Huang. Controlling Catalytic Properties of Pd Nanoclusters through Their Chemical Environment at the Atomic Level Using Isorecticular Metal-Organic Frameworks. *ACS Catal.* **6**, 3461-3468. (2016).
14. W. Liang, H. Xu, F. Carraro, N. K. Maddigan, Q. Li, S. G. Bell, D. M. Huang, A. Tarzia, M. B. Solomon, H. Amenitsch, L. Vaccari, C. J. Sumby, P. Falcaro, C. J. Doonan. Enhanced Activity of Enzymes Encapsulated in Hydrophilic Metal-Organic Frameworks. *J. Am. Chem. Soc.* **141**, 2348-2355. (2019).

15. S. A. A. Razavi, A. Morsali. Function-Structure Relationship in Metal-Organic Frameworks for Mild, Green, and Fast Catalytic C-C Bond Formation. *Inorg. Chem.* **58**, 14429. (2019).
16. B. M. Trost, R. C. Bunt. On Ligand Design for Catalytic Outer Sphere Reactions: A Simple Asymmetric Synthesis of Vinylglycinol. *Angew. Chem. Int. Edit.* **35**, 99-102. (1996).
17. S. Carboni, C. Gennari, L. Pignataro, U. Piarulli. Supramolecular ligand-ligand and ligand-substrate interactions for highly selective transition metal catalysis. *Dalton T.* **40**, 4355-4373. (2011).
18. D. E. Prokopchuck, R. H. Morris. Inner-Sphere Activation, Outer-Sphere Catalysis: Theoretical Study on the Mechanism of Transfer Hydrogenation of Ketones Using Iron(II) PNNP Eneamido Complexes. *Organometallics.* **31**, 7375-7385. (2012).
19. J. L. Bolliger, A. M. Belenguer, J. R. Nitschke. Enantiopure Water-Soluble [Fe<sub>4</sub>L<sub>6</sub>] Cages: Host-Guest Chemistry and Catalytic Activity. *Angew. Chem. Int. Edit.* **52**, 7958-7962. (2013).
20. V. Ramamurthy, J. Sivaguru. Controlling Photoreactions Through Noncovalent Interactions within Zeolite Nanocages. In *Supramolecular Photochemistry: Controlling Photochemical Processes*. Ramamurthy, V. and Inoue, Y. Eds. Wiley. **2011**. pp. 389-442.
21. J. Klimeš, D. P. Tew. Efficient and accurate description of adsorption in zeolites. *J. Chem. Phys.* **151**, 243108. (2019).
22. S. Mollick, S. Fajal, S. Mukherjee, S. K. Ghosh. Stabilizing Metal-Organic Polyhedra (MOP): Issues and Strategies. *Chem.-Asian J.* **14**, 3096-3108. (2019).
23. M. Moshoeshe, M. S. Nadiye-Tabbiruka, V. Obuseng. A Review of the Chemistry, Structure, Properties, and Applications of Zeolites. *Am. J. Mater. Sci.* **7**, 196-221. (2017).
24. P. Z. Moghadam, A. Li, S. B. Wiggin, A. Tao, A. G. P. Maloney, P. A. Wood, S. C. Ward, D. Fairen-Jimenez. Development of a Cambridge Structural Database Subset: A Collection of Metal-Organic Frameworks for Past, Present, and Future. *Chem. Mater.* **29**, 2618-2625. (2017).
25. S. M. Cohen. The Postsynthetic Renaissance in Porous Solids. *J. Am. Chem. Soc.* **139**, 2855-2863. (2017).
26. M. J. Katz, Z. J. Brown, Y. J. Colon, P. W. Siu, K. A. Scheidt, R. Q. Snurr, J. T. Hupp, O. K. Farha. A facile synthesis of UiO-66, UiO-67 and their derivatives. *Chem. Comm.* **82**, 9449-9451. (2013).
27. M. Kalaj, J. M. Palomba, K. C. Bentz, S. M. Cohen. Multiple functional groups in UiO-66 improve chemical warfare agent simulant degradation. *Chem. Commun.* **55**, 5367-5370. (2019).
28. Y. Katayama, K. C. Bentz, S. M. Cohen. Defect-Free MOF-Based Mixed-Matrix Membranes Obtained by Corona Cross-Linking. *ACS Appl. Mater. Interfaces.* **11**, 13029-13037. (2019).
29. C. J. Doonan, W. Morris, H. Furukawa, O. M. Yaghi. Isoreticular Metalation of Metal-Organic Frameworks. *J. Am. Chem. Soc.* **131**, 9492-9493. (2009).
30. S. Kar, R. Sen, J. Kothandaraman, A. Goepfert, R. Chowdhury, S. B. Munoz, R. Haiges, G. K. S. Prakash. Mechanistic insights into ruthenium -pincer-catalyzed amine-

- assisted homogeneous hydrogenation of CO<sub>2</sub> to methanol. *J. Am. Chem. Soc.* **141**, 3160-3170. (2019).
31. M. Everett, D. F. Wass. Highly productive CO<sub>2</sub> hydrogenation to methanol – a tandem catalytic approach via amide intermediates. *Chem. Commun.* **53**, 95029504. (2017).
  32. Z. Li. Design of a Host-guest Hybrid Catalytic System Through Aperture-opening Encapsulation Using Metal-Organic Framework. PhD Thesis, Boston College, Chestnut Hill, MA.
  33. K. M. Choi, K. Na, G. A. Somorjai, O. M. Yaghi. Chemical Environment Control and Enhanced Catalytic Performance of Platinum Nanoparticles Embedded in Nanocrystalline Metal–Organic Frameworks. *J. Am. Chem. Soc.* **137**, 7810-7816. (2015).
  34. G. A. Filonenko, E. J. M. Hensen, E. A. Pidko. Mechanism of CO<sub>2</sub> hydrogenation to formates by homogeneous Ru-PNP pincer catalyst: from a theoretical description to performance optimization. *Catal. Sci. Technol.* **4**, 3474-3485. (2014).
  35. F. G. Cirujano, A. Corma, F. X. Llabres i Xamena. Conversion of levulinic acid into chemicals: synthesis of biomass derived levulinate esters over Zr-containing MOFs. *Chem. Eng. Sci.* **124**, 52-60. (2015).
  36. M. J. Hanton, S. Tin, B. J. Boardman, P. Miller. Ruthenium-catalysed hydrogenation of esters using tripodal phosphine ligands. *J. Mol. Catal. A-Chem.* **346**, 70-78. (2011).
  37. B. J. Burger, J. E. Bercaw. Vacuum Line Techniques for Handling Air-Sensitive Organometallic Compounds. In *Experimental Organometallic Chemistry*; Wayda, A. L. and Darensbourg M. Y. Eds.; ACS Symposium Series 357; American Chemical Society: Washington D.C. **1987**, pp 79-115.
  38. G. C. Shearer, S. Chavan, J. Ethiraj, J. G. Vitillo, S. Svelle, U. Olsbye, C. Lamberti, S. Bordiga, K. P. Lillerud. Tuned to Perfection: Ironing Out the Defects in Metal–Organic Framework UiO-66. *Chem. Mater.* **26**, 4068-4071. (2014).
  39. M. J. Katz, Z. J. Brown, Y. J. Colon, P. W. Siu, K. A. Scheidt, R. Q. Snurr, J. T. Hupp, O. K. Farha. A facile synthesis of UiO-66, UiO-67 and their derivatives. *Chem. Comm.* **82**, 9449-9451. (2013).
  40. D. Hermann, M. Gandelman, H. Rozenberg, L. J. W. Shimon, D. Milstein. Synthesis, structure, and reactivity of new rhodium and iridium complexes, bearing a highly electron-donating PNP system. Iridium-mediated vinylic C-H bond activation. *Organometallics*. **21**, 812-818. (2002).
  41. G. A. Filonenko, R. Van Putten, E. N. Schulpen, E. J. M. Hensen, and E. A. Pidko. Highly efficient reversible hydrogenation of carbon dioxide to formates using a ruthenium PNP-pincer catalyst. *ChemCatChem*. **6**, 1526-1530. (2014).
  42. T. Garber, S. V. Wallendaal, D. P. Rillema, M. Kirk, W. Hatfield, J. H. Welch, P. Singh. A novel copper(II) complex containing the ligand 1,2-bis(2,2'-bipyridyl-6-yl)ethane: structural, magnetic, redox, and spectral properties. *Inorg. Chem.* **29**, 2863-2868. (1990).
  43. E. Balaraman, B. Gnanaprakasam, L. J. W. Shimon, and D. Milstein. Direct Hydrogenation of Amides to Alcohols and Amines under Mild Conditions. *J. Am. Chem. Soc.* **132**, 16756-16758. (2010).